UAB
Universitat Autònoma de Barcelona

Functional nanostructured molecular materials for antimicrobial and biosensing applications

Xavier Rodríguez Rodríguez

ADVERTIMENT. L'accés als continguts d'aquesta tesi queda condicionat a l'acceptació de les condicions d'ús establertes per la següent llicència Creative Commons:  https://creativecommons.org/licenses/?lang=ca

ADVERTENCIA. El acceso a los contenidos de esta tesis queda condicionado a la aceptación de las condiciones de uso establecidas por la siguiente licencia Creative Commons:  https://creativecommons.org/licenses/?lang=es

WARNING. The access to the contents of this doctoral thesis it is limited to the acceptance of the use conditions set by the following Creative Commons license:  https://creativecommons.org/licenses/?lang=en

Universitat Autònoma de Barcelona

Functional nanostructured molecular materials for antimicrobial and biosensing applications

Xavier Rodríguez Rodríguez

Doctoral Thesis

PhD Programme in Materials Science

Directors: Dr. Judith Guasch and Dr. Imma Ratera

Tutor: Dr. Imma Ratera

Chemistry Department, Science Faculty

2024

This Thesis is presented to obtain the degree of Doctor of Philosophy by:

Xavier Rodríguez Rodríguez

Accepted by:

Dr. Imma Ratera

Dr. Judith Guasch

Bellaterra, May 2024

Dr. IMMA RATERA and Dr. JUDITH GUASCH Scientific Researcher of the Spanish Research Council at the Materials Science Institute of Barcelona (ICMAB-CSIC)

CERTIFIY

That **Xavier Rodríguez Rodríguez**, master's degree in advanced Nanoscience and Nanotechnology, has performed, under their supervision, the research entitled " **Functional nanostructured molecular materials for antimicrobial and biosensing applications**". This work has been performed under the framework of the Materials Science PhD program of the Chemistry Department of the Autonomous University of Barcelona.

And in witness of this, below this is signed,

Directors

Dr. Imma Ratera

Dr. Judith Guasch

Bellaterra, May 2024

Preface

This thesis has been presented as a compendium of publications. As such, the results presented herein are divided in five chapters. The first chapter is an introduction of the topic. The second and the fifth chapters correspond to two published research articles, which are preceded by an introduction and a summary of my contribution. The third chapter corresponds to a submitted publication and the fourth one corresponds to results obtained during the development of this thesis in a work that is still ongoing.

Acknowledgements

És un honor per mi expressar el meu sincer agraïment a totes les persones que han contribuït directa o indirectament a la realització d'aquesta tesi doctoral. Sense el suport, la orientació i l'encoratjament de molts de vosaltres, aquesta investigació no hauria estat possible.

En primer lloc, vull agrair a les meves directores de tesi, la Dra. Imma Ratera i Dra. Judith Guasch, per la seva paciència, el seu suport continu i la seva confiança en mi durant tot el procés. La seva dedicació i coneixement han estat fonamentals per al desenvolupament d'aquest treball. Estic molt content d'haver tingut l'oportunitat de fer el meu doctorat aquí amb vosaltres i, malgrat molta gent diu que es un camí difícil i que molts cops pensa en deixar-ho, res més lluny de la realitat, he estat molt a gust i m'enduc un record molt bonic. No em queda més que tornar-vos a donar les gràcies per tot el vostre suport durant tots aquests anys.

En segon lloc, a tot el consorci del projecte de la Marató amb els que he treballat aquests darrers anys. A les doctores Anna Arís i Elena García i als doctors Ramon Roca i Adrià López de l'IRTA, als doctors Oriol Gasch i Oscar Quijada, a la Paula Bierge i a la Inma Gómez del Parc Taulí de Sabadell i al professor Josep Maria Miró i a la doctora Cristina García de l'hospital Clínic de Barcelona. Moltes gràcies a tots pel vostre suport, les vostres idees i per crear un grup de feina tan exquisit. Espero que la nostra vida professional ens torni a ajuntar en algun moment. Una especial menció també al professor Jaume Veciana, gràcies per aportar llum amb les teves idees, comentaris i preguntes.

M'agradaria fer una especial menció a certes persones que han estat claus per a la realització d'aquesta tesi tan en l'àmbit acadèmic com en el personal. En primer lloc, a la ja Dra. Nerea González per tots els consells, totes les estones de xerrameca al laboratori mentre esperàvem que pugessin els dissolvents per les interminables plaques de capa fina i tota l'ajuda que m'has donat. Moitas grazas e bo nadal. En segon lloc, a la Sara Ruiz per totes les experiències viscudes aquests darrers 4 anys. Tot el suport que he rebut de tu, els consells, els "cotilleos", alguna que altra setmana sense dirigir-nos la paraula i les festes que se'ns dubte quedaran a la nostra memòria t'han convertit en una companya de feina excepcional i iiremplaçable. En tercer lloc, a la Sara Garrido per totes les converses i discussions, en català perfecte, tan productives que hem tingut, tots els esmorzars i dinars, sobretot els dilluns després d'un cap de setmana dur, i els riures que ens hem fet. Moltes gràcies per ser la meva veïna d'oficina i per portar-me sempre la contrària. A la Judit Tomsen per aguantar els meus comentaris i per les converses tan profundes que hem tingut al confocal. Al Guillem Vargas per aguantar-me durant 12 llargs anys i per ajudar-me en qualsevol cosa que he necessitat. Al Marc Martínez per tots els problemes que m'has resolt i per estar sempre disposat a ajudar. A l'Eduardo Pérez per tots els moments que hem compartit al laboratori, sobretot la meva primera purificació, i per tots els "jo mai mai" que tantíssims bons moments ens ha regalat. Al

David Piña, amb el qui a partir d'ara treballaré més conjuntament, per tota l'ajuda que m'has donat i per les nostres discussions tan enriquidores, en les que òbviament mai tenies raó. A l'Adrián Rodríguez per tots els "cotilleos" i els somriures que m'has tret. Al Miquel Castellote per les grans partides d'escacs que hem compartit i per aportar llum a discussions amb comentaris clau que m'han tret molt somriures. A la Francesca Merlina per ensenyar-me italià de la manera més graciosa. A més, vull donar les gràcies als companys de despatx i a tots els membres del grup de Nanomol per la seva assistència i suport durant aquesta etapa de la meva vida acadèmica. Les seves idees i discussions han estat inspiradores i enriquidores: Ruben García, Júlia Piqué, Laia Avilés, Aida Carreño, Ehsan Shirdel, Núria Pujol, Elba Guasch i als que segur que em deixo que per aquí ha passat molta gent.

Mirant una mica els inicis d'aquest llarg viatge m'agradaria agrair tot el coneixement que m'han inculcat tan professional com personalment a l'Adriana Kyvik, al Tommaso Salzillo, al Mario Juárez i a l'Adrián Tamayo. També al "lunch team", composat pel Sergi Riera, el Raphael Pfattner i la Judith Guasch, on hem viscut grans moments a les diferents cafeteries del campus.

Dins de l'institut també voldria mencionar persones d'altres grups que han tingut la seva contribució en el meu dia a dia a la feina. Al Ferran Vallés pels grans partits de pàdel que hem disputat i la gran rivalitat als tornejos de ping-pong pels quals hauries d'entrenar una mica que ja estic cansat de guanyar, a l'Amanda Muñoz per tots els consells i l'ajuda tan en l'àmbit d'investigació com en el descobriment de la Rioja i al Mario Villa pels consells gastronòmics sobre la ciutat de Madrid i les festes que hem compartit. Per últim, al nou equip d'esmorzars i de gimnàs que han fet de la recta final una situació mes suportable. Al Marc Mosqueda i al José Angel Algar, àlies "Pepe", per tots els riures i a la vegada patiments que hem passat al gimnàs. Agrair també a l'Adrián Crespo, a la Carla Torres, al Victor Vallejo, a la "Coco" i al Toni Miquel pels grans moments viscuts als curts esmorzars i dinars i les grans tardes de cerveses que hem compartit.

Després d'aquests llargs agraïments, puc afirmar que el temps en aquest institut m'ha brindat moments inoblidables amb persones que sens dubte espero que estiguin la resta de la meva vida i que puc considerar... AMICS. (si, ja ho he dit, pesats)

Ja per anar fent via, desitjaria també agrair el suport de la meva família, al meu germà al meu pare i a la meva àvia, i de la meva parella, la Cristina, que m'han acompanyat en tot aquest llarg trajecte ple d'emocions i d'altibaixos. La vostra influència i ajuda ha estat fonamental. I per últim, als meus amics; els de ben petitons: Rafel, Ricard, Rodri, Sergi, Ochavo, Plana i Uri, els del futsal: Carles, Kevin, Ot, Godi, Llucsi, Victor, Calle i Sergi, i un mix de pàdel i de la carrera: Gerard, Àlex, AlexRa, Sebas i Josep.

Abstract

This PhD thesis is devoted to functional nanostructured molecular materials for biological applications. Among the different types of nanostructured molecular materials, the research is based on self-assembled monolayers (SAMs) and organic nanoparticles (ONPs). SAMs were selected due to their high chemical versatility especially in the immobilization of biomolecules on surfaces, whereas ONPs are highly tuneable and interesting to be applied for sensing applications, in addition to their small size, biocompatibility and ease of processing.

In chapter 2, in light of the oncoming antibiotic crisis, a surface biofunctionalization strategy based on SAMs on gold is developed to successfully immobilize novel antimicrobial proteins made by recombinant DNA technology, thereby producing a bactericidal surface. Furthermore, the inhibition of biofilm growth by these surfaces is demonstrated, thus proving that the used proteins maintain their antimicrobial function even after they are immobilized.

In chapter 3, the gold model surface is adapted to a thermoplastic polyurethane (TPU) surface, which is the material used for medical devices such as catheters. In this case, TPU is functionalized with a mixed SAM via a three-step procedure to create antibiofilm surfaces. Additionally, these surfaces are characterized by a multi-technique approach based on contact angle (CA), Fourier transformed infrared spectroscopy (FTIR), X-ray photoelectron spectroscopy (XPS), atomic force microscopy (AFM), and scanning electron microscopy (SEM). Finally, a biofilm assay is performed to verify the antibacterial effect of the functionalized surface against three relevant bacteria strains in hospitals: *Pseudomonas aeruginosa* (gram-negative), methicillin-resistant *Staphylococcus aureus* (MRSA) (gram-positive) and *Staphylococcus Epidermidis* (gram-positive).

Chapter 4 focuses on actual medical devices, particularly catheters, made of TPU. These catheters are functionalized following the optimized three-step procedure of chapter 3 to finally perform *in vitro* static, *in vitro* dynamic and *in vivo* experiments. To increase the biocompatibility of the developed strategy, the catalyst used for the first activation step is changed to a greener one as a potential alternative to toxic catalysts. The stability of the functionalized catheter is demonstrated after a pressure flow, mimicking *in vivo* conditions, and also after sterilization with ethylene oxide and storage during 3 months at 37°C. *In vitro* static antibiofilm experiments are performed with promising results against methicillin-resistant *Staphylococcus aureus* (MRSE) strain. Finally, *in vivo* biofilm assays are carried out with the functionalized catheters in a rabbit model. The catheters do not prevent the formation of biofilm, which can be hypothesized that is due to the high inoculum used to infect the rabbits or its passivation caused by the complex *in vivo* environment. In conclusion, the established functionalization may be primarily used to prevent infections, rather than treating them once arisen. Moreover, it can be improved to enhance the accessibility of the active proteins to the biofilm-forming bacteria.

Finally, chapter 5 is focused on a different strategy to prepare nanostructured molecular materials for biomedical applications. Specifically, fluorescent ONPs made of trichlorotriphenylmethyl (TTM) radical are synthetized. The developed ONPs exhibit fluorescence at two distinct emission wavelengths, one associated to monomers and the other to excimer species. The excimer band, which is in the "first biological window", is investigated at various temperatures and exhibits highly sensitive ratiometric nanothermometer behaviour. Finally, these ONPs demonstrated to exhibit no cytotoxicity allowing the ratiometric nanothermometer to be used in an *in vivo* assay using *Caenorhabditis elegans* (*C. elegans*).

In summary, the strategies developed in this PhD thesis reside at the interface of materials science and biology and open new perspectives for the use of controlled nanostructured functional molecular materials for biomedical applications.

Abbreviations

μCP Micro-contact printing

AFM Atomic force microscope

AMPs Antimicrobial peptides

Ar Argon

ARMP Antimicrobial recombinant multidomain protein

ATR Attenuated total reflectance

Bi *Bismuth*

CA Contact angle

Cath Catheter

CAUTI Catheter-associated urinary tract infections

CRBSI Catheter-related bloodstream infections

CV Cyclic voltammetry

Cys *Cysteine*

DD *Dibutyltin dilaurate*

DLS Dynamic light scattering

EDL Electric double layer

EPR Electron paramagnetic resonance

FTIR Fourier-transform infrared

GFP *Green fluorescent protein*

GMPs *Good manufacturing practices*

HAIs Hospital-acquired infections

HD5 Human α-defensin 5

HDI *Hexamethylene diisocyanate*

HDPs *Host defense peptides*

His_6 Six histidine-tagged

IE Intensity of excimers

IM Intensity of monomers

IRTA Institute of agrifood research and technology

Mal Maleimide

MD *Medical device*

MRD *Modified Robbins Device*

MRSA Methicillin-resistant *Staphylococcus aureus*

MRSE Methicillin-resistant *Staphylococcus epidermidis*

MTT 3-[4,5-dimethylthiazol-2-yl]-2,5 diphenyl tetrazolium bromide

NI Nosocomial infections

Ni-NTA nickel (II)-chelated nitrilotriacetic acid

ONPs Organic nanoparticles

PBMCs *Peripheral blood mononuclear cells*

PDMS Polydimethylsiloxane

PEG Polyethylene glycol

pNP Protein nanocluster

PUs *Polyurethanes*

RMS *Root mean square*

ROIs Regions of interest

ROS Reactive oxygen species

RT Room temperature

S Sensitivity

SAMs Self assembled monolayers

SEM Scanning electron microscopy

SH-NTA NTA terminated tiol

TEM Transmission electron microscopy

THF Tetrahydrofuran

TPU Thermoplastic polyurethane

TTBrM Tris(2,4,6-tribromophenyl) methyl

TTM-*α*H tris(2,4,6-trichlorophenyl)methane

TTM Tris(2,4,6-trichlorophenyl) methyl

UV-Vis Ultraviolet-visible spectroscopy

XPS X-ray photoelectron

Contents

1 Introduction and Objectives 1

1.1 Functional nanostructured molecular materials for biological applications 1

1.1.1 Self-assembled monolayers 2

1.1.2 Organic nanoparticles 4

1.2 Analytical techniques for functional nanostructured materials characterization 5

1.2.1 Contact angle 5

1.2.2 X-ray photoelectron spectroscopy 5

1.2.3 Atomic force microscopy 6

1.2.4 Fourier-transform infrared spectroscopy 7

1.2.5 Scanning electron microscopy 8

1.2.6 Dynamic light scattering 9

1.3 Applications of functional nanostructured molecular materials for biological applications 9

1.3.1 SAMs for antimicrobial activity 10

1.3.2 Organic nanoparticles for biological applications 11

1.4 General objectives 12

1.5 References 13

2 Antibiofilm surfaces based on the immobilization of a novel recombinant antimicrobial multidomain protein using self-assembled monolayer 18

2.1 Introduction 18

2.2 Objectives 20

2.3 SAMs preparation 21

2.4 Multi-technique characterization 21

2.4.1 Fluorescence microscopy 21

2.4.2 X-ray photoelectron microscopy 22

2.5 Antimicrobial activity 23

2.6 Summary and future perspectives 24

2.7 References 25

Publication #1 27

3 Thermoplastic polyurethane surfaces activated with Human α-Defensin 5 self-assembled monolayers to prevent infections 47

3.1 Introduction 47

3.2 Objectives 50

3.3 Results 51

3.3.1 TPU discs fabrication 51

3.3.2 TPU surface activation and functionalization 51

3.3.3 Multi-technique characterization 52
3.4 Summary and future perspectives 56
3.5 References 57
Publication #2 60

4 Stable antibiofilm surface coating of thermoplastic polyurethane catheters – towards *in vivo* infection prevention 97
4.1 Introduction 97
4.2 Objectives 100
4.3 Functionalization of the discs with the new multidomain protein 101
4.4 Biocompatibility of the functionalized surfaces 102
4.5 Functionalization of medical grade TPU catheters 103
4.6 Biocompatibility of the functionalized TPU catheters 105
4.7 *In vitro* biofilm assay: static and dynamic models 105
4.7.1 *In vitro* static antibiofilm assay and stability study 105
4.7.2 *In vitro* dynamic antibiofilm assay 107
4.8 *In vivo* biofilm assay: rabbit model 108
4.9 Summary and future perspectives 109
4.10 References 110
Manuscript #1 114

5 A ratiometric nanothermometer based on radical excimer-based organic nanoparticles for in vivo sensing 143
5.1 Introduction 143
5.2 Objectives 145
5.3 ONPs preparation and characterization 146
5.4 Temperature dependence of excimer emission: reversibility study and sensitivity 147
5.5 Cell viability test 149
5.6 Local sensing of temperature 150
5.7 Summary and future perspectives 151
5.8 References 153
Publication #3 156

6 General conclusions and future perspectives 191

Annex I: Scientific contributions 193

Chapter 1
Introduction and objectives

1.1. Functional nanostructured molecular materials for biological applications

During the last few decades, molecule-based nanomaterials have received much attention in chemistry, materials science, and pharmaceutics/medicine, since their properties can vary significantly from the corresponding macro-sized bulk materials.[1] A "nanostructure" must have at least one of its dimensions within the range of 1 to 100 nm.[2] The two basic approaches to create functional nanomaterials are 'top-down' and 'bottom-up'.[3] The so-called top-down procedures—more associated with physical approaches—typically begin with macroscopic materials that are cut into smaller pieces using photolithography and other related processes. As a result of its relative simplicity and ability to produce several nanosystems in large quantities, this is the approach that is most used on an industrial scale. However, it faces severe restrictions for sizes smaller than 100 nm, particularly when it comes to the manufacture of electrical integrated circuits and does not offer an exhaustive control over both the structure's size and morphology.[4] Contrarily, bottom-up methods utilise and combine sub- or nanoscale items (atoms or molecules) to create nanostructures, which typically exhibit novel or distinctive functions. This strategy, which enables a more controlled system design, can be seen as the logical progression of supramolecular chemistry, which focuses on intermolecular bonding and examines the structures and functions of the entities created by the association of two or more chemical species. The primary drawback of this approach is large-scale synthesis, as its reproducibility and precision can be challenging (Figure 1.1).[4]

There are many types of nanostructures such as individual nanostructures, which involve clusters, nanoparticles, nanovesicles, nanocrystals, quantum dots, nanowires, and nanotubes, but also collections of nanostructures that involve arrays, self-assemblies, and superlattices of individual nanostructures.[5]

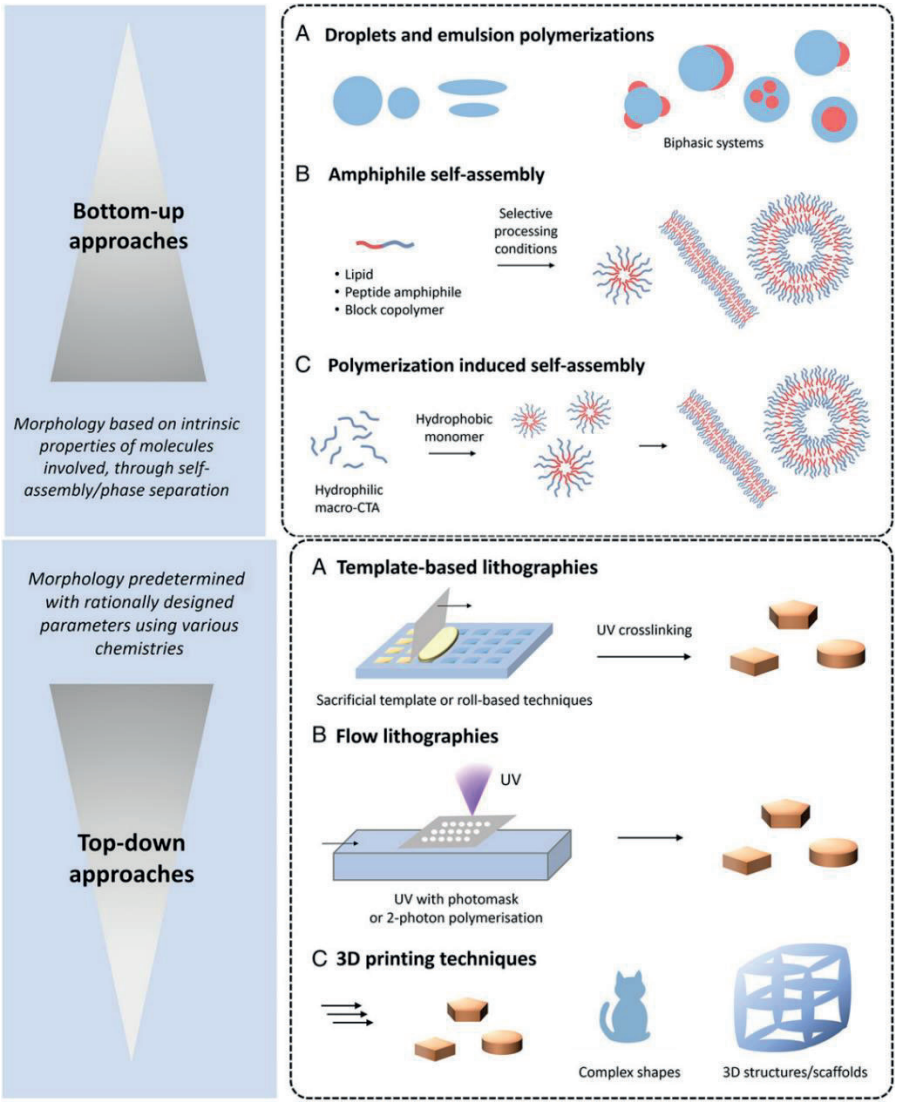


Figure 1.1. Bottom-up (left) and top-down (right) approaches to the formation of size- and shape-defined nanoparticles and microparticles.[4]

1.1.1. Self-assembled monolayers

One simple but effective bottom-up technique consists of the production of self-assembled monolayers (SAMs). The term "self-assembly" refers to the spontaneous formation of discrete units from simpler subunits or building blocks.[6] It offers a molecular-level control of material structure, composition, morphology, and dimensions, thus enabling the construction of an extensive variety of 1-, 2- and 3-D nanostructures.[7,8]

SAMs are highly oriented two-dimensional arrangements of molecules that form spontaneously on the surface of a variety of materials.[9,10] They are created by the chemisorption of the molecule onto a substrate from either vapor or liquid phase.[11] This self-assembly phenomenon was firstly observed in 1983 by Nuzzo and Allara, who reported the self-assembly of bifunctional dialkyl disulfides on gold covered surfaces.[12]

Molecules which form SAMs have a chemical "head" group, which binds moderately to strongly to the underlying substrate, a spacer group, generally an alkyl chain which

gives place to well-ordered monolayers through intermolecular Van der Waals interactions, as well as a terminal functional group, which confers the surface specific properties (Figure 1.2a). By carefully selecting the chemical structures of the molecules which form the SAM, resulting surface properties can be precisely tailored, down to the nanoscale. SAMs are most commonly formed by alkane thiols and disulfides on gold and silver, and by alkylsiloxanes on hydroxylated surfaces such as silica, glass, or alumina.[13]

The advantageous properties of SAMs are that (i) they are a technology platform and their preparation is easy, (ii) they allow studies which can probe the dependence of different biological signals in an independent way, (iii) they can be formed on surfaces which are translucid, allowing the observation of cells with inverted microscopes, and (iv) generally the molecules used for SAMs are commercially available.[14] Importantly, SAMs have provided a very useful platform for making fundamental research in different areas due to the ability to modify and choose different head and tail groups.[15]

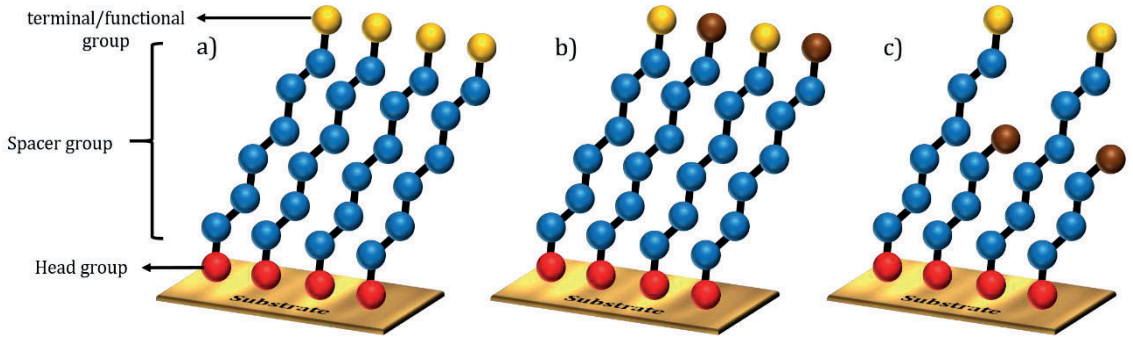


Figure 1.2. Schematic representation of three different SAM approaches. A) SAM of one single molecule, b) mixed SAM of two different molecules with the same length, and c) mixed SAM of two different molecules with different length to enhance the surface functionality or reactivity.

To ensure the exposure of functional groups and avoid steric hindrance, mixed SAMs are used. Mixed SAMs are constituted by two or more compounds (Figure 1.2b and c), one compound with a functional terminal group and another one for dilution and/or preventing nonspecific surface adsorption.[16] Mixed SAMs can also be used to provide multi-functional surfaces incorporating different reactive end groups (Figure 1.2b). For example, they can be used to control the overall hydrophilicity of the surface, which is particularly important in biosensing, or to increase its reactivity (Figure 1.2c).

One of the most popular techniques for SAM patterning is micro-contact printing (μCP), which spatially confines molecules to produce SAMs in a controlled manner. By stamping alkanethiols onto gold surfaces, μCP has been frequently utilized to create patterned SAMs.[17] Typically, an alkanethiol ink is applied to a prefabricated polydimethylsiloxane elastomeric stamp (PDMS stamp) before being applied to a gold surface. To do this, first of all, the stamps are prepared by mixing a variety of silicone oligomers with a curing agent, which hardens the polymer by interconnecting their chains. This mixture is then casted onto a silicon master mold that has been hydrophobically silanized and has the required pattern's template. The flexible PDMS stamp is obtained by peeling it away from the silicon master after curing. The solution

containing the SAM-forming molecules is then applied to the PDMS, either by submerging the stamp or by dabbing it with a few drops.[18]

In the end, the SAM is created when the stamp contacts the substrate's surface. This one displays the pattern transferred from the stamp after its peeling from the substrate. To generate a pattern in which two types of alkanethiols are restricted to particular locations, bare gold sections of already patterned surfaces can be backfilled with a different type of alkanethiol. For the purpose of preventing non-specific biomolecule adsorption on the functional surface, one of the alkanethiols often includes a pegylated spacer group. On the other hand, a hydrophobic alkanethiol is occasionally used for the adsorption of ECM proteins like fibronectin and laminin which is interesting for biological applications.[19]

1.1.2. Organic nanoparticles

Organic nanoparticles (ONPs) are organized structures consisting of molecular components with at least one dimension in the nanoscale, whose properties are given by the properties of these forming molecules. ONPs can be classified as solid ONPs, liposomes/vesicles, micelles, or polymeric assemblies (Figure 1.3). The use of organic molecules is appealing for tailoring the surface and properties of particles with specific functionalities. Additionally, their small size, biocompatibility, low cytotoxicity, and ease of processing make them highly advantageous. Consequently, ONPs are gaining interest in applications such as drug delivery, bioimaging, and phototherapy.[20]

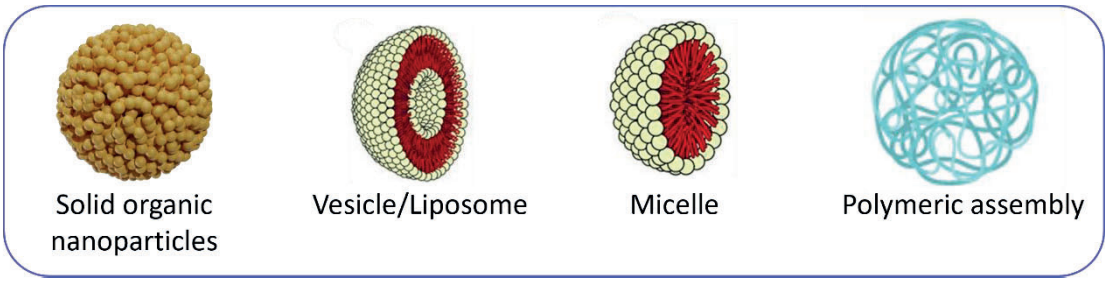


Figure 1.3. Organic nanoparticle classification.

There are different fabrication strategies to produce ONPs, being the most common ones those based on the "bottom-up" approach (for example, microemulsion, reprecipitation, and layer-by-layer assembling). Surfactants are used in some of them to stabilize the ONPs in the suspension, which may result in undesirable residues. (Figure 1.4).[21]

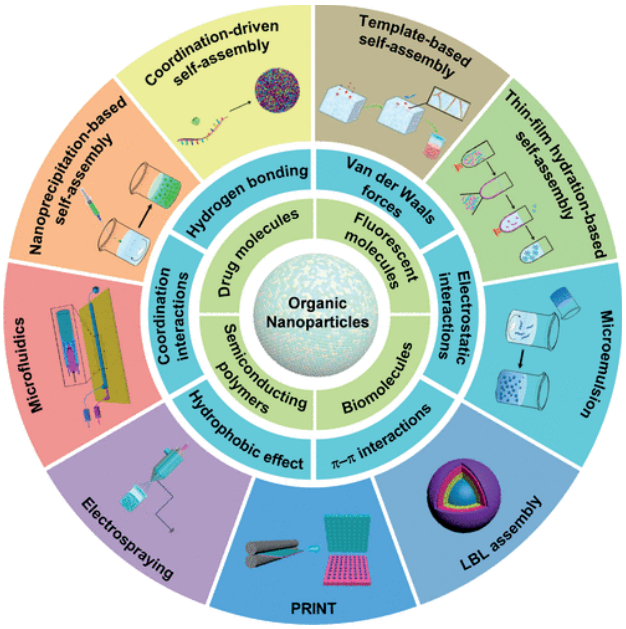


Figure 1.4. Illustration of the typical components, driving forces or methods for preparing organic nanoparticles.[22]

1.2. Analytical techniques for functional nanostructured materials characterization

Different techniques can be used to characterize SAMs, evaluating their quality or its chemical nature, which can be macroscopic or probe the film with molecular resolution.[23] Below, the techniques used in the research presented in this dissertation are briefly introduced.

1.2.1. Contact angle

The contact angle (CA) is employed to assess the hydrophobicity or hydrophilicity of surfaces. It involves placing a water droplet on a surface to measure the angle formed between the surface and the liquid. Surfaces that are more hydrophilic typically exhibit lower measured CAs, while hydrophobic surfaces tend to have higher contact angles (Figure 1.5). CA serves as a means to gauge the effectiveness of functionalization and evaluate surface wettability.[23]

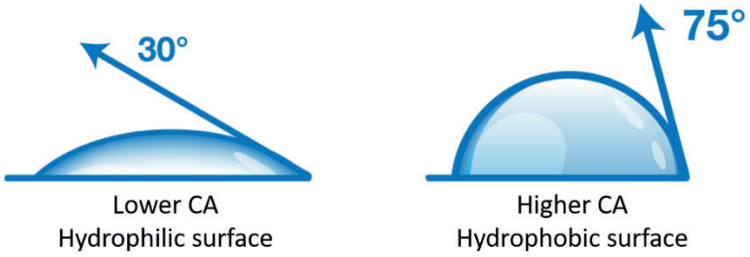


Figure 1.5. CA differences between a hydrophilic surface and a hydrophobic surface.

1.2.2. X-Ray photoelectron spectroscopy

X-ray photoelectron spectroscopy (XPS) is an analytical technique sensitive to surface properties, wherein x-rays bombard a material's surface and measure the kinetic energy

of emitted electrons. [24,25] Widely used for determining elemental composition and chemical environment near the surface (within 10 nm), XPS offers sensitivity as low as 0.1%. [26] The equipment utilized for XPS is a photoelectron spectrometer (Figure 1.6), operating on the principle of the photoelectric effect, where photons eject initially bound electrons from atoms/ions. Soft X-rays (with energies below ~6 keV) irradiate the sample, and the kinetic energy of emitted electrons is analyzed. [27] This energy is indicative of the electron's binding energy, providing insight into the element and its chemical environment.

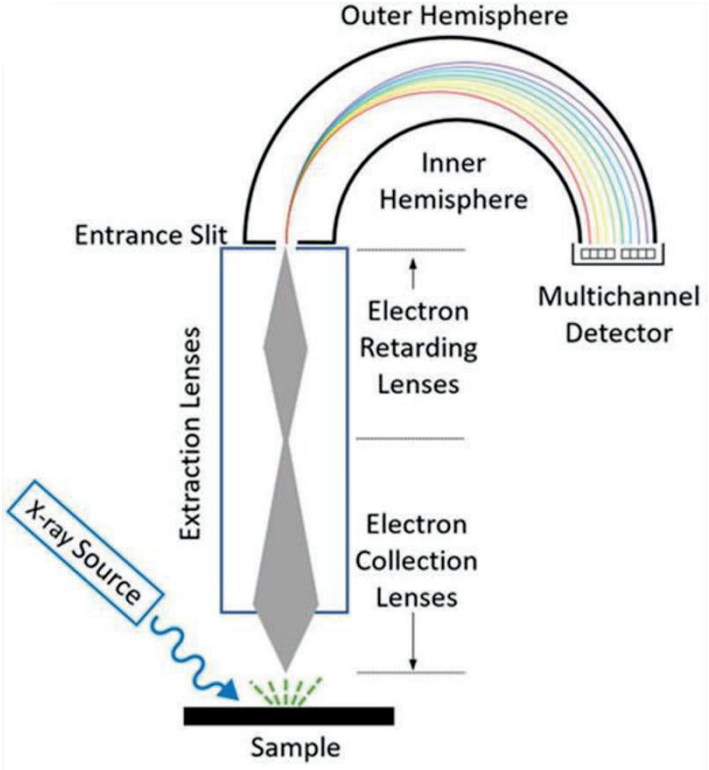


Figure 1.6. Main components of a photoelectron spectrometer.[29]

1.2.3. Atomic force microscopy

The atomic force microscope (AFM), developed in 1986, is a scanning near-field tool utilized for nanoscale investigations.[30] AFM enables the acquisition of structural information about surfaces with spatial resolutions reaching subnanometer levels. [31] Its fundamental principle involves scanning a sharp tip over a sample surface while detecting interactions between the tip and the sample. [32] This tip, attached to a flexible cantilever, is mounted on a piezoelectric material that serves as a three-dimensional scanner. During sample analysis, a laser diode emits a beam onto the cantilever's back, just above the tip. Interaction forces between the tip and the sample cause the cantilever to deflect, resulting in angular deflection of the reflected laser beam. The magnitude of this deflection is captured by a position-sensitive photodiode (Figure 1.7).[33]

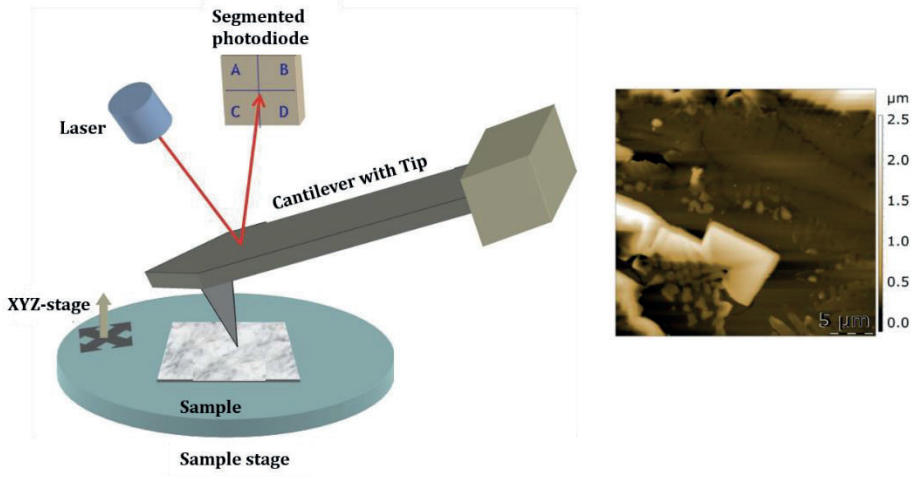


Figure 1.7. AFM working basic mechanism (left) and AFM topography image of a drop-casted solution of myoglobin on glass (right).

1.2.4. Fourier-transform infrared spectroscopy

The use of Fourier-transform infrared (FTIR) spectroscopy has been considered one of the most effective techniques to study and understand the chemistry of molecules and also surface chemistry.[34] IR or FTIR spectroscopy has a large application range, from the analysis of small molecules or molecular complexes to the analysis of cells and tissues.[35] Each molecule has a spectrum fingerprint that makes it unique and allows it to be distinguished from other molecules. In general, a molecule composed of N atoms displays 3N-6 vibrational degrees of freedom (3N-5 for linear molecules). This corresponds to the number of independent so-called normal modes of vibration. For them to be IR active, the electric dipole of the molecule must change.[36] The IR radiations then have impacts on the atomic vibrations of a molecule in the sample, resulting the specific absorption and/or transmission of energy.[37] The IR region of the electromagnetic spectrum ranges in wavelengths from 0.8–100 μm.

An alternative to transmission spectroscopy is the use of attenuated total reflectance (ATR). The ATR mode of IR spectroscopy allows the evaluation of analytes using minimal amount of the test sample. Moreover, it improves sample-to-sample reproducibility and reduces the user-to-user spectral variation. ATR-FTIR allows the analysis of penetration depth into the sample between 0.5 and 5 μm.[36,38] For ATR the IR beam is passed through a crystal of a material with a high refractive index (high optical density) at an angle greater than the so-called critical angle that leads to total internal reflection of the beam at the crystal surface that is in contact with the sample enhancing its sensitivity (Figure 1.8).[39]

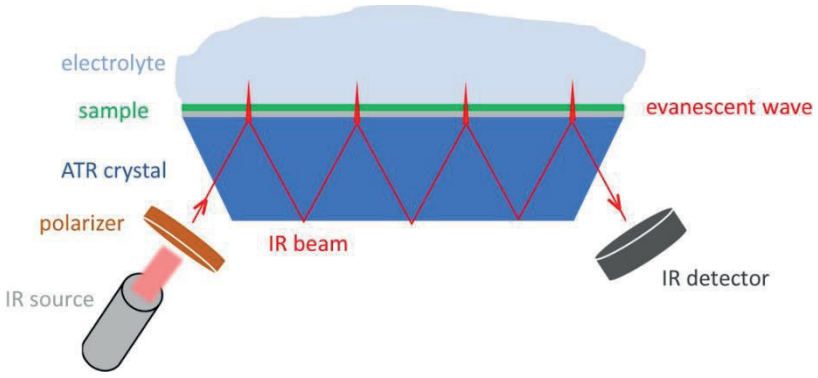


Figure 1.8. General principle of ATR-FTIR spectroscopy.[39]

1.2.5. Scanning electron microscopy

Scanning electron microscopy (SEM) was discovered in 1942 by Zworykin, Hillier, and Snijder.[40] Nowadays, it is widely used in many disciplines as an effective method to analyse organic and inorganic materials on a nanometer to micrometer scale. The SEM yields information about the morphology (shape and size of the particles), topography (surface features of an object), composition (the elements and compounds that make the object and their relative amounts), and crystallographic information (how the atoms are arranged in the object).[41]

The scanning electron microscopes work on high voltages between 2 to 50 kV. The electron gun at the top of the SEM operating column (Figure 1.9) produces an electron beam whose width ranges from 5 nm to 2 μm that is focused and scanned over the specimen surface. The SEM produces images (Figure 1.9) from three types of electron interaction with the specimen: secondary electron images, backscattered electrons, and electron dispersive spectroscopy utilizing X-ray scattering, which enables the user to analyse elemental composition.[42]

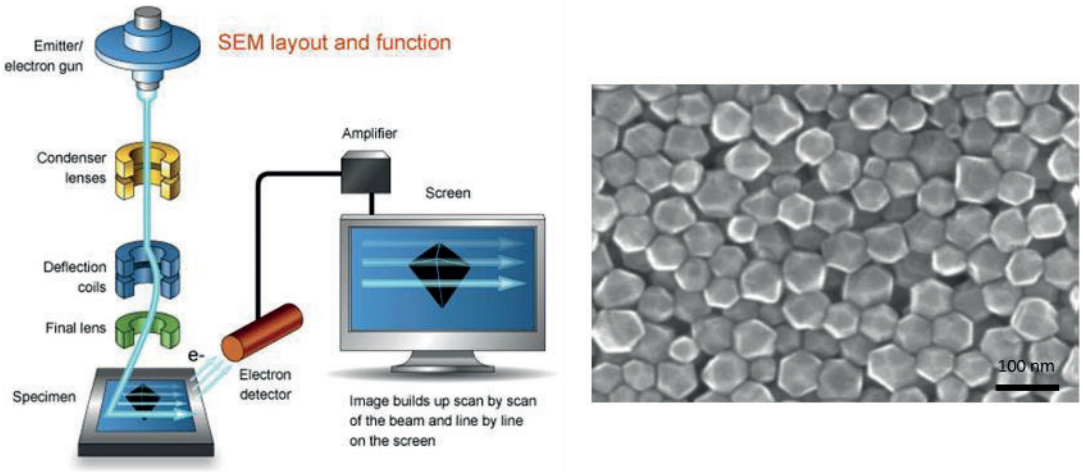


Figure 1.9. Scheme of all SEM components (left)[40] and an image of cobalt ferrite inorganic NPs (right) obtained by SEM.

1.2.6. Dynamic light scattering

Dynamic light scattering (DLS) is a technique for sizing submicron particles in suspensions and emulsions by monitoring the thermal motion (diffusion) (Figure 1.10). More specifically, DLS uses the time variation of scattered light from suspended particles moving with Brownian motion to determine their hydrodynamic size distribution.[43] Although the Stokes-Einstein equation, which links particle size and diffusion coefficient, is valid only for spherical particles at very low concentrations,[44] DLS has applications in many scientific fields.[43]

Along with size, the particles' surface charges can also be determined. The zeta-potential is a measure of potential at the slipping plane of a particle when subjected to an electrical field.[45] This potential represents the difference between the electric double layer (EDL) of mobile particles and the surrounding dispersant layer (aqueous or organic environment) at the slipping plane. The EDL, formed instantly in a particle solution, comprises a Stern layer of tightly coupled oppositely charged particles close to the particle's core, and an outer diffusive layer containing both oppositely and similarly charged ions/molecules. When an electrical field is applied, particles move towards the opposite electrode, and within the diffusive layer, a hypothetical slipping/shear plane acts as the interface between the moving particles and the surrounding dispersant layer. The zeta-potential is the potential measured at this particle-fluid interface.[45,46] The zeta-potential is measured by the electrophoretic mobility of charged particles under an applied electric field.[46]

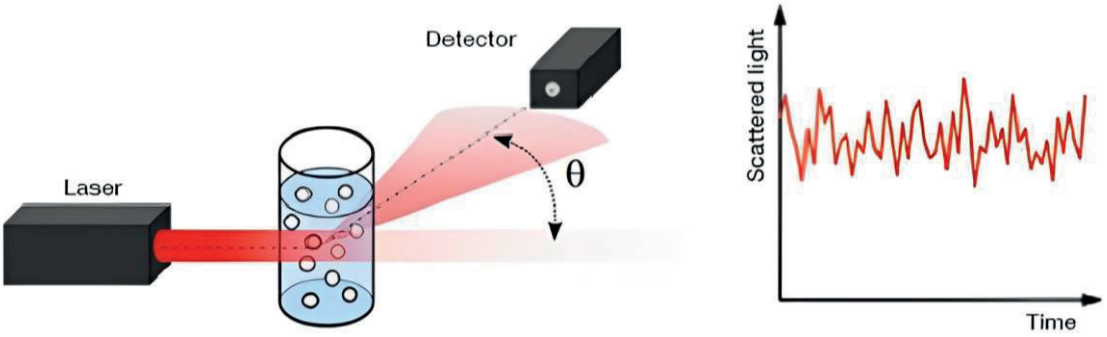


Figure 1.10. Principle of DLS: light scattered by fine particles illuminated with a laser is measured with high time resolution under a defined angle θ; the fluctuation of the scattering signal reflects the dynamics of microstructural processes such as the particles' Brownian motion.[47]

1.3. Applications of functional nanostructured molecular materials for biological applications

Over the past three decades, the synthesis and application of functional nanostructured molecular materials has become one of the most active and promising areas of research, positioned at the intersection of chemistry, materials science, bioengineering, and medicine. Considering the challenger that biomaterial science have been able to overcome, it is believed that the field of bioactive surfaces and nanoparticles will continue to grow tremendously in the future.[48]

1.3.1. SAMs for antimicrobial activity

Hospital-acquired (HAIs) or nosocomial infections (NI) are an important public health problem, due to the associated morbidity and mortality, and the economic burden that they represent for the healthcare system. In the last decades, the consequences of NI have become more severe due to the continuous emergence of antibiotic-resistant strains. In addition, biofilm formation on surfaces is a major concern as conventional antibiotics become ineffective against them.[49]

Scientists have tried to tackle this medical challenge with various antibiofilm approaches, spanning from chemical modification of implant surfaces to trigger a biocidal effect, to physical removal of the biofilm with shear stress, pressure, lasers, electric waves or enzymatic treatments, as well as the application of NPs or small molecules for the degradation of the extracellular matrix of the biofilms.[50] Among them, NPs of silver, gold, copper, titanium dioxide and zinc oxide have been extensively utilized as antibacterial agents.[51,52] These approaches provide an effective treatment, but they come with some drawbacks as they possess side effects which include cytotoxicity, short-term bacterial protection, and hypersensitivity.[53]

Antimicrobial surfaces can be classified in three different groups: anti-adhesive or repelling surfaces, surfaces treated with leaching antibacterial agents, and contact-killing surfaces (Figure 1.11). The first ones work by reducing the adhesion force between a solid surface and bacteria meaning that the bacteria can easily be removed before a biofilm is formed. Anti-adhesive strategies include superhydrophobic surfaces, zwitterionic polymers, and tailoring of surface nanostructures.[54] Antibacterial substrates incorporated with leaching type agents such as silver and triclosan show their activity as the encapsulated biocides leach out to kill bacteria.[55,56] However, as mentioned before, most of the leached biocides are cytotoxic and accumulate in the environment which makes this approach quite unsustainable. Moreover, the intensive use of such leaching biocides is one of the major reasons for bacterial resistance.[56] Contact-active surfaces work to kill microbes without the release of biocides and can be created by fixing certain biocides through covalent bonding.[57] Generally, they are based on (i) the optimization of a spacer effect in which the biocide is attached to the surface through a polymer chain, allowing the biocide to reach and perforate the cytoplasmic membrane of the bacteria; or (ii) the use of positively-charged quaternary ammonium compounds which can kill the bacteria by detaching phospholipids from their cell membranes.[58]

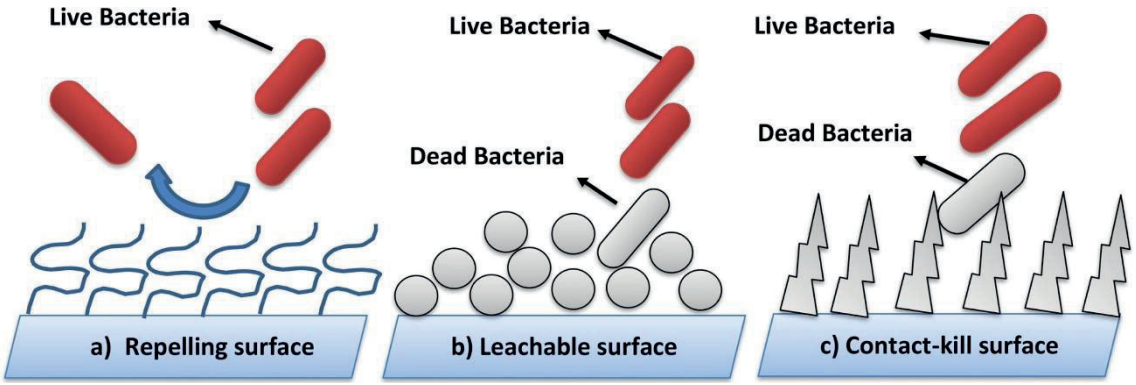


Figure 1.11. Classification of antibacterial surfaces (a) surfaces that resist bacteria attachment (b) surfaces treated with leaching antibacterial agents (c) contact–killing surfaces.[56]

According to this classification SAMs for biological applications and more specifically for antimicrobial activity, generally need to fulfil three main characteristics. First, they should be able to prevent nonspecific adsorption of proteins or other biomolecules and allow only the molecules of interest to interact with the surface and show a repulsion effect to bacteria attachment. Moreover, the molecular composition and density of SAMs should be controllable in order not to have holes where bacteria could start forming the biofilm. Lastly, molecules immobilized should present the functional groups of interest in a structured manner, in this way minimizing effects of the surface, such as limited mass transport, blocked binding sites or conformational changes.[14] All these characteristics should result in a better offensive to bacteria preventing the formation of the biofilm.

1.3.2. Organic nanoparticles for biological applications

One of the key advantages of ONPs lies in their tuneable properties. Through precise control over their composition, size, and surface characteristics, researchers can tailor these NPs to meet specific biological requirements. This tunability enables the design of drug delivery carriers with enhanced stability, prolonged circulation time, and targeted delivery to specific cells or tissues.[59] In the realm of drug delivery, there's considerable enthusiasm for creating nanocarriers capable of precisely targeting disease sites. This approach aims to circumvent potential side effects and diminish the necessary injection dosage. Furthermore, surface modifications with targeting ligands enable these NPs to selectively bind to receptors on the surface of target cells, improving drug delivery precision and reducing off-target effects.[60] In this context, fluorescent ONPs serve not only as drug carriers but also as trackers of their whereabouts, enabling enhanced precision and monitoring of treatment efficacy.

Over the past years, there has been a steady increase in publications concerning fluorescent ONPs. Their appealing optoelectronic properties and adaptable synthesis methods have rendered them attractive across various fields.[61] ONPs have been used as contrast agents for bioimaging applications, with enhanced resolution and most importantly, providing non-invasive systems due to their luminescent properties. This is particularly valuable in techniques like fluorescence imaging, magnetic resonance imaging, and photoacoustic imaging.[62] The use of ONPs helps to visualize biological structures and facilitates real-time monitoring of physiological processes. These NPs, typically ranging in size from 1 to 100 nanometers, exhibit unique properties owing to their organic composition, making them ideal candidates for interfacing with biological systems.[63]

There are reports on fluorescent ONPs that can also be used for sensing applications, such as temperature sensors or ion sensors.[64] Most of them are based on inorganic NPs with concerns related to toxicity, which indicates the need to find biocompatible substitutes. Thus, ONPs are considered a good strategy to enable the development of

biocompatible and sensitive biosensors for detecting specific biomarkers associated with diseases.[65]

1.4. General objectives

The main objective of this PhD thesis is the preparation and characterization of functional nanostructured molecular materials for biological applications with the aim of overcoming existing biological challenges. In particular, we will focus on (i) the preparation of novel antimicrobial coatings on gold and on relevant medical surfaces to avoid nosocomial infections using SAMs, and (ii) the preparation of ONPs for local nanoscale biosensing.

Towards the first aim, two approaches will be followed:

- In chapter 2 (publication #1), using a SAM and an interfacial coordination strategy, antimicrobial proteins are immobilized on gold surfaces and characterized using a multi-technique approach. After that, a biofilm assay is conducted to evaluate the bactericidal properties of the modified surfaces.

- In chapters 3 and 4 (publication submitted #2 and manuscript in preparation #4), using a PEG-based mixed maleimide-terminated SAM, antimicrobial peptides are anchored on medical grade thermoplastic polyurethane (TPU) surfaces and catheters and characterized using a multi-technique approach to avoid nosocomial infections. After that, a biofilm assay is performed to evaluate the antimicrobial activity of the modified surfaces in three clinically relevant bacteria strains. Finally, an *in vivo* evaluation is carried out in a rabbit model comparing the developed modified TPU catheters with catheters impregnated with commercial antibiotics.

Towards the second aim, in chapter 5 (publication #3), the main objective is to prepare and characterize ONPs based on blends of organic radical molecules and its protonated precursor; namely TTM-αH and TTM radical molecules for local nanoscale temperature biosensing performing an *in vitro* assay with *C. Elegans*. Temperature sensing relies on the fluorescence emission of the ONPs, where radicals form excimers. This emission's strength gradually varies with temperature.

1.5. References

1. Yan D. Micro-/Nanostructured Multicomponent Molecular Materials: Design, Assembly, and Functionality. *Chem – A Eur J*. 2015;21(13):4880-4896. doi:https://doi.org/10.1002/chem.201405456

2. Escudero A, Carrillo-Carrión C, Romero-Ben E, et al. Molecular Bottom-Up Approaches for the Synthesis of Inorganic and Hybrid Nanostructures. *Inorganics (Basel)*. 2021;9(7). doi:10.3390/inorganics9070058

3. Min Y, Nasrallah H, Poinsot D, et al. 3D Ruthenium Nanoparticle Covalent Assemblies from Polymantane Ligands for Confined Catalysis. *Chem Mat*. 2020;32(6):2365-2378. doi:10.1021/acs.chemmater.9b04737

4. Cook AB, Clemons TD. Bottom-Up versus Top-Down Strategies for Morphology Control in Polymer-Based Biomedical Materials. *Adv Nanobiomed Res*. 2022;2(1):2100087. doi:https://doi.org/10.1002/anbr.202100087

5. Jortner J, Rao CNR. *Nanostructured Advanced Materials. Perspectives and Directions**. Vol 74.; 2002.

6. Vericat C, Vela ME, Benitez G, Carro P, Salvarezza RC. Self-assembled monolayers of thiols and dithiols on gold: new challenges for a well-known system. *Chem Soc Rev*. 2010;39(5):1805-1834. doi:10.1039/B907301A

7. Wang L, Gong C, Yuan X, Wei G. Controlling the Self-Assembly of Biomolecules into Functional Nanomaterials through Internal Interactions and External Stimulations: A Review. *Nanomaterials*. 2019;9(2). doi:10.3390/nano9020285

8. Dhotel A, Chen Z, Delbreilh L, Youssef B, Saiter JM, Tan L. Molecular Motions in Functional Self-Assembled Nanostructures. *Int J Mol Sci*. 2013;14(2):2303-2333. doi:10.3390/ijms14022303

9. Halik M, Hirsch A. The Potential of Molecular Self-Assembled Monolayers in Organic Electronic Devices. *Adv Mat*. 2011;23(22-23):2689-2695. doi:https://doi.org/10.1002/adma.201100337

10. Singh M, Kaur N, Comini E. The role of self-assembled monolayers in electronic devices. *J Mater Chem C*. 2020;8(12):3938-3955. doi:10.1039/D0TC00388C

11. Newton L, Slater T, Clark N, Vijayaraghavan A. Self assembled monolayers (SAMs) on metallic surfaces (gold and graphene) for electronic applications. *J Mater Chem C*. 2013;1(3):376-393. doi:10.1039/C2TC00146B

12. Nuzzo R, Allara D. Adsorption of Bifunctional Organic Disulfides on Gold Surfaces. *J Am Chem Soc*. 1983;105:4481-4483. doi:10.1021/ja00351a063

13. Holmes C, Tabrizian M. Chapter 14 - Surface Functionalization of Biomaterials. In: Vishwakarma A, Sharpe P, Shi S, Ramalingam M, eds. *Stem Cell Biology and Tissue Engineering in Dental Sciences*. Academic Press; 2015:187-206. doi:https://doi.org/10.1016/B978-0-12-397157-9.00016-3

14. Love JC, Estroff LA, Kriebel JK, Nuzzo RG, Whitesides GM. Self-Assembled Monolayers of Thiolates on Metals as a Form of Nanotechnology. *Chem Rev*. 2005;105(4):1103-1170. doi:10.1021/cr0300789

15. Birdi KS. *Self-Assembly Monolayer Structures of Lipids and Macromolecules at Interfaces*. 1st ed. 2002. Kluwer Academic Publishers; 2002. doi:10.1007/b114152

16. Rissner F, Egger DA, Romaner L, Heimel G, Zojer E. The Electronic Structure of Mixed Self-Assembled Monolayers. *ACS Nano*. 2010;4(11):6735-6746. doi:10.1021/nn102360d

17. Valencia Ramirez A, Bonneux G, Terfort A, Losada-Pérez P, Renner FU. Nanomechanical Stability of Laterally Heterogeneous Films of Corrosion Inhibitor Molecules Obtained by Microcontact Printing on Au Model Substrates. *Langmuir*. 2022;38(50):15614-15621. doi:10.1021/acs.langmuir.2c02276

18. Qiu S, Ji J, Sun W, et al. Recent advances in surface manipulation using micro-contact printing for biomedical applications. *Smart Mater Med*. 2021;2:65-73. doi:https://doi.org/10.1016/j.smaim.2020.12.002

19. Koepsel JT, Murphy WL. Patterned Self-Assembled Monolayers: Efficient, Chemically Defined Tools for Cell Biology. *ChemBioChem*. 2012;13(12):1717-1724. doi:https://doi.org/10.1002/cbic.201200226

20. Feracci H, Gutierrez BS, Hempel W, Gil IS. Chapter 8 - Organic Nanoparticles. In: de la Fuente JM, Grazu V, eds. *Frontiers of Nanoscience*. Vol 4. Elsevier; 2012:197-230. doi:https://doi.org/10.1016/B978-0-12-415769-9.00008-X

21. Miyazawa T, Itaya M, Burdeos GC, Nakagawa K, Miyazawa T. A Critical Review of the Use of Surfactant-Coated Nanoparticles in Nanomedicine and Food Nanotechnology. *Int J Nanomedicine*. 2021;16:3937-3999. doi:10.2147/IJN.S298606

22. Fang F, Li M, Zhang J, Lee CS. Different Strategies for Organic Nanoparticle Preparation in Biomedicine. *ACS Mater Lett*. 2020;2(5):531-549. doi:10.1021/acsmaterialslett.0c00078

23. Smith RK, Lewis PA, Weiss PS. Patterning self-assembled monolayers. *Prog Surf Sci*. 2004;75(1):1-68. doi:https://doi.org/10.1016/j.progsurf.2003.12.001

24. Stevie FA, Donley CL. Introduction to x-ray photoelectron spectroscopy. *J Vac Sci Technol, A*. 2020;38(6):063204. doi:10.1116/6.0000412

25. Greczynski G, Haasch RT, Hellgren N, Lewin E, Hultman L. X-ray photoelectron spectroscopy of thin films. *Nat Rev Methods Primers*. 2023;3(1):40. doi:10.1038/s43586-023-00225-y

26. Holguin A, NS, & GG. X-ray Photoelectron Spectroscopy: An introduction to Principles and Practices. In: ; 2011. https://api.semanticscholar.org/CorpusID:135613576

27. Fadley CS. X-ray photoelectron spectroscopy: Progress and perspectives. *J Electron Spectros Relat Phenomena*. 2010;178-179:2-32. doi:https://doi.org/10.1016/j.elspec.2010.01.006

28. Holguin A, Navidad S, Gonzalez G. X-Ray Photoelectron Spectroscopy. In: ; 2011. https://api.semanticscholar.org/CorpusID:135613576

29. Stevie FA, Donley CL. Introduction to x-ray photoelectron spectroscopy. *Journal of Vacuum Science & Technology A*. 2020;38(6):063204. doi:10.1116/6.0000412

30. Liu S, Wang Y. Application of AFM in microbiology: a review. *Scanning*. 2010;32(2):61-73. doi:https://doi.org/10.1002/sca.20173

31. Yang H, Wang Y, Lai S, An H, Li Y, Chen F. Application of Atomic Force Microscopy as a Nanotechnology Tool in Food Science. *J Food Sci*. 2007;72(4):R65-R75. doi:https://doi.org/10.1111/j.1750-3841.2007.00346.x

32. Goksu EI, Vanegas JM, Blanchette CD, Lin WC, Longo ML. AFM for structure and dynamics of biomembranes. *Biochimica et Biophysica Acta (BBA) - Biomembranes*. 2009;1788(1):254-266. doi:https://doi.org/10.1016/j.bbamem.2008.08.021

33. Fulekar MH. *Environmental Nanotechnology / by M.H. Fulekar and Bhawana Pathak.* Taylor & Francis, CRC Press; 2018.

34. Mohamed MA, Jaafar J, Ismail AF, Othman MHD, Rahman MA. Chapter 1 - Fourier Transform Infrared (FTIR) Spectroscopy. In: Hilal N, Ismail AF, Matsuura T, Oatley-Radcliffe D, eds. *Memb Charact*. Elsevier; 2017:3-29. doi:https://doi.org/10.1016/B978-0-444-63776-5.00001-2

35. Movasaghi Z, Rehman S, ur Rehman DrI. Fourier Transform Infrared (FTIR) Spectroscopy of Biological Tissues. *Appl Spectrosc Rev*. 2008;43(2):134-179. doi:10.1080/05704920701829043

36. Blum MM, John H. Historical perspective and modern applications of Attenuated Total Reflectance – Fourier Transform Infrared Spectroscopy (ATR-FTIR). *Drug Test Anal*. 2012;4(3-4):298-302. doi:https://doi.org/10.1002/dta.374

37. Nandiyanto A, Oktiani R, Ragadhita R. How to Read and Interpret FTIR Spectroscope of Organic Material. *Indonesian J Sci Tech*. 2019;4:97-118. doi:10.17509/ijost.v4i1.15806

38. Salari A, Young RE. Application of attenuated total reflectance FTIR spectroscopy to the analysis of mixtures of pharmaceutical polymorphs. *Int J Pharm*. 1998;163(1):157-166. doi:https://doi.org/10.1016/S0378-5173(97)00378-5

39. Bieberle-Hütter A, Bronneberg AC, George K, van de Sanden MCM. Operando attenuated total reflection Fourier-transform infrared (ATR-FTIR) spectroscopy for water splitting. *J Phys D Appl Phys*. 2021;54(13):133001. doi:10.1088/1361-6463/abd435

40. Abdullah A, Mohammed A. *Scanning Electron Microscopy (SEM): A Review*.; 2019.

41. Sayid S, Garba A, Enenche D, Ikyo B. Scanning Electron Microscopy (SEM) of the Bug Eye and Sand Coral. *Microscopy Research*. 2020;08:1-7. doi:10.4236/mr.2020.81001

42. Paredes AM. MICROSCOPY | Scanning Electron Microscopy. In: Batt CA, Tortorello M Lou, eds. *Encyclopedia of Food Microbiology (Second Edition)*. Academic Press; 2014:693-701. doi:https://doi.org/10.1016/B978-0-12-384730-0.00215-9

43. Stetefeld J, McKenna SA, Patel TR. Dynamic light scattering: a practical guide and applications in biomedical sciences. *Biophys Rev*. 2016;8(4):409-427. doi:10.1007/s12551-016-0218-6

44. Carvalho PM, Felício MR, Santos NC, Gonçalves S, Domingues MM. Application of Light Scattering Techniques to Nanoparticle Characterization and Development. *Front Chem*. 2018;6:237. doi:10.3389/fchem.2018.00237

45. Habib I, Thotagamuge R, Lim C, Mahadi A. Dynamic Light Scattering and Zeta Potential Studies of Ceria Nanoparticles. *Solid State Phenom*. 2018;278:112-120. doi:10.4028/www.scientific.net/SSP.278.112

46. Bhattacharjee S. DLS and zeta potential – What they are and what they are not? *J Controlled Release*. 2016;235:337-351. doi:https://doi.org/10.1016/j.jconrel.2016.06.017

47. Babick F. Chapter 3.2.1 - Dynamic light scattering (DLS). In: Hodoroaba VD, Unger WES, Shard AG, eds. *Characterization of Nanoparticles*. Elsevier; 2020:137-172. doi:https://doi.org/10.1016/B978-0-12-814182-3.00010-9

48. Mabrouk M, Das DB, Salem ZA, Beherei HH. Nanomaterials for Biomedical Applications: Production, Characterisations, Recent Trends and Difficulties. *Molecules*. 2021;26(4):1077. doi:10.3390/molecules26041077

49. Khan J, Tarar SM, Gul I, Nawaz U, Arshad M. Challenges of antibiotic resistance biofilms and potential combating strategies: a review. *3 Biotech*. 2021;11(4):169. doi:10.1007/s13205-021-02707-w

50. Geissel FJ, Platania V, Gogos A, et al. Antibiofilm activity of nanosilver coatings against Staphylococcus aureus. *J Colloid Interface Sci*. 2022;608:3141-3150. doi:https://doi.org/10.1016/j.jcis.2021.11.038

51. Bhardwaj A, Pandey LM. Design of antibiofilm surfaces by immobilization of biogenic silver nanoparticles on amine self-assembled monolayers. *Mater Lett*. 2022;311:131574. doi:https://doi.org/10.1016/j.matlet.2021.131574

52. Gargioni C, Borzenkov M, D'Alfonso L, et al. Self-Assembled Monolayers of Copper Sulfide Nanoparticles on Glass as Antibacterial Coatings. *Nanomaterials*. 2020;10(2). doi:10.3390/nano10020352

53. Bagheri M, Beyermann M, Dathe M. Immobilization Reduces the Activity of Surface-Bound Cationic Antimicrobial Peptides with No Influence upon the Activity Spectrum. *Antimicrob Agents Chemother*. 2009;53(3):1132-1141. doi:10.1128/aac.01254-08

54. Tiller JC. Antimicrobial Surfaces. In: Börner HG, Lutz JF, eds. *Bioactive Surfaces*. Springer Berlin Heidelberg; 2011:193-217. doi:10.1007/12_2010_101

55. Jeon HJ, Yi SC, Oh SG. Preparation and antibacterial effects of Ag–SiO2 thin films by sol–gel method. *Biomaterials*. 2003;24(27):4921-4928. doi:https://doi.org/10.1016/S0142-9612(03)00415-0

56. Kaur R, Liu S. Antibacterial surface design – Contact kill. *Prog Surf Sci*. 2016;91(3):136-153. doi:https://doi.org/10.1016/j.progsurf.2016.09.001

57. Sheridan M, Winters C, Zamboni F, Collins MN. Biomaterials: Antimicrobial surfaces in biomedical engineering and healthcare. *Curr Opin Biomed Eng*. 2022;22:100373. doi:https://doi.org/10.1016/j.cobme.2022.100373

58. Elena P, Miri K. Formation of contact active antimicrobial surfaces by covalent grafting of quaternary ammonium compounds. *Colloids Surf B Biointerfaces*. 2018;169:195-205. doi:https://doi.org/10.1016/j.colsurfb.2018.04.065

59. Harish V, Tewari D, Gaur M, et al. Review on Nanoparticles and Nanostructured Materials: Bioimaging, Biosensing, Drug Delivery, Tissue Engineering, Antimicrobial, and Agro-Food Applications. *Nanomaterials*. 2022;12(3). doi:10.3390/nano12030457

60. Mitchell MJ, Billingsley MM, Haley RM, Wechsler ME, Peppas NA, Langer R. Engineering precision nanoparticles for drug delivery. *Nat Rev Drug Discov*. 2021;20(2):101-124. doi:10.1038/s41573-020-0090-8

61. Wani WA, Shahid M, Hussain A, AlAjmi MF. Applications of Fluorescent Organic Nanoparticles. In: Wani WA, Shahid M, Hussain A, AlAjmi MF, eds. *Fluorescent Organic Nanoparticles: New Generation Materials with Diverse Analytical and Biomedical Applications*. Springer Singapore; 2018:15-59. doi:10.1007/978-981-13-2655-4_3

62. Nune SK, Gunda P, Thallapally PK, Lin YY, Forrest ML, Berkland CJ. Nanoparticles for biomedical imaging. *Expert Opin Drug Deliv*. 2009;6(11):1175-1194. doi:10.1517/17425240903229031

63. Khan Y, Sadia H, Ali Shah SZ, et al. Classification, Synthetic, and Characterization Approaches to Nanoparticles, and Their Applications in Various Fields of Nanotechnology: A Review. *Catalysts*. 2022;12(11). doi:10.3390/catal12111386

64. Ng SM, Koneswaran M, Narayanaswamy R. A review on fluorescent inorganic nanoparticles for optical sensing applications. *RSC Adv*. 2016;6(26):21624-21661. doi:10.1039/C5RA24987B

65. Yoon J, Shin M, Lee T, Choi JW. Highly Sensitive Biosensors Based on Biomolecules and Functional Nanomaterials Depending on the Types of Nanomaterials: A Perspective Review. *Materials (Basel)*. 2020;13(2):299. doi:10.3390/ma13020299

Chapter 2
Antibiofilm surfaces based on the immobilization of a novel recombinant antimicrobial multidomain protein using self-assembled monolayers

2.1. Introduction

Antibiotic resistance is a global problem which affects human health.[1] One of the reasons of this resistance is microbial gene transfer, which originates when bacteria adapt and grow in the presence of antibiotics.[2] Bacterial biofilms, in addition to antibiotic resistance, are a serious concern to contemporary healthcare.[3] Biofilms are formed by accumulation of microorganisms, such as bacteria and their extracellular, which is permanently attached to living or non-living surfaces like the surfaces of medical devices.[4] There are multiple steps involved in the production of the three-dimensional architecture of biofilms, including adsorption, adhesion, microcolony formation, maturation, and dispersion (Figure 2.1).[5] Biofilm is a helpful adaptation of microbes that enables them to thrive in specific conditions. The amount and kind of microorganisms to which the device is exposed, the length of time that it is used, the presence of vital nutrients, the nature of the device surface material, the environment, and the expression of certain genes are all related with the creation of biofilms.[6]

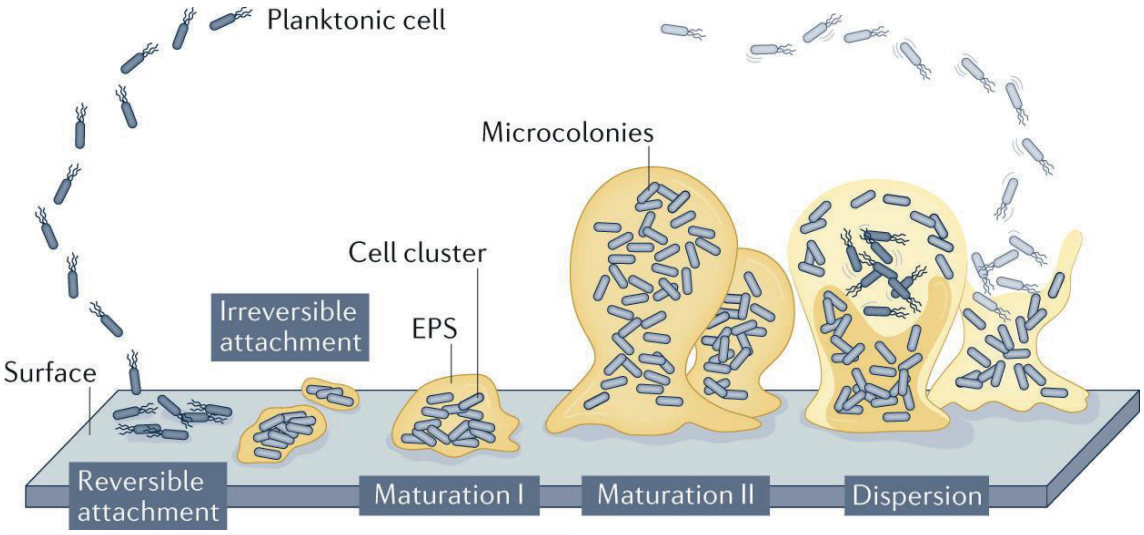


Figure 2.1. Scheme of the biofilm development.[7]

Recently, scientists are trying to find ways to avoid the biofilm growth and colonization on the surface of medical devices by incorporating special coating and structures on them. Different antibacterial surfaces have been designed, which can be divided into

three categories based on their operating mechanisms: (i) bactericidal surfaces for killing attached bacteria; (ii) bacteria-resistant surfaces for preventing the initial attachment of bacteria; and (iii) bacteria-release surfaces for reducing the adhesion between bacteria and material surfaces and facilitating the release of attached bacteria by an external force (see chapter 1).[8]

In parallel, antimicrobial peptides (AMPs) have emerged as natural defence mechanisms found in diverse organisms, including humans, plants, and animals. These peptides are small proteins with the ability to disrupt the membranes of microorganisms, leading to their destruction.[9,12,13,14] They are promising candidates as antimicrobial agents to be used on surfaces thanks to their broad spectrum of activity, low toxicity for mammalian cells, high activity, and also long-term and high structural stability.[10–12] Importantly, it is known that the cellular action of AMPs is separated from those mechanisms inducing antibiotic-resistance and most of them kill bacterial cells quickly by affecting the cytoplasmic membrane.[13]

Recently, our collaborators from institute of agrifood research and technology (IRTA, Spain) have described a new generation of AMP based on different complementary functional domains.[14] Specifically, a new antimicrobial multidomain recombinant protein has been reported, named JAMF1,[15] in both; soluble and protein nanoparticle (pNP) forms (Figure 2.2A). JAMF1 combines three functional domains based on human-α-defensin-5, human XII-A secreted phospholipase A2, and a gelsolin-based bacterial-binding domain. The soluble form is obtained by solubilizing pNPs by performing a treatment with mild detergent and a subsequent purification by affinity chromatography. Not only the soluble, but also the pNPs are interesting since aggregated antimicrobial peptides and proteins can present not only membrane perturbations, but also bactericidal intracellular activity. It has been demonstrated that the internalization of these peptides and proteins can occur without severe disruption of the cell wall[16], which means that this bactericidal approach can take place independently of the effectiveness of the membrane perturbation activity. In fact, it has been reported that anchoring AMP on surfaces is a good approach to avoid degradation and toxicity and to increase stability due to the use of high concentrations.[17,18]

SAMs are a good approach to anchor AMPs on surfaces and study their antimicrobial effect.[19] Protein binding can be carried out through several types of interactions such as electrostatic, covalent, or supramolecular/coordination. The advantages of supramolecular/coordination interactions are that protein attachment, reversibility and orientation can be controlled thanks to the immobilization of the protein via specific binding sites.[20–22] An example of supramolecular interaction is the binding of nickel (II)-chelated nitrilotriacetic acid (Ni-NTA) with six histidine-tagged proteins (His_6-tag), which is a strategy widely used in metal affinity chromatography for purifying proteins labelled with a short histidine sequence. [23–25] The multidomain protein JAMF1 in both

forms, soluble and as pNPs, presents a His_6-tag at the C-terminus, which enables its immobilization on surfaces via the His-tag-Ni-NTA interaction.

In this chapter, the objective is to use this strong interaction of the protein terminal His_6-tag with the Ni-NTA complex to confer antimicrobial properties to a gold model surface. Specifically, homogeneous SAMs will be prepared using polyethylene glycol (PEG) and NTA molecules on gold. For the first time this system allows the immobilization of the JAMF1, in both soluble and pNP forms (Figure 2.2B).

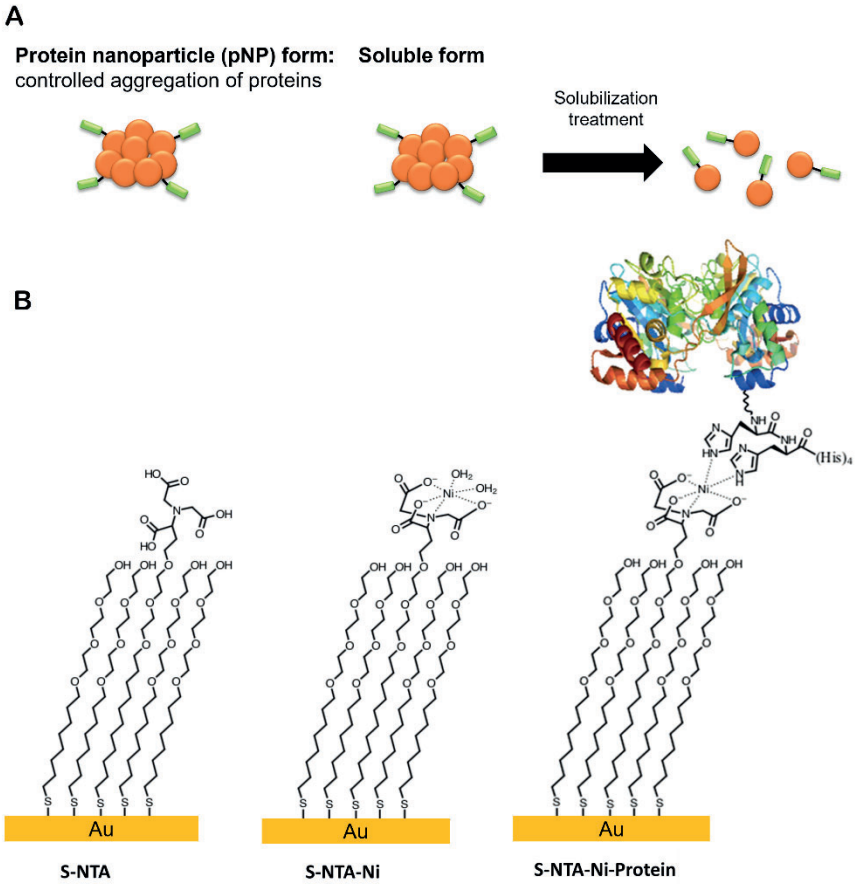


Figure 2.2. (A) Schematic representation of the antimicrobial protein construct for the pNP and the soluble form, (B) Sketch of the immobilization of His-tagged JAMF1 using the Ni-NTA strategy.

2.2. Objectives

The objectives of this chapter presented here are:

1) Formation of an antimicrobial surface through the immobilization of a novel antimicrobial protein, in its soluble and pNP forms, using a patterned and non-patterned mixed PEG and NTA SAM on gold.
2) Characterization of these SAMs using a multi-technique approach to:
    a. Verify the successful realization of each SAM formation step, and thus, the specific immobilization of the protein in soluble and pNP form.

b. Compare the differences between immobilizing the soluble versus the pNP forms.

3) Perform a biofilm assay to evaluate the antimicrobial activity of the surfaces modified with the novel antimicrobial protein in both, soluble and pNP, forms.

The results of this chapter have been included in the publication #1: Antibiofilm Surfaces Based on the Immobilization of a Novel Recombinant Antimicrobial Multidomain Protein Using Self-Assembled Monolayers. *Mater. Adv.*, **2023**, 4, 2354-2364 (see the Scientific Contributions section).

2.3. SAMs preparation

Homogeneous SAMs were prepared using the wet chamber technique (Figure 2.3). First, 80 µL of NTA terminated thiol (SH-NTA) 1 mM solution in ethanol were deposited on a petri dish and after that the gold surface was deposited, upside down, on top of the drop for 2 h at room temperature (RT). Then, substrates were immersed in 10 mM $NiCl_2$ in HEPES buffer for 30 min. Patterned substrates followed the same procedure (Figure 2.3) but before, a solution of SH-PEG 1 mM in ethanol was dropped on top of a polydimethylsiloxane stamp and then, they were printed with the inked stamp following the microcontact printing (µCP) procedure. Finally, substrates were incubated, upside down, with the His-tagged JAMF1 protein in a humid wet chamber during 1 h at RT.

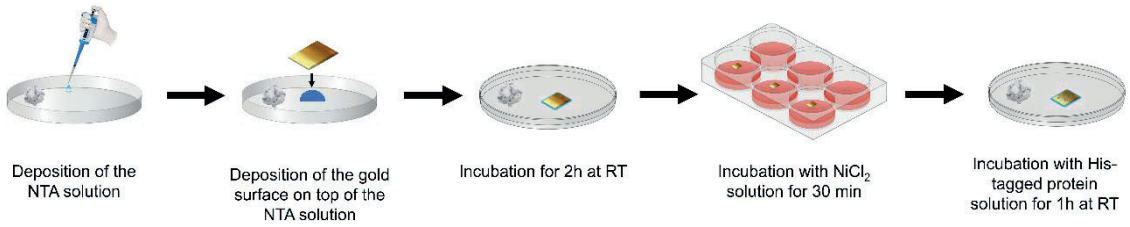


Figure 2.3. Scheme of the functionalization of gold substrates with NTA SAMs using the wet chamber strategy.

2.4. Multi-technique characterization

A multi-technique approach, based on XPS, AFM, cyclic voltammetry (CV) analysis and fluorescence microscopy, were used to characterize the patterned and non-patterned mixed PEG and Ni-NTA SAM formation and the subsequent antimicrobial protein immobilization, both in soluble and pNP forms. Specifically, I have been involved with the XPS and fluorescence microscopy experiments, which are two of the key techniques to conclude the correct immobilization of the protein.

2.4.1. Fluorescence microscopy

To visualize the antimicrobial surface through fluorescence microscope, we performed an immunostaining, which involved primary and secondary antibodies, as our AMP is

not fluorescent. The fluorescent stripes appear well delimited, and a uniform coverage of the protein is found along the pattern for both soluble and pNP forms (Figure 2.4A and B). The absence of fluorescent pattern in the controls were EDTA was used, demonstrated that Ni is sequestered from the NTA and, therefore, the protein is removed from the surface (Figure 2.4C and D). Moreover, in Figure 2.4E, dark images were obtained from the negative control, that consisted of the immunostaining of a patterned S-NTA sample, without protein, which is a proof that the immunostaining technique worked correctly, and that the fluorescence is specific for the immunostained proteins. In addition, the fluorescence intensity profiles of the patterned substrates indicate that the His-tagged protein is specifically attached only onto the Ni-NTA groups, producing gold-S-NTA-Ni-Protein surfaces, and the SH-PEG molecules form a protein repelling surface. These results also confirm that μCP allows a correct spatial control of the protein immobilization.

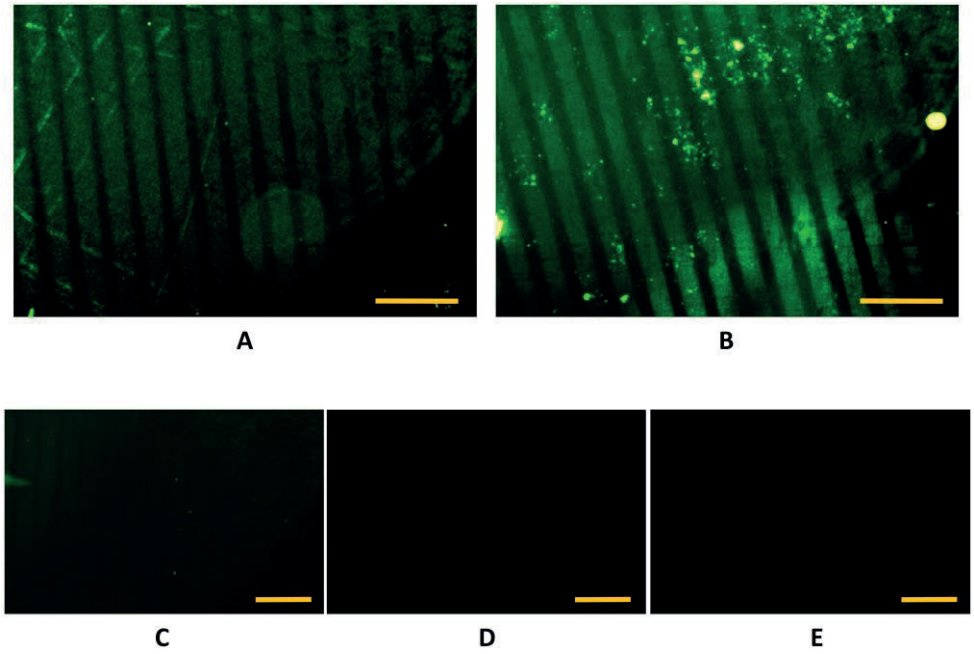


Figure 2.4. Fluorescence images of a 20 μm striped pattern of (A) S-NTA-Ni-Sol and (B) S-NTA-Ni-pNP. Fluorescence images of the negative controls (by immersion in EDTA (10 mM)) of a 20 μm striped pattern of (C) S-NTA-Ni-Sol-Ctrl and (D) S-NTA-Ni-pNP-Ctrl. (E) A generic negative control of the immunostaining technique, which consisted in patterned S-NTA. The scale bars correspond to 100 μm.

2.4.2. X-Ray Photoelectron Spectroscopy

To get more chemical information about the proper binding of the JAMF1 protein onto the non-patterned mixed PEG and Ni-NTA SAM, XPS measurements were performed. Firstly, for the N 1s spectra two peaks can be observed, one at 400-401 eV and another one at 402 eV. The peak at around 400-401 eV corresponds to the N-C bond found in the NTA, in amino acids, and also attributed to 'pyrrole-like nitrogen' (typically assigned to peaks around 400.4 eV). NTA SAMs with the protein anchored; SH-NTA-Ni-Sol and SH-

NTA-Ni-pPN (Figure 2.5A and C) present the His-tag, which has imidazole groups that contain 'pyrrole-like' nitrogen, and the amino acid tryptophan, which also has 'pyrrole-like' nitrogen. Negative controls (Figure 2.5B and D) which have only the NTA SAM on the surface present N-C bonds and secondary amides and therefore, also present this peak. The peak at 402.5 eV is clearly observed in the samples with the protein but for the negative controls, it is absent or very small. This peak is present only in the samples containing protein and it is assigned to pyridine-like nitrogen present in the His-tag.

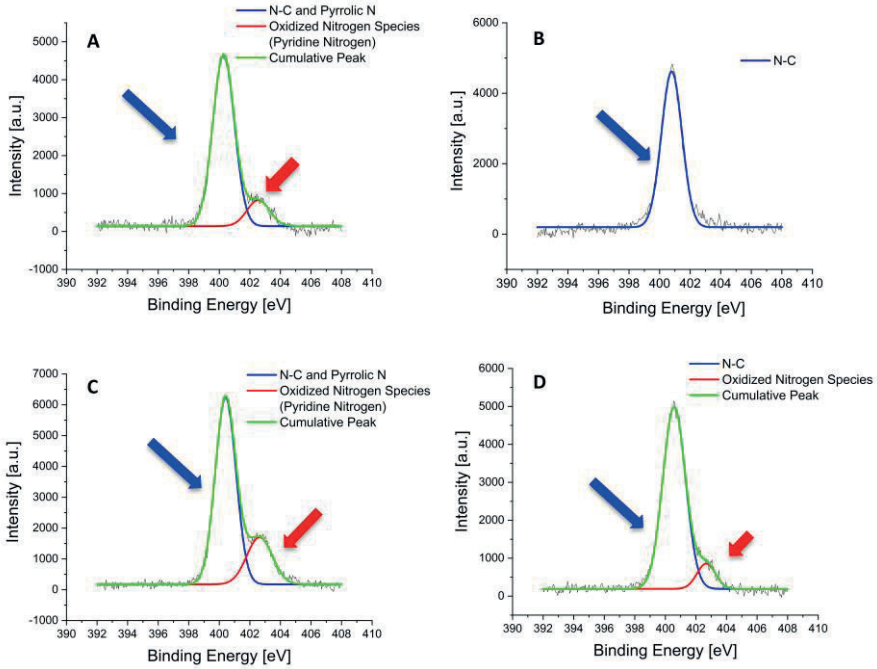


Figure 2.5. XPS deconvolutions of N 1s spectra for (A) S-NTA-Ni-Sol, (B) S-NTA-Ni-Sol-Ctrl (treatment with EDTA 10 mM), (C) S-NTA-Ni-pNP and (D) S-NTA-Ni-pNP-Ctrl (treatment with EDTA 100 mM). The red arrow indicates the contribution of 'pyridine-like' nitrogen and blue arrow of 'pyrrole-like' nitrogen.

2.5. Antimicrobial assay

Furthermore, a biofilm assay was performed with the samples that I prepared to evaluate their biofilm inhibition capacity. The JAMF1 multidomain AMP, in both soluble and pNP forms, can significantly reduce biofilm formation of *E.Coli* (Figure 2.6A) and, in particular, the pNP form is also active against the antibiotic-resistant *Klebsiella pneumoniae carbapenemase* (KPC) strain (Figure 2.6B) which belongs to a group of emerging highly drug-resistant Gram-negative bacteria causing infections associated with severe morbidity and mortality.

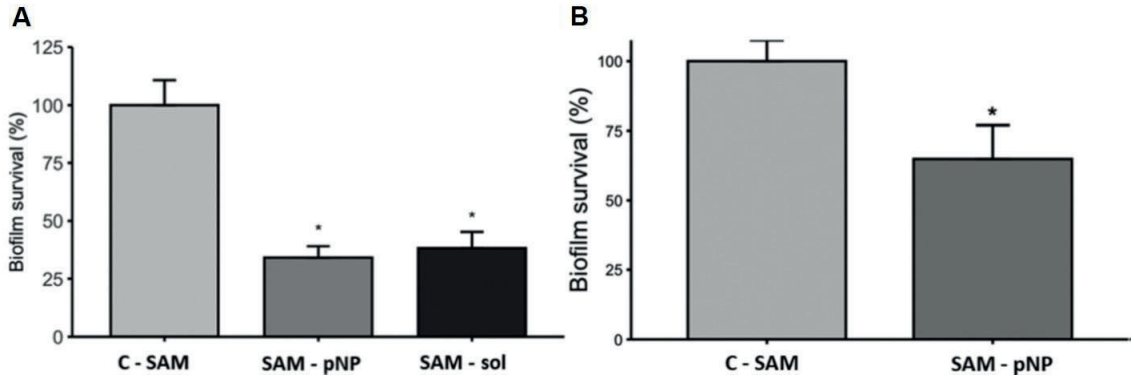


Figure 2.6. Biofilm formation ability (%) of (A) *E.Coli* DH5α on S-NTA-Ni-JAMF1-Sol and S-NTA-Ni-JAMF1-pNP and (B) of KPC on S-NTA-Ni-JAMF1-pNP. * Indicates significant differences ($p \leq 0.05$) when performing a student t-test.

The strategy presented is a promising approach for the design of materials with antimicrobial properties and could be a good manner to immobilize other recombinant AMPs produced with His-tag.

2.6. Summary and future perspectives

A novel biofunctionalized surface on gold with antimicrobial properties has been developed and well characterized in response to the need of new antimicrobial agents to overcome the antibiotic crisis. This promising platform could have other applications such as coating surfaces of medical devices (e.g. catheters) or being incorporated into food packaging materials, among others.

2.7. References

1. Aslam B, Wang W, Arshad MI, et al. Antibiotic resistance: a rundown of a global crisis. *Infect Drug Resist*. 2018;11(null):1645-1658. doi:10.2147/IDR.S173867

2. Yadav S, Kapley A. Antibiotic resistance: Global health crisis and metagenomics. *Biotechnol Rep (Amst)*. 2021;29:e00604-e00604. doi:10.1016/j.btre.2021.e00604

3. Lundin PM, Fiser BL, Blackledge MS, Pickett HL, Copeland AL. Functionalized Self-Assembled Monolayers: Versatile Strategies to Combat Bacterial Biofilm Formation. *Pharmaceutics*. 2022;14(8). doi:10.3390/pharmaceutics14081613

4. Assefa M, Amare A. Biofilm-Associated Multi-Drug Resistance in Hospital-Acquired Infections: A Review. *Infect Drug Resist*. 2022;15(null):5061-5068. doi:10.2147/IDR.S379502

5. Kostakioti M, Hadjifrangiskou M, Hultgren SJ. Bacterial biofilms: development, dispersal, and therapeutic strategies in the dawn of the postantibiotic era. *Cold Spring Harb Perspect Med*. 2013;3(4):a010306. doi:10.1101/cshperspect.a010306

6. Sharma S, Mohler J, Mahajan SD, Schwartz SA, Bruggemann L, Aalinkeel R. Microbial Biofilm: A Review on Formation, Infection, Antibiotic Resistance, Control Measures, and Innovative Treatment. *Microorganisms*. 2023;11(6). doi:10.3390/microorganisms11061614

7. Sauer K, Stoodley P, Goeres DM, et al. The biofilm life cycle: expanding the conceptual model of biofilm formation. *Nat Rev Microbiol*. 2022;20(10):608-620. doi:10.1038/s41579-022-00767-0

8. Yu Q, Wu Z, Chen H. Dual-function antibacterial surfaces for biomedical applications. *Acta Biomater*. 2015;16:1-13. doi:https://doi.org/10.1016/j.actbio.2015.01.018

9. Reddy KVR, Yedery RD, Aranha C. Antimicrobial peptides: premises and promises. *Int J Antimicrob Agents*. 2004;24(6):536-547. doi:10.1016/J.IJANTIMICAG.2004.09.005

10. Lim K, Chua RRY, Saravanan R, et al. Immobilization Studies of an Engineered Arginine–Tryptophan-Rich Peptide on a Silicone Surface with Antimicrobial and Antibiofilm Activity. *ACS Appl Mater Interfaces*. 2013;5(13):6412-6422. doi:10.1021/am401629p

11. Hancock REW, Sahl HG. Antimicrobial and host-defense peptides as new anti-infective therapeutic strategies. *Nat Biotechnol*. 2006;24(12):1551-1557. doi:10.1038/nbt1267

12. Håvard J, Pamela H, W HRE. Peptide Antimicrobial Agents. *Clin Microbiol Rev*. 2006;19(3):491-511. doi:10.1128/cmr.00056-05

13. Park SC, Park Y, Hahm KS. The Role of Antimicrobial Peptides in Preventing Multidrug-Resistant Bacterial Infections and Biofilm Formation. *Int J Mol Sci*. 2011;12(9):5971-5992. doi:10.3390/ijms12095971

14. Roca-Pinilla R, López-Cano A, Saubi C, Garcia-Fruitós E, Arís A. A new generation of recombinant polypeptides combines multiple protein domains for effective antimicrobial activity. *Microb Cell Fact*. 2020;19(1):122. doi:10.1186/s12934-020-01380-7

15. Kyvik AR, Roca-Pinilla R, Mayolo-Deloisa K, et al. Antibiofilm surfaces based on the immobilization of a novel recombinant antimicrobial multidomain protein using self-assembled monolayers. *Mater Adv*. 2023;4(10):2354-2364. doi:10.1039/D2MA00978A

16. Wu G, Khodaparast L, Khodaparast L, et al. Investigating the mechanism of action of aggregation-inducing antimicrobial Pept-ins. *Cell Chem Biol*. 2021;28(4):524-536.e4. doi:10.1016/J.CHEMBIOL.2020.12.008

17. Costa F, Carvalho IF, Montelaro RC, Gomes P, Martins MCL. Covalent immobilization of antimicrobial peptides (AMPs) onto biomaterial surfaces. *Acta Biomater*. 2011;7(4):1431-1440. doi:https://doi.org/10.1016/j.actbio.2010.11.005

18. Silva RR, Avelino KYPS, Ribeiro KL, Franco OL, Oliveira MDL, Andrade CAS. Chemical immobilization of antimicrobial peptides on biomaterial surfaces. *FBS*. 2016;8(1):129-142.

19. Monteiro C, Costa F, Pirttilä AM, Tejesvi M V, Martins MCL. Prevention of urinary catheter-associated infections by coating antimicrobial peptides from crowberry endophytes. *Sci Rep*. 2019;9(1):10753. doi:10.1038/s41598-019-47108-5

20. Cardoso P, Glossop H, Meikle TG, et al. Molecular engineering of antimicrobial peptides: microbial targets, peptide motifs and translation opportunities. *Biophys Rev*. 2021;13(1):35-69. doi:10.1007/s12551-021-00784-y

21. Bednarska NG, van Eldere J, Gallardo R, et al. Protein aggregation as an antibiotic design strategy. *Mol Microbiol*. 2016;99(5):849-865. doi:https://doi.org/10.1111/mmi.13269

22. Galzitskaya O V, Kurpe SR, Panfilov A V, et al. Amyloidogenic Peptides: New Class of Antimicrobial Peptides with the Novel Mechanism of Activity. *Int J Mol Sci*. 2022;23(10). doi:10.3390/ijms23105463

23. Zhao X, Liao C, Ma YT, Ferrell JB, Schneebeli ST, Li J. Top-down Multiscale Approach To Simulate Peptide Self-Assembly from Monomers. *J Chem Theory Comput*. 2019;15(3):1514-1522. doi:10.1021/acs.jctc.8b01025

24. Uhlenheuer DA, Milroy LG, Neirynck P, Brunsveld L. Strong supramolecular control over protein self-assembly using a polyamine decorated β-cyclodextrin as synthetic recognition element. *J Mater Chem*. 2011;21(47):18919-18922. doi:10.1039/C1JM12736E

25. Malekkhaiat Häffner S, Malmsten M. Influence of self-assembly on the performance of antimicrobial peptides. *Curr Opin Colloid Interface Sci*. 2018;38:56-79. doi:10.1016/J.COCIS.2018.09.002

Publication #1

Title: Antibiofilm surfaces based on the immobilization of a novel recombinant antimicrobial multidomain protein using self-assembled monolayers

Authors: Kyvik, A. R., Roca-Pinilla, R., Mayolo-Deloisa, K., Rodriguez Rodriguez, X., Martinez-Miguel, M., Martos, M., Köber, M., Ventosa, N., Veciana, J., Guasch, J., Garcia-Fruitós, E., Arís, A. & Ratera, I.

Publication: Mater. Adv., 2023,4, 2354-2364

Materials Advances

ROYAL SOCIETY OF CHEMISTRY

PAPER

View Article Online
View Journal | View Issue

Check for updates

Cite this: *Mater. Adv.*, 2023, 4, 2354

Antibiofilm surfaces based on the immobilization of a novel recombinant antimicrobial multidomain protein using self-assembled monolayers†

Adriana R. Kyvik, [a] Ramon Roca-Pinilla, [df] Karla Mayolo-Deloisa, [ae] Xavier Rodriguez Rodriguez, [a] Marc Martinez-Miguel, [ab] Marta Martos, [a] Mariana Köber, [ab] Nora Ventosa, [ab] Jaume Veciana, [ab] Judith Guasch, [abc] Elena Garcia-Fruitós, [d] Anna Arís [d] and Imma Ratera *[ab]

The constant increase of microorganisms resistant to antibiotics has been classified as a global health emergency, which is especially challenging when biofilms are formed. Herein, novel biofunctionalized gold surfaces with the antimicrobial multidomain recombinant protein JAMF1, both in the soluble form and nanostructured as nanoparticles, were developed. The interaction between His-tag termination of the protein and a nitriloacetic acid–Ni complex formed on mixed self-assembled monolayers (mixed SAMs) was exploited. The obtained antibiofilm surfaces based on the immobilization of the novel JAMF1 protein using self-assembled monolayers were characterized using a multi-technique approach including: cyclic voltammetry, X-ray photoelectron spectroscopy, atomic force microscopy and fluorescence, proving that the modification and immobilization of JAMF1 were successfully done. The antibiofilm activity against *Escherichia coli* and carbapenem-resistant *Klebsiella pneumoniae* showed that the immobilized antimicrobial proteins were able to reduce biofilm formation of both microorganisms. This strategy opens up new possibilities for controlled biomolecule immobilization for fundamental biological studies and biotechnological applications, at the interface of materials science and molecular biology.

Received 14th October 2022,
Accepted 6th April 2023

DOI: 10.1039/d2ma00978a

rsc.li/materials-advances

Open Access Article. Published on 13 April 2023. Downloaded on 5/30/2024 2:35:54 PM.
This article is licensed under a Creative Commons Attribution-NonCommercial 3.0 Unported Licence.

Introduction

The increasing appearance of antibiotic resistant bacteria has become a global health emergency.[1,2] The main pathogens responsible for resistance-associated deaths (*Escherichia coli*, *Staphylococcus aureus*, *Klebsiella pneumoniae*, *Streptococcus pneumoniae*, *Acinetobacter baumannii*, and *Pseudomonas aeruginosa*) were responsible for 929 000 deaths attributable directly to antimicrobial resistance in 2019.[3] The antibiotic resistance problem is even more complicated when bacteria form biofilms because they are 1000-fold resistant as compared with planktonic bacteria.[2,4,5] Biofilms may form on a wide variety of surfaces, including living tissues, medical devices,[6,7] or water system piping.[8] Biofilms cause approximately 80% of chronic and recurrent human microbial infections.[6] In this context, it is imperative to find new surface coating approaches to avoid biofilm formation. Antimicrobial peptides (AMPs) with antimicrobial activity due to the innate immunity of a variety of species are gaining interest as a possible alternative to antibiotics, also for biofilm-forming bacteria.[9] Recently, we have described a new generation of antimicrobial multidomain proteins that combine several AMPs and complementary functional domains in a single polypeptide recombinantly produced as protein nanoclusters named protein nanoparticles (pNPs).[10] However, the antibiofilm activity of such multidomain proteins has not been explored in detail.

One of the strategies recently used to provide antimicrobial properties to medical devices, to avoid the need of systematic treatments, is based on the immobilization of AMPs achieved through their binding on different surfaces. Moreover, it has

[a] *Institute of Materials Science of Barcelona (ICMAB-CSIC), Campus UAB, 08193 Bellaterra, Spain. E-mail: iratera@icmab.es*
[b] *Networking Research Center on Bioengineering, Biomaterials and Nanomedicine (CIBER-BBN), Campus UAB, 08193 Bellaterra, Spain*
[c] *Dynamic Biomimetics for Cancer Immunotherapy, Max Planck Partner Group, ICMAB-CSIC, Campus UAB, 08193 Bellaterra, Spain*
[d] *Department of Ruminant Production, Institut de Recerca i Tecnologia Agroalimentàries (IRTA), 08140 Caldes de Montbui, Spain*
[e] *Tecnologico de Monterrey, Institute for Obesity Research, School of Engineering and Sciences, Av. Eugenio Garza Sada 2001, 64849 Monterrey, Nuevo León, México*
[f] *Translational Vectorology Research Unit, Children's Medical Research Institute, The University of Sydney, Westmead, Australia*

† Electronic supplementary information (ESI) available. See DOI: https://doi.org/10.1039/d2ma00978a

© 2023 The Author(s). Published by the Royal Society of Chemistry

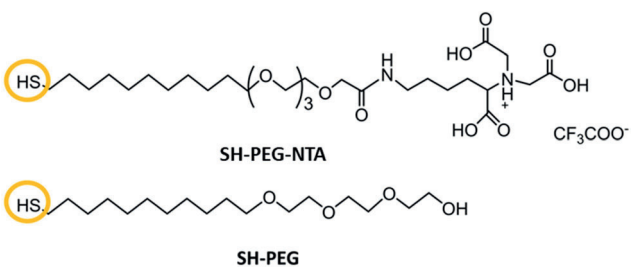
Open Access Article. Published on 13 April 2023. Downloaded on 5/30/2024 2:35:54 PM.
This article is licensed under a Creative Commons Attribution-NonCommercial 3.0 Unported Licence.

also been shown that the immobilized AMPs are capable of keeping their antimicrobial activity under specific conditions.[11–14] This strategy allows higher availability of AMPs on the surface and more uniform distribution in comparison to the incorporation of AMPs through other adsorption methods that give place to non-homogeneous peptide distributions. In addition, the anchoring of AMPs on the surfaces has been reported to be a good strategy to avoid proteolytic degradation. Such advantages allow increasing stability and completely avoid toxicity associated with the use of high AMP dosages.[15,16]

Using self-assembled monolayers (SAMs) is a strategy used to anchor AMPs on surfaces and study the effect of their immobilization. SAMs are based on well-organized molecules on surfaces which are easy to prepare and functionalize, allowing a fine control at the molecular level.[17,18] Thus, the use of the SAM strategy to anchor AMPs on surfaces has been shown to be one of the best strategies for achieving a controlled design of antibiofilm surfaces to coat medical devices.[19]

Herein, we report biofunctionalized gold surfaces using a new antimicrobial multidomain protein (JAMF1) formed by several AMPs by means of DNA recombinant technology in a soluble and protein nanoparticle (pNP) form, which has the potential to be a protein-slow release form. Furthermore, we report the formation of an antimicrobial surface through the immobilization of this novel generation of recombinant multidomain antimicrobial protein, JAMF1, using a mixed SAM strategy, as a proof of concept for coating medical devices. The mixed SAM is based on a mixture of ((1-mercapto-11-undecyl)-(tetra(ethylene glycol)) (SH-PEG) and nitriloacetic acid (NTA)-terminated (SH-PEG-NTA) molecules on gold (Scheme 1). Specifically, after Ni complexation of the NTA termination, we have used the interaction of the JAMF1 protein terminal His-tag with the S-PEG-NTA–Ni complex found on the gold functionalized with the mixed SAMs to anchor the protein to the surface (Fig. 1).

Then, the immobilized novel antimicrobial protein in its soluble and pNP forms on mixed SAMs was characterized using a multi-technique approach to (i) verify the successful achievement of each SAM formation step, (ii) the specific immobilization of the protein and (iii) compare the differences when immobilizing the soluble *versus* the pNP form. Cyclic voltammetry (CV), X-ray photoelectron spectroscopy (XPS), atomic force microscopy (AFM) and fluorescence microscopy measurements were performed. Moreover, for in depth characterization of the



Scheme 1 Structure of the molecules used for mixed SAMs formation. The NTA terminated thiol (SH-PEG-NTA) and the commercial pegylated alkanethiol (SH-PEG).

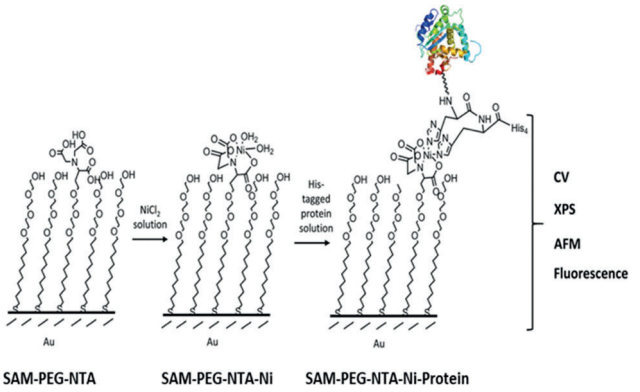


Fig. 1 Strategy used for the immobilization of His-tagged JAMF1 protein: SAMs formation using SH-PEG-NTA, immersion in a $NiCl_2$ solution to obtain SAM-PEG-NTA-Ni, followed by the incubation with the His-tagged protein, obtaining SAM-PEG-NTA-Ni-Protein (Protein: JAMF1 or mGFPH6, soluble or as pNP). A multi-technique approach was used for its characterization.

functionalized surfaces, prefunctionalized patterned and non-patterned mixed polyethylene glycol (SH-PEG) and SH-PEG-NTA–Ni were prepared. Based on our previous expertise, to achieve spatial control of the distribution of the molecules[20] and pNPs,[21] the optimization of the microcontact printing (μCP) procedure of the NTA-terminated thiol (SH-PEG-NTA) and pegylated alkanethiol (SH-PEG) molecules was performed and a His-tagged green fluorescent protein (mGFPH6) as a reporter was used to optimize the procedure, easily visualizing the pattern.[22–25]

Finally, an antibiofilm activity assay was carried out to evaluate the actual antimicrobial effect of the surfaces modified with the novel recombinant antimicrobial protein in its soluble and pNP forms. The antimicrobial activity was tested against *E. coli* and *K. pneumoniae* carbapenemase (KPC) bacteria, this last one being an example of an antibiotic-resistant strain.

Materials and methods

Bacterial strains and medium

We used *Escherichia coli* BL21 (DE3) and *E. coli* Origami B strains for heterologous protein expression of antimicrobial proteins and a modified version of green fluorescent protein (mGFPH6), respectively. *E. coli* DH5α and carbapenem-resistant *K. pneumoniae* (KPC) were used to evaluate the antibiofilm activities. *E. coli* strains were grown in Luria–Bertani (LB) medium and KPC in Brain Heart-Infusion (BHI) broth (Scharlau, Barcelona, Spain).

Antimicrobial protein genetic construct design

The gene encoding for the JAMF1 construct consisted of the sequences encoding Jun257-318 (Uniprot entry P05412), human α-defensin-5 (HD5) precursor (Uniprot entry Q01523), gelsolin 188–196 (Uniprot entry P06396), group-XIIA secretory phospholipase A2 ($sPLA_2$) precursor (Uniprot entry Q9BZM1) and Fos118-210 (Uniprot entry P01100), from N-terminal to C-terminal.

Open Access Article. Published on 13 April 2023. Downloaded on 5/30/2024 2:35:54 PM. This article is licensed under a Creative Commons Attribution-NonCommercial 3.0 Unported Licence.

A linker sequence consisting of serine and glycine residues (SGGGSGGS) was used between each of the domains and a 6-histidine tag (H6-tag) at the C-terminal for protein purification. The fusion construct was codon optimized by GeneArt (Life technologies, Regensburg, Germany) and then cloned into pET22b (Amp^R) (Novagen, Darmstadt, Germany) backbone for further *E. coli* transformation and recombinant production.

Production of recombinant multidomain antimicrobial protein JAMF1

An *E. coli* BL21 (DE3)/pET22b-JAMF1[10] culture (0.5 L) was grown at 37 °C and 250 rpm in LB broth with ampicillin at 100 μg mL^{-1}. Protein expression was induced by 1 mM isopropyl-β-D-thiogalactoside (IPTG) at OD_{600} = 0.4–0.6. Cultures were grown for 3 h post-induction. To obtain JAMF1 as pNP, the bacterial culture was processed with a mechanical disruption and washing steps, as described elsewhere.[10] For soluble protein production, a 2 L culture was grown and centrifuged at 6000 × *g* and the pellets were recovered and resuspended in 120 mL of phosphate-buffered saline (PBS) with protease inhibitors (complete EDTA-free; Roche, Indianapolis, USA). The samples were sonicated for 4 rounds of 5 min at 10% amplitude under 0.5 s cycles, intercalated by a minimum of 5 min of rest in ice. Protein pellets were again recovered and washed twice with distilled water. The pellets were weighted and solubilized in 0.2% *N*-lauroyl sarcosine, 40 mM Tris and protease inhibitors at a ratio of 40 mL g^{-1} of the wet pellet as described previously.[26] The mixture was incubated 40 h overnight (O/N) at room temperature (RT) under agitation and the supernatant was recovered through centrifugation (15 000 × *g* for 45 min at 4 °C), for purification. NaCl and imidazole were added to the solubilized protein to equilibrate the samples, and immobilized metal affinity chromatography (IMAC) purification was carried out in an Äkta purifier 10 system (GE Healthcare; Uppsala, Sweden) using a 1 mL HisTrap HP column (GE Healthcare; Uppsala, Sweden). Both the binding and the elution buffer contained 0.2% *N*-lauroyl sarcosine. The final imidazole concentration in the elution buffer was 0.5 mM. Finally, the buffer of the selected purified protein fractions was changed to KPi (potassium phosphate buffer: 80.2% v/v 10 mM K_2HPO_4 and 19.8% v/v 10 mM KH_2PO_4) using a desalting column (Cytiva, US).[10] Purified pNP and soluble protein were quantified by western blotting using a monoclonal anti-His antibody (1 : 1000) (His-probe, Santa Cruz). As secondary anti-body, we used an anti-mouse IgG – alkaline phosphatase (1 : 20 000) produced in goat (Sigma-Aldrich) (See Fig. S8, ESI†).

Production of mGFPH6

E. coli Origami B/pET22b-T22GFPH6 (mGFPH6)[27] culture (2 L) was grown at 37 °C and 250 rpm in LB broth with ampicillin at 100 μg mL^{-1}, kanamycin at 15 μg mL^{-1} and tetracycline at 12.5 μg mL^{-1}. When OD600 = 0.5 was reached, protein production was induced with 1 mM IPTG (isopropyl-β-D-thiogalactoside) and the culture was grown O/N at 20 °C and 250 rpm. After O/N production, cultures were centrifuged at 6000 × *g* and 4 °C for 45 min. Then, the pellets were resuspended in 20 mM Tris-HCl (pH 8.0), with 500 mM NaCl, 20 mM imidazole and protease inhibitors (complete EDTA-free; Roche, Indianapolis, USA). Intracellular soluble protein was extracted by sonication with 4 × 5 min rounds (0.5 on, 0.5 off cycles) at 10% amplitude, with a minimum 10 min rest in ice between rounds. Finally, the protein was purified by IMAC using a 1 mL HisTrap HP column (GE Healthcare; Uppsala, Sweden) in an Äkta start protein purification system (GE Healthcare; Uppsala, Sweden). Protein separation was achieved with a linear imidazole gradient from 20 mM to 500 mM. Fractions were collected and dialyzed against 166 mM $NaHCO_3$ at pH 7.4. The amount of protein was determined using a Nanodrop 1000 spectrophotometer (Thermo Scientific) at 280 nm and protein integrity was evaluated using western blot analysis as described above (See Fig. S8, ESI†).

Preparation of patterned and non-patterned His-tagged protein SAMs

Substrates used were either glass slides with a 2-nm titanium adhesion layer and a 10-nm gold layer or silicon wafers with a 50-nm titanium adhesion layer and 100-nm gold layer. The substrates were cut to have an area of 1.5 × 1 cm and cleaned with HPLC gradient solvents during 5 min; first isopropanol, then acetone, and lastly ethanol. After drying them with a nitrogen gun very carefully, they were exposed to ozone (UVO CLEANER, Model No. 42-220) for 20 min and immersed in ethanol during 30 min.

For the μCP procedure, the polydimethylsiloxane (PDMS) stamp of interest was cut using a scalpel, rinsed with ethanol, and dried off with a stream of nitrogen. Then, a solution of SH-PEG (ProChimia Surfaces, Scheme 1) 1 mM in ethanol was dropped (40 μL) on top of the PDMS stamp. The stamp was then dried off using a nitrogen gun. The substrates were then printed with the inked stamp by carefully placing the stamp on the substrate and leaving them in contact for 2 min. An empty and flat Petri dish was placed on top of the stamp to increase and homogenize the pressure. The stamp was removed carefully with tweezers and the substrates were incubated with 80 μL of SH-PEG-NTA (ProChimia Surfaces, Scheme 1) 1 mM in ethanol in a humid chamber during 2 h at RT. The substrates were transferred to a 6-well plate to perform the following immersions at RT: (i) Milli-Q water during 5 min (×2); (ii) HEPES buffer solution for 10 min (×1), (iii) 10 mM $NiCl_2$ in HEPES during 30 min; (iv) HEPES for 2 min (×3).

Then, the substrates were incubated with mGFPH6 or antimicrobial protein JAMF1 in soluble (20 μM) and insoluble pNP forms (23 μM for evaluation against *E. coli* DH5α or 500 μM for evaluation against KPC) in a humid chamber during 1 h at RT. For the preliminary trials, 45 μL of mGFPH6 (20 μM) was used and the Petri dish was covered with an aluminum foil to avoid photobleaching. For the soluble JAMF1, we used 50 μL of 20 μM and for the pNP, 50 μL of 23 μM and 500 μM, for E. Coli and KPC, respectively, were used.

The samples were immersed in HEPES during 5 min (×2). For the negative control samples, a further treatment with EDTA was performed. EDTA acts as a competitive chelator for NTA because it cleaves the chelated Ni from NTA to form

 © 2023 The Author(s). Published by the Royal Society of Chemistry

Open Access Article. Published on 13 April 2023. Downloaded on 5/30/2024 2:35:54 PM.
This article is licensed under a Creative Commons Attribution-NonCommercial 3.0 Unported Licence.

a Ni–EDTA complex. The effectiveness of this competition lies on the higher stability constant of the Ni–EDTA complex (18.56 in logarithmic) than the NTA–Ni complex (11.26 in logarithmic). Therefore, the His-tagged protein can no longer bind to S-PEG-NTA. The detailed steps were the following: (i) the substrates were immersed in 10 mM EDTA solution (or 100 mM for the NPs) during 20 min and rinsed again with HEPES afterwards; (ii) if they were not characterized straight away, the substrates were left immersed in HEPES in the fridge at 4 °C. The pH values of both HEPES and EDTA solutions were adjusted before their use to values of 8.0 and 7.31, respectively, using 0.1 M NaOH and 0.1 M H_2SO_4 solutions. For non-patterned substrates, no μCP procedure was used, and instead the entire area of the surface was functionalized with SH-PEG-NTA.

Immunostaining

The following immunostaining steps were performed: (1) after protein immobilization, the substrates were incubated with a solution of primary antibody $sPLA_2$ (E-9) (Santa Cruz Biotechnology, Inc.) in a ratio of 1 : 400 in bovine serum albumin (BSA) solution (1% in PBS). Each substrate was incubated with 50 μL in a humid chamber for 1 h. (2) The substrates were rinsed in PBS on the shaker at 50 rpm for 10 min. (3) The substrates were incubated with a solution of a secondary antibody, Alexa goat anti-mouse 488 IgG (Thermo Fisher Scientific), in a ratio of 1 : 100 in the BSA solution. Again, each substrate was incubated with 50 μL in a dark humid chamber for 45 min. (4) The substrates were rinsed in PBS on the shaker at 50 rpm during 10 min. (5) The substrates were mounted on glass slides with 50 μL of ProLong Gold Antifade Reagent (Thermo Fisher Scientific). They were left to dry O/N in a dark chamber.

Fluorescence microscopy

The instruments employed for the visualization of the samples were an Olympus BX51 microscope equipped with a CCD camera Olympus DP20 for S-PEG-NTA-Ni-mGFPH6 samples and an Axio Observer Z1m optical microscope (ZEISS) for the rest of the samples. The software Image J was used to extract the intensity profile of the striped pattern. The substrates observed were the following: patterned S-PEG-NTA-Ni-mGFPH6, immunostained patterned S-PEG-NTA-Ni-JAMF1-Sol, immunostained patterned S-PEG-NTA-Ni-JAMF1-pNP, together with the negative controls.

Cyclic voltammetry

A solution of 5 mM of $[Ru(NH_3)_6)]_3^+$ was prepared in an electrolyte solution consisting in a 50 mM KCl aqueous solution. A platinum wire was employed as the counter electrode (CE) and an Ag/AgCl electrode as the reference electrode (RE). The working electrode (WE) was, depending on the measurement, the bare gold substrate, S-PEG-NTA, S-PEG-NTA–Ni-JAMF1-Sol, S-NTA–Ni-JAMF1-pNP or S-PEG-NTA–Ni-mGFPH6. The potentiostat used was AUTOLAB 204 and the software used for the data acquisition and analysis was Nova 2.3. The scan rate used was 0.1 V s^{-1} and the area of the WE immersed into the electrolyte solution was around 1.5 cm^2.

Atomic force microscopy

Surface topography and film thickness were examined by a Keysight 5500 SPM system from Agilent. The images were processed using the Gwyddion software. The samples analyzed had a 2-μm striped pattern of (A) S-PEG-NTA–Ni-JAMF1-Sol, (B) S-PEG-NTA–Ni-JAMF1-Sol-Ctrl (by treatment with 10 mM EDTA) (C) S-PEG-NTA–Ni-JAMF1-pNP, (D) S-NTA–Ni-JAMF1-pNP-Ctrl (by treatment with 100 mM EDTA), (E) S-PEG-NTA–Ni and (F) S-PEG-NTA. It is important to mention that the measurements were conducted under dry conditions and that surfaces analyzed are biological samples, so the protein on the surface is dehydrated. The topography images shown in Fig. 5 and 6 were processed using a mean plane subtraction and the 'Revolve Arc' function for flattening (30 pixels, 2.9 μm, horizontal direction). No image processing was applied on phase images. For profile extraction (Fig. 7), the images were processed using a mean plane subtraction, flattened base and offset subtraction.

X-ray photoelectron spectroscopy (XPS)

The measurements were performed using a Phoibos 150 analyzer (SPECS GmbH) under ultrahigh vacuum conditions (base pressure 5×10^{-10} mbar) with a monochromatic aluminum K alpha X-ray source (1486.74 eV). The energy resolution measured by the FWHM of the Ag 3d5/2 peak for a sputtered silver foil was 0.6 eV. The spot size was 3.5 mm by 0.5 mm. Compositional survey and detailed scans (N 1s, S 2p, Ni 2p and O 1s,) were acquired. The samples measured were S-PEG-NTA–Ni-JAMF1-Sol, S-PEG-NTA–Ni-JAMF1-Sol-Ctrl (by treatment with 10 mM EDTA), S-PEG-NTA–Ni-JAMF1-pNP, S-PEG-NTA–Ni-JAMF1-pNP-Ctrl (by treatment with 100 mM EDTA), S-PEG-NTA–Ni and S-PEG-NTA. In all substrates, the prepared S-PEG-NTA was not patterned, so the incubation with SH-PEG-NTA was done directly without previous μCP of SH-PEG.

Antibiofilm activity assay

Bacterial strains were grown O/N at 37 °C and 250 rpm. Before adding bacteria to a 24-well sterile plate for biofilm formation, either His-tagged protein-mixed SAMs were placed under sterile conditions in each well. After that, bacteria from the O/N culture were diluted 1 : 200 in fresh medium supplemented with 0.2% (w/v) glucose. A total of 400 μL of diluted bacterial culture supplemented with glucose was incubated in each well at 37 °C for 24 h under static conditions. After the incubation, the supernatant was removed and wells were washed 3 times with 500 μL NaCl 0.9%, then fixated with 500 μL methanol for 10 min at RT. Methanol was removed and the plate was dried for 15 min at 37 °C. The remaining biofilm cells in the well were stained with crystal violet 1% (v/v) for 15 min at RT and washed 3 times with sterile dH_2O. Finally, the stained cells were diluted in 33% (v/v) acetic acid and the absorbance was measured at 595 nm.[28] All measurements were done by triplicate under sterile conditions.

Statistical analysis

For all assays, each condition was used in triplicate or quintuplicate (Fig. 9 and 10 are represented as the mean ± standard

Open Access Article. Published on 13 April 2023. Downloaded on 5/30/2024 2:35:54 PM.
This article is licensed under a Creative Commons Attribution-NonCommercial 3.0 Unported Licence.

error of the mean. All data were checked for normality. The *P*-values correspond to *t*-test analyses for the antibiofilm activity assay.

Results and discussions

Production of a novel antimicrobial protein

We used a multidomain AMP named JAMF1, which combines human α-defensin 5 (HD5), a bacterial binding domain (gelsolin), and an enzymatic antimicrobial peptide, group-XIIA secretory phospholipase A2 ($sPLA_2$), flanked by two aggregation-seeding domains (a fragment of c-Jun and c-Fos leucine zippers at N- and C-terminals) (Fig. 2).[10] The AMP was produced as pNP or as a source to obtain soluble protein. Both formats have previously shown activity against Gram-positive and Gram-negative bacteria[10] in solution. JAMF1 pNPs also showed antibiofilm activity when they were used to decorate plastic surfaces.[10] However, the activity of this protein anchored in SAMs has not been explored so far.

HD5 and $sPLA_2$ are those domains forming JAMF1 that have antimicrobial activity. The mechanism of action of HD5 is based on its cationic and amphipathic nature. HD5 is attracted by electrostatic forces to the negatively charged lipid bilayer forming the bacterial membrane and this induced a change on the membrane structure and, consequently, a pore is formed.[29] $sPLA_2$ is an enzyme also from the innate immunity, which effectively hydrolyses the phospholipids components of the bacterial membrane. Thus, the combination of both HD5 and $sPLA_2$ domains makes JAMF1 protein a promising antimicrobial candidate against Gram-negative and Gram-positive bacteria.[10]

The gelsolin domain also included in JAMF1 is a bacterial binding domain whose role is to increase the efficiency of the JAMF1 molecule binding the pathogen to be treated.

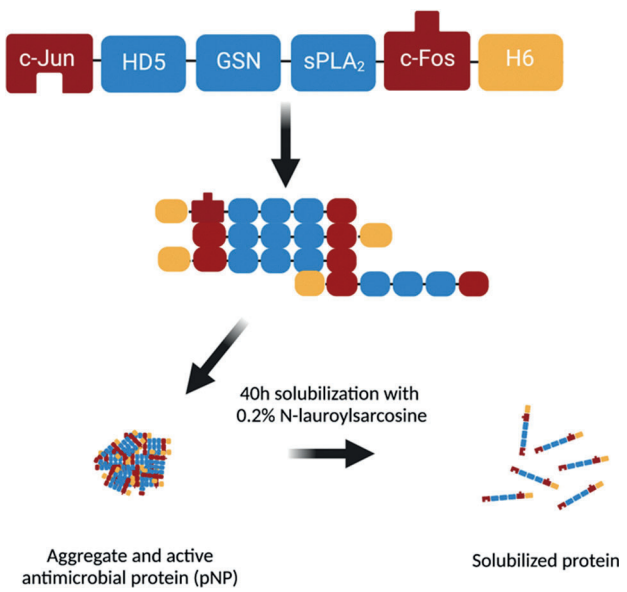


Fig. 2 Scheme of the multidomain antimicrobial protein JAMF1 containing (from N-terminal to C-terminal) amino acids 257-318 from c-Jun leucine zipper, the sequence of human α-defensin 5 (HD5), amino acids 188–196 from gelsolin (GSN), group-XIIA secretory phospholipase A2 ($sPLA_2$), amino acids 118–210 from c-Fos and a six-histidine tag (H6). Bottom: JAMF1-forming pNPs and their soluble form after a solubilization process.

His-tagged AMPs anchoring on micropatterned S-PEG-NTA-Ni SAMs

In order to improve the characterization of the AMPs anchoring process, surfaces with the immobilized proteins have been prepared using the μCP technique through a spatial control of the distribution of the SH-PEG-NTA and SH-PEG mixed SAMs (Fig. 3). Before using JAMF1, a His-tagged green fluorescent protein (mGFPH6) has been used for surface protein immobilization to easily visualize the pattern by fluorescence microscopy and optimize its spatial distribution. Briefly, a PDMS stamp inked with a SH-PEG ethanolic solution (1 mM) was put in contact with the clean gold surface and peeled off carefully. Thereafter, they were incubated with a SH-PEG-NTA ethanolic solution (1 mM) to backfill the non-patterned areas, obtaining a patterned S-PEG-NTA. Afterwards, the samples were incubated in a $NiCl_2$ solution, obtaining S-PEG-NTA–Ni. Negative controls were prepared in the same way but finally treated with EDTA which acts as a competitive chelator, cleaving the Ni from NTA and leading to S-PEG-NTA again.

The patterned S-NTA–Ni-mGFPH6 samples were prepared following the procedure depicted in Fig. 3. A fluorescent striped pattern was obtained as visualized in Fig. S1 (ESI†), demonstrating that mGFPH6 is correctly immobilized on the S-PEG-NTA–Ni samples. These results showed the successful optimization of the spatial control by SAM formation using the μCP technique and also the good affinity of the His-tag of the recombinant proteins for the NTA–Ni complex on the surface.

The absence of fluorescent patterns in the negative controls demonstrates that Ni is removed from the NTA and chelated by EDTA, inducing the removal of the His-tagged protein and, therefore, of the protein from the surface.

CV has also been used to examine the current barrier properties of the functionalized surface and further corroborate the integrity of the SAM and correct anchoring of mGFPH6.

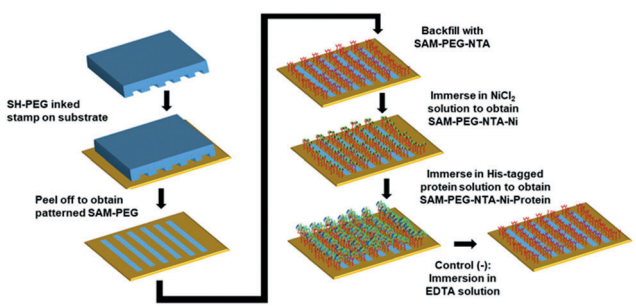


Fig. 3 Schematic representation of the experimental procedure followed to prepare patterned SH-PEG-NTA and SH-PEG mixed SAMs, using the μCP technique. Subsequent protein immobilization *via* their His-tag termination led to protein anchoring. Negative controls were prepared by immersing the substrates in an EDTA solution (10 or 100 mM).

© 2023 The Author(s). Published by the Royal Society of Chemistry

Open Access Article. Published on 13 April 2023. Downloaded on 5/30/2024 2:35:54 PM.
This article is licensed under a Creative Commons Attribution-NonCommercial 3.0 Unported Licence.

For this experiment, non-patterned surfaces were used. When performing CV experiments with mGFPH6 functionalized gold substrates, as working electrodes, (Fig. S2, ESI†) in the presence of a redox probe ($[Ru(NH_3)_6)]^{3+}$), the current decreases when the mixed SAM is formed on the gold surface and decreases even more when mGFPH6 is immobilized. This fact is indicative of a higher blocking effect which hinders electrons to travel from the redox probe to the gold surface and *vice versa*. The anchoring of mGFPH6 on the surface hinders even more the access of electrons to the gold surface, not only because they imply a larger separation distance between the gold and redox probe acting like a new layer of impedance for the electrons to overcome, but because their bigger size and volume in comparison to the SAM molecules make the electron transfer even harder. In view of these results, we can conclude that a densely packed mixed SAM has been assembled and that mGFPH6 is correctly immobilized.

Patterned anchoring of AMP JAMF1

The correct immobilization of the JAMF1 active antimicrobial polypeptide using mixed SAMs was monitored using: (i) immunostaining and subsequent fluorescence microscopy, (ii) AFM, (iii) CV, and (iv) XPS. To produce the functional surfaces to be characterized by these techniques, first a S-PEG SAM is μCP on the substrate (20 μm stripes) and then the empty stripes are back filled with the NTA-terminated SAM. Finally, the substrate is immersed in the JAMF1 protein solution for its spatially controlled anchoring through His-tag termination (see Fig. 3).

Immunostaining and fluorescence microscopy

In this case, proteins are depleted of fluorescence, thus, to visualize the pattern, immunostaining had to be performed using a primary and secondary antibody as described in the experimental section. Following the procedure described in Fig. 3, a homogeneous functionalization of the antimicrobial protein onto patterned S-PEG-NTA–Ni samples was achieved, both with the soluble and pNP forms of the protein (Fig. 4A and B, respectively). In fact, it is the first time that the NTA–Ni strategy is used to anchor pNPs on surfaces. Even some aggregates are observed (Fig. 4B) due to the aggregation nature of the protein,[24,25] the fluorescent stripes remain well delimited, and a uniform coverage of the protein is found along the pattern.

The absence of fluorescent patterns in the negative controls, achieved by immersing the substrates in EDTA (10 mM), as shown in Fig. 4(C) and (D), indicates the reversibility of the union. Moreover, the dark images obtained from the generic negative control (Fig. 4(E)), which consisted in the immunostaining of a patterned S-PEG-NTA sample, show that the immunostaining technique worked correctly, and that the fluorescence is specific for the immunostained proteins.

In addition, the fluorescence intensity profiles (Fig. S3, ESI†) for the patterning of the soluble form and also with the pNP formats of the JAMF1 protein, show peaks with practically the same intensity in both cases, indicating a homogeneous coverage of the protein on the desired areas. A periodicity in the intensity peaks is observed: there is low or no fluorescence intensity between peaks, implying that there are no luminescent antibodies and therefore, no antimicrobial protein. Hence, the antimicrobial His-tagged protein is specifically attached only onto the NTA–Ni groups, and the SH-PEG molecules form a protein-repelling surface, as desired. These results also confirm that μCP allows a correct spatial control of protein immobilization.

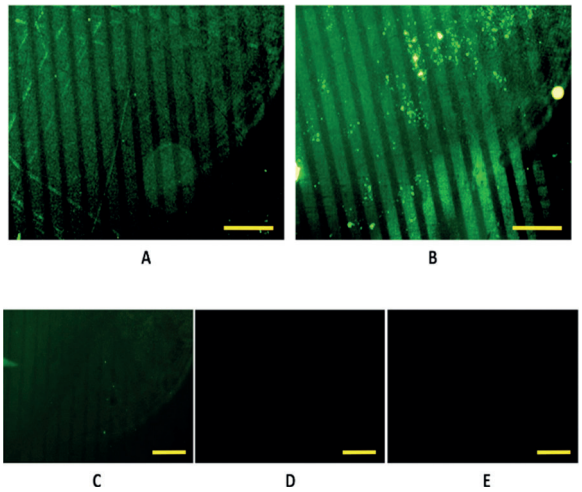


Fig. 4 Fluorescence microscopy images of a 20-μm striped pattern of immunostained (A) S-PEG-NTA-Ni-JAMF1-Sol in soluble form and (B) S-PEG-NTA-Ni-JAMF1-pNP. The fluorescence images of the negative controls (by immersion in EDTA (10 mM)) of a 20-μm striped patterns of (C) S-PEG-NTA-Ni-JAMF1-Sol-Ctrl and (D) S-PEG-NTA-Ni- JAMF1-pNP-Ctrl. (E) A generic negative control of the immunostaining technique, which consisted in patterned S-PEG-NTA. The scale yellow bars correspond to 100 μm.

Atomic force microscopy

In order to match with the lateral resolution of the AFM technique, in this case, 2-μm wide striped patterns were printed (Fig. 3) for both soluble and pNP forms of the antimicrobial protein. Both topographical (Fig. 5(A) and Fig. 6(A)) and phase shift images (Fig. 5(B) and Fig. 6(B)) confirmed the correct protein immobilization. Fig. 5 and 6C, D are the topography and phase images of negative controls based on samples treated with EDTA which demonstrate the correct removal of the protein from the surface.

With the topographical profiles (Fig. 7), we observed that the stripes of the soluble protein are better delimited than the ones of the pNP pattern which are also wider than the those of the soluble protein. The height of pNP is greater than the one from the soluble protein, indicative of the successful immobilization of both soluble and pNP. For analysis purposes, the average measurements of the height and the width of each sample are shown in Table 1.

The difference in height between the negative controls (Fig. 7(B and D)) consisting in a patterned S-PEG-NTA sample, and the ones with bound protein (Fig. 7(A) and (C)), corresponds to the presence of the immobilized antimicrobial protein. Fig. 7C and 7D show that the EDTA strategy for the removal of pNP to generate the negative control is not as

Open Access Article. Published on 13 April 2023. Downloaded on 5/30/2024 2:35:54 PM.
This article is licensed under a Creative Commons Attribution-NonCommercial 3.0 Unported Licence.

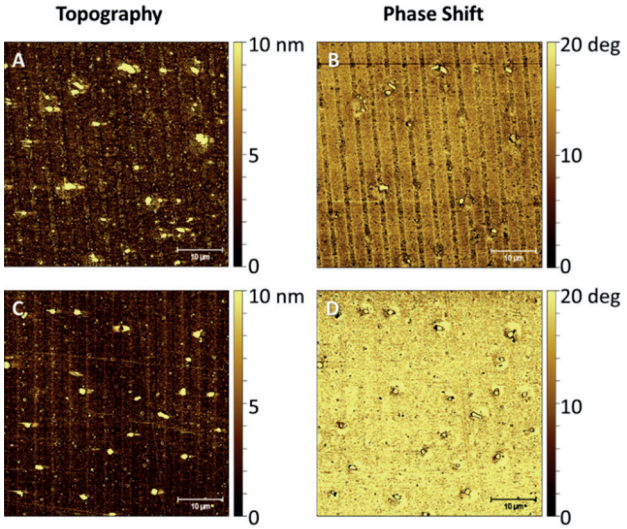


Fig. 5 (A) and (C) Topographical and (B) and (D) phase shift AFM images of the 2-μm wide striped pattern of S-PEG-NTA–Ni-JAMF1-Sol (A) and (B) and their negative controls treated with EDTA (10 mM), S-PEG-NTA–Ni-JAMF1-Sol-Ctrl (C) and (D).

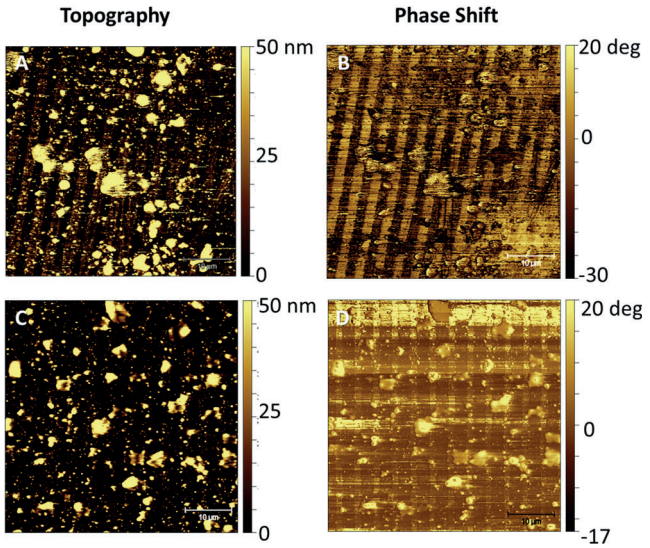


Fig. 6 (A) and (C) Topographical and (B) and (D) phase shift AFM images of the 2-μm wide striped pattern of S-PEG-NTA–Ni-JAMF1-pNP (A) and (B) and their negative controls treated with EDTA (100 mM), S-PEG-NTA–Ni-JAMF1-pNP-Ctrl (C) and (D).

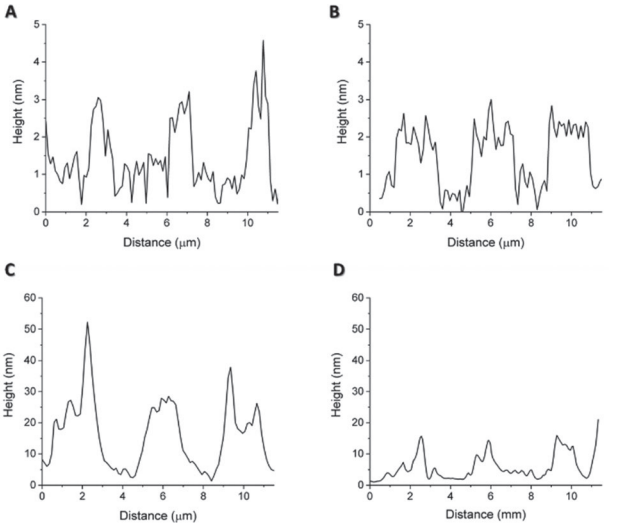


Fig. 7 Topographic profiles of (A) patterned S-PEG-NTA–Ni-Sol, (B) patterned S-PEG-NTA–Ni-Sol-Ctrl, (C) patterned S-PEG-NTA–Ni-JAMF1-pNP and (D) patterned S-PEG-NTA–Ni-JAMF1-pNP-Ctrl.

Table 1 Values corresponding to the average peak width and height extracted from the AFM images

Sample	Mean peak width [μm]	Mean peak height [nm]
S-PEG-NTA–Ni-JAMF1-Sol	1.3 ± 0.1	3.0 ± 0.6
S-PEG-NTA–Ni-JAMF1-Sol-Ctrl	2.30 ± 0.02	2.0 ± 0.1
S-PEG-NTA–Ni-JAMF1-pNP	2.56 ± 0.08	37 ± 8
S-PEG-NTA–Ni-JAMF1-pNP-Ctrl	2.00 ± 0.09	12.7 ± 0.6

effective as it is for the soluble protein. It is important to note that measurements were conducted under dry conditions and the proteins on the surface are dehydrated, thus the measured value of their height is not comparable with other reported protein sizes, because normally, these measurements were done under aqueous conditions.[30] As expected, the pNP sample is found to have higher values than those of the soluble one (Table 1). The measured values of their heights are not comparable with the other reported protein sizes, which are measured under aqueous conditions, important for protein hydration, 3D structure, dynamics and activity.[31] AFM measurements are performed under dry conditions and thus, aqueous media around the protein provides a hydration layer which enhances the measured protein size.[30,32] The removal of water from our substrates may have provoked a reduction in protein size and probably even the loss of their 3D structure. Nonetheless, these measurements give an insight regarding the protein mass immobilized on the surface. In fact, comparing the height of the soluble protein and the pNP, the height of the pNP is greater than the one from the soluble protein, indicative of the successful immobilization of both soluble and pNP forms. The width differences observed between peaks may be again due to the aggregated nature of the pNP, which when immobilized on the edge of the patterned NTA, can surpass the extension of the pattern, resulting in wider peaks compared to those obtained with the soluble protein.

Stiffness variations on the surface can be analyzed using phase imaging maps. A stiffer region has a more positive phase shift than a less stiff region and appears brighter in a phase image.[33,34] In soft materials, the phase shift is highly dependent on the viscoelastic properties of the material.[35] The antimicrobial protein in both soluble and pNP forms can be detected in the negative phase shift regions, appearing darker. The areas functionalized with SH-PEG appear stiffer than the areas with immobilized protein, which are only attached to the SAM by the His-tag, and are more likely to deform.

© 2023 The Author(s). Published by the Royal Society of Chemistry

Open Access Article. Published on 13 April 2023. Downloaded on 5/30/2024 2:35:54 PM.
This article is licensed under a Creative Commons Attribution-NonCommercial 3.0 Unported Licence.

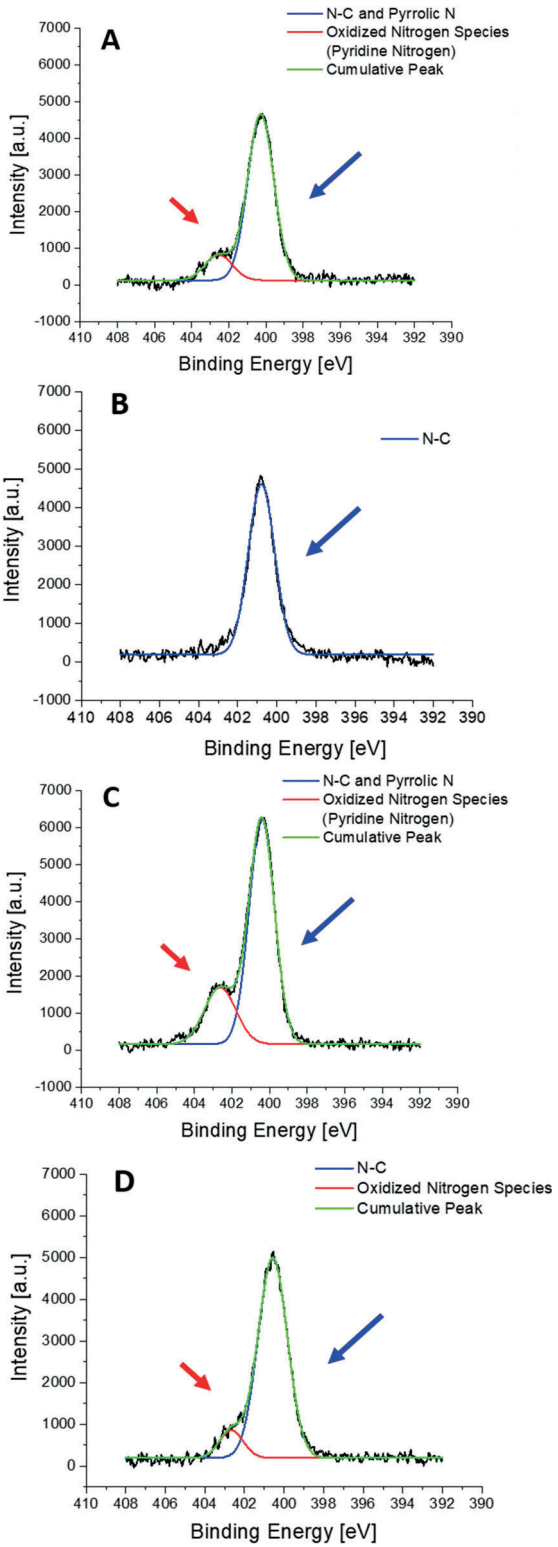


Fig. 8 XPS deconvolutions of N 1s spectra for (A) S-PEG-NTA–Ni-JAMF1-Sol, (B) S-PEG-NTA–Ni-JAMF1-Sol-Ctrl (treatment with EDTA 10 mM), (C) S-PEG-NTA–Ni-JAMF-pNP and (D) S-PEG-NTA-Ni–JAMF1-pNP-Ctrl (treatment with EDTA 100 mM). The red arrow indicates the contribution of 'pyridine-like' nitrogen and the blue arrow indicates the contribution of 'pyrrole-like' amino and amide nitrogen.

In negative controls, the pattern is not detected in the phase shift images, as shown in Fig. 5D since both SH-NTA and SH-PEG form a compact SAM with similar stiffness and viscoelastic properties, with their aliphatic chains interacting between each other.

Cyclic voltammetry

We have used CV to study the correct formation of the SAMs and the immobilization of the antimicrobial protein using the modified substrates as WE (Fig. S2 and S4, ESI†). A decrease in current is observed after S-PEG-NTA SAM formation (Fig. S2 and S4, red line, ESI†), as expected. From the NTA SAM, the protein immobilization gives rise to a current reduction which is not as large as in the case of mGFPH6 (Fig. S2, ESI†). The reason may be that mGFPH6 is much smaller than the antimicrobial protein: mGFPH6 has 238 amino acids, while the novel antimicrobial protein has 487 amino acids. Therefore, the attachment of mGFPH6 to NTA–Ni is easier than in the case of the larger antimicrobial multidomain protein. Also, due to its size, steric hindrance may play a role, making it more difficult to occupy all the NTA–Ni units. This is an indication that when the protein anchors the SAM, even a higher layer is formed, it becomes less compact. Hence, the coverage of the S-PEG-NTA–Ni-JAMF1-Sol, even if efficiently performed, as seen before, is not as homogeneous as with the smaller GFP. It presents more defects.

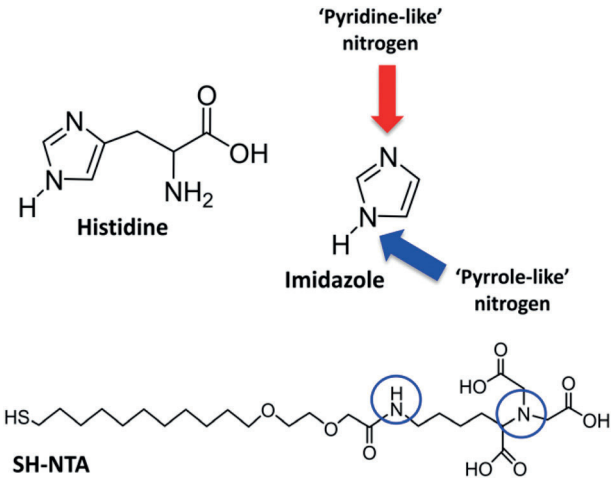
The voltammogram obtained after immobilization of the pNP (S-PEG-NTA–Ni-JAMF1-pNP) shows a decrease of current for the positive voltage which is in accordance with the biggest size of the nanoparticles in comparison with the soluble protein thus, impairing more current flow.

X Ray photoelectron spectroscopy

XPS measurements were performed for 4 different samples: (i) S-PEG-NTA–Ni-JAMF1-Sol, (ii) S-PEG-NTA–Ni-JAMF1-Sol-Ctrl (treatment with EDTA 10 mM), (iii) S-PEG-NTA–Ni-JAMF1-pNP and (iv) S-PEG-NTA–Ni-JAMF1-pNP-Ctrl (treatment with EDTA 100 mM). Nitrogen, sulfur, and oxygen were analyzed and their spectra deconvoluted, showing peaks, shifts and intensity relations that agree with the expected results, demonstrating successful protein immobilization.

For the N 1s spectra (see Fig. 8 and Scheme 2), two peaks can be observed, one at 400–401 eV and another one at 402.5 eV. The peak at around 400–401 eV, which is observed for all the samples, corresponds to the N–C bond found in the NTA present in all the samples, but also in amino acids, and it is also attributed to 'pyrrole-like nitrogen' (typically assigned to peaks around 400.4 eV) present in histidine and tryptophan of the anchored proteins. Thus, samples presenting the His-tag, which in turn has imidazole groups that contain 'pyrrole-like' nitrogen, and the amino acid tryptophan, which also has 'pyrrole-like' nitrogen present this peak. Negative controls, which only have the NTA exposed on the surface, present N–C bonds and secondary amides and therefore, also present this peak. Also, amines and secondary amides present in the

Open Access Article. Published on 13 April 2023. Downloaded on 5/30/2024 2:35:54 PM.
This article is licensed under a Creative Commons Attribution-NonCommercial 3.0 Unported Licence.



Scheme 2 Representation of the different contribution to the nitrogen spectra: 'pyrrole-like' nitrogen (blue arrow and circles) and 'pyridine-like' amines (N–C) and secondary amides (red arrow).

studied samples are attributed to the peaks with energies of 400.5 eV.

The peak at 402.5 eV is clearly observed in the samples with the protein (Fig. 8(A) and (C)) but for the negative controls, it is absent in Fig. 8(B) and it decreases in Fig. 8(D). This peak is assigned to pyridine-like nitrogen present in the His-tag and therefore only in the samples containing protein.

The S 2p spectra (Fig. S6, ESI†) show four peaks. The peak at 161.9 eV and the peak at around 162.8–163.4 eV are attributed to the split of the orbital 2p into the doublet 2p3/2 and 2p1/2, respectively. These peaks come from the thiol bond (S–Au) of the thiolated NTA chains to the gold surface, present in all samples. On the other hand, there are two more peaks, one at 168.5 eV and the other at around 169.7–171.8 eV, both corresponding to oxidized sulfur species, which can come from the thiol groups in the alkanethiols or from cysteine amino acids present in the antimicrobial proteins. These peaks only appear in the sample with immobilized protein, with this peak less intense in samples without protein (Fig. S6B, ESI†).

The O 1s spectra, shown in Fig. S6 (ESI†), present a big peak that can be deconvoluted in two. The peak at 532 eV corresponds to the C–O bond and the one at around 532.7–532.9 eV corresponds to the C═O bond. Besides, a peak at 537 eV is also observed with more intensity in the protein samples which is attributed to either adsorbed water, acetate species or oxygen species interacting with Ni. Therefore, it can be associated either to the presence of –COOH groups in the amino acids or to the interaction of oxygen and Ni in the chelating complexes. Both cases demonstrate the presence of His-tag and soluble protein/pNP, which is also confirmed by the fact that there is no peak in the S-PEG-NTA–Ni-JAMF1-Sol-Ctrl (Fig. S6(B), ESI†). The peak present in the negative control S-PEG-NTA–Ni-JAMF1-pNP-Ctrl (Fig. S7(D), ESI†) can be attributed to undesired oxidation due to the aging of the sample, which was analyzed three days after preparation. The ratio difference between the C–O and C═O peaks in the positive samples can be attributed to the differences between the soluble protein and pNP.

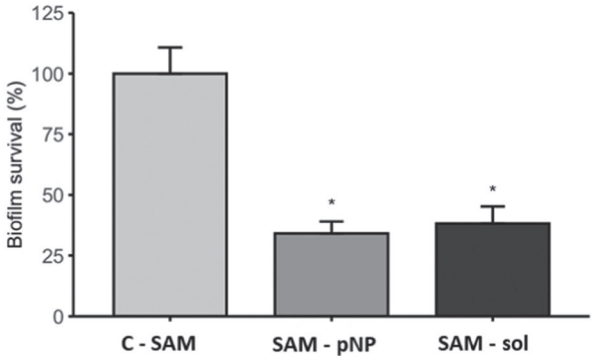


Fig. 9 Biofilm formation ability (%) of *E. coli* DH5α on S-PEG-NTA-Ni-JAMF1-Sol and S-PEG-NTA-Ni-pNP. * indicates significant differences ($p \leq 0.05$).

Antibiofilm activity assay

The antibiofilm activity assay showed that the JAMF1 multidomain antimicrobial protein in both soluble and pNP forms can significantly reduce biofilm formation (Fig. 9). S-PEG-NTA–Ni-Sol and S-PEG-NTA–Ni-pNP surfaces reduce *E. coli* survival up to 38% and 34%, respectively, showing that the strategy used to anchor the protein to the surface is highly promising. The same behavior is observed when S-PEG-NTA–Ni-pNP surfaces are used against an antibiotic-resistant KPC strain (Fig. 10), demonstrating that JAMF1 is also active against severe bacterial strains not responding to standard antibiotic treatments.

Although after the immobilization process of JAMF1 using SAMs, the activity of these molecule is slightly decreased compared to those proteins with no specific binding to the surface,[10] the remaining activity is still high, which demonstrates that the strategy presented in this study is a promising approach for the design of materials with antimicrobial properties. Especially when the microorganism growth is observed in biofilm formation, this type of formation makes the microorganism more resistant, requiring up to 1000 times more antibiotic doses than in its soluble form.[36] Furthermore, the strategy presented in this work, NTA–Ni interaction with

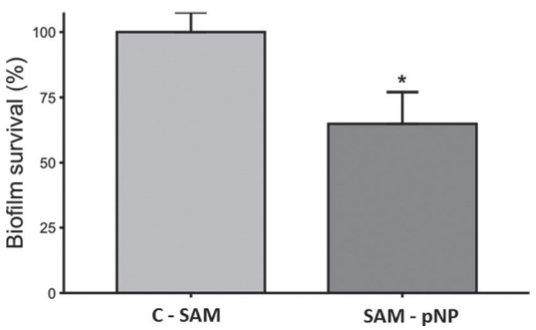


Fig. 10 Biofilm formation ability (%) of KPC on S-PEG-NTA-Ni-pNP. * indicates significant differences ($p \leq 0.05$).

© 2023 The Author(s). Published by the Royal Society of Chemistry

Open Access Article. Published on 13 April 2023. Downloaded on 5/30/2024 2:35:54 PM. This article is licensed under a Creative Commons Attribution-NonCommercial 3.0 Unported Licence.

His-tag, represents a platform for the immobilization of recombinant antimicrobial proteins produced with His-tag which can be easily exploited for the immobilization of other proteins.

Conclusions

Micropatterns of AMPs were successfully formed using the μCP technique through the NTA functionalization of gold surfaces assisted by a thiol group, combined with the His-tagged antimicrobial protein JAMF1, both in the soluble form and nanostructured as pNPs. The successful pattern formation not only was verified by fluorescence microscopy, but also by AFM and XPS measurements. This functionalization strategy was then applied to fully coated surfaces, demonstrating their effectiveness in preventing biofilm formation against *E. coli*. Specifically, the immobilized soluble and pNP forms reduced bacteria survival up to 38% and 34%, respectively. Moreover, the pNP surfaces also inhibited biofilm formation in a *K. pneumoniae* strain, which are unresponsive to standard antibiotic treatments. In conclusion, novel biofunctionalized surfaces with multidomain AMPs were developed and characterized in response to the need of new antimicrobial agents to overcome the antibiotic crisis, which could be applied to coat medical devices (*e.g.* catheters) or be incorporated into food packaging materials, among others.

Abbreviations

AFM	Atomic force microscopy
AMPs	Antimicrobial peptides
BHI	Brain heart infusion
BSA	Bovine serum albumin
CE	Counter electrode
CV	Cyclic voltammetry
HD5	Human α-defensin-5
IBs	Inclusion bodies
IMAC	Immobilized metal affinity chromatography
IPTG	Isopropyl-β-D-thiogalactoside
JAMF1	Recombinant antimicrobial multidomain protein
KPC	*Klebsiella pneumoniae*
KPi	Potassium phosphate buffer
LB	Luria-Bertani
GFPH6	His-tagged green fluorescent protein
Mixed SAMs	A mix of SH-PEG-NTA (%) and SH-PEG (%) on the self-assembled monolayers
NTA	Nitriloacetic acid
SAMs	Self-assembled monolayers
SH-PEG-NTA	NTA terminated tetra(ethylene glycol)-SAM
O/N	Overnight
PBS	Phosphate-buffered saline
PDMS	Polydimethylsiloxane
SH-PEG	((1-Mercapto-11-undecyl)-(tetra(ethylene glycol))
PEG	Polyethylene glycol
pNP	Protein nanoparticles
RE	Reference electrode
RT	Room temperature
S-NTA-Ni	NTA-Ni terminated SAMs
S-PEG-NTA-Ni-JAMF1-pNP	Mixed SAM with antimicrobial multidomain protein as inclusion bodies
S-PEG-NTA-Ni-JAMF1-Sol	Mixed SAM with soluble antimicrobial multidomain protein
S-PEG-NTA-Ni-mGFPH6	His-tagged green fluorescent protein immobilized on SAMs
SAMs	Self-assembled monolayersSH-NTA, NTA terminated thiol
SH-PEG	Pegylated alkanethiol
$sPLA_2$	Group-XIIA secretory phospholipase A2
WE	Working electrode
XPS	X-ray photoelectron spectroscopy
μCP	Microcontact printing

Author contributions

The manuscript was written through contributions of all authors. All authors have given approval to the final version of the manuscript.

Conflicts of interest

There are no conflicts to declare.

Acknowledgements

This work has been developed under the Biochemistry and Biomedicine and Materials Science Program of Universitat Autònoma de Barcelona (UAB). The characterization has been performed by the ICTS ''NANBIOSIS'', more specifically by the Biomaterial Processing and Nanostructuring Unit (U6), Unit of CIBER-BBN located at ICMAB-CSIC. Authors are grateful for the financial support received from MICINN (PID2020-115296 RA-I00 and PID2019–105622RB-I00), the Networking Research Center on Bioengineering, Biomaterials, and Nanomedicine (CIBER-BBN), GenCat (grant 2017-SGR-918, SGR Cat 2021-00438 and CERCA programme), the European Social Fund, and Fundació La Marató de TV3 (Nr. 201812). This project has received funding from the European Union's Horizon 2020 research and innovation program under the HORIZON-RIA project NABIHEAL (GA number 101092269), the Marie Skłodowska-Curie grant agreement No. 801342 (Tecniospring INDUSTRY) and the Government of Catalonia's Agency for Business Competitiveness (ACCIÓ; TECSPR19-1-0065). J.G. is grateful to MICINN for a ''Ramón y Cajal'' fellowship (RYC-2017-22614) as well as to the Max Planck Society through the Max Planck Partner Group ''Dynamic Biomimetics for Cancer Immunotherapy'' in collaboration with the Max Planck Institute for Medical Research (Heidelberg, Germany). R.R-P received a

Open Access Article. Published on 13 April 2023. Downloaded on 5/30/2024 2:35:54 PM. This article is licensed under a Creative Commons Attribution-NonCommercial 3.0 Unported Licence.

PhD fellowship from Secretaria d'Universitats i Recerca del Departament d'Economia i Coneixement de la Generalitat de Catalunya (AGAUR) and E.G-F a post-doctoral fellowship from INIA (DOC-INIA). ICMAB-CSIC acknowledges the support from the Severo Ochoa Programme for Centres of Excellence in R&D (FUNFUTURE, CEX2019-000917-S). Table of contents entry and Fig. 2 were designed with BioRender.com.

References

1 R. Smith and J. Coast, *BMJ [Br. Med. J.]*, 2013, 346.
2 N. Goel, S. W. Fatima, S. Kumar, R. Sinha and S. K. Khare, *Biotechnol. Rep.*, 2021, **30**, e00613.
3 C. J. Murray, *et al.*, *Lancet*, 2022, **399**, 629.
4 V. Nandakumar, S. Chittaranjan, V. M. Kurian and M. Doble, *Polym. J.*, 2013, **45**, 137.
5 R. M. Donlan and J. W. Costerton, *Clin. Microbiol. Rev.*, 2002, **15**, 167.
6 D. Sharma, L. Misba and A. U. Khan, *Antimicrob. Res. Infec. Control*, 2019, **76**, 1.
7 S. L. Percival, L. Suleman, C. Vuotto and G. Donelli, *J. Med. Microbiol.*, 2015, **64**, 323.
8 S. Srivastava and A. Bhargava, *Biotechnol. Lett.*, 2016, **38**, 1.
9 A. di Somma, A. Moretta, C. Canè, A. Cirillo and A. Duilio, *Biomolecules*, 2020, **10**, 1.
10 R. Roca-Pinilla, A. López-Cano, C. Saubi, E. Garcia-Fruitós and A. Arís, *Microb. Cell Fact.*, 2020, **19**, 122.
11 K. Yu, J. C. Y. Lo, M. Yan, X. Yang, D. E. Brooks, R. E. W. Hancock, D. Lange and J. N. Kizhakkedathu, *Biomaterials*, 2017, **116**, 69.
12 F. Costa, S. Maia, J. Gomes, P. Gomes and M. C. L. Martins, *Acta Biomater.*, 2014, **10**, 3513.
13 F. M. T. A. Costa, S. R. Maia, P. A. C. Gomes and M. C. L. Martins, *Biomaterials*, 2015, **52**, 531.
14 A. Rai, S. Pinto, M. B. Evangelista, H. Gil, S. Kallip, M. G. S. Ferreira and L. Ferreira, *Acta Biomater.*, 2016, **33**, 64.
15 F. Costa, I. F. Carvalho, R. C. Montelaro, P. Gomes and M. C. L. Martins, *Acta Biomater.*, 2011, **7**, 1431.
16 R. R. Silva, K. Avelino, K. L. Ribeiro, O. L. Franco, M. D. L. Oliveira and C. A. S. Andrade, *Front. Biosci. Scholar*, 2016, **1**, 129.
17 Z. Wang, X. Han, N. He, Z. Chen and C. L. Brooks, *J. Phys. Chem. B*, 2014, **118**, 5670.
18 V. Humblot, J. F. Yala, P. Thebault, K. Boukerma, A. Héquet, J. M. Berjeaud and C. M. Pradier, *Biomaterials*, 2009, **30**, 3503.
19 C. Monteiro, F. Costa, A. M. Pirttilä, M. V. Tejesvi and M. C. L. Martins, *Sci. Rep.*, 2019, **9**, 10753.
20 A. R. Kyvik, C. Luque-Corredera, D. Pulido, M. Royo, J. Veciana, J. Guasch and I. Ratera, *J. Phys. Chem. B*, 2018, **122**, 4481.
21 M. Martínez-Miguel, A. R. Kyvik, L. M. Ernst, A. Martínez-Moreno, O. Cano-Garrido, E. García-Fruitós, E. Vazquez, N. Ventosa, J. Guasch, J. Veciana, A. Villaverde and I. Ratera, *J. Mater. Chem. B*, 2020, **8**, 5080.
22 O. Cano-Garrido, A. Sánchez-Chardi, S. Parés, I. Giró, W. I. Tatkiewicz, N. Ferrer-Miralles, I. Ratera, A. Natalello, R. Cubarsi, J. Veciana, A. Bach, A. Villaverde, A. Arís and E. Garcia-Fruitós, *Acta Biomater.*, 2016, **43**, 230.
23 W. I. Tatkiewicz, J. Seras-Franzoso, E. García-Fruitós, E. Vazquez, A. R. Kyvik, N. Ventosa, J. Guasch, A. Villaverde, J. Venciana and I. Ratera, *ACS Biomater. Sci. Eng.*, 2019, **5**, 10.
24 M. Martínez-Miguel, W. Tatkiewicz, M. Köeber, N. Ventosa, J. Venciana, J. Guasch and I. Ratera, *Methods Mol. Biol.*, 2022, **2406**, 479.
25 M. Martínez-Miguel, W. Tatkiewicz, M. Köeber, N. Ventosa, J. Venciana, J. Guasch and I. Ratera, *Methods Mol. Biol.*, 2022, **2406**, 517.
26 Š. Peternel, J. Grdadolnik, V. Gaberc-Porekar and R. Komel, *Microb. Cell Fact.*, 2008, **7**, 1.
27 U. Unzueta, M. V. Céspedes, N. Ferrer-Miralles, I. Casanova, J. Cedano, J. L. Corchero, J. Domingo-Espín, A. Villaverde, R. Mangues and E. Vázquez, *Int. J. Nanomed.*, 2012, **7**, 4533.
28 L. Shi, Y. Wu, C. Yang, Y. Ma, Q. Zhang, W. Huang, X. Zhu, Y. Yan, J. Wang, T. Zhu, D. Qu, C. Zheng and K. Zhao, *Sci. Rep.*, 2019, **9**, 20243.
29 Y. Shai, *Biochim. Biophys. Acta*, 1999, **1462**, 55.
30 M. C. Bellissent-Funel, A. Hassanali, M. Havenith, R. Henchman, P. Pohl, F. Sterpone, D. van der Spoel, Y. Xu and A. E. Garcia, *Chem. Rev.*, 2016, **116**, 7673.
31 A. R. Bizzarri and S. Cannistraro, *J. Phys. Chem. B*, 2002, **106**, 6617.
32 J. W. Bye, S. Meliga, D. Ferachou, G. Cinque, J. A. Zeitler and R. J. Falconer, *J. Phys. Chem. A*, 2014, **118**, 83.
33 E. Nagao and J. A. Dvorak, *Biophys. J.*, 1999, **76**, 3289.
34 S. N. Magonov, V. Elings and M. H. Whangbo, *Surface Sci. Lett.*, 1997, **375**, L385.
35 J. Tamayo and R. García, *Langmuir*, 1996, **12**, 4430.
36 M. Kazemzadeh-Narbat, B. F. L. Lai, C. Ding, J. N. Kizhakkedathu, R. E. W. Hancock and R. Wang, *Biomaterials*, 2013, **34**, 5969.

© 2023 The Author(s). Published by the Royal Society of Chemistry

Electronic Supplementary Material (ESI) for Materials Advances.
This journal is © The Royal Society of Chemistry 2023

Supplementary Information

Antibiofilm surfaces based on the immobilization of a novel recombinant antimicrobial multidomain protein using self-assembly monolayers

Adriana R. Kyvik,[a] Ramon Roca-Pinilla,[d,f] Karla Mayolo-Deloisa,[a,e] Xavier Rodriguez Rodriguez,[a] Marc Martinez-Miguel,[a,b] Marta Martos,[a] M. Köber,[a,b] Nora Ventosa,[a,b] Jaume Veciana,[a,b] Judith Guasch,[a,b,c] Elena Garcia-Fruitós,[d] Anna Arís,[d] Imma Ratera[a,b]†

1. Fluorescence microscopy images of patterned mGFPH6

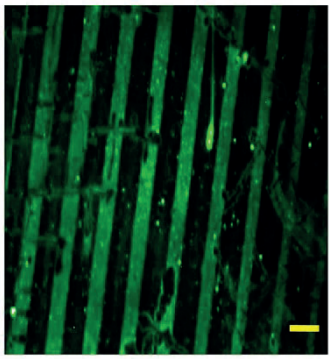


Figure S1. Fluorescence microscopy images of patterned mGFPH6 using the S-PEG-NTA-Ni SAMs strategy, obtaining **S-NTA-Ni-mGFPH6**. Micropatterns observed were created using the μCP technique with a PDMS stamp with a pattern of 20 μm. Scale yellow bars correspond to 30 μm.

2. Cyclic Voltammetry

A redox probe was used in order to study the electron transfer reactions between the redox probe and the gold surface under the functional mixed SAMs. As a redox probe it has been used hexaammineruthenium(III) chloride ($[Ru(NH_3)_6)]^{3+}$) because it is reported that can detect even the smallest defects in SAMs, which are invisible for other markers such as ferrocyanide [25]. The greater sensitivity of the $[Ru(NH_3)_6)]^{3+}$ probe can be explained by the location of its excess charge, located on the metal core in the ion center, whereas, in the case of hexacyano metal complexes, it is located on the terminal nitrogen atoms of cyano ligands [26]. Thus, as a consequence, [Ru(NH3)6)]3+ species can penetrate further into SAMs and diffuse along the SAM chains, so despite forming a very compact SAM, with the probable presence of some collapsed sites current signal can still appear in the recorded

voltammogram. Several studies have confirmed that the thicker the SAMs the higher the blocking properties [27].

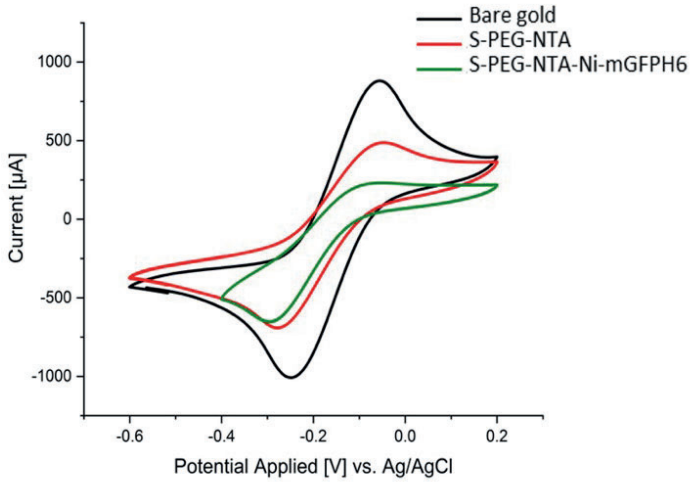


Figure S2. Cyclic voltammograms of bare gold, mixed SAMs and S-PEG-NTA-Ni-mGFPH6 SAMs. The electrolyte used is an aqueous KCl solution (50 mM) containing the redox probe $[Ru(NH_3)_6)]^{3+/2+}$ (5 mM). Scan rate used is 0.1 V/s.

3. Fluorescence profiles extracted from fluorescence images of immobilized JAMF1

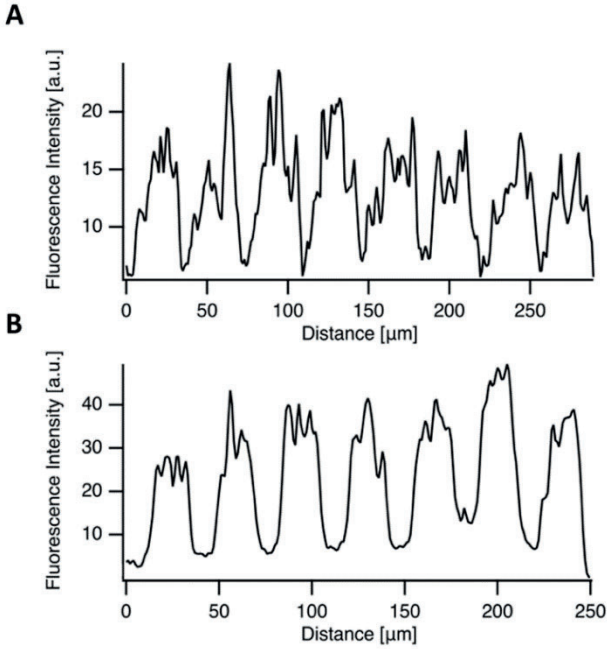


Figure S3. Fluorescence profiles extracted from fluorescence images of immobilized JAMF1: (A) soluble protein and (B) pNP after an immunostaining treatment. Specifically, these profiles correspond to the images portrayed in Figure 6 (A) and (B).

4. Cyclic voltammograms

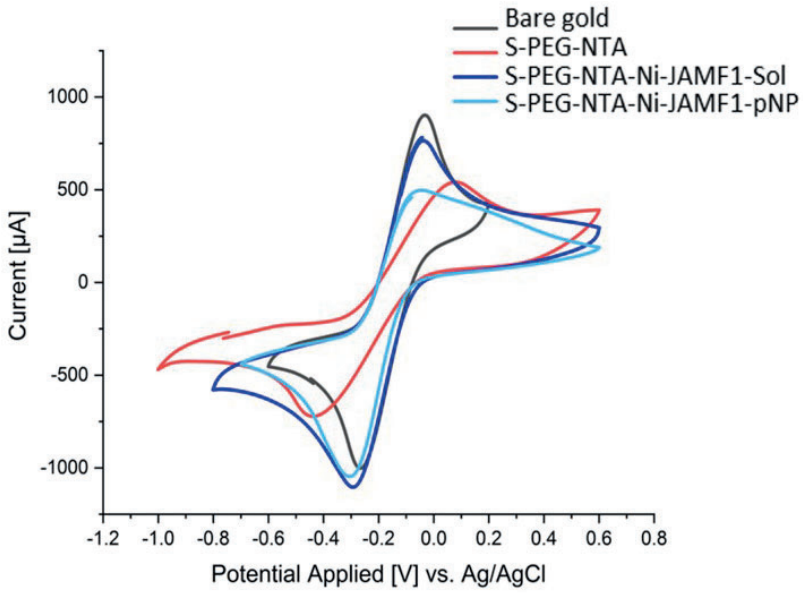


Figure S4. Cyclic voltammograms of bare gold, S-PEG-NTA, S-PEG-NTA-Ni-JAMF1-Sol and S-PEG-NTA-Ni-JAMF1-pNP. The electrolyte used was an aqueous KCl solution (50 mM) containing the redox probe $[Ru(NH_3)_6)]^{3+/2+}$ (5 mM). Scan rate used is 0.1 V/s.

5. Processing of AFM images (Figures 5 and 6)

For the AFM Image processing it has been used the software "Gwyddion". For the image processing of the topography the data has been leveled by mean plane subtraction and a flatten using 'Revolve Arc' function (30 pixel, 2,9 um, horizontal direction). No image processing for phase images. Only using the 'Revolve Arc' Flattening it has been possible to get a good image contrast to visualize the striped pattern. For the hight profiles, images have been treated with a mean Plane subtraction, a flatten base and offset subtraction.

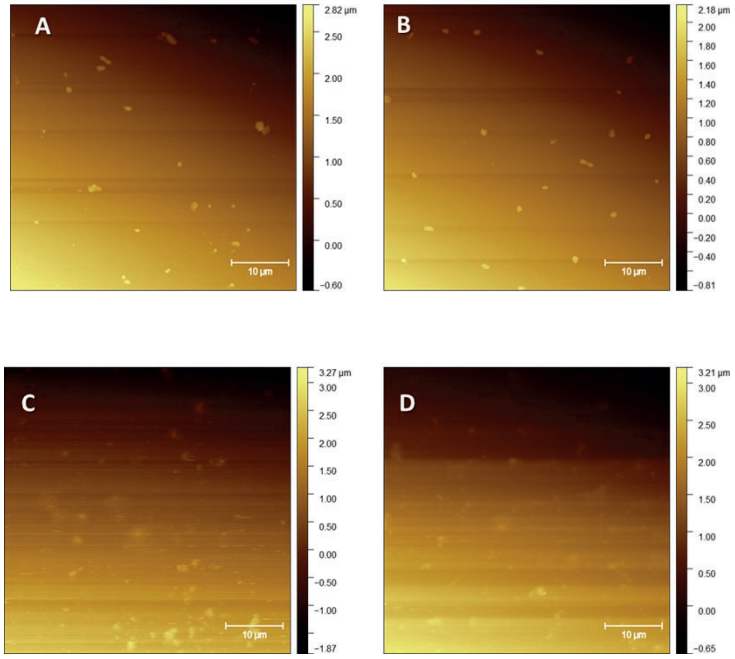


Figure S5. Unprocessed AFM images of A) 2 µm wide striped pattern of S-PEG-NTA-Ni-JAMF1-Sol; B) and their negative controls treated with EDTA (100 mM) S-PEG-NTA-Ni-JAMF1-Sol-Ctrl; C) 2 µm wide striped pattern of S-PEG-NTA-Ni-JAMF1-pNP and its negative control treated with EDTA (100 mM), S-PEG-NTA-Ni-JAMF1-pNP-Ctrl

6. XPS spectra

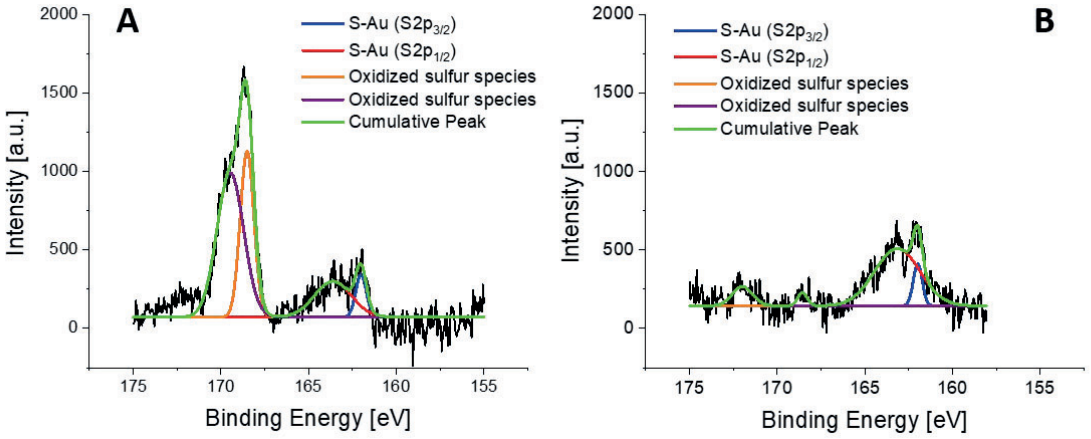


Figure S6. XPS deconvolutions of S 2p spectra for (A) S-PEG-NTA-Ni-JAMF1-Sol and (B) S-PEG-NTA-Ni-JAMF1-Sol-Ctrl (treatment with EDTA 10 mM).

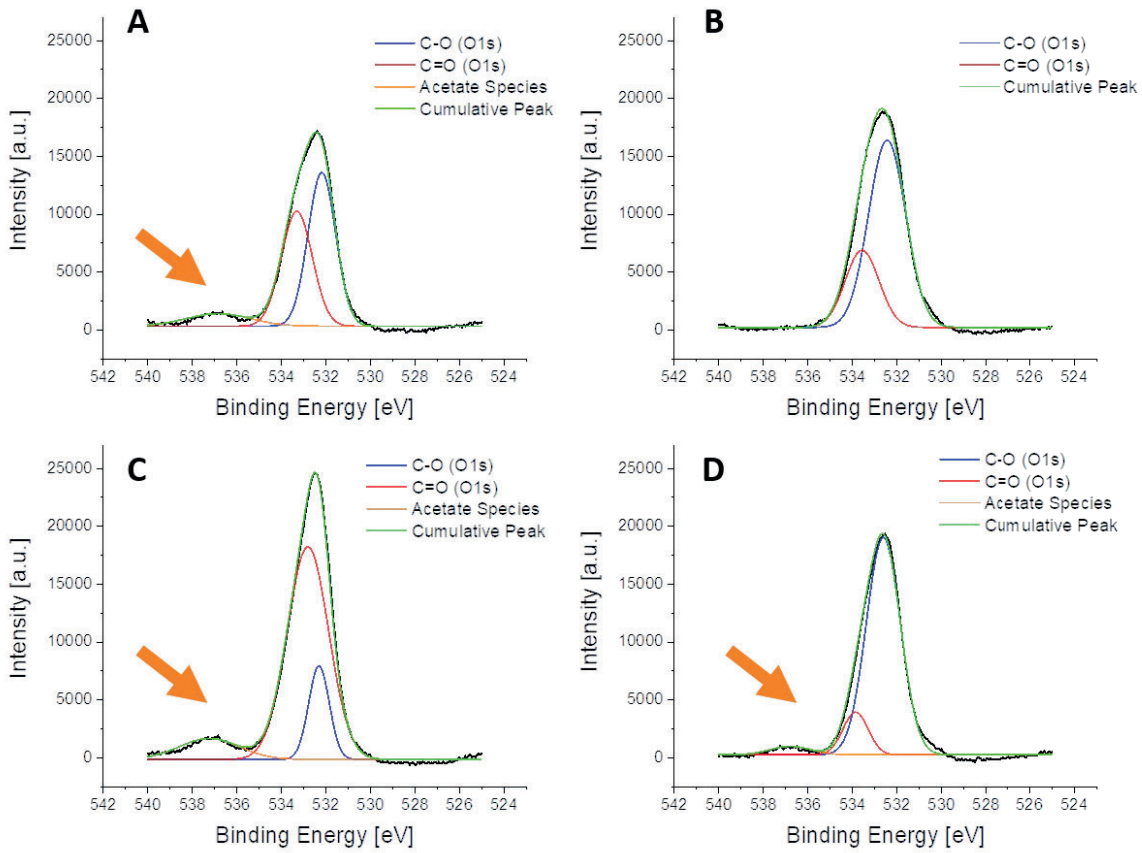


Figure S7. XPS deconvolutions of O 1s spectra for (A) S-PEG-NTA-Ni-JAMF1-Sol, (B) S-PEG-NTA-Ni-Sol- Ctrl (treatment with EDTA 10 mM), (C) S-PEG-NTA-Ni-pNP and (D) S-PEG-NTA-Ni-pNP-Ctrl (treatment with EDTA 100 mM). The yellow arrow indicates the contribution of acetate species.

7. Western Blots

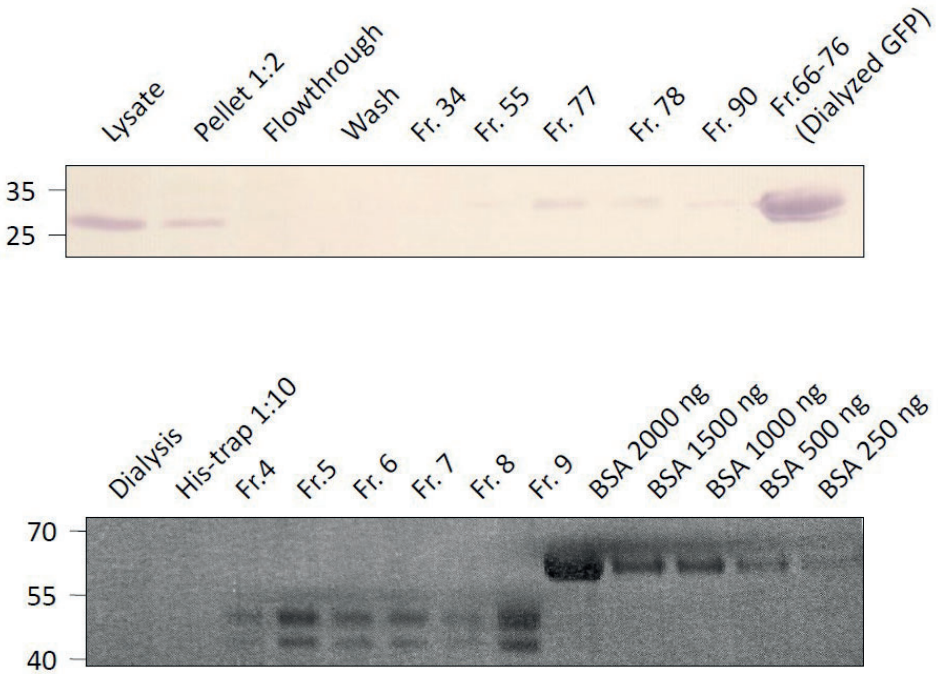
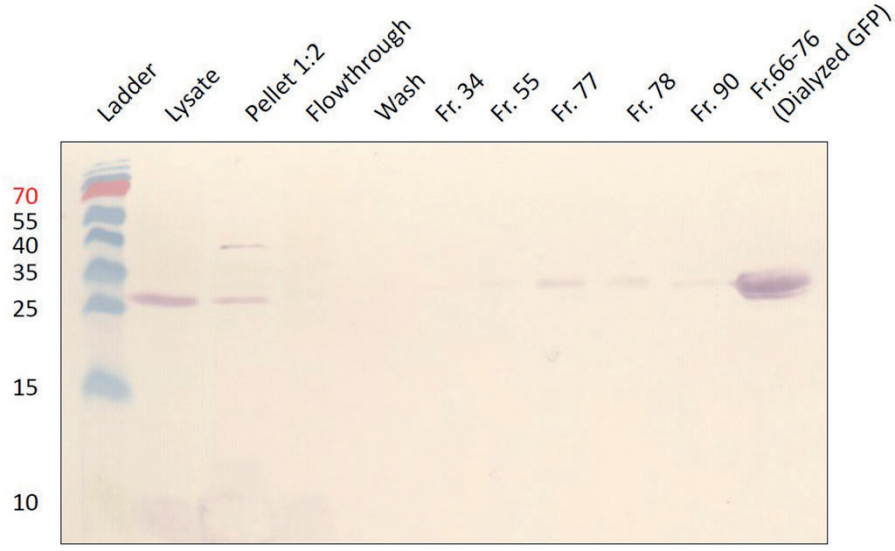


Figure S8. Western blot analysis to quantify JAMF1 (Bottom) and GFPH6 (Top).



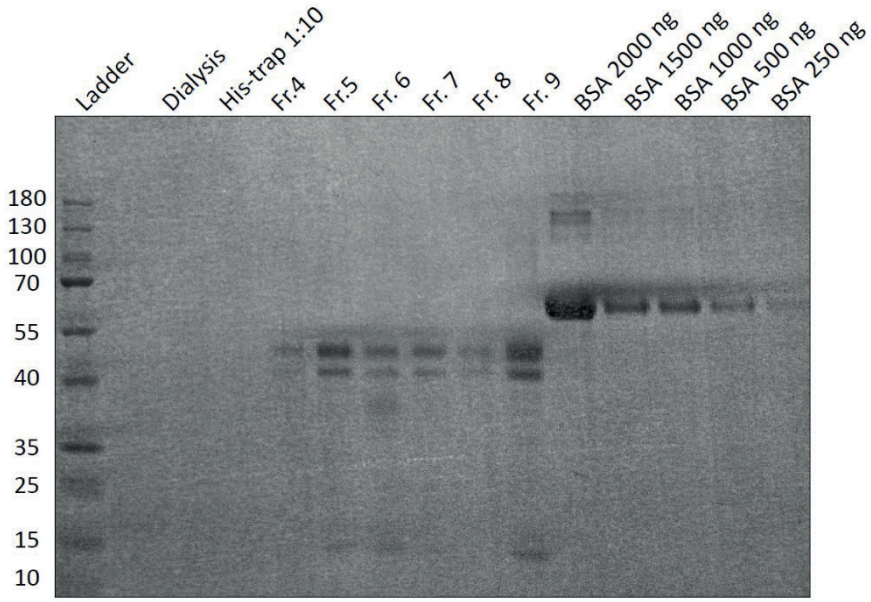


Figure S9. Uncropped images of the Western blot data with all samples and controls in the same blot with labelled lanes. JAMF1 (Bottom) and GFPH6 (Top).

Chapter 3

Thermoplastic polyurethane surfaces activated with Human α-Defensin 5 self-assembled monolayers to prevent infections

3.1. Introduction

Since the discovery of antibacterial medications more than 70 years ago, they have played a crucial role in the development of contemporary healthcare systems by enabling the treatment of bacterial diseases that were once fatal. Nowadays, antibiotics are widely used in hospitals to treat a wide range of illnesses, but their rapid development and improper use have resulted in many challenges.[1] Antimicrobial resistance poses a threat to the health advantages that antibiotics provide, and it is recognized as a global concern.[2] Around 700 000 deaths globally are attributable to antibiotic resistance, which has the potential to kill 10 million people by 2050. Thus, the need for novel antibiotic-free strategies for the management and avoidance of bacterial infections is critical.[3]

As described in the previous chapter, bacterial biofilms, in addition to antibiotic resistance, are a serious concern to contemporary healthcare.[4] Hospital wastewater, high-touch solid surfaces, unused medications, and medical equipment can all develop bacterial biofilms, which can lead to the development of common hospital-acquired infections (HAI), also called nosocomial infections (NI), including ventilator-associated pneumonia, surgical site infections, catheter-associated urinary tract infections (CAUTI), and bloodstream infections (Figure 3.1).[5] These infections are associated with a great deal of morbidity, mortality and increased financial burden.[6] They prolong the treatment period and make both patients and health centers pay high costs, including increased drug intakes and tests.[7] From all types of NI, CAUTI is one of the most prevalent globally. Placing catheters into the body makes it a key entry point for bacteria.[8]

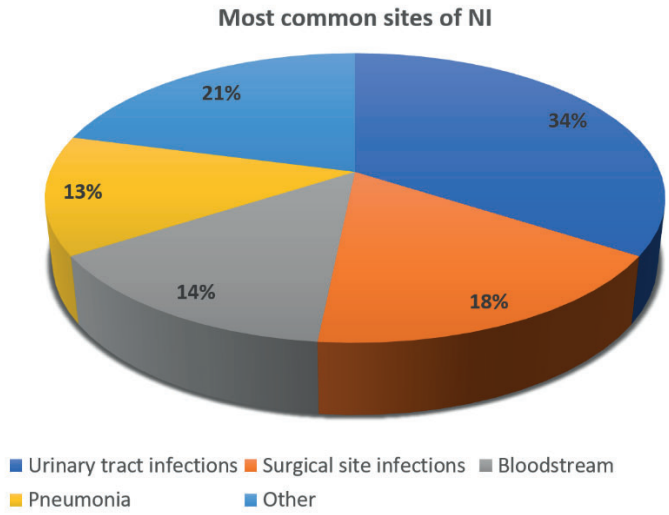


Figure 3.1. Relative distribution of NI. Adapted from.[9]

In fact, Ninety percent of infections are caused by bacteria, while fewer than one percent of infections are caused by protozoans, fungi, viruses, and mycobacteria. Both Gram-positive and Gram-negative bacteria can cause NI, with the most prevalent biofilm-forming bacteria being methicillin-resistant *Staphylococcus aureus (MRSA), Staphylococcus epidermidis, Viridans Streptococci, Enterococcus faecalis, vancomycin-resistant Enterococci, Escherichia coli, Pseudomonas aeruginosa, Acinetobacter baumannii, Proteus mirabilis,* and *Klebsiella pneumonia.* [10,11]

Recently, scientists are trying to find ways to avoid the biofilm growth and colonization on the surface of the medical devices by covering them with special coatings and structures. The surface chemistry and structure of materials have a major influence on how biological systems react to materials and technologies. Surface modification attempts to modify a material's surface properties for a particular use without adversely changing the material's bulk properties.[12]

Due to its special combination of toughness and flexibility, excellent resistance to impact and abrasion, biocompatibility, and ease of processing using standard techniques, polyurethanes (PUs) are widely used materials for a variety of medical applications.[13] PUs, first discovered by Otto Mayer in 1937, are a class of polymers that, independent of the composition of the rest of the macromolecule, have a large number of urethane linkages in their molecular backbone. This bond is formed via the reaction between an isocyanate group and a hydroxyl group (Figure 3.2).[14]

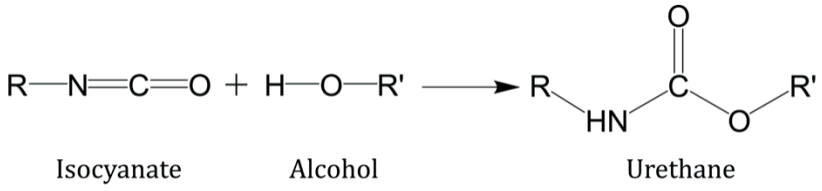


Figure 3.2. Isocyanate reaction with an alcohol group to form urethane.

Chapter 3: thermoplastic polyurethane surfaces activated with Human α-Defensin 5 self-assembled monolayers to prevent infections

Thermoplastic polyurethane (TPU) is one of many varieties of PU. TPU is attracting significant interest because it possesses wide useful properties, including, high elasticity, chemical resistance, durability, and transparency.[15]

TPU is a linear multiblock copolymer formed by appropriately combining polyol, chain extender, and diisocyanate (Figure 3.3).[16] TPU backbone chain alternates hard and soft segments. The soft segments are composed of long-chain diols (most typically silicone, polyester, polyether, or polycaprolactone-based) with a molecular weight of 1000–4000 g/mol, whilst the hard segments commonly consist of alternating diisocyanates and short-chain extender sequences.[17] TPUs are widely utilized in medical devices, including oxygen masks, gloves, tissue adhesives, catheters, surgical drapes, hospital beds, and wound dressing materials.[18]

To enhance its performance for specific applications, researchers have focused on modifying TPU surfaces but, due to its chemical resistant properties, there are only a few of examples. Mainly, TPU surfaces can be modified by plasma treatment or by chemical grafting.[19] Plasma treatment involves exposing TPU surfaces to ionized gases, leading to the formation of reactive species that can chemically modify the surface. This process enhances surface wettability, adhesion, and compatibility with other materials. Plasma treatment is effective in introducing functional groups onto TPU surfaces without compromising its bulk properties.[20] Chemical grafting involves the covalent attachment of molecules or polymers onto TPU surfaces. This method allows for precise control over surface properties by selecting appropriate grafting agents. For instance, the introduction of hydrophilic groups can improve TPU's adhesion to polar substrates, while hydrophobic groups can enhance its resistance to moisture.[21]

Antimicrobial peptides (AMPs), also known as host defense peptides (HDPs), are produced by the innate immune system of all living kingdoms, and are short peptides with a conserved sequence and structure. Because of their hydrophobicity and cationic character, these peptides have a strong and wide-ranging microbicidal action.[22] Utilizing a rational design of recombinant multidomain proteins based on HDPs, our collaborators form IRTA (Dr. Anna Arís and Dr. Elena García-Fruitós) have previously created a new generation of customized antimicrobials, showcasing its enormous potential against HAI-causing bacteria in both biofilm and planktonic forms.[23] Because HDPs exhibit minimal toxicity to mammalian cells and are efficient against a wide range of bacteria, they represent an intriguing alternative to antibiotics.[24] In this chapter, to confer antimicrobial properties to TPU we have used a human α-defensin 5 (HD5) protein with a green fluorescent protein (GFP) reporter and a cysteine (cys) terminal group (cys-HD5-GFP), which will be anchored to a reactive SAM on the TPU surface by a click reaction.

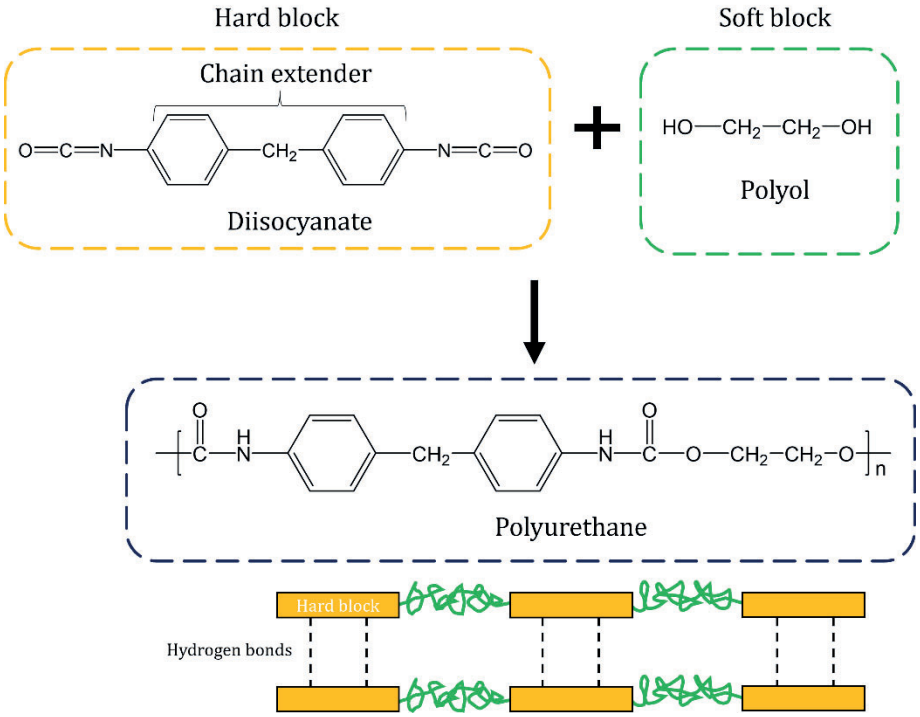


Figure 3.3. Scheme of the molecular structure of TPU.

3.2. Objectives

The objective of this chapter is to develop an antibacterial, medical relevant TPU surface with a dual function; capable of promoting bacterial repellence and at the same time, kill them by disrupting their membranes. Towards this aim the following specific objectives are proposed:

1) Activation and functionalization of the TPU surfaces with different PEG-based SAMs to promote bacterial repellence.
2) Functionalization of the PEG-based SAMS with AMP to kill bacteria.
3) Characterization of these SAMs using a multi-technique approach to verify the successful activation and functionalization of the TPU surfaces.
4) Perform a biofilm assay to evaluate the antimicrobial effect of the surfaces modified with the AMPs against three different and relevant bacteria strain in hospitals.

The results of this chapter are part of the publication #2: Activating Thermoplastic Polyurethane Surfaces with Polyethylene Glycol-Based Recombinant Human α-Defensin 5 Self-Assembled Monolayers for Infection Prevention, *Submitted* (see the Scientific Contributions section)

3.3. Results

3.3.1. TPU discs fabrication

TPU discs were produced custom-made by the company Mecanizados del Besós (Spain) for this project. The process consisted of extruding TPU beads from Lubrizol (USA). Specifically, these beads were melted and extruded to form a TPU bar of 12 mm diameter. Then, they were cut in 1 mm thickness pieces and finally the pieces were pierced with a punch of 7,5 mm of diameter. The resulting material consist of medical grade aromatic polyether based TPUs with a specific hardness, chemical resistance, and mechanical properties.

3.3.2. TPU surface activation and functionalization

The surface modification of the TPU sample was done in a two-step's procedure. Both steps were carried out under argon atmosphere, using dried toluene as solvent (and swelling agent) and dibutyltin dilaurate 95% as the catalyst. In the first step, the TPU discs were activated with hexamethylene diisocyanate (HDI) by immersing them in a solution containing the three above components for 1h at 70 °C. In the second step, different polyethylene glycol (PEG) molecules, one of 4 000 g/mol molecular weight and another one of 5 000 g/mol with one maleimide terminated group, were grafted onto the TPU surface by letting the hydroxyl groups react with the isocyanate ends groups of HDI. This reaction was carried out by immersing them in a 10% (w/v) of the PEG mixture in toluene overnight at 45°C. Afterwards, the TPU film was finally dried in a vacuum oven again at 45°C overnight. Finally, the cys-HD5-GFP protein was anchored by immersing the preactivated TPU surfaces in a 10 μM solution of the protein in water with 0.01% of acetic acid. In particular, the cysteine group of the HD5 protein reacts with the maleimide group of the PEG molecules, through a Michael addition reaction. In this reaction, a nucleophile (the thiol group of the cysteine) attacks an electrophile (the electron-deficient double bond of the maleimide group) to form a covalent bond (Figure 3.4).[25]

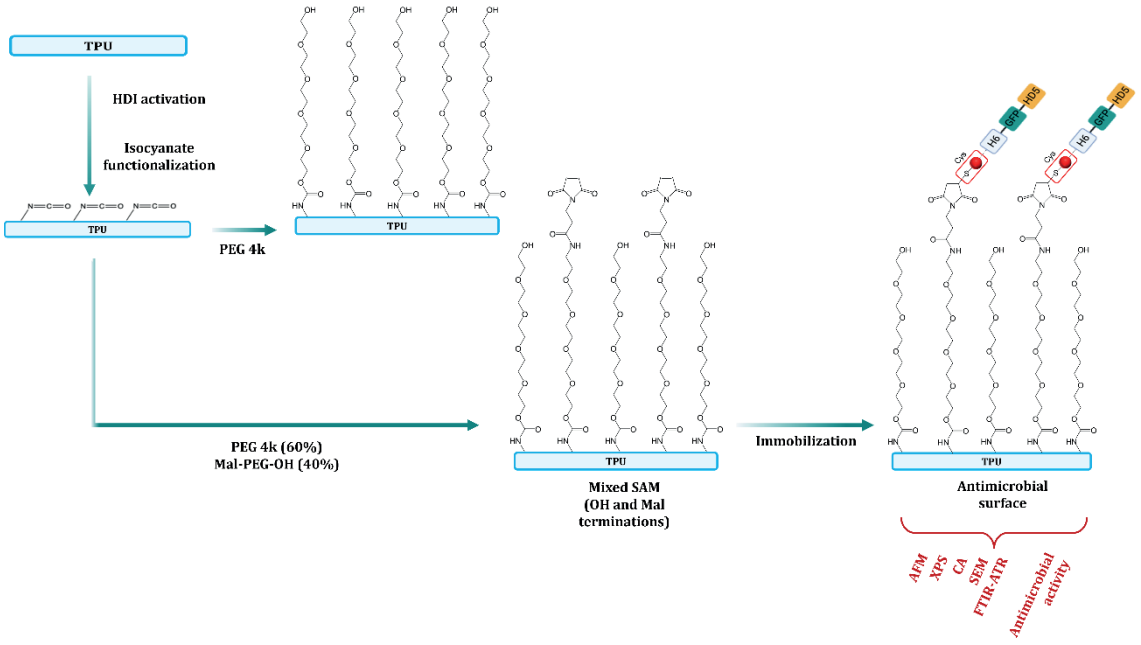


Figure 3.4. General strategy used for the immobilization of HD5-GFP-His_6-Cys on TPU through the formation of a mixed SAM and a click reaction.

3.3.3. Multi-technique characterization

The activation of the TPU, the preparation of the SAM and the subsequent immobilization of AMPs were characterized using a multi-technique approach based on contact angle (CA), Fourier transformed infrared spectroscopy (FTIR), X-ray photoelectron spectroscopy (XPS), atomic force microscopy (AFM), and scanning electron microscopy (SEM) analysis. In addition, a biofilm assay was performed in collaboration with IRTA (Dr. Anna Arís and Dr. Elena García-Fruitós) to get a preliminary understanding of the bactericidal properties of the biofunctionalized surface.

a. Contact angle (CA)

CA is used to evaluate the hydrophobicity or hydrophilicity of surfaces. In this case, we measured the water CA of the TPU surface and the resulting systems after its functionalization. The unmodified TPU surface has a water CA of 79°. After the first step of the functionalization, this angle importantly increases to 100° due to the HDI molecules, and sharply decreases to 19° after the PEG SAM formation because of its hydrophilicity. The formation of the mixed SAM contributes to the increase of the CA to 72°. Nevertheless, there is a large standard deviation due to the hydrolyzation of the maleimide terminated groups. Once the protein is anchored, as expected, the water CA raises to 85° (Figure 3.5B).

b. Fourier transformed infrared spectroscopy (FTIR)

FTIR spectroscopy is an effective technique to study and understand the chemistry and with the ATR more specifically, the surface chemistry of different types of substrates. Our material, TPU, contains NH and C=O groups. As a result, two distinct peaks show up at 3500-3000 cm^{-1} (NH) and 1800-1640 cm^{-1} (C=O), which correspond to the stretching vibrations of these groups. From the spectra in Figure 3.5A, a new band appears at 2250 cm^{-1} corresponding to the isocyanate group which is indicative of the successfully functionalization of TPU with HDI (TPU-HDI). This peak disappears in the second step of the process, indicating that the functionalization was successfully accomplished after the isocyanate groups react with the PEG molecules. Additionally, the bending vibrations of $-CH_2$ and $-CH_3$ are assigned to the peaks at 1343 cm^{-1} and 1466 cm^{-1} that come from the PEG modification, and the peaks at 842 cm^{-1} and 957 cm^{-1} are attributed to the bending vibrations of $-CH_2CH_2O-$ and -COC–, respectively (Figure 3.5A).[26] Based on the existence of the typical peaks predicted for the chemicals employed in the TPU functionalization, the FTIR analysis shows that the TPU surfaces were successfully modified.

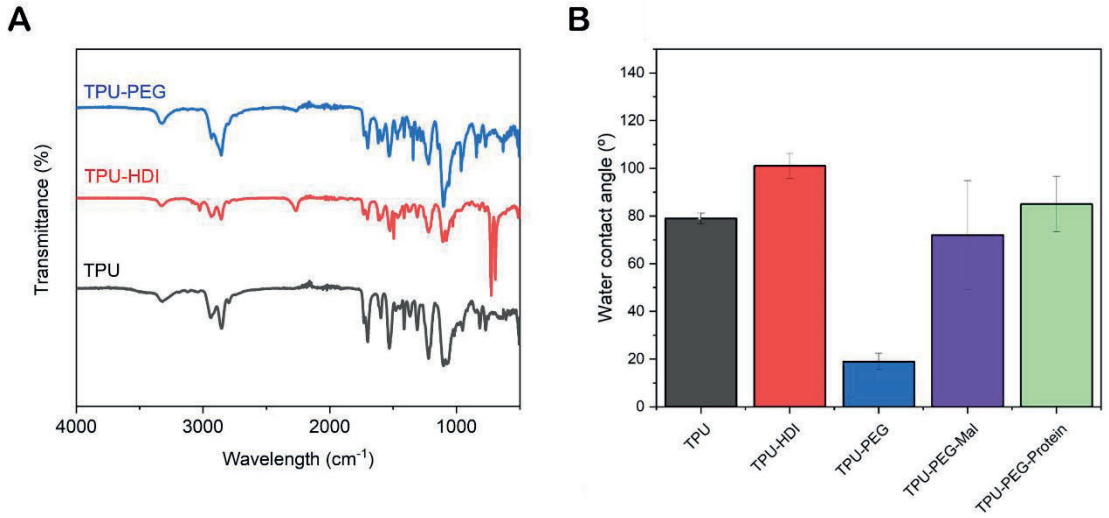


Figure 3.5. (A) FTIR spectra of unmodified TPU (black), functionalization of TPU with HDI (red) and TPU with a PEG 4K SAM (TPU-PEG) (blue). (B) Water CA of the unmodified TPU (black), TPU-HDI (red), TPU-PEG (blue), TPU-PEG-Mal (purple) and TPU-PEG-Protein (green).

c. X-ray photoelectron spectroscopy (XPS)

XPS is a surface sensitive analytical technique which gives information about the elemental composition and chemical environment of the atoms near the surface. XPS results indicate that the TPU surface contain C), N and O . The C1s peak is resolved in three components: i) the C-C and C-H at ~281-282 eV; ii) the C-O-C and C-OH at ~283 eV and iii) the N-COO at ~284-285 eV from the urethane and isocyanate termination. After the functionalization with the PEG and PEG-Mal molecules, it is observed an increase of the C-O-C and C-OH peak and a decrease of the C-C and C-H peak confirming the covalent anchoring of the PEG units. An increase of the N-COO peak is also observed after the modification of the TPU due to the HDI activation performed

previously to the PEG reaction. The TPU-PEG-Protein surface shows a small decrease of the HNCOO due to the covering of the maleimide groups by the protein. The C-O-C/C-OH and C-C/C-H peaks slightly increase, which is attributed to the aminoacids of the protein. Regarding the N 1s peak between ~396-397 eV, the TPU-PEG substrate presents a considerable decrease due to the hindering of the nitrogen atom of the TPU by the PEG molecules. The N 2p peak follows an increase after the PEG-maleimide anchoring due to the N atoms of the maleimide and a more intense increase is observed after the functionalization with the protein due to its high N content demonstrating the successful functionalization of the TPU surface with the antimicrobial protein (Figure 3.6).

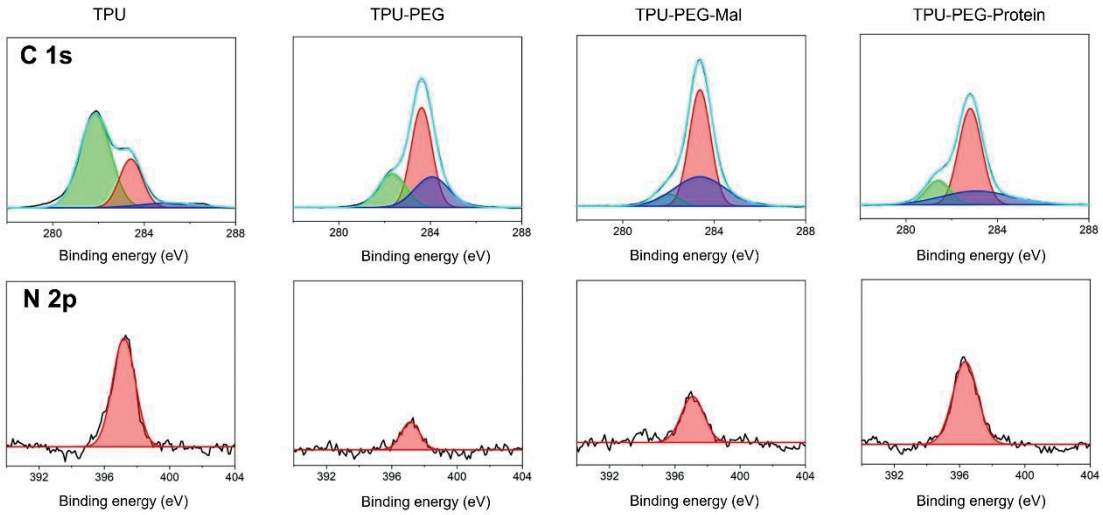


Figure 3.6. XPS spectra of C1s for unmodified TPU, TPU-PEG, TPU-PEG-Mal and TPU-PEG-Protein. XPS spectra of N2p for unmodified TPU, TPU-PEG, TPU-PEG-Mal and TPU-Protein.

d. Roughness

SEM and AFM analyses were performed on the samples to examine how the functionalization affect the roughness of the surface . As shown in Figure 3.7 and Table 3.1, the surface topography changes significantly after the PEG and PEG-Mal functionalization becoming rougher than the unmodified TPU.

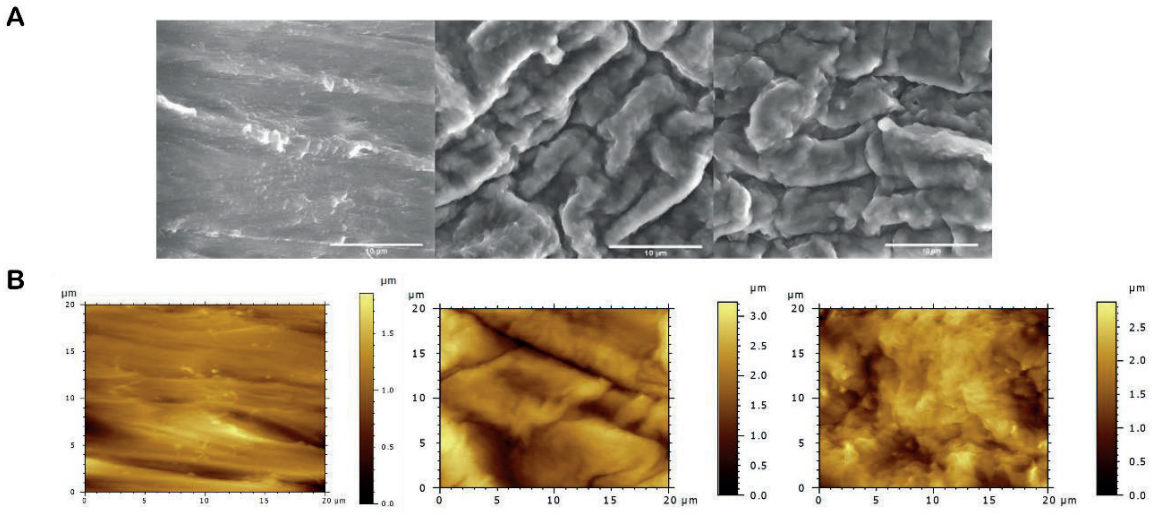


Figure 3.7. (A) SEM images of unmodified TPU (left), TPU-PEG (centre) and TPU-PEG-Mal (right). Scale bar: 10 µm. (B) AFM images of unmodified TPU (left), TPU-PEG (centre) and TPU-PEG-Mal (right)

	RMS Values (µm)
TPU	0.375 ± 0.001
TPU-PEG	1.159 ± 0.122
TPU-PEG-Mal	1.323 ± 0.339

Table 3.1. Root mean square (RMS) values extracted from the AFM images.

e. Antibiofilm activity

The biofilm inhibition capacity of the biofunctionalized TPU surfaces was assessed to investigate their antibacterial properties. Samples coated with the proteins were exposed to 3 different bacteria strains: *MRSA* (Gram-negative), *Staphylococcus epidermidis* (Gram-negative) and *Pseudomonas Aeruginosa* (Gram-positive). Compared to unmodified TPU, the TPU functionalized surfaces show a decrease of biofilm formation against the three bacteria strains. (Figure 3.8).

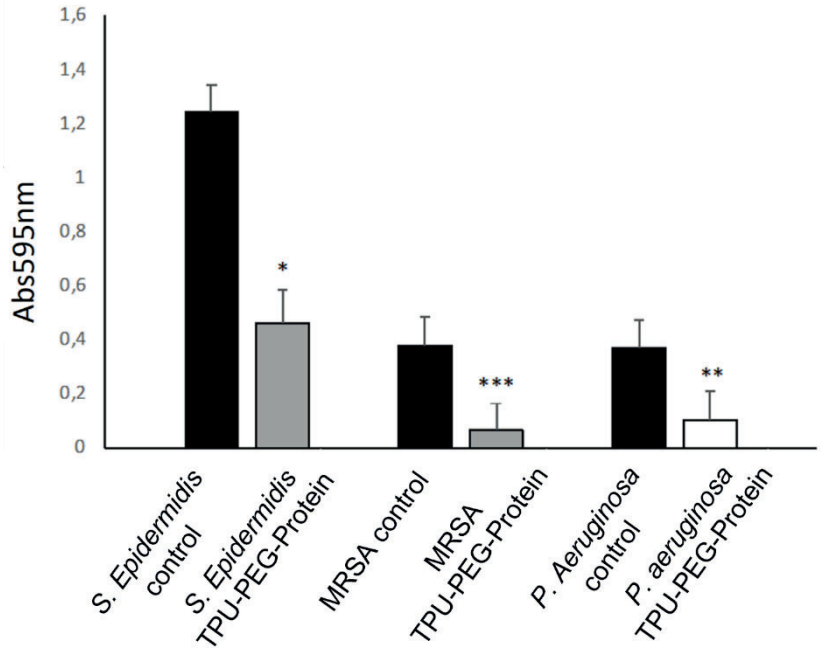


Figure 3.8. Inhibition of *Pseudomonas aeruginosa* (Gram-negative), methicillin-resistant *Staphylococcus aureus* (MRSA) (Gram-positive) and *S. Epidermidis* (Gram-positive) biofilm by the TPU-PEG-Protein surfaces. Asterisks depict significant differences compared to the control (*p-value≤0.05, **p-value≤0.005, ***p-value≤0.0005).

3.4. Summary and future perspectives

Successful activation and functionalization of medical grade TPU surfaces with a PEG SAM decorated with the HD5 protein have been achieved and confirmed through a multi-technique surface characterization approach. In particular, the proper SAM formation was verified by XPS, FTIR, and CA. Finally, the biofilm assay verified that the surface anchored AMP inhibit biofilm formation of three relevant bacteria strains in hospitals, including Gram-positive and Gram-negative

In conclusion, in response to the demand for new antimicrobial agents to overcome the antibiotic crisis, this research contributes to the development of tailored antimicrobial surfaces to mitigate HAIs, particularly those related to medical devices. Specifically, it is developed a novel strategy to biofunctionalize medical relevant TPU surfaces with antibacterial capabilities which represents an important step towards alternative strategies to traditional antibiotics and metals to improve patient outcomes in healthcare settings. This strategy could be used to coat the surface of TPU bandages to avoid wound healing infections or the surface of different medical devices. Specifically, in the framework of this PhD Thesis this strategy will be used to coat the surfaces of catheters (see chapter 4).

3.5. References

1. Riaz L, Yang Q, Sikandar A, et al. Antibiotics Use in Hospitals and Their Presence in the Associated Waste. In: Hashmi MZ, ed. *Antibiotics and Antimicrobial Resistance Genes: Environmental Occurrence and Treatment Technologies*. Springer International Publishing; 2020:27-49. doi:10.1007/978-3-030-40422-2_2

2. Khan J, Tarar SM, Gul I, Nawaz U, Arshad M. Challenges of Antibiotic Resistance Biofilms and Potential Combating Strategies: A Review. *3 Biotech*. 2021;11(4):169. doi:10.1007/s13205-021-02707-w

3. Sabio L, González A, Ramírez-Rodríguez GB, et al. Probiotic Cellulose: Antibiotic-free Biomaterials with Enhanced Antibacterial Activity. *Acta Biomater*. 2021;124:244-253. doi:https://doi.org/10.1016/j.actbio.2021.01.039

4. Lundin PM, Fiser BL, Blackledge MS, Pickett HL, Copeland AL. Functionalized Self-Assembled Monolayers: Versatile Strategies to Combat Bacterial Biofilm Formation. *Pharmaceutics*. 2022;14(8). doi:10.3390/pharmaceutics14081613

5. Peleg AY, Hooper DC. Hospital-Acquired Infections Due to Gram-Negative Bacteria. *New England J Med*. 2010;362(19):1804-1813. doi:10.1056/NEJMra0904124

6. Inweregbu K, Dave J, Pittard A. Nosocomial infections. *Continuing Education in Anaesthesia Critical Care & Pain*. 2005;5(1):14-17. doi:10.1093/bjaceaccp/mki006

7. Raoofi S, Pashazadeh Kan F, Rafiei S, et al. Global Prevalence of Nosocomial Infection: A Systematic Review and Meta-Analysis. *PLoS One*. 2023;18(1):e0274248-. https://doi.org/10.1371/journal.pone.0274248

8. Teshager T, Hussien H, Merahi M, Wondimneh F, Ketema I, Habte S. Knowledge, Practice and Associated Factors of Nurses Towards Prevention of Catheter-associated Urinary Tract Infection in Intensive Care Unit of Public Hospitals Administered by Federal Government in Addis Ababa, Ethiopia: A Cross-sectional Institutional-based Study. *BMC Nurs*. 2022;21:186. doi:10.1186/s12912-022-00968-1

9. Raffa R, Pergolizzi J, Taylor Jr R, Choudhuri S, Rodenbeck R. Persistence of Healthcare-Associated (Nosocomial) Infections Due to Inadequate Hand Hygiene: Part 1—Biological and Treatment Factors. *Pharmacol Pharm*. 2018;09:293-309. doi:10.4236/pp.2018.98023

10. Nimer NA. Nosocomial Infection and Antibiotic-Resistant Threat in the Middle East. *Infect Drug Resist*. 2022;15(null):631-639. doi:10.2147/IDR.S351755

11. Khan HA, Ahmad A, Mehboob R. Nosocomial infections and their control strategies. *Asian Pac J Trop Biomed*. 2015;5(7):509-514. doi:https://doi.org/10.1016/j.apjtb.2015.05.001

12. Alves P, Coelho JFJ, Haack J, Rota A, Bruinink A, Gil MH. Surface modification and characterization of thermoplastic polyurethane. *Eur Polym J*. 2009;45(5):1412-1419. doi:https://doi.org/10.1016/j.eurpolymj.2009.02.011

13. Thomson T. *Polyurethanes as Specialty Chemicals: Principles and Applications*.; 2004. doi:10.1201/9781420039665

14. Martin DJ, Osman AF, Andriani Y, Edwards GA. 11 - Thermoplastic polyurethane (TPU)-based polymer nanocomposites. In: Gao F, ed. *Adv Polym Nanocomp*. Woodhead Publishing; 2012:321-350. doi:https://doi.org/10.1533/9780857096241.2.321

15. Datta J, Kasprzyk P. Thermoplastic polyurethanes derived from petrochemical or renewable resources: A comprehensive review. *Polym Eng Sci*. 2017;58. doi:10.1002/pen.24633

16. Khalifa M, Anandhan S, Wuzella G, Lammer H, Mahendran AR. Thermoplastic Polyurethane Composites Reinforced with Renewable and Sustainable Fillers-A Review. *Polym Plast Technol Eng*. Published online May 10, 2020. doi:10.1080/25740881.2020.1768544

17. Lu QW, Macosko CW. Comparing the compatibility of various functionalized polypropylenes with thermoplastic polyurethane (TPU). *Polymer (Guildf)*. 2004;45(6):1981-1991. doi:https://doi.org/10.1016/j.polymer.2003.12.077

18. Rogalsky S, Bardeau JF, Lyoshina L, et al. New promising antimicrobial material based on thermoplastic polyurethane modified with polymeric biocide polyhexamethylene guanidine hydrochloride. *Mater Chem Phys*. 2021;267:124682. doi:https://doi.org/10.1016/j.matchemphys.2021.124682

19. Alves P, Cardoso R, Correia TR, Antunes BP, Correia IJ, Ferreira P. Surface modification of polyurethane films by plasma and ultraviolet light to improve haemocompatibility for artificial heart valves. *Colloids Surf B Biointerfaces*. 2014;113:25-32. doi:10.1016/j.colsurfb.2013.08.039

20. Lu Z, Wu Y, Cong Z, et al. Effective and biocompatible antibacterial surfaces via facile synthesis and surface modification of peptide polymers. *Bioact Mater*. 2021;6(12):4531-4541. doi:https://doi.org/10.1016/j.bioactmat.2021.05.008

21. Alves P, Coelho JFJ, Haack J, Rota A, Bruinink A, Gil MH. Surface modification and characterization of thermoplastic polyurethane. *Eur Polym J*. 2009;45(5):1412-1419. doi:10.1016/j.eurpolymj.2009.02.011

22. Kazemzadeh-Narbat M, Cheng H, Chabok R, et al. Strategies for antimicrobial peptide coatings on medical devices: a review and regulatory science perspective. *Crit Rev Biotechnol*. 2021;41(1):94-120. doi:10.1080/07388551.2020.1828810

23. López-Cano A, Ferrer-Miralles N, Sánchez J, et al. A Novel Generation of Tailored Antimicrobial Drugs Based on Recombinant Multidomain Proteins. *Pharmaceutics*. 2023;15(4). doi:10.3390/pharmaceutics15041068

24. Steinstraesser L, Kraneburg UM, Hirsch T, et al. Host defense peptides as effector molecules of the innate immune response: a sledgehammer for drug resistance? *Int J Mol Sci*. 2009;10(9):3951-3970. doi:10.3390/ijms10093951

25. Northrop BH, Frayne SH, Choudhary U. Thiol–maleimide "click" chemistry: evaluating the influence of solvent, initiator, and thiol on the reaction mechanism, kinetics, and selectivity. *Polym Chem*. 2015;6(18):3415-3430. doi:10.1039/C5PY00168D

26. Vrandečić NS, Erceg M, Jakić M, Klarić I. Kinetic analysis of thermal degradation of poly(ethylene glycol) and poly(ethylene oxide)s of different molecular weight. *Thermochim Acta*. 2010;498(1):71-80. doi:https://doi.org/10.1016/j.tca.2009.10.005

Publication #2

Title: Activating Thermoplastic Polyurethane Surfaces with Polyethylene Glycol-Based Recombinant Human α-Defensin 5 Self-Assembled Monolayers for Infection Prevention

Authors: Xavier Rodríguez Rodríguez, Adrià López-Cano, Karla Mayolo-Deloisa, Oscar Q Pich, Paula Bierge, Nora Ventosa, Cristina García-de-la-Maria, José M. Miró, Oriol Gasch, Jaume Veciana, Judith Guasch, Anna Arís, Elena Garcia-Fruitós, Imma Ratera and the FUNCATH investigators

Publication: *Submitted*

Activating Thermoplastic Polyurethane Surfaces with Polyethylene Glycol-Based Recombinant Human α-Defensin 5 Self-Assembled Monolayers for Infection Prevention

Xavier Rodríguez Rodríguez,[1,2] Adrià López-Cano,[3] Karla Mayolo-Deloisa,[1,4] Oscar Q Pich,[5,6] Paula Bierge,[5,6] Nora Ventosa,[1,2] Cristina García-de-la-Maria,[6] José M. Miró,[6,7] Oriol Gasch,[8] Jaume Veciana,[1,2] Judith Guasch,[1,2,9] Anna Arís,[3] Elena Garcia-Fruitós,[3] Imma Ratera[1,2] and the FUNCATH investigators[10]

[1] Institute of Materials Science of Barcelona (ICMAB-CSIC), Campus UAB, Bellaterra, 08193, Spain.

[2] Networking Research Center on Bioengineering, Biomaterials and Nanomedicine (CIBER-BBN), Campus UAB, Bellaterra, 08193, Spain.

[3] IRTA, Torre Marimon, Ctra C-59, Km 12,1, 08140 Caldes de Montbui, Barcelona, Spain

[4] Tecnologico de Monterrey, Institute for Obesity Research, School of Engineering and Sciences, Av. Eugenio Garza Sada 2001, 64849 Monterrey, Nuevo León, México.

[5] Laboratori de Recerca en Microbiologia i Malalties Infeccioses, Hospital Universitari Parc Taulí, Institut d'Investigació i Innovació Parc Taulí (I3PT-CERCA), Universitat Autònoma de Barcelona, 08208, Sabadell, Spain.

[6] Infectious Diseases Service. Hospital Clinic-FCRB-IDIBAPS. Universitat de Barcelona, Barcelona, Spain.

[7] Infectious Diseases Biomedical Research Networking Center (CIBERINFEC), Instituto de Salud Carlos III, Madrid, Spain.

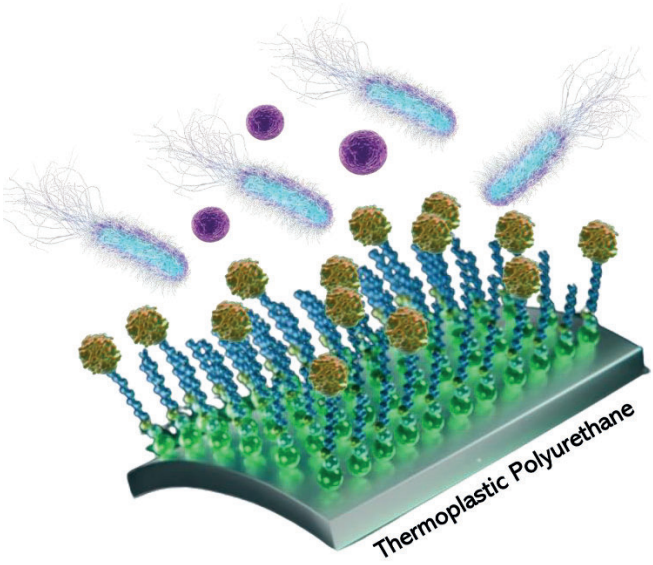
[8] Servei de Malalties Infeccioses, Hospital Universitari Parc Taulí, Institut d'Investigació i Innovació Parc Taulí (I3PT-CERCA), Universitat Autònoma de Barcelona, 08208, Sabadell (Spain)

[9] Dynamic Biomimetics for Cancer Immunotherapy, Max Planck Partner Group, ICMAB-CSIC, Campus UAB, Bellaterra, 08193, Spain.

[10] FUNCATH Investigators are indicated in the Appendix.

ABSTRACT: Addressing multidrug-resistant microbial infections linked to implantable biomedical devices is an urgent need. In recent years, there has been an active exploration of different surface coatings to prevent and combat drug-resistant microbes. Following such a target, our latest study focused on the development of a new generation of tailored antimicrobials using a rational design of recombinant proteins based on host defense peptides (HDPs) with high bactericidal efficiency combined with its anchoring on gold model surfaces obtaining effective antibiofilm surfaces. In this research, we present a facile chemical modification of thermoplastic polyurethane (TPU) surfaces which is one of the most relevant materials used for medical devices with good mechanical properties but also good chemical resistance which makes it difficult to be modified. The chemical modification of TPU surfaces is achieved via a three-step procedure based on i) TPU activation using hexamethylene diisocyanate (HDI); ii) interfacial reaction with polyethylene glycol (PEG) derivatives and finally, iii) an easy click reaction between the PEG-maleimide terminated self-assembled monolayers (SAMs) on the TPU and the cysteine (-thiol) terminated human α-defensin 5 (HD5) protein. The obtained PEG based HD5 self-assembled monolayers on TPU were characterized using a surface science multi-technique approach including scanning electron microscopy, atomic force microscopy, contact angle and X-ray photoelectron spectroscopy, proving the successful functionalization of the TPU. Moreover, the modified TPU surfaces with HD5 derivative exhibit broad-spectrum antibacterial properties reducing biofilm formation against *Pseudomonas aeruginosa* (Gram-negative), methicillin-resistant *Staphylococcus aureus* (MRSA) (Gram-positive) and methicillin-resistant *Staphylococcus epidermidis* (MRSE) (Gram-positive). These finding underscore the substantial potential of peptide-modified TPU surfaces for applications in combating bacterial infections associated with implantable materials and devices.

TOC GRAPHIC



Highlight: An easy surface modification of TPU exhibiting broad-spectrum antibacterial performance demonstrate a great potential to fight bacterial infections associated with implantable materials and medical device like catheters.

Keywords: Antimicrobial surfaces; Biofilm inhibition; Thermoplastic polyurethane (TPU); Self-Assembled Monolayers (SAMs); Click reaction, Host defense peptides (HDP); MRSA, MRSE; *Pseudomonas aeruginiosa.*

1. Introduction

Over the last 50 years, the utilization of implantable biomaterials and medical devices like catheters has played a crucial role in treating diseases. However, the use of such devices has been linked to bacterial infections, which usually need to be managed with the device withdrawn, prolonged antibiotic therapies and longer hospital admissions. This situation imposes a substantial economic burden on both the government and society.[1–6] Healthcare-associated infections (HAIs) are related with high morbidity, mortality, and excess of costs in care patients[7] with over 60% attributed to medical devices.[8] According to research, over 2.5 million HAIs episodes occur every year in Europe with more than 90,000 deaths attributed to the 6 most common types: healthcare-associated pneumonia, health care-associated urinary tract infection, surgical site infection, health care-associated *Clostridium difficile*, healthcare-associated neonatal sepsis, and healthcare-associated bloodstream infection.[9] According to a study involving 15 European countries, one of the most frequently isolated microorganism from patients suffering HAI are bacteria such as *Pseudomonas aeruginosa*, coagulase-negative *Staphylococcus* spp., and *Escherichia coli*.[10]

Despite the widespread use of antibiotics for treating bacterial infections, their overuse and misuse done during decades have accelerated the emergence and spread of multidrug-resistant (MDR) bacteria in clinical settings.[11–16] Conventional antibiotics demonstrate limited efficacy against MDR bacteria, posing a severe threat to human life. Consequently, efforts have been directed towards exploring alternative strategies to combat bacterial infections, such as incorporating antibacterial modifications on materials.[17–26]

Biofilm is the primary form of surface bacterial contamination, which causes serious problems and can easily lead to drug resistance. In the biofilm, bacterial cells can exhibit

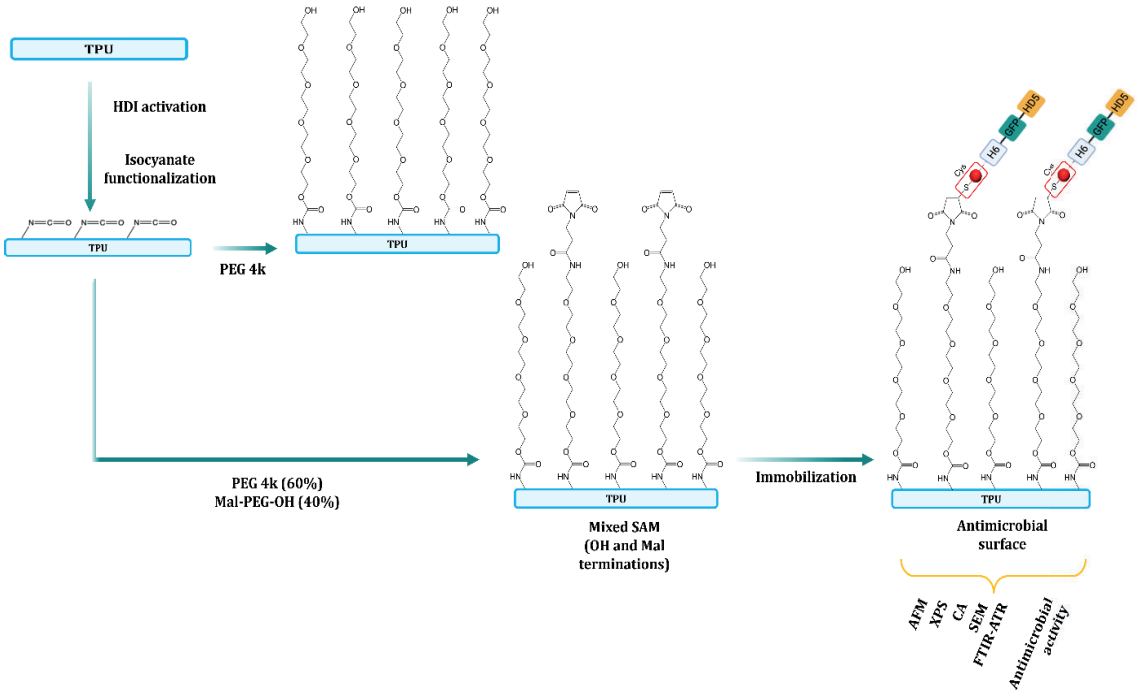
up to a 100-fold increase in antimicrobial resistance (AMR) when compared to planktonic cells.[27] In fact, in more than 60% of cases HA-UTI are associated with biofilm formation on the surface of catheters.[28] The surface antibacterial methods can be categorized into repelling or contact-killing surfaces. The widely investigated release-killing reagents in modified surface modification of materials mainly contain inorganic metal particles, antibiotics, or antibacterial enzymes. The conventional contact-killing materials for antibacterial materials surfaces mainly include quaternary ammonium salts (QAs), antimicrobial peptides (AMPs), and N-halamines (N-X).[29]

AMPs, also called Host Defense Peptides (HDPs), are short peptides with a conserved sequence and structure produced by the innate immune system of organisms of all life kingdoms. These peptides have a potent and broad-spectrum microbiocidal activity because of their cationic nature and hydrophobicity.[27] In addition, their multiple ways of action allow a very low induction of resistance, compared to the traditional antimicrobials.[30] We have previously developed a new generation of tailored antimicrobials, using a rational design of recombinant multidomain proteins based on HDPs, demonstrating their great potential against HAI-causing bacteria either in biofilm or planktonic forms.[31] HDPs are an interesting alternative because are effective against a broad antibacterial spectrum, while presenting low toxicity to mammalian cells.[31] Moreover, recently developed surface biofunctionalization strategies[32–37] have been used to covalently anchor such novel recombinant proteins on gold model surfaces obtaining effective antibiofilm surfaces.[38]

Thermoplastic Polyurethane (TPU) based catheters represent an indispensable class of implantable biomaterials used in hospitals for the transfer of body fluids or administration of medication. As far as developing antibacterial TPUs is concerned, various active moieties have already been incorporated along with a segmented polyurthane such as

antibiotics like chloramphenicol, or metallic (cobalt, or silver) nanoparticles,[39] but presenting important concerns regarding antibiotic resistance, efficiency or toxicity in all cases. For this reason, it is urgent to find alternatives to antibiotics and metals such as silver to avoid nosocomial infections on TPU surfaces. TPU surfaces can be activated by using different strategies like ultra-violet irradiation (UV), gamma irradiation (GI) and interfacial modification (IM).[40] The process of activation improves the TPU surfaces' functionality,[41,42] however, it is still challenging to chemically modify TPU surfaces due to its chemical resistant properties.

In this study, we propose a controlled design and synthesis of antibiofilm surfaces by coating medical grade TPU surfaces with recombinant HDPs to confer broad-spectrum antibacterial properties to medically relevant TPU surfaces. The chemical modification of TPU surfaces is achieved via a three-step procedure based on activation of the surface using hexamethylene diisocyanate (HDI) followed by an interfacial reaction with polyethylene glycol (PEG) derivatives with a maleimide terminal group forming a mixed SAM. Finally, a click reaction between the PEG-maleimide termination on the TPU with the cysteine (-thiol) terminated HD5 (HD5-GFP-H6-Cys) antimicrobial protein giving place to the anti-biofilm surface. A multi-technique approach using Atomic force microscopy (AFM), X-ray photoelectron spectroscopy (XPS), scanning electron microscope (SEM), Water contact angle (WCA), Fourier transform infrared spectroscopy – attenuated total reflectance (FTIR-ATR) and fluorescent microscopy was used to perform a physico-chemical characterization of the surfaces.



Scheme 1. General strategy used for the chemical activation and immobilization of HD5-GFP-H6-Cys on TPU surfaces using a bioclickable self-assembled monolayer strategy.

2. Results and discussion

TPU surfaces (discs) have been prepared through and extrusion process from medical grade Tecothane TPU (TT-1085A) pellets. After the extrusion process, a bar is obtained from which slices of 1 mm thick are cut and from them, discs of 7,5 mm of diameter are obtained with a punch.

The surface modification of the TPU discs was done in a three-steps procedure. In the first step, the TPU films were functionalized with HDI. In the second step, PEG4K for the control SAMs (TPU-PEG) and 60% of PEG 4k and 40% of Mal-PEG5K-OH, for the mixed SAMs (TPU-PEG-Mal), were grafted onto the TPU surface to obtain the functionalized TPU. The length of the maleimide tail was longer than the PEG one to increase the availability of the reactive unit towards the click reaction with the protein. Specifically, TPU films were immersed in a 10% (w/v) of 100% PEG4K or mixed 40%

Mal-PEG5K-OH and 60% PEG 4K solutions in dried toluene and left to react overnight at 45°C letting the hydroxyl groups reacts with the isocyanate ends groups of the activated TPU surface. After that, the samples were consecutively washed in order to remove all the unreacted monomer with toluene, isopropyl alcohol and MilliQ water for 15 min each. The TPU film was finally dried in a vacuum oven at 45°C overnight (Scheme 1).

In the last step, the protein HD5-GFP-H6-Cys was anchored to the prefunctionalized TPU surface via a click Diels-Alder reaction between the thiol of the cysteine group of the protein and the maleimide terminated group of the mixed SAM. Specifically, 80 µL of a 10 µM protein solution were deposited on top of the TPU surfaces that were previously functionalized with a mixed SAM of PEG4K and Mal-PEG5K-OH (TPU-PEG-Mal) and left to react in a wet chamber for 1 hour at room temperature (Scheme 1).

Then, a multi-technique approach was used to characterize the resulting modified surfaces. FTIR, XPS, WCA and fluorescence plate reader were used to characterize the chemical modification of the surface. The discs of non-modified TPU contain NH and C=O groups (Figure S1), thus, its FTIR spectra shows two defined peaks corresponding to the stretching vibrations of these groups, one at ~3400 cm^{-1} (NH) and the other at ~1650 cm^{-1} (C=O). For the activated TPU-HDI surface, a new band that was not present on the unmodified TPU appears at 2250 cm^{-1} which is indicative of the successful activation of the TPU surface with the isocyanate molecules. Moreover, in the second step of the functionalization, this peak clearly disappears, indicating that the reaction of the isocyanate groups with the hydroxyl groups of the PEG molecules was effectively achieved. Additionally, the PEG modification of the surface originates peaks at 1343 cm^{-1} and 1466 cm^{-1} which correspond to the bending vibration of $–CH_2$ and $–CH_3$ and at 842 cm^{-1} and 957 cm^{-1} that are attributed to the bending vibrations of $–CH_2CH_2O–$ and –COC–, respectively. The FTIR analysis indicates the successfully modification of TPU surfaces

based on the presence of the characteristic peaks expected for the compounds used for the TPU functionalization (Figures 1 and S2-S4).

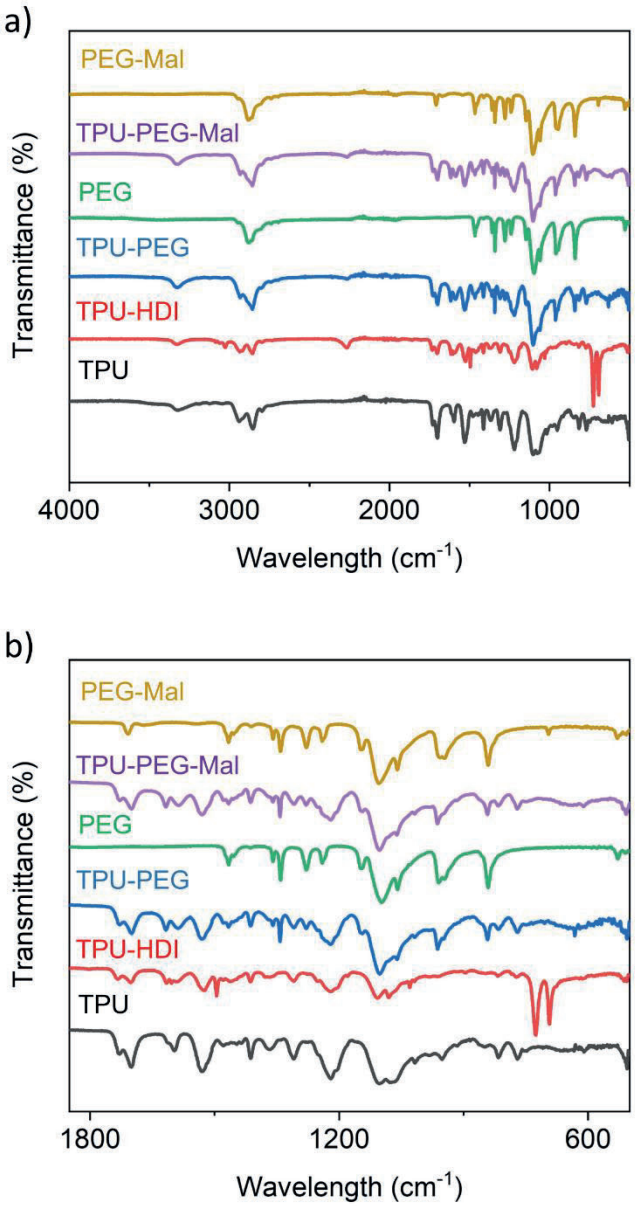


Figure 1. FTIR spectra were: a) (black) unmodified thermoplastic polyurethane, (red) functionalization of TPU with HDI, (blue) TPU with a PEG4K SAM (TPU-PEG), (green) PEG4K, (purple) thermoplastic polyurethane with a mixed SAM (40% PEG4K and 60% Mal-PEG5K-OH) (TPU-PEG-Mal), (yellow) Mal-PEG5K-OH.; b) The graph below is a zoom of the one above.

The WCA of the unmodified TPU substrate was 79°. Its increase to 101° after the modification with HDI and its decrease to 19° when anchoring the hydrophilic PEG is a clear indication of the successful functionalization steps of the process. For the mixed SAM (TPU-PEG-Mal) and the final protein functionalized surfaces, the WCA increases again to 72º and 85º, indicating its more hydrophobic nature, as expected (Figure 2).

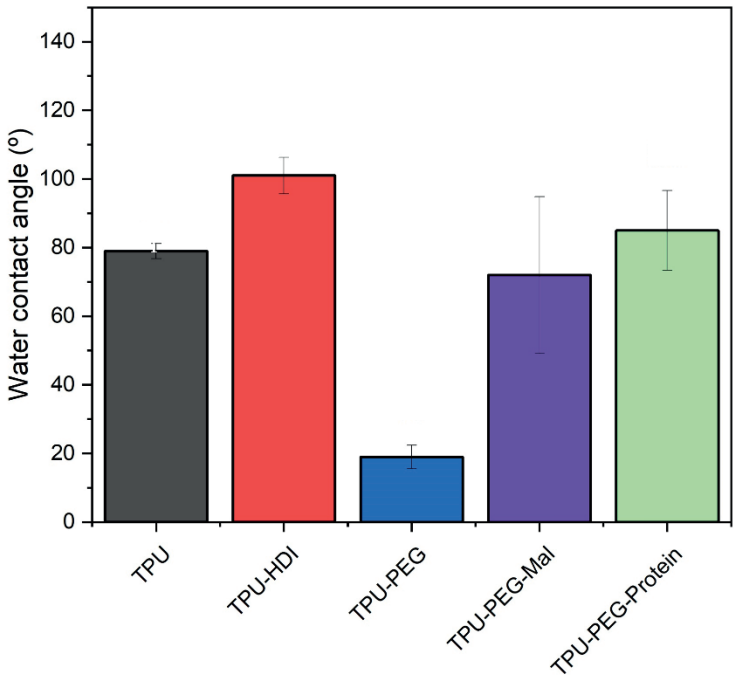


Figure 2. Water contact angle of: (black) the unmodified TPU, (red) TPU-HDI, (blue) TPU-PEG, (purple) TPU-PEG-Mal and (green) protein anchored to TPU-PEG-Mal substrate (TPU-PEG-Protein).

Moreover, WCA and FTIR of TPU-PEG surfaces have been measured during 24 and 48 h in water, PBS and cell culture media (RPMI) confirming the robustness and stability of the PEG anchored on the TPU surfaces in different media relevant for its final applications (Figure S2-S5) due to the covalent chemical functionalization of TPU.

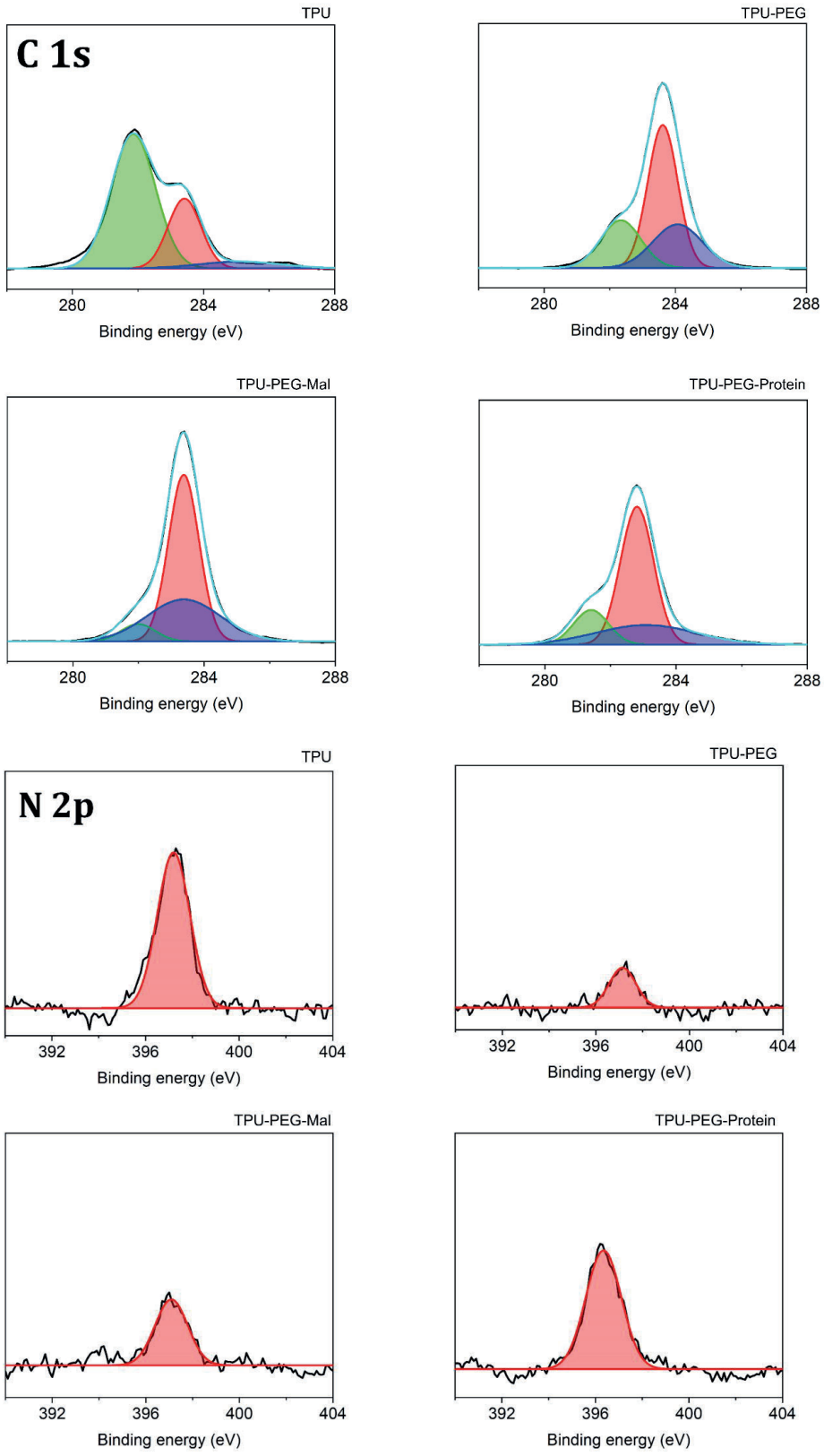


Figure 3. XPS spectra of C1s and N2p for unmodified TPU, TPU-PEG, TPU-PEG-Mal and TPU-PEG-Protein.

The TPU substrates were further characterized using high-resolution XPS spectra to determine the nature and the level of functionalization present on the surface in each synthetic step. Table 1 summarizes the percentage of the elements present on the TPU modified surfaces. The elemental composition (carbon, nitrogen and oxygen) of the surfaces were calculated from the XPS spectra. Figures 3 and S6 show the different spectra obtained for the different samples; unmodified and modified TPU. The relative composition ratio based on the area of the deconvoluted peaks is shown in Table 1.

The C1s peak is resolved in three components: i) the C-C and C-H at ~281-282 eV; ii) the C-O-C and C-OH at ~283 eV and iii) the N-COO at ~284-285 eV from the urethane and isocyanate termination. After the functionalization with the PEG and PEG-Mal molecules, it is observed an increase of the C-O-C and C-OH peak and a decrease of the C-C and C-H peak confirming the covalent anchoring of the PEG units. An increase of the N-COO peak is also observed after the modification of the TPU due to the HDI activation performed previously to the PEG reaction. The TPU-PEG-Protein surface shows a small decrease of the HNCOO due to the covering of the maleimide groups by the protein. The C-O-C/C-OH and C-C/C-H peaks slightly increase, which is attributed to the aminoacids of the protein. Regarding the N 1s peak between ~396-397 eV, the TPU-PEG substrate presents a considerable decrease due to the hindering of the nitrogen atom of the TPU by the PEG molecules. The N 2p peak follows an increase after the PEG-maleimide anchoring due to the N atoms of the maleimide and a more intense increase is observed after the functionalization with the protein due to its high N content demonstrating the successful functionalization of the TPU surface with the antimicrobial protein (Figure 3 and Table 1). Regarding the oxigen, two peaks are identified ~527-528 eV of the C=O and C-OH and ~529-530 eV of the C-O-C and NCOO, which increase

after the functionalization due to the incorporation of oxygen containing molecules like the PEG for TPU-PEG and TPU-PEG-Mal. The oxigen content decreases for the TPU-PEG-Protein due to the presence of the protein which increases the number of carbon atoms with respect to oxygen (Figure S6).

	TPU		**TPU-PEG**		**TPU-PEG-Mal**		**TPU- PEG-Protein**	
	BE (eV)	%	BE (eV)	%	BE (eV)	%	BE (eV)	%
C 1s	281.9	50.8	282.34	16.3	282	4.7	281.4	11.2
	283.4	19.6	283.62	36.3	283.37	40.5	282.8	42.3
	285.1	4.9	284.07	18.1	283.73	24.4	283.1	18.0
N 2p	397.2	3.0	397.1	0.4	397.1	0.7	396.4	1.9
O 1s	527.6	1.2	528.5	1.3	528.3	1.6	527.7	1.6
	529.63	20.6	530.1	27.6	529.9	28.1	529.3	25.0

Table 1. Binding energy (eV) and relative composition ratio based on the area in % of each peak for the atomic percentages obtained from the XPS spectra of the different samples studied.

Surface morphology and topography were evaluated by scanning electron microscopy (SEM) and AFM. SEM and AFM images of the TPU surfaces before and after each step of the modification are shown in Figures 4 and 5. It is observed a clear increase of the roughness of the samples after the functionalization steps, for the TPU-PEG and TPU-PEG-Mal surfaces. Specifically, the roughness root mean square (RMS) increases from 0,375 µm for the unmodified TPU to 1,159 µm and 1,323 µm for the TPU-PEG and TPU-PEG-Mal, respectively. Such roughness increase is also indicative that the TPU surface has been successfully modified.

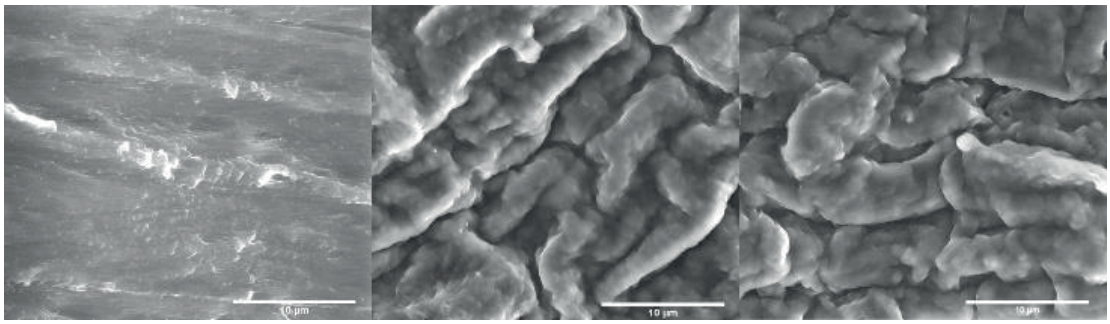


Figure 4. SEM images of: (left) unmodified TPU, (centre) TPU functionalized with a 100% of PEG4K SAM, TPU-PEG; and (right) TPU functionalized with a mixed self-assembled monolayer of 60% PEG4K and 40% Mal-PEG5K-OH, TPU-PEG-Mal. Scale bar: 10 µm.

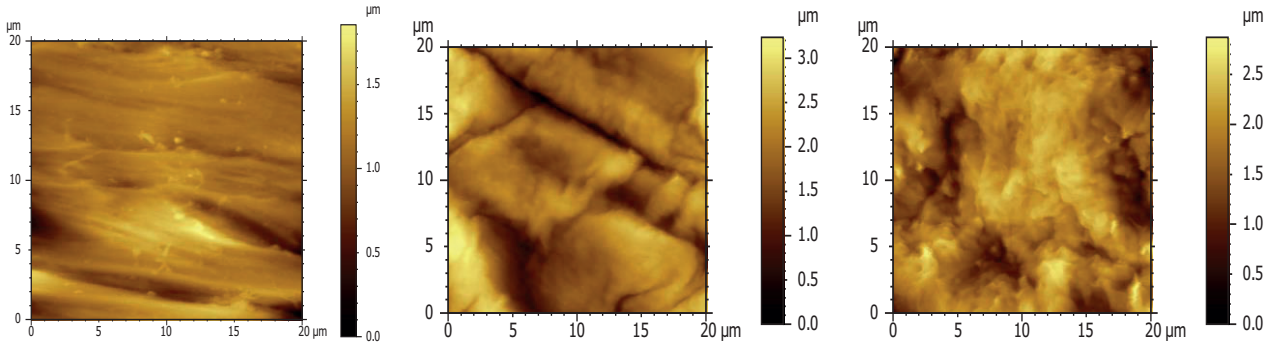


Figure 5. AFM images of: (left) unmodified TPU, (center) TPU functionalized with a 100% of polyethylene glycol 4K self-assembled monolayer, TPU-PEG; and (right) TPU functionalized with a mixed SAM of 60% PEG4K and 40% Mal-PEG5K-OH, TPU-PEG-Mal.

The homogeneity of the surface functionalization was measured using a microplate reader with luminescence (Figure S7) taking advantage of the Green Fluorescent Protein (GFP) fused to the antimicrobial active moiety of the protein used, i.e., HD5-GFP-H6-Cys. From

these images it was determined that the optimal protein concentration to be used to get a homogeneous click reaction was 10 µM incubated during 2 h in a wet chamber.

Finally, the antimicrobial activity regarding inhibition of the formation of biofilm was assessed against three bacteria relevant in HAIs: *Pseudomonas aeruginosa* (Gram-negative), methicillin-resistant *Staphylococcus aureus* (MRSA, Gram-positive) and methicillin-resistant *Staphylococcus epidermidis* (MRSE, Gram-positive). Results demonstrated that TPU surfaces functionalized with antimicrobial protein HD5-GFP-H6-Cys avoid the formation of biofilm from 50% to 99% in the three different pathogens studied and involved in HAI, whereas non-functionalized TPU surfaces did not (Figure 6). Among the pathogens tested (*P. aeruginosa*, MRSA and MRSE) there were either Gram-negative or Gram-positive bacteria and AMR bacteria such as MRSA or MRSE, showing the versatility and broad-spectrum activity of the tested strategy.

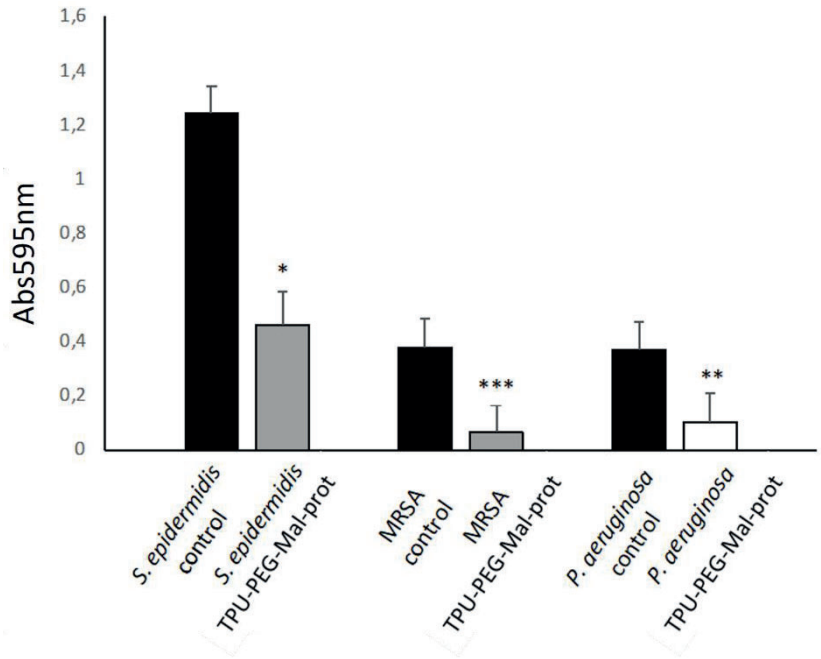


Figure 6. Inhibition of *Pseudomonas aeruginosa* (Gram-negative), methicillin-resistant *Staphylococcus aureus* (MRSA) (Gram-positive) and methicillin-resistant *Staphylococcus epidermidis* (MRSE) (Gram-positive) biofilms by HD5-GFP-H6-Cys

protein anchored on the TPU-PEG-Mal surfaces (TPU-PEG-Mal-Prot). Asterisks depict significant differences compared to the control (*p-value≤0.05, **p-value≤0.005, ***p-value≤0.0005).

3. Conclusions

Biofilm formation on medical device surfaces enhances antimicrobial resistance, emphasizing the need for innovative solutions alternative to conventional antibiotic or the use of metals like silver. The use of AMPs, particularly HDPs, has emerged as a promising approach due to their broad-spectrum activity and low propensity for inducing resistance. Recently, we have demonstrated the efficacy of recombinant multidomain proteins based on HDPs in combating HAI, both in biofilm and planktonic forms.[31] This study proposes a novel method for modifying TPU surfaces, one of the materials mostly used for medical devices, with recombinant HDPs, offering broad-spectrum antibacterial properties. Through a controlled design and synthesis process, TPU surfaces were coated with HDPs, achieved via a chemically mediated surface activation and modification procedure. Specifically, an easy antibacterial modification of TPU surfaces has been achieved using an initial isocyanate activation of the chemical resistant TPU surface. Then, an interfacial reaction with PEG derivatives and an easy click reaction between the PEG-maleimide terminated SAM on the TPU and the cysteine (-thiol) terminated HD5 protein gives place to TPU surfaces with broad-spectrum antibiofilm activity. Characterization using a multi-technique approach confirms the efficacy and stability of the antibiofilm surfaces. The convenient surface modification strategy developed together with the performance of the protein modified TPU surfaces, along with the cost-effective synthesis, low induction of resistance, low toxicity and broad-spectrum activity of the

protein, suggest the potential applications of this study to fight surface-associated bacterial infections of medical devices like catheters or tissue engineering scaffolds.

In conclusion, this research contributes to the development of tailored antimicrobial surfaces to mitigate HAIs, particularly those related to medical devices. Specifically, it represents an important step towards the development of alternative strategies to traditional antibiotics and metals which is crucial for addressing the challenges posed by MDR bacteria and improving patient outcomes in healthcare settings.

4. Materials and Methods

4.1. Materials

The dibutyltin dilaurate 95% (DD), hexamethylene diisocyanate 98% (HDI), poly(ethylene) glycol 4000 (PEG4K) and poly(ethylene) glycol maleimide (Mal-PEG5K-OH) were purchased from Merk. Thermoplastic Polyurethane (TPU) beads were ordered from Lubrizol (Tecothane 2085A-B20 and Tecothane 1085A). Toluene was ordered from Chem-Lab.

4.2. TPU discs fabrication

The TPU discs fabrication was based in an extrusion process of the TPU beads. These beads were melted to form a TPU bar of 7.8 mm diameter and then they were cut in 1 mm thickness pieces. From them, discs of 7,5 mm of diameter were cut with a punch.

4. 3. HD5-GFP-H6-Cys production

The HD5-GFP-H6-Cys was based on the mature sequences of HD5 fused to the green fluorescent protein (GFP) gene through the linker sequence (GGSSRSS) and C-terminally fused to a 6 histidine (H6)-tag for protein purification and a cysteine, as described in ref.

¡Error! Marcador no definido.. The HD5-GFP-H6-Cys sequence was codon-optimized by GeneArt (GeneArt®, Life technologies, Regensburg, Germany) for the recombinant expression in *E. coli* platform. The sequence was cloned into pET22b (amp^R) and transformed by heat shock in competent *E. coli* BL21 (DE3) cells.

E. coli/pET22b-HD5-GFP-H6-Cys was grown overnight at 37ºC and 250 rpm in Luria–Bertani (LB) medium with ampicillin at 100 μg/mL. The overnight was used as inoculum in shake flasks with fresh LB medium and ampicillin at 100 μg/mL starting at OD_{600nm}=0.05. Cultures were grown at 37ºC and 250 rpm and HD5-GFP-H6-Cys protein expression was induced by 1 mM IPTG when cultures reached an OD_{600nm}=0.4-0.6. After 3 h, cultures were centrifuged at 6,000 *x g* for 15 min at 4ºC and the pellet was stored at -80ºC.

For protein purification, pellets were resuspended in binding buffer (500 mM NaCl, 20 mM Tris, 20 mM Imidazole) with protease inhibitor and disrupted as described in.[43] Supernatant obtained was further purified by Immobilized Metal Affinity Chromatography (IMAC) in an ÄKTA Start (GE Healthcare Bio-Sciences AB, Uppsala, Sweden) as described in.[43]

4. 4. TPU surface functionalization

The TPU discs were sonicated with isopropyl alcohol for 15 min. Then, the TPU surfaces were dried under a gently N_2 flow. After, the modification of the surface of the TPU was done in a three-steps procedure. All steps were carried out under argon atmosphere, using dried toluene as solvent (and swelling agent) and dibutyltin dilaurate 95% as the catalyst. In the first step, the surface of the TPU discs were activated with HDI. Specifically, TPU samples were immersed into 5 mL of toluene containing 5% (v/v) HDI and 0.25% (v/v) dibutyltin dilaurate 95% for 1h at 70 °C. Then, the TPU sample were washed with dried

toluene for 30 min. In the second step, i) PEG 4K or ii) PEG 4K and Mal-PEG5K-OH were grafted onto the TPU surface by letting the hydroxyl groups reacts with the isocyanate ends groups of the activated surface to obtain the TPU-PEG homogeneous SAM and the TPU-PEG-Mal mixed SAM, respectively. Specifically, the TPU surfaces were immersed in a 10% (w/v) of PEG4K solution or a mixed solution of 40% Mal-PEG5K-OH and 60% PEG4K in dried toluene and left to react overnight at 45°C. After that, the samples were washed in order to remove all the unreacted monomer with toluene, isopropyl alcohol and MilliQ water for 15 min each. The TPU disc were finally dried in a vacuum oven at 45°C overnight.

4.5. Bioclickable protein anchoring

The protein was anchored via a click reaction between the thiol of the cysteine group of the HD5 (HD5-GFP-H6-Cys**)** and the maleimide terminated group of the SAM. Specifically, 80 µL of a 10 µM protein solution were deposit on top of the TPU surfaces that were functionalized with a mixed SAM of PEG4K and Mal-PEG5K-OH and left to react in a wet chamber for 2 h at room temperature. Then, the substrates were rinsed 3 times with MilliQ water and dried under a gentle N_2 flow.

4.6. Instruments used for the characterization

The functionalized TPU discs were characterized using a multi-technique approach using FTIR, WCA, XPS, AFM and a micro plate reader with luminiscence. FTIR spectra were obtained in a Spectrophotometer Jasco 4700, using an Attenuated Total Reflectance accessory. Resolution was 2 and the number of scans 32. WCA was performed at room temperature in a Drop Shape Analyzer DSA 100 from KRÜSS. WCA of the samples were evaluated by static contact angle measurements using the sessile drop method. XPS

measurements were performed at room temperature with a SPECS PHOIBOS 150 hemispherical analyzer (SPECS GmbH, Berlin, Germany)) in a base pressure of $5x10^{-10}$ mbar using monochromatic Al K alpha radiation (1486.74 eV) as excitation source operated at 300W. The energy resolution as measured by the FWHM of the Ag 3d5/2 peak for a sputtered silver foil was 0.62 eV. Charge neutralization was done through a flood gun. AFM characterization was performed using a Keysight 5100 AFM in tapping mode with an AppNano FORT tip in ambient conditions. SEM images were taken on a Quanta 650 FEG microscope at 5,0 kV. The luminescence experiment was measured at 520 nm at room temperature using the LUMIstar Omega microplate reader (BMG Labtech).

4.7. Antimicrobial activity in biofilm

To evaluate antimicrobial activity of the functionalized TPU surfaces, the strains selected were methicillin-resistant *S. aureus* ATCC-33592 (MRSA), *S. epidermidis* ATCC-35984 (MRSE) and *P. aeruginosa* ATCC-10145. MRSA, MRSE and *P. aeruginosa* were grown in Brain Heart Infusion (BHI) broth (Scharlau, Barcelona, Spain) and tryptic soy broth (TSB) medium was used for biofilm formation.

An overnight culture of the selected strains was reinoculated in 10 mL of fresh BHI broth and grown at 250 rpm and 37 °C. Then a 1/200 dilution was done in TSB and adding 1% and 0.25% glucose for MRSA and MRSE, respectively. The TPU discs (functionalized or not with HD5-GFP-H6-Cys) were added by forceps to a 48-well plate and a total of 250 µL/well of pathogen or control media were added. After 24 h of static incubation at 37ºC the remaining liquid was removed with the vacuum pump and wells washed with 3 rounds of 300 µL/well of NaCl 0.9% (Ringer). A total of 400 µL/well of Ringer was added, plate was covered with parafilm to avoid volume loss and sonicated with the

ultrasonic bath for 1 min, left in the refrigerator for 1 min. and sonicated again for 1 min. The content of the sonicated wells was transferred to eppendorf tubes and centrifuged at 6,200 *x g*, 15 min and 4ºC. Supernatant were removed and pellets fixed with 400 µL of 100% methanol for 10 min. Then the methanol was removed and pellets left to dry for 5 min more. A staining with 1% crystal violet (CV) in ddH_2O was performed (400uL/Eppendorf) for 20 min at room temperature. At the end of incubation, tubes were washed 3 rounds with 500 µL/Eppendorf ddH_2O and stained pellets dissolved with 100 µL of 70% ethanol. Finally, the content of the tubes was transferred to a non-maxisorp plate and read at 595 nm in a microplate reader.

Acknowledgements

Financial support by the MICIU of Spain (projects PID2019-105622RBI00, PID2020-115296RA-I00, PID2022-137332OB-I00, CEX2019-000917-S, CEX2023- 001263-S), CSIC (project 2023AEP092), the Marató de TV3 foundation (project number 201812-30-31-32-33 and 202326-30-31-32-33) and the Generalitat de Catalunya (project SGR Cat 2021-00438 and 2021-01552). The authors are also grateful for the financial support received from Instituto de Salud Carlos III through and the Networking Research Center on Bioengineering, Biomaterials, and Nanomedicine (CIBER-BBN). J.G. is grateful to the Max Planck Institute for Medical Research (Heidelberg, Germany) for their collaboration through the Max Planck Partner Group "Dynamic Biomimetics for Cancer Immunotherapy". ICMAB-CSIC acknowledges support from the Severo Ochoa Programme for Centres of Excellence in R&D (FUNFUTURE, CEX2019-000917-S). JMM received a personal 80:20 research grant from the Institut d'Investigacions Biomèdiques August Pi i Sunyer (IDIBAPS), Barcelona, Spain, during 2017–24. This work has been developed inside the Materials Science PhD program of Universitat

Autonoma de Barcelona. XRR was supported by a grant PTA2021-020955-I funded by MCIN/AEI/10.13039/501100011033 and the FSE. This project has received funding from the European Union's Horizon 2020 research and innovation program under the Marie Skłodowska-Curie grant agreement No. 801342 (Tecniospring INDUSTRY) and the Government of Catalonia's Agency for Business Competitiveness (ACCIOÅL; TECSPR19-1-0065). AL-C received a pre-doctoral fellowship from Generalitat de Catalunya (FI-AGAUR) and PB was supported by a PFIS predoctoral fellowship (FI20/00009) from the Instituto de Salud Carlos III. The authors also acknowledge the ICTS NANBIOSIS for the support of the Biomaterial Processing and Nanostructuring Unit (U6) at ICMAB-CSIC (https://www.nanbiosis.es/portfolio/u6-biomaterialprocessing-and-nanostructuring-unit/).

Conflicts of Interest: J.M.M. has received consulting honoraria and/or research grants from Angelini, Contrafect, Cubist, Genentech, Gilead Sciences, Jansen, Lysovant, Medtronic, MSD, Novartis, Pfizer and ViiV Healthcare, outside the submitted work.

FUNCATH investigators: Hospital Clinic-IDIBAPS, University of Barcelona, Barcelona, Spain: J.M.M., C.G.-d.-l.-M., Maria A. Cañas-Pacheco, Javier Garcia-Gonzalez, Marta Hernández-Meneses, Guillermo Cuervo and Asunción Moreno. Institute of Materials Science of Barcelona (ICMAB-CSIC): I.R., J.G., J.V and X.R.R. Hospital Universitari Parc Taulí: Oriol Gasch, O.Q.P. and P.B. IRTA: A.L.C., E.G.-F. and A.A.

Corresponding author: Imma Ratera; iratera@icmab.es

References

1. Neoh KG, Li M, Kang ET, Chiong E, Tambyah PA. Surface modification strategies for combating catheter-related complications: recent advances and challenges. *J Mater Chem B*. 2017;5(11):2045-2067. doi:10.1039/c6tb03280j

2. Lynch AS, Robertson GT. Bacterial and fungal biofilm infections. *Annu Rev Med*. 2008;59:415-428. doi:10.1146/annurev.med.59.110106.132000

3. Nandakumar V, Chittaranjan S, Kurian VM, Doble M. Characteristics of bacterial biofilm associated with implant material in clinical practice. *Polym J*. 2013;45(2):137-152. doi:10.1038/pj.2012.130

4. Alves D, Olívia Pereira M. Mini-review: Antimicrobial peptides and enzymes as promising candidates to functionalize biomaterial surfaces. *Biofouling*. 2014;30(4):483-499. doi:10.1080/08927014.2014.889120

5. Edmiston CE, Krepel CJ, Marks RM, et al. Microbiology of explanted suture segments from infected and noninfected surgical patients. *J Clin Microbiol*. 2013;51(2):417-421. doi:10.1128/JCM.02442-12

6. Chen L, Bai H, Xu JF, Wang S, Zhang X. Supramolecular Porphyrin Photosensitizers: Controllable Disguise and Photoinduced Activation of Antibacterial Behavior. *ACS Appl Mater Interfaces*. 2017;9(16):13950-13957. doi:10.1021/acsami.7b02611

7. Renes Carreño E, Escribá Bárcena A, Catalán González M, et al. Study of risk factors for healthcare-associated infections in acute cardiac patients using categorical principal component analysis (CATPCA). *Sci Rep*. 2022;12(1). doi:10.1038/s41598-021-03970-w

8. Magill SS, Edwards JR, Bamberg W, et al. Multistate Point-Prevalence Survey of Health Care–Associated Infections. *New England Journal of Medicine*. 2014;370(13):1198-1208. doi:10.1056/nejmoa1306801

9. Cassini A, Plachouras D, Eckmanns T, et al. Burden of Six Healthcare-Associated Infections on European Population Health: Estimating Incidence-Based Disability-Adjusted Life Years through a Population Prevalence-Based Modelling Study. *PLoS Med*. 2016;13(10). doi:10.1371/journal.pmed.1002150

10. Fürnkranz U, Walochnik J. Nosocomial infections: Do not forget the parasites! *Pathogens*. 2021;10(2):1-21. doi:10.3390/pathogens10020238

11. Brown ED, Wright GD. Antibacterial drug discovery in the resistance era. *Nature*. 2016;529(7586):336-343. doi:10.1038/nature17042

12. Santajit S, Indrawattana N. Mechanisms of Antimicrobial Resistance in ESKAPE Pathogens. *Biomed Res Int*. 2016;2016. doi:10.1155/2016/2475067

13. Konai MM, Haldar J. Fatty Acid Comprising Lysine Conjugates: Anti-MRSA Agents That Display in Vivo Efficacy by Disrupting Biofilms with No Resistance Development. *Bioconjug Chem*. 2017;28(4):1194-1204. doi:10.1021/acs.bioconjchem.7b00055

14. Tossi A, Sandri L, Giangaspero A, et al. Biocidal Activity of Polystyrenes That Are Cationic by Virtue of Protonation. *Proc Natl Acad Sci USA*. 2002;1(2):557-560. doi:10.1021/ol036341

15. Association for the Advancement of Science A. *The Bacteria Fight Back*.; 2008. www.sciencemag.org

16. Wang S, Gao Y, Jin Q, Ji J. Emerging antibacterial nanomedicine for enhanced antibiotic therapy. *Biomater Sci*. 2020;8(24):6825-6839. doi:10.1039/d0bm00974a

17. Priyamvada P, Debroy R, Anbarasu A, Ramaiah S. A comprehensive review on genomics, systems biology and structural biology approaches for combating antimicrobial resistance in ESKAPE pathogens: computational tools and recent advancements. *World J Microbiol Biotechnol*. 2022;38(9). doi:10.1007/s11274-022-03343-z

18. Velazquez-Meza ME, Galarde-López M, Carrillo-Quiróz B, Alpuche-Aranda CM. Antimicrobial resistance: One Health approach. *Vet World*. 2022;15(3):743-749. doi:10.14202/vetworld.2022.743-749

19. Ghosh S, Mukherjee R, Basak D, Haldar J. One-Step Curable, Covalently Immobilized Coating for Clinically Relevant Surfaces That Can Kill Bacteria, Fungi, and Influenza Virus. *ACS Appl Mater Interfaces*. 2020;12(25):27853-27865. doi:10.1021/acsami.9b22610

20. Zhang Y, Hu K, Xing X, et al. Smart Titanium Coating Composed of Antibiotic Conjugated Peptides as an Infection-Responsive Antibacterial Agent. *Macromol Biosci*. 2021;21(1). doi:10.1002/mabi.202000194

21. Wei T, Yu Q, Chen H. Responsive and Synergistic Antibacterial Coatings: Fighting against Bacteria in a Smart and Effective Way. *Adv Healthc Mater*. 2019;8(3). doi:10.1002/adhm.201801381

22. Zhao YQ, Sun Y, Zhang Y, et al. Well-Defined Gold Nanorod/Polymer Hybrid Coating with Inherent Antifouling and Photothermal Bactericidal Properties for Treating an Infected Hernia. *ACS Nano*. 2020;14(2):2265-2275. doi:10.1021/acsnano.9b09282

23. Song J, Liu H, Lei M, et al. Redox-Channeling Polydopamine-Ferrocene (PDA-Fc) Coating to Confer Context-Dependent and Photothermal Antimicrobial Activities. *ACS Appl Mater Interfaces*. 2020;12(7):8915-8928. doi:10.1021/acsami.9b22339

24. Ye Z, Zhu X, Mutreja I, et al. Biomimetic mineralized hybrid scaffolds with antimicrobial peptides. *Bioact Mater*. 2021;6(8):2250-2260. doi:10.1016/j.bioactmat.2020.12.029

25. Sun J, Tan H, Liu H, et al. A reduced polydopamine nanoparticle-coupled sprayable PEG hydrogel adhesive with anti-infection activity for rapid wound sealing. *Biomater Sci*. 2020;8(24):6946-6956. doi:10.1039/d0bm01213k

26. Wang D, Haapasalo M, Gao Y, Ma J, Shen Y. Antibiofilm peptides against biofilms on titanium and hydroxyapatite surfaces. *Bioact Mater*. 2018;3(4):418-425. doi:10.1016/j.bioactmat.2018.06.002

27. Kazemzadeh-Narbat M, Cheng H, Chabok R, et al. Strategies for antimicrobial peptide coatings on medical devices: a review and regulatory science perspective. *Crit Rev Biotechnol*. 2021;41(1):94-120. doi:10.1080/07388551.2020.1828810

28. Kranz J, Schmidt S, Wagenlehner F, Schneidewind L. Catheter- Associated Urinary Tract Infections in Adult Patients. *Dtsch Arztebl International*. 2020;117(6):83-88. https://www.aerzteblatt.de/int/article.asp?id=212332

29. Huang L, Liu CJ. Progress for the development of antibacterial surface based on surface modification technology. *Supramolecular Materials*. 2022;1. doi:10.1016/j.supmat.2022.100008

30. Steinstraesser L, Kraneburg UM, Hirsch T, et al. Host defense peptides as effector molecules of the innate immune response: A sledgehammer for drug resistance? *Int J Mol Sci*. 2009;10(9):3951-3970. doi:10.3390/ijms10093951

31. López-Cano A, Ferrer-Miralles N, Sánchez J, et al. A Novel Generation of Tailored Antimicrobial Drugs Based on Recombinant Multidomain Proteins. *Pharmaceutics*. 2023;15(4). doi:10.3390/pharmaceutics15041068

32. Tatkiewicz WI, Seras-Franzoso J, García-Fruitós E, et al. Two-dimensional microscale engineering of protein-based nanoparticles for cell guidance. *ACS Nano*. 2013;7(6):4774-4784. doi:10.1021/nn400907f

33. Tatkiewicz WI, Seras-Franzoso J, Garcia-Fruitós E, et al. Surface-Bound Gradient Deposition of Protein Nanoparticles for Cell Motility Studies. *ACS Appl Mater Interfaces*. 2018;10(30):25779-25786. doi:10.1021/acsami.8b06821

34. Coronel-Meneses D, Sánchez-Trasviña C, Ratera I, Mayolo-Deloisa K. Strategies for surface coatings of implantable cardiac medical devices. *Front Bioeng Biotechnol*. 2023;11. doi:10.3389/fbioe.2023.1173260

35. Martínez-Miguel M, Kyvik AR, Kyvik AR, et al. Stable anchoring of bacteria-based protein nanoparticles for surface enhanced cell guidance. *J Mater Chem B*. 2020;8(23):5080-5088. doi:10.1039/d0tb00702a

36. Tatkiewicz WI, Seras-Franzoso J, García-Fruitós E, et al. High-Throughput Cell Motility Studies on Surface-Bound Protein Nanoparticles with Diverse Structural and Compositional Characteristics. *ACS Biomater Sci Eng*. 2019;5(10):5470-5480. doi:10.1021/acsbiomaterials.9b01085

37. Díez-Gil C, Martínez R, Ratera I, Tárraga A, Molina P, Veciana J. Nanocomposite membranes as highly selective and sensitive mercury(ii) detectors. *J Mater Chem*. 2008;18(17):1997-2002. doi:10.1039/B800708J

38. Kyvik AR, Roca-Pinilla R, Mayolo-Deloisa K, et al. Antibiofilm surfaces based on the immobilization of a novel recombinant antimicrobial multidomain protein using self-assembled monolayers. *Mater Adv*. 2023;4(10):2354-2364. doi:10.1039/d2ma00978a

39. Al Nakib R, Toncheva A, Fontaine V, Vanheuverzwijn J, Raquez JM, Meyer F. Thermoplastic polyurethanes for biomedical application: A synthetic, mechanical, antibacterial, and cytotoxic study. *J Appl Polym Sci*. 2022;139(4). doi:10.1002/app.51666

40. Alves P, Coelho JFJ, Haack J, Rota A, Bruinink A, Gil MH. Surface modification and characterization of thermoplastic polyurethane. *Eur Polym J*. 2009;45(5):1412-1419. doi:10.1016/j.eurpolymj.2009.02.011

41. Qi F, Qian Y, Shao N, et al. Practical Preparation of Infection-Resistant Biomedical Surfaces from Antimicrobial β-Peptide Polymers. *ACS Appl Mater Interfaces*. 2019;11(21):18907-18913. doi:10.1021/acsami.9b02915

42. Lu Z, Wu Y, Cong Z, et al. Effective and biocompatible antibacterial surfaces via facile synthesis and surface modification of peptide polymers. *Bioact Mater*. 2021;6(12):4531-4541. doi:https://doi.org/10.1016/j.bioactmat.2021.05.008

43. López Cano A, Sicilia P, Gaja C, Aris A, Garcia-Fruitos E. Quality comparison of recombinant soluble proteins and proteins solubilized from bacterial inclusion bodies. *N Biotechnol*. 2022;72. doi:10.1016/j.nbt.2022.09.003

Supplementary Information

Activating Thermoplastic Polyurethane Surfaces with Polyethylene Glycol-Based Recombinant Human α-Defensin 5 Self-Assembled Monolayers for Infection Prevention

Xavier Rodríguez Rodríguez,[1,2] Adrià López-Cano,[3] Karla Mayolo-Deloisa,[1,4] Oscar Q Pich,[5,6] Paula Bierge,[5,6] Nora Ventosa,[1,2] Cristina García-de-la-Maria,[6] José M. Miró,[6,7] Oriol Gasch,[8] Jaume Veciana,[1,2] Judith Guasch,[1,2,9] Anna Arís,[3] Elena Garcia-Fruitós,[3] Imma Ratera[1,2] and the FUNCATH investigators[10]

[1] Institute of Materials Science of Barcelona (ICMAB-CSIC), Campus UAB, Bellaterra, 08193, Spain.

[2] Networking Research Center on Bioengineering, Biomaterials and Nanomedicine (CIBER-BBN), Campus UAB, Bellaterra, 08193, Spain.

[3] IRTA, Torre Marimon, Ctra C-59, Km 12,1, 08140 Caldes de Montbui, Barcelona, Spain

[4] Tecnologico de Monterrey, Institute for Obesity Research, School of Engineering and Sciences, Av. Eugenio Garza Sada 2001, 64849 Monterrey, Nuevo León, México.

[5] Laboratori de Recerca en Microbiologia i Malalties Infeccioses, Hospital Universitari Parc Taulí, Institut d'Investigació i Innovació Parc Taulí (I3PT-CERCA), Universitat Autònoma de Barcelona, 08208, Sabadell, Spain.

[6] Infectious Diseases Service. Hospital Clinic-FCRB-IDIBAPS. Universitat de Barcelona, Barcelona, Spain.

[7] Infectious Diseases Biomedical Research Networking Center (CIBERINFEC), Instituto de Salud Carlos III, Madrid, Spain.

[8] Servei de Malalties Infeccioses, Hospital Universitari Parc Taulí, Institut d'Investigació i Innovació Parc Taulí (I3PT-CERCA), Universitat Autònoma de Barcelona, 08208, Sabadell (Spain)

[9] Dynamic Biomimetics for Cancer Immunotherapy, Max Planck Partner Group, ICMAB-CSIC, Campus UAB, Bellaterra, 08193, Spain.

[10] FUNCATH Investigators are indicated in the Appendix.

1. Basic chemistry of Thermoplastic Polyurethane (TPU)
2. Stability test with Fourier transform infrared (FTIR) characterization
3. Stability test with Water Contact Angle (WCA) characterization
4. X-Ray photoelectron spectroscopy (XPS) of the oxygen (O1s)
5. Atomin Force Microscopy (AFM) profiles
6. Fluorescence microscopy images to optimize the protein anchoring step and the homogeneity of the functionalization.

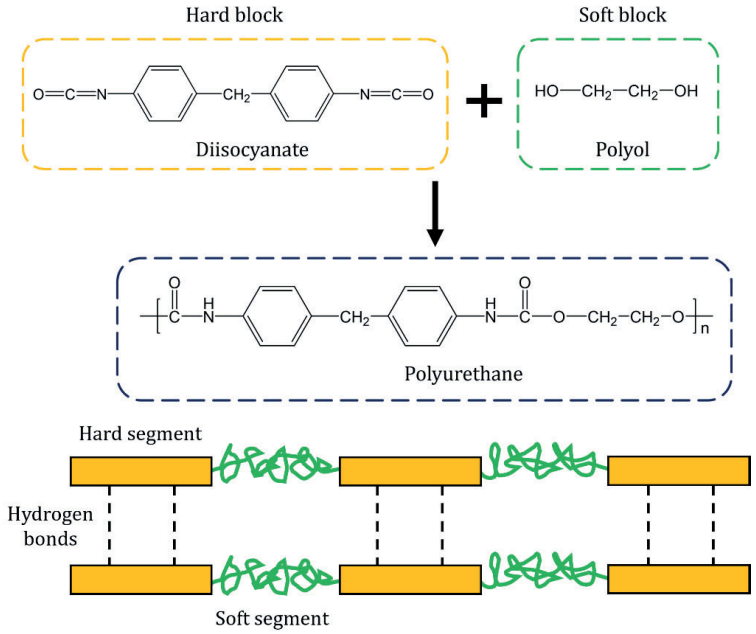


Figure S1. Basic chemistry of the TPU.

2. Stability test with FTIR characterization

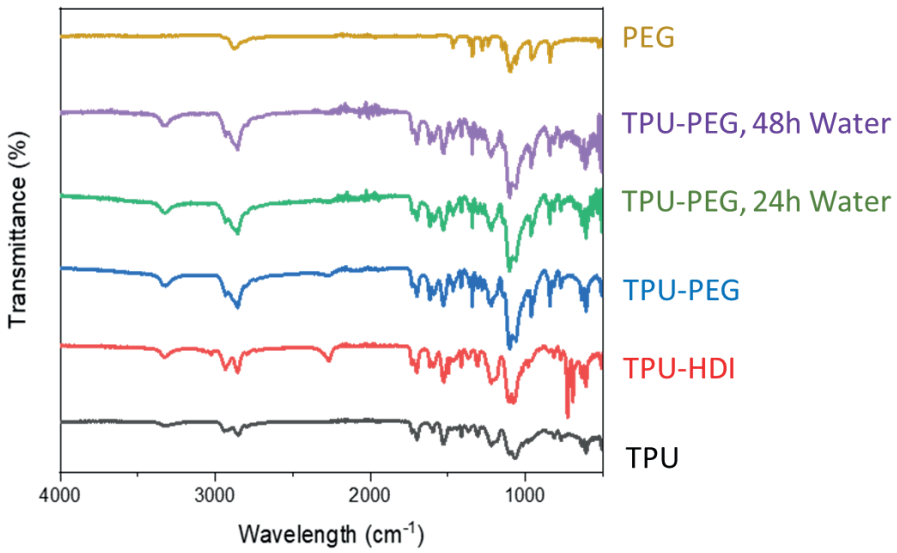


Figure S2. FTIR spectra were: (black) unmodified thermoplastic polyurethane (TPU); (red) functionalization of thermoplastic polyurethane with HDI (TPU-HDI); (blue) thermoplastic polyurethane with a PEG4K self-assembled monolayer (TPU-PEG); (green) thermoplastic polyurethane with a PEG4K self-assembled monolayer after 24h in water (TPU-PEG, 24h Water); (purple) thermoplastic polyurethane with a PEG 6000 self-assembled monolayer after 48h in water (TPU-PEG, 48 h Water); (yellow) PEG 6000 (PEG).

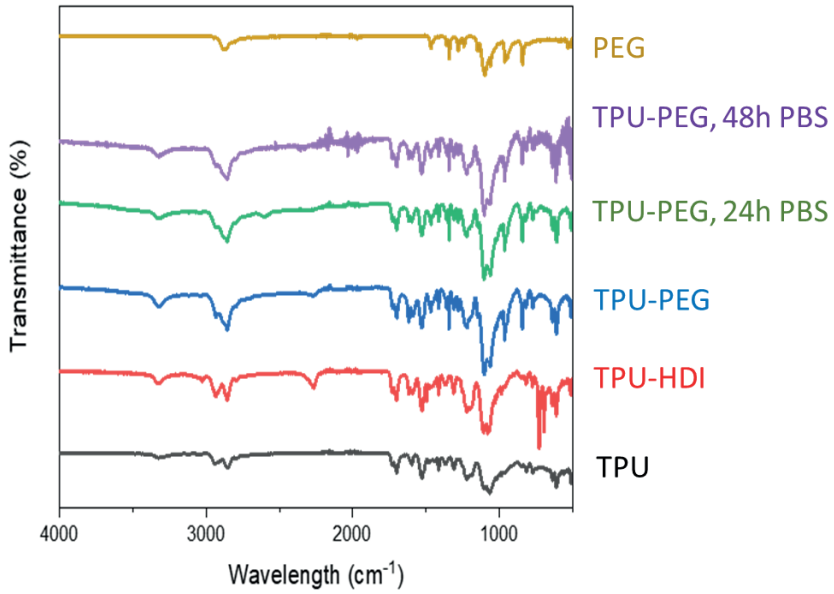


Figure S3. FTIR spectra were: (black) unmodified thermoplastic polyurethane (TPU); (red) functionalization of thermoplastic polyurethane with HDI (TPU-HDI); (blue) thermoplastic polyurethane with a PEG4K self-assembled monolayer (TPU-PEG); (green) thermoplastic polyurethane with a PEG4K self-assembled monolayer after 24h in PBS (TPU-PEG, 24h PBS); (purple) thermoplastic polyurethane with a PEG 6000 self-assembled monolayer after 48h in PBS (TPU-PEG, 48 h PBS); (yellow) PEG 6000 (PEG).

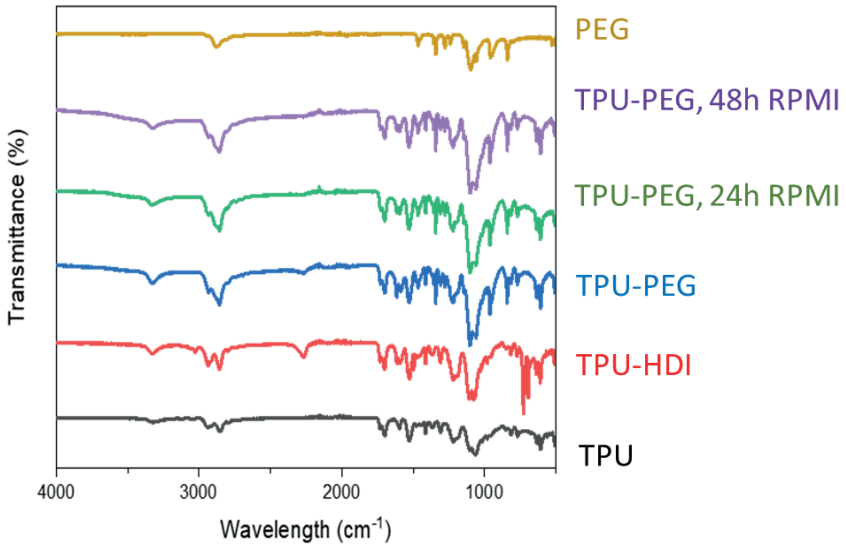


Figure S4. FTIR spectra were: (black) unmodified thermoplastic polyurethane (TPU); (red) functionalization of thermoplastic polyurethane with HDI (TPU-HDI); (blue) thermoplastic polyurethane with a PEG4K self-assembled monolayer (TPU-PEG); (green) thermoplastic polyurethane with a PEG4K self-assembled monolayer after 24h in RPMI media (TPU-PEG, 24h RPMI); (purple) thermoplastic polyurethane with a PEG 6000 self-assembled monolayer after 48h in RPMI media (TPU-PEG, 48 h RPMI); (yellow) PEG 6000 (PEG).

3. Stability test with WCA characterization

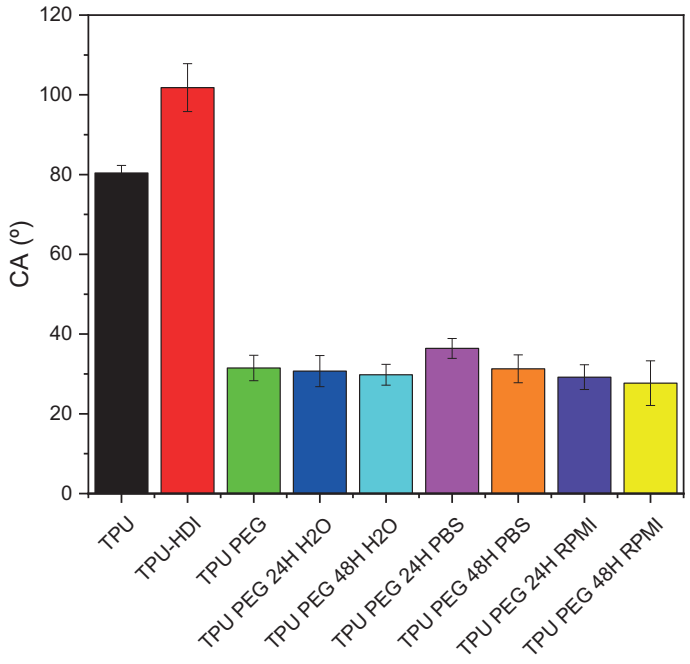


Figure S5. Water contact angle of: (black) the unmodified TPU; (red) functionalization of TPU with HDI; (green) thermoplastic polyurethane with a PEG4K self-assembled monolayer; thermoplastic polyurethane with a PEG4K self-assembled monolayer after (blue) 24h and (cyan) 48h in water, (magenta) 24h and (orange) 48h in PBS and (purple) and (purple) 24h and (yellow) 48h in RPMI media.

4. X-Ray photoelectron spectroscopy of oxygen (O1s)

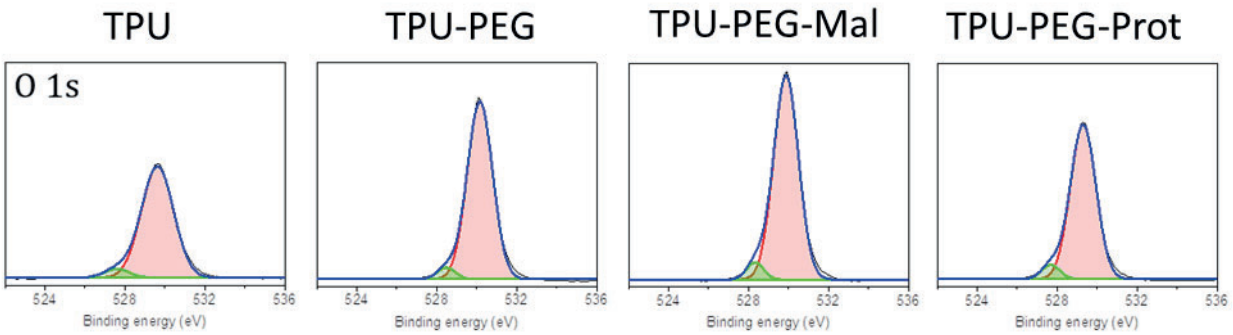
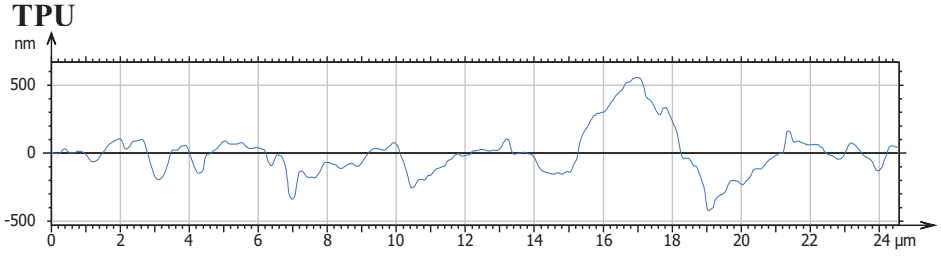
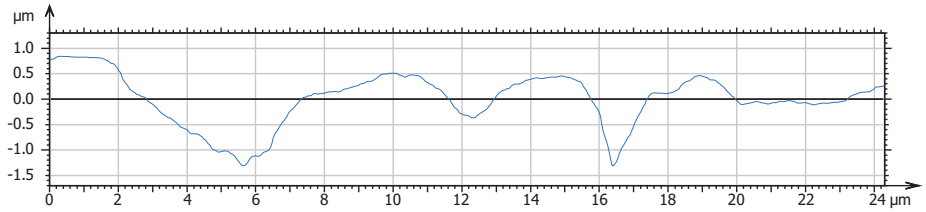


Figure S6. XPS spectra of O1s for unmodified TPU, TPU-PEG, TPU-PEG-Mal and TPU-Protein.

5. AFM profiles



TPU-PEG



TPU-PEG-Mal

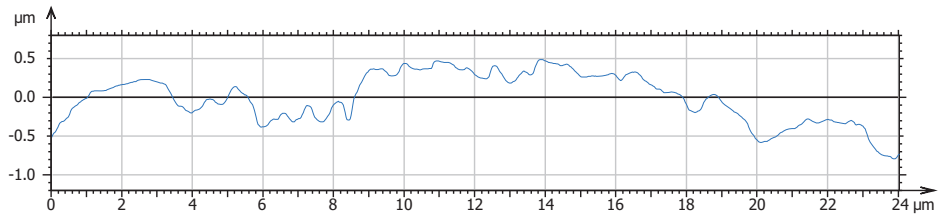


Figure S6. Profiles of the AFM images of: (top) unmodified thermoplastic polyurethane, (centre) thermoplastic polyurethane with a PEG 6000 self-assembled monolayer and (bottom) thermoplastic polyurethane with a 40% maleimide terminated PEG and 60% PEG self-assembled monolayer.

6. Fluorescence microscopy images to optimize the protein anchoring step and the homogeneity of the functionalization.

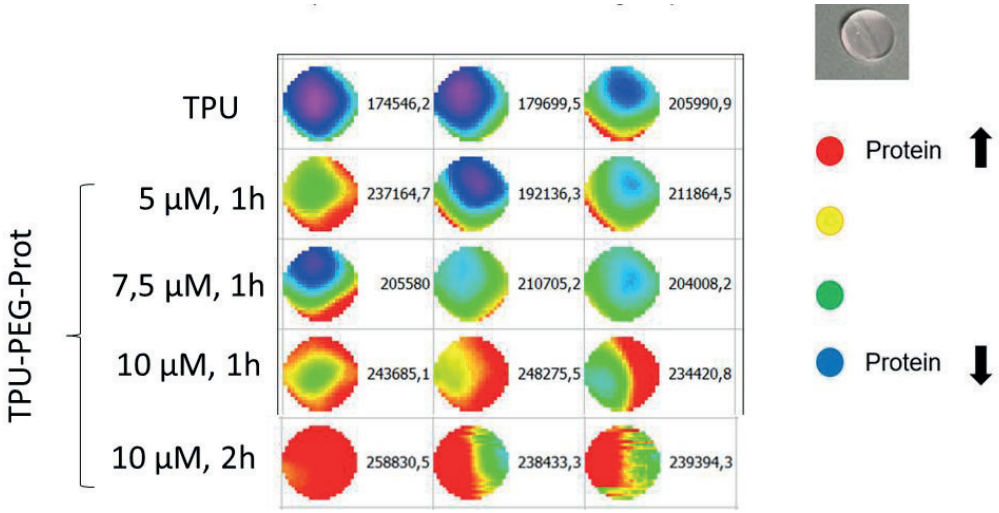


Figure S7. Fluorescent microscopy images using a microplate reader of the surface of the functionalized discs (PEG-Mal-prot) and non-functionalized TPU discs measured at 520 nm were the intensity of the luminescence (which is proportional to the concentration of HD5-GFP-H6-Cys) is quantified as red > yellow > green > blue. Different protein concentrations and incubation times were analysed.

Chapter 4
Stable Antibiofilm Surface Coating of Thermoplastic Polyurethane Catheters – Towards *In Vivo* Infection Prevention

4.1. Introduction

According to the World Health Organization, a medical device (MD) is any product or equipment used with a medical purpose, i.e., an equipment for diagnosis, prevention, monitoring, and treatment of a health condition.[1] MDs have played a transformative role in revolutionizing healthcare, contributing to improved diagnostics, treatments, and patient outcomes. These devices range from sophisticated imaging equipment to simple yet indispensable tools like catheters, each serving a unique purpose in the delivery of medical care.[2]

The materials used in a MD influence costs, manufacturing process, availability, maintenance, and patient safety. MDs such as prostheses, bone replacement implants, and catheters are composed by polymers made mostly of the following biomaterials: poly(dimethyl siloxane), polyethylene, poly(ethylene terephthalate), silicone rubber, poly(methyl methacrylate), polypropylene, poly(tetrafluoro ethylene)(Teflon®), polyvinyl chloride, polystyrene, and polyurethane.[3,4] Desirable properties of these biomaterials are their biocompatibility, mechanical properties, ease of molding into desirable shapes and low cost.[5]

Catheters play a crucial role in modern healthcare, facilitating the management of various medical conditions.[6] However, their use in hospitals comes with a set of challenges and concerns that healthcare professionals constantly grapple with. Understanding and addressing these issues is essential for enhancing patient care and minimizing associated risks.[7] Catheter-associated infections pose a significant threat to patients in hospitals[8] and is one of the most commonly health care-associated infection.[9–11] There are several types of catheters depending on their use: urinary, vascular, gastrointestinal, and intracranial pressure monitoring catheters. Additionally, there are also several infections associated with catheters such as urinary tract infections, catheter-related bloodstream infections (CRBSI), and surgical site infections.[12] Therefore, there are several ways that bacteria can enter and colonize the catheter (Figure 4.1): (1) migration of microorganisms from the patient's skin through the catheter tract at the exit site; (2) pathogen colonization of the catheter hub or connection; (3) hematogenous seeding (from contaminated intravenous fluids); and (4) infused fluid contamination.

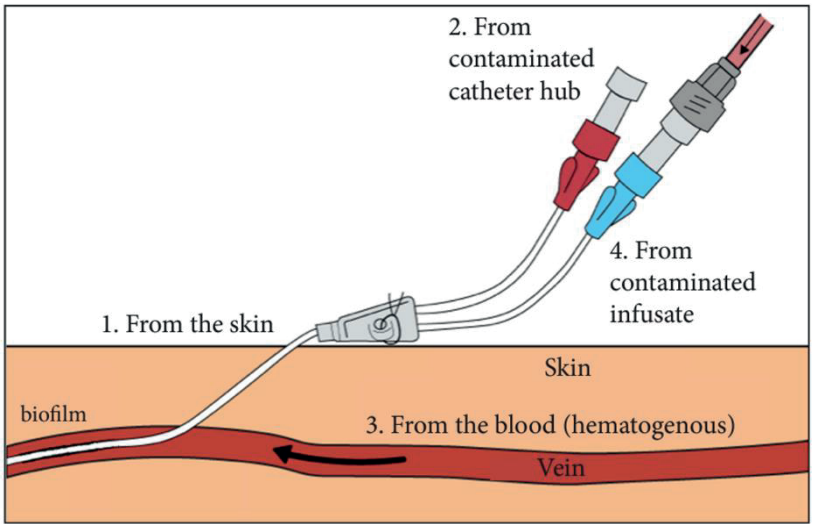


Figure 4.1. Potential routes CRBSI.[13]

Indwelling intravascular and urinary catheters are essential components of modern medical care. Unfortunately, indwelling devices significantly increase the risk of iatrogenic infection, particularly in an already fragile patient population.[14]

Managing the formation of bacterial biofilms on bloodstream (central venous) catheters is a critical focus to prevent associated infections that occurs both internally and externally. A full understanding of how biofilm arises on the external but also internal surfaces of indwelling catheters, whether intravascular or urinary, is crucial to understanding the causes of infection of these devices.[15] As seen in Chapter 3, biofilms not only provide a conducive environment for bacterial growth but also make it challenging for antibiotics and the immune system to eliminate the infection.

Moreover, the growing emergence of antibiotic-resistant microorganisms and consumption of antibiotics, which will increase up to (67% by 2030, challenge the treatment of infections.[1617] Biofilm formation is considered the underlying reason responsible for the lack of success of antimicrobial agents. To prevent catheter-related infections, some coatings have been developed to reduce bacterial adhesion by altering the physicochemical properties of the substrate.[18]

Currently available coatings are classified into five categories based on how they prevent biofilm formation: (1) release of antimicrobial compounds; (2) contact-killing; (3) altering the catheter surface to prevent microbial adhesion; (4) disruption of biofilm architecture; and (5) using benign bacterial biofilms to prevent pathogen colonization (Figure 4.2).[19] In contrast to release-based coatings, which work by slowly leaching antimicrobial compounds to expose and kill adhered and planktonic microbial cells that enter the catheterized bladder through the intraluminal route, contact-killing surfaces work by attaching antimicrobial agents to the surface material, which inhibits bacterial

attachment and proliferation. This is typically achieved by as a result of cell membrane disruption via physical lysis or charge disruption.[20]

Silver-based products belong to the most used local treatments for active coatings to prevent catheter-related infections,[21] but may be hampered by costs, environmental concerns, and safety considerations.[22,23] Moreover, its use is limited due to its toxicity and silver-resistant bacteria, able to avoid silver ions by ion-pumps and biofilms formation have been repeatedly observed.[24,25] Therefore, considering the aging of the population and the global health threat of antibiotic resistant microorganisms, there is an urgent need to develop new cost-efficient antimicrobial coatings for catheters with a superior biocompatibility and improved antimicrobial activity.

As mentioned in previous chapters, among new antimicrobial molecules, the use of antimicrobial peptides (AMPs) synthesized by the innate immunity, such as host defense peptides (HDPs), arises as an interesting alternative, as reported by our collaborators from Institute of Agrifood Research and Technology (IRTA).[26,27]

These peptides are cationic amphiphilic peptides able to kill bacteria through the disruption of their basic cell wall structures.[28] They present broad-spectrum microbicide activity against Gram-negative and Gram-positive bacteria, including those resistant to antibiotics.[29] Importantly, the development of bacterial resistance against HDPs is expected to be rare, because they act rapidly against integral components of the bacterial structure.[30] Therefore, these peptides are useful to fight CRBSIs such as the ones related to *Staphylococcus epidermidis*, which is one of the most prevalent pathogens implicated in these infections.[31]

Recently, our collaborators from IRTA have developed a new generation of tailored antimicrobials, using a rational design of antimicrobial recombinant multidomain proteins (ARMP) based on HDPs. This strategy is built on a two-phase procedure that begins with the use of single HDPs to produce first generation molecules. Subsequently, those HDPs with higher bactericidal efficiency are selected and combined to create the second generation, which have proven to be broad-spectrum antimicrobials, as mentioned before.[32] Therefore, these peptides could be useful to fight infections such as the ones related to *Staphylococcus epidermidis*, which is one of the most prevalent pathogens implicated in catheter related infections.[31] In this chapter, we used the multidomain protein called D5L37βD3,[32] developed at the group of Drs. Anna Arís and Elena García-Fruitós from IRTA.

TPU is one of the polymers mostly used for MDs, especially in catheters. It is very convenient for its mechanical and inert properties but on the other side, its inert surface is very challenging to be modified. In the previous chapter it has been developed a protocol of surface activation and covalent coating of TPU discs and catheters with polyethylene glycol (PEG) based SAMs of HDPs through a click reaction, with good

antibiofilm properties against different "gram positive" and "gram negative" strains. The conjugation of AMPs with PEG based molecular materials that exclude the bacterial adhesion is found to present good synergy and excellent antibiofilm properties being an interesting and promising alternative to fight against nosocomial infections (NI). But up to now, there are no reports about the inhibition of biofilm formation on thermoplastic polyurethane (TPU) catheters using HDPs as alternative to silver or antibiotics.

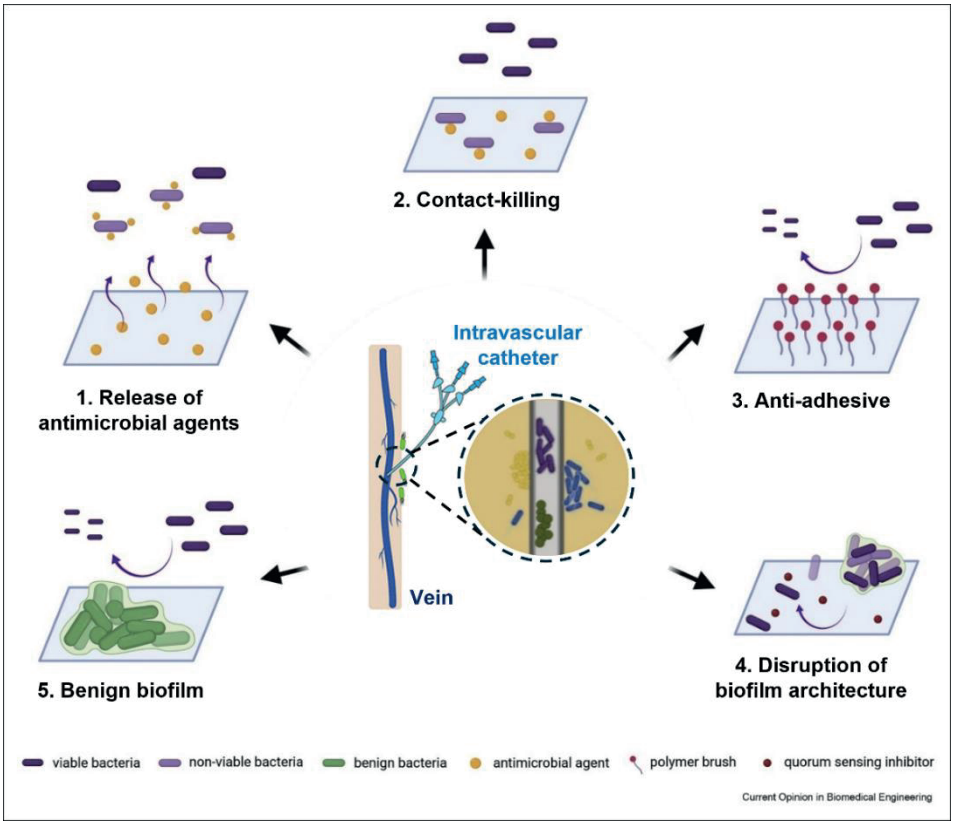


Figure 4.2. Strategies applied for the design of antimicrobial and antifouling surfaces on catheters. Adapted from references 18,32.

4.2. Objectives

The main objective of this chapter is to develop a novel and stable catheter, inner and outer, coating strategy alternative to silver and antibiotics to be used for prevention of infection using multidomain AMPs and the clickable strategy described in chapter 3.

The following specific objectives have been pursued:

1. Functionalization of TPU surfaces with PEG-based SAMs of novel multidomain AMPs and evaluation of its antibiofilm activity.
2. Evaluation of the cytotoxicity of the developed antimicrobial surfaces.
3. Functionalization of the inner and outer surface of medical grade TPU catheters with mixed PEG-based SAMs of multidomain AMPs.

4. Perform *in vitro* static biofilm assays to evaluate the antimicrobial activity of the functionalized catheters against the relevant bacteria strain *S.epidermidis*.
5. Study the stability of the functionalized surfaces with time, sterilization and under the pressure of a flow mimicking the real conditions using a dynamic model.
6. Perform an *in vivo* test with functionalized catheters in a rabbit model.

Part of the results of this chapter are included in the manuscript "Highly Stable Surface Coating of Thermoplastic Polyurethane Catheters with Tailored Recombinant Multidomain Protein -Towards In Vivo Infection Prevention" which will be soon submitted for publication.

4.3. Functionalization of the discs with the new multidomain protein

HDP production has traditionally been carried out using chemical synthesis, although recombinant production has been shown to be an alternative that allows creating these peptides through a scalable and cost-effective technique, without constraints in peptide length. HDPs must, however, be linked to a carrier protein when produced in recombinant hosts in order to shield the peptide from host proteases and mask any possible harmful effects on the producer cell.[32] However, the synthesis of a strong antimicrobial protein was possible by combining several functional HDP-based domains in a single polypeptide, which did not affect the viability of the recombinant host or need the use of protein carriers.[33]

Following this strategy, our collaborators from IRTA have synthetized the new multidomain protein D5L37βD3, which has been anchored to the TPU discs and medical grade catheters via the same procedure described in chapter 3 (Figure 4.3).

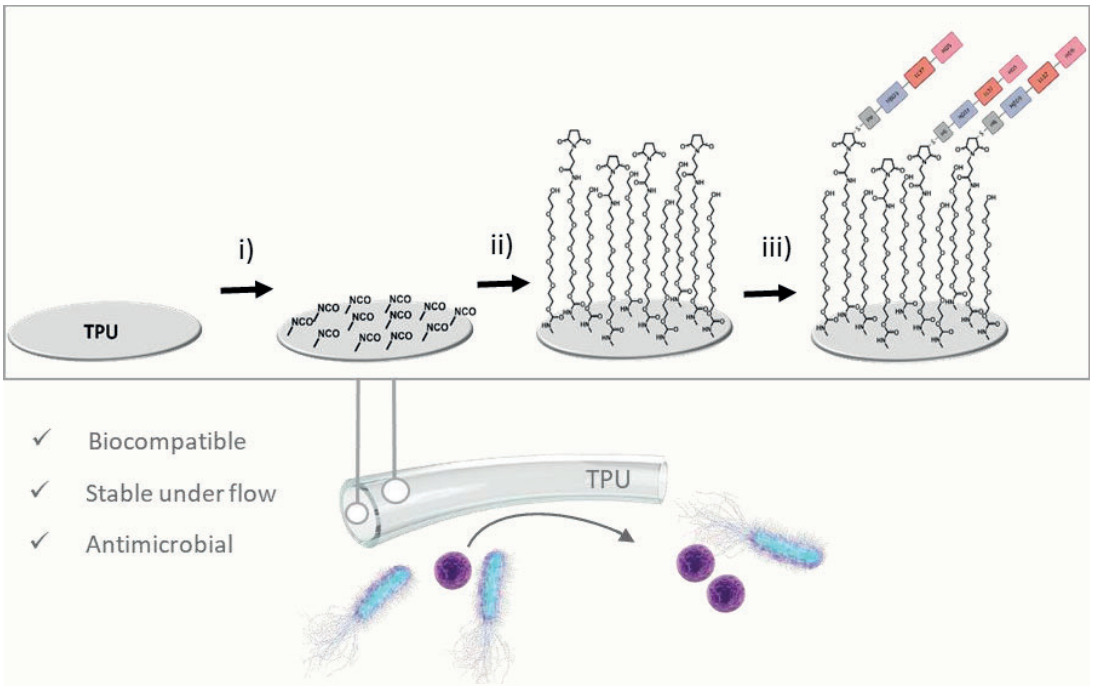


Figure 4.3. General strategy used for the chemical activation and immobilization of D5L37bD3 on TPU via 3 steps reaction: i) activation of the TPU surface with hexamethylene diisocyanate (HDI); ii) grafting of different PEG molecules onto the TPU surface and iii) click reaction with the ARMP through a Michael addition reaction.

4.4. Biocompatibility of the functionalized surfaces

To move towards the use of our functionalization strategy to coat catheters for *in vivo* experiments, first we studied the biocompatibility of the TPU surfaces functionalized with the novel ARMP (D5L37βD3), which is anchored to the PEG based SAMs. To perform the cell viability tests, we chose peripheral blood mononuclear cells (PBMCs) since in the final application, the intravascular catheters, will be in contact with blood. A dead/alive test was done with propidium iodide.

As shown in figure 4.4, the control positive, which are cells in solution, and the cells in contact with the TPU disc present very low toxicity. Nevertheless, the functionalized TPU-PEG substrate using dibutyltin dilaurate (DD) as a catalyst presents high toxicity, as reported before for Tin catalysts.[34] To reduce it, the catalyst has been changed to a greener one called bismuth (Bi) neodecanoate ($Bi(OCOC(CH_3)_2(CH_2)_5CH_3)_3$), which has recently gained significant attention as a potential alternative to toxic catalysts.[35] In this case, the toxicity was lowered. For the functionalization of the catheters, we will use this catalyst.

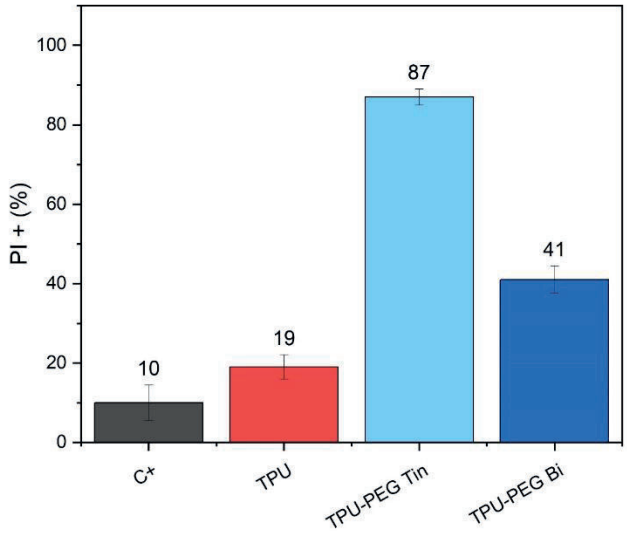


Figure 4.4. Viability test using propidium iodide of PBMCs seeded: in solution (black), on an unmodified TPU disc (red), on a TPU-PEG disc using the dibutyltin catalyst (light blue) and on a TPU-PEG disc (dark blue) using bismuth neodecanoate catalyst, which is more biocompatible.

4.5. Functionalization of medical grade TPU catheters

Catheters of 1.05 mm and 2 mm inner and outer diameter were acquired from Raumedic (Helmbrechts, Germany) and made from the same TPU (Tecothane 1085A) that we used previously for the discs. The discs have been used as a model to define the functionalization protocol.

Catheters were activated with HDI using the bismuth-based catalyst and functionalized with the same PEG molecules following the same protocol reported in chapter 3 but adapting the methodology due to the tube shape of the catheter. Moreover, the protein was changed from a single peptide to an ARMP, as previously explained. Briefly, 5 cm of the TPU catheters, which had a total length of 15 cm, were immersed in a dried toluene solution containing bismuth neodecanoate and HDI under Ar atmosphere for 1h at 70 °C. Then, the same length of the catheters was immersed in another dried toluene solution containing the different PEG molecules and left to react overnight at 45 °C. After that, the catheters were rinsed and dried in a vacuum oven again overnight at 45 °C. Finally, this 5 cm were immersed in a 10 μM solution of the protein in water with 0.01% of acetic acid. Then, we evaluated the effectiveness of the new ARMP (D5L37βD3) once anchored on the catheters to perform *in vitro* static and dynamic measurements as well as *in vivo* biofilm assays in a rabbit model.

First of all, after its functionalization, the TPU catheters (Cath-TPU) were characterized using the FTIR technique. In the TPU material, two distinct peaks corresponding to stretching vibrations can be seen at 3500 and 3000 cm^{-1} for NH and 1800 and 1640 cm^{-1} for C=O, respectively. As expected, PEG modification results in new peaks in the spectra

(Figure 4.5). In particular, we observe peaks at 842 cm^{-1} and 957 cm^{-1}, which are attributable to the bending vibrations of CH_2CH_2O and C-O-C, respectively, and at 1343 cm^{-1} and 1466 cm^{-1}, which are associated with the bending vibrations of CH_2. Thus, by comparing the functionalized discs (TPU-PEG) with the functionalized catheters (Cath-TPU-PEG), it can be confirmed the correct functionalization of the catheters both inside and outside.

Due to the morphology of the catheter, it has not been possible to perform the same characterization study done for the surfaces (discs) but based on the existence of the characteristic peaks assigned to the chemicals used for the TPU functionalization, the FTIR study suggests that the modification of TPU surfaces of the catheters was effective outside and also inside.

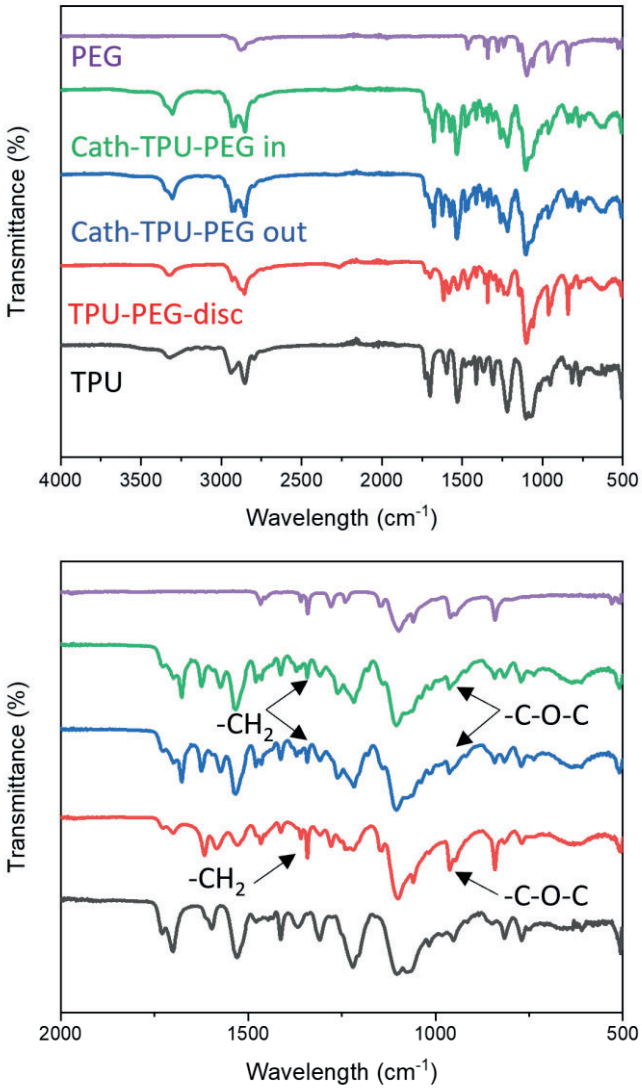


Figure 4.5. FTIR spectra of Cath-TPU (black), TPU-PEG (red), outside surface of the Cath-TPU-PEG (blue), inside surface of the Cath-TPU-PEG (green), PEG violet). The graph below is a zoom of the one above.

4.6. Biocompatibility of the functionalized TPU catheters

The biocompatibility of the functionalized catheters using the Bi-based catalyst was performed with a cell viability test using primary human PBMCs (Figure 4.6).

Both the unmodified and PEG-functionalized catheters with the Bi catalyst, do not present relevant toxicity to PBMCs. Moreover, although slightly more cytotoxic than untreated catheters, catheters impregnated with the protein are also suitable for use in *in vitro* and *in vivo* tests.

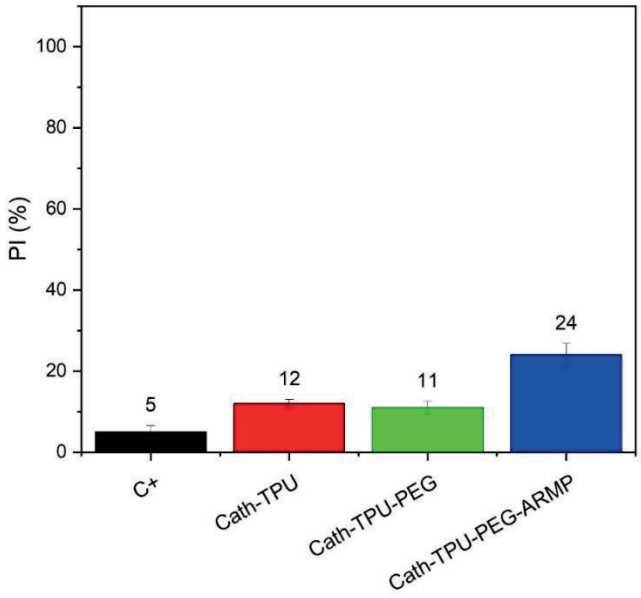


Figure 4.6. PBMCs (black), PBMCs with Cath-TPU (red), PBMCs with Cath-TPU-PEG (green), PBMCs with HD5LL37HβD3 multi-domain protein anchored to TPU catheter (Cath-TPU-ARMP) (blue).

4.7. *In vitro* biofilm assay: static and dynamic models

To evaluate the ability of the functionalized catheter to avoid the formation of biofilms, two types of *in vitro* studies were performed; the static one, using the same conditions as the ones performed with the TPU discs, explained in chapter 3, and the dynamic one, which was performed using a Modified Robbins Device (MRD).[36] This model will be used to mimic and study the influence of the fluid flow that the catheter will sense in the *in vivo* study.

4.7.1. *In vitro* static antibiofilm assay and stability study

The *in vitro* static model has been developed in collaboration with IRTA. Inhibition of the biofilm formation was studied using the Cath-TPU-ARMP and the Cath-TPU as a reference. To evaluate the effect of the sterilization process needed for the *in vivo* experiment on the functionalization stability, the assay has been done before and after

the treatment. For this process, we have used ethylene as it does not require high temperatures.

The bacteria strain chosen for this study is the Methicillin-resistant *Staphylococcus epidermidis* (MRSE), which is one of the most predominant bacteria related with NI related to intravascular catheters. Moreover, it is well characterized, and it has been shown to build mature and reproducible biofilms. Biofilms were grown in brain heart infusion broth medium with glucose and the suspension was incubated with the catheters at 37 °C overnight with a gentle rotation. During this time, a biofilm formed in the lumen and on the outside of the Cath-TPU. A crystal violet assay, which stains the bacteria and reads absorbance at 595 nm, has been performed to evaluate the biofilm inhibition capacity.

As seen in Figure 4.7A, there was a good inhibition of the biofilm formation by the Cath-TPU-ARMP. This confirms that the activity of the novel multidomain protein, anchored on the catheter, induces the enhancement of biofilm inhibition. Moreover, in Figure 4.7B, it is observed that, after the sterilization process, Cath-TPU- ARMP still inhibits the biofilm formation, confirming that the sterilization process is not affecting its activity.

Stability tests were carried out 3 months after sterilization of the catheters stored at 37 °C. In Figure 4.7C, it is observed that, there is no loss of the antibiofilm activity after the storage time. This result is remarkable because simulates the physiological temperature and the time that the catheter can be implanted without losing its antimicrobial activity. Additionally, it shows that it will allow reasonable shelf storage time of the manufactured catheters.

To sum up, the sterilization process does not negatively affect the antibiofilm properties (*in vitro*) of the protein-based catheters and they are stable and active (*in vitro*) even 3 months after production.

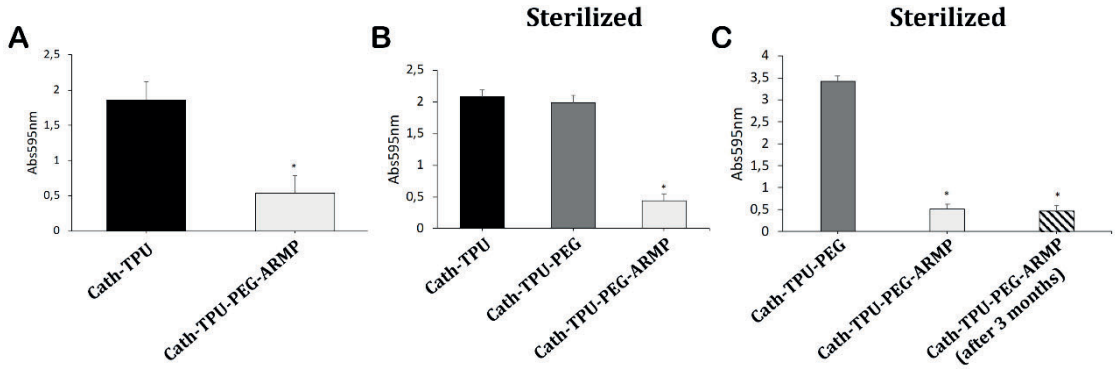


Figure 4.7. Determination of the inhibition of MRSE (gram-positive) biofilm formation by (A) Cath-TPU (black) and Cath-TPU-ARMP (white)($P = 0.0202$); (B) Cath-TPU (black), Cath-TPU-PEG (grey) and Cath-TPU-ARMP after the sterilization process by ethylene oxide (white) ($p<0.0001$) and (C) Cath-TPU-PEG (grey), Cath-TPU-ARMP (white) and Cath-TPU-ARMP after 3 months at 37 °C once sterilized by ethylene oxide (striped) ($p<0.0001$).

4.7.2. *In vitro* dynamic antibiofilm assay

To better mimic the flow inside the catheter, an *in vitro* dynamic model in the presence of a laminar flow of medium was evaluated using a modified Robbins device (MRD) (Figure 4.8) in collaboration with the group of Dr. O. Gasch form Hospital Parc Taulí (Sabadell, Spain).

Using this model, we assessed the HD5LL37HβD3 coating strength on the catheter. To perform the experiment, we first used different discs of TPU (coated and non-coated), which were fixed on the bioreactor. The test was carried out with a 1 mL/min flow of 1% Muller Hinton medium at 37 °C for 24 hours.

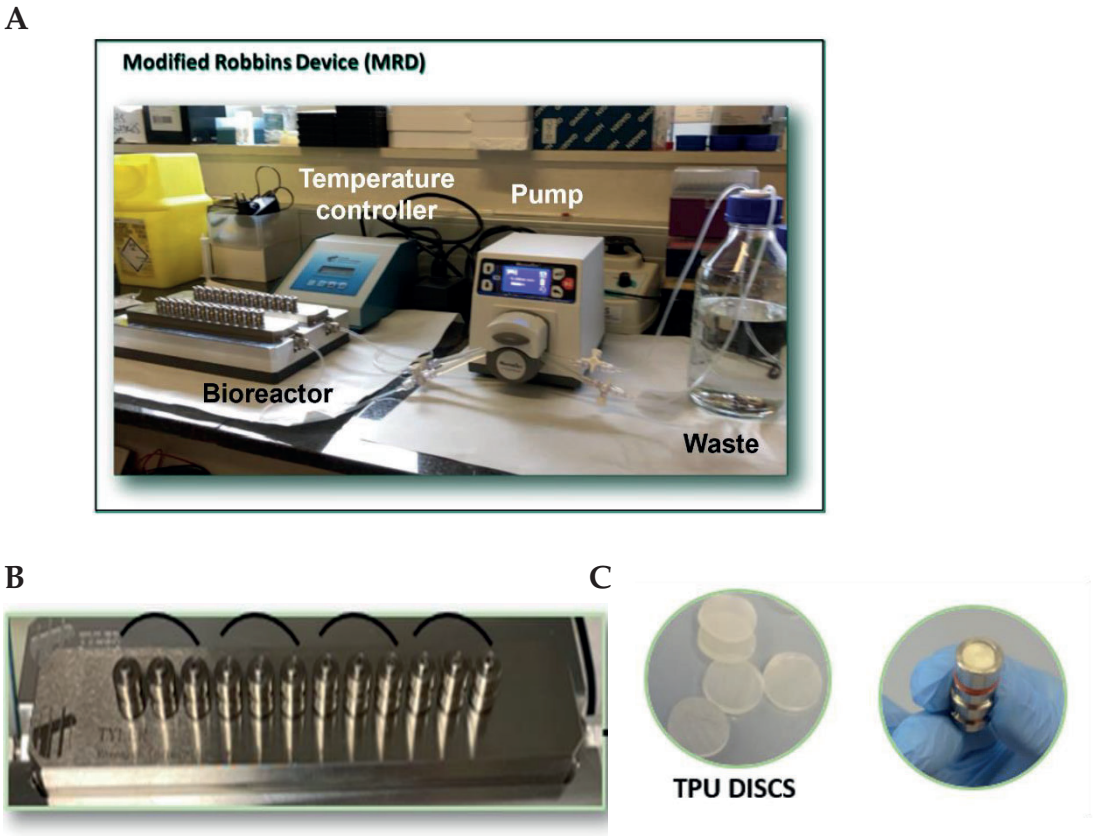


Figure 4.8. Scheme of the bioreactor used for the *in-vitro* dynamic model. A) Picture of the different parts of the bioreactor (Bioreactor, temperature controller, pump and waste); B) Inner part of the bioreactor showing the 12 positions where the 12 TPU discs with different coatings are attached; C) TPU discs used for the functionalization simulating the surface of the catheter; and cupons with the disc sticked on it.

Then, we characterized the discs chemically and biologically by XPS and a biofilm static assay, respectively. The XPS analysis of the nitrogen (N2p) atoms shows the same

intensity of the peaks before and after the *in vitro* dynamic experiment confirming the presence of the protein on the surface of the discs (Figure 4.9). Furthermore, to determine if the protein present on the surface was still active, an *in vitro* biofilm assay was performed. As shown in Table 4.1, there are two orders of magnitude of difference between the bacteria grown on the TPU--PEG-ARMP and the two controls (TPU and TPU-PEG). This result demonstrates the robustness of the protein anchoring strategy and the protein antibiofilm activity even after sterilization and the *in vitro* dynamic experiment with a flow of 1 mL/min.

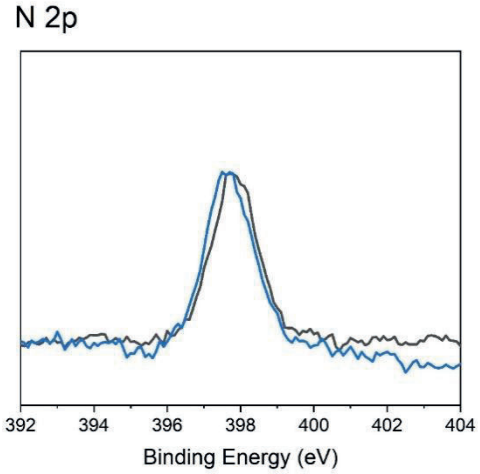


Figure 4.9. XPS spectra of N2p for TPU-ARMP (black) and TPU-ARMP after the *in vitro* dynamic experiment (blue).

TPU	TPU-PEG	TPU-PEG-ARMP
$3{,}5x10^5$ CFU/mL	$6{,}3x10^6$ CFU/mL	$5{,}0x10^4$ CFU/mL

Table 4.1. *In vitro* biofilm assay of the discs of TPU, TPU-PEG and TPU-PEG-ARMP after the *in vitro* dynamic experiment

4.8. *In vivo* biofilm assay: rabbit model

Once evaluated the robustness of the antibiofilm activity of the HD5LL37HβD3 anchoring to the TPU surface, we evaluated its ability to avoid biofilm formation *in vivo*, in collaboration with Dr. J. M Miró from Hospital Clínic (Barcelona, Spain). For these experiments, we used functionalized and sterilized catheters and an *in vivo* model of rabbit catheter infection caused by MRSE. The efficacy of the coated catheter to prevent infection was compared with that of commercially available TPU catheters which are impregnated with rifampicin and miconazole antibiotics. The concentration of MRSE inoculum used to infect the rabbits had been previously optimized in order to be sure that the non-treated catheters that we use as a control were infected, getting $5\text{-}8{\cdot}10^5$ CFUs/mL, which are very high values of bacterial concentration. The catheters were implanted in the right internal jugular vein of the rabbit and the rabbits were inoculated with the previously determined MRSE concentration. After 4 days, the catheters were

extracted, and the biofilm production was analyzed with a Maki quantitative method and with a semi-quantitative culture by sonication of the extracted catheters.

As it is observed in Table 4.2, the catheters functionalized with HD5LL37HβD3 (Cath-TPU-ARMP) even slightly decrease, did not prevent the formation of biofilms, having bacterial counts similar to the non-functionalized catheter (Cath-TPU). In the group of commercial catheters impregnated with antibiotics that were used as a reference, no biofilm was formed.

Study groups*	Maki semi-quantitative method**	Quantitative cultures (Median (IQR) of log CFU/mL)
Cath-TPU	Positive	4.9 (4.2-5.6)
Cath-TPU-PEG	Positive	5.6 (5.4-5.9)
Cath-TPU-ARMP	Positive	4.5 (4.1-5.6)[a]
Rifampicin-Micronazol impregnated catheter©	Negative	0(0-0)[a]
*n = 10 animals/group; **Positive > 15 CFU/plate; negative = 0 CFU/plate; [a]P<0.0001		

Table 4.2. In vivo Maki semi-quantitative method and quantitative cultures results for the unmodified catheters (Cath-TPU), catheters modified with a SAM of PEG (Cath-TPU-PEG), catheters modified with the AMP (Cath-TPU-ARMP) and commercial catheters impregnated with antibiotics.

Regarding the almost no activity of the ARMP functionalized catheters in the *in vivo* assays, there can be different explanations. First, the inoculum used might have been too high to appreciate differences. In view of these results, we hypothesize that the proposed coating could be primarily utilized to prevent infection, rather than treating it once it has already established. Additionally, the complex *in vivo* environment of the vascular catheter could be passivating the functional protein through a protein corona effect reducing its activity. In the future, the group will develop new strategies to improve the accessibility (protection to avoid passivation) of the proteins anchored to the surfaces to biofilm-forming bacteria.

4.9. Summary and future perspectives

First of all, it has been optimized the protocol of functionalization of TPU surfaces changing the DD catalyst to the bismuth neodecanoate, which increased the biocompatibility of the coating. Then, the procedure of functionalization has been modified passing from the functionalization of a disc to the inner and outer surface of a real catheter tube. The different shape of the TPU material implied the design of specific small equipment for the incubations of the tubes and optimization of the protocol with the new set-up. Finally, the functionalization of catheters was confirmed through FTIR

characterization, and its toxicity has been studied via a propidium iodide viability test using primary human PBMCs with favourable results.

In an *in vitro* static model, the functionalized catheters inhibited the biofilm formation of the MRSE strain, one of the most predominant bacteria related with NI in intravascular catheters, before and after the sterilization process by ethylene oxide and even after 3 months of storage at 37 °C, which is a promising result for their potential translation to the clinics. Furthermore, the results obtained in the *in vitro* dynamic model confirm the strength of the ARMP anchoring after pressure flow which is an advantage considering its real medical *in vivo* application. Nevertheless, the *in vivo* rabbit model requires further optimization and validation. We have identified different possibilities of the inactivity of the functionalized catheters in real environments which will be the focus of future research.

In any case, it has been developed a novel and stable catheter inner and outer coating strategy alternative to silver and antibiotics to be used for prevention of infection using ARMPs and a clickable strategy. These results open a pathway of research to assess these and other peptides anchoring to MD surfaces, such as pacemakers, orthopaedic prosthesis, etc. as an interesting and promising alternative to fight against NI.

This work has been done in the framework of the Marató project (project number 201812-30-31-32-33) in collaboration with IRTA, Hospital Parc Taulí and Hospital Clínic de Barcelona.

4.10. References

1. Almeida HA, Ruben RB. Medical Devices: from Design to Production. *AIME*. 2017;9(9):1687814017729895. doi:10.1177/1687814017729895
2. Bitkina OVl, Kim HK, Park J. Usability and User Experience of Medical Devices: An Overview of the Current State, Analysis Methodologies, and Future Challenges. *Int J Ind Ergon*. 2020;76:102932. doi:https://doi.org/10.1016/j.ergon.2020.102932
3. Treter J, Macedo A. Catheters: A Suitable Surface for Biofilm Formation. *Sci Microb Pathog Commun Curr Res Technol Adv*. Published online January 1, 2011.
4. Maitz MF. Applications of Synthetic Polymers in Clinical Medicine. *Biosurf and Biotribol*. 2015;1(3):161-176. doi:https://doi.org/10.1016/j.bsbt.2015.08.002
5. Oleksy M, Dynarowicz K, Aebisher D. Advances in Biodegradable Polymers and Biomaterials for Medical Applications - A Review. *Mol*. 2023;28(17). doi:10.3390/molecules28176213
6. Leonidou L, Gogos CA. Catheter-related Bloodstream Infections: Catheter Management According to Pathogen. *Int J Antimicrob Agents*. 2010;36:S26-S32. doi:https://doi.org/10.1016/j.ijantimicag.2010.11.004
7. Meddings J, Chopra V, Saint S. *Preventing Hospital Infections: Real-World Problems, Realistic Solutions*.; 2021. doi:10.1093/med/9780197509159.001.0001
8. Letica-Kriegel AS, Salmasian H, Vawdrey DK, et al. Identifying the Risk Factors for Catheter-associated Urinary Tract Infections: a Large Cross-sectional Study of Six Hospitals. *BMJ Open*. 2019;9(2):e022137. doi:10.1136/bmjopen-2018-022137
9. Medina M, Castillo-Pino E. An Introduction to the Epidemiology and Burden of Urinary Tract Infections. *TAU*. 2019;11:1756287219832172-1756287219832172. doi:10.1177/1756287219832172
10. Shuman EK, Chenoweth CE. Urinary Catheter-Associated Infections. *Infect Dis Clin North Am*. 2018;32(4):885-897. doi:https://doi.org/10.1016/j.idc.2018.07.002
11. Chenoweth CE, Saint S. Urinary Tract Infections. *Infect Dis Clin North Am*. 2016;30(4):869-885. doi:https://doi.org/10.1016/j.idc.2016.07.007
12. Eggimann P, Sax H, Pittet D. Catheter-related Infections. *Microbes and Infect*. 2004;6(11):1033-1042. doi:https://doi.org/10.1016/j.micinf.2004.05.018
13. Henriques P, Ferreira M, Gonçalves I. Devices to Fight Catheter-related Infections. *Biomec*. 2023;29. doi:10.5821/sibb.29.1.10917
14. Trautner BW, Darouiche RO. Catheter-Associated Infections: Pathogenesis Affects Prevention. *Arch Intern Med*. 2004;164(8):842-850. doi:10.1001/archinte.164.8.842
15. Trautner BW, Darouiche RO. Role of Biofilm in Catheter-Associated Urinary Tract Infection. *Am J Infect Control*. 2004;32(3):177-183. doi:https://doi.org/10.1016/j.ajic.2003.08.005

16. Bilal Aslam Wei Wang MIAMKSMMHRMANRFAMAAMUQMKFS, Baloch Z. Antibiotic resistance: a rundown of a global crisis. *Infect Drug Resist*. 2018;11:1645-1658. doi:10.2147/IDR.S173867

17. Van Boeckel TP, Pires J, Silvester R, et al. Global Trends in Antimicrobial Resistance in Animals in Low- and Middle-Income Countries. *Sci*. 2019;365(6459):eaaw1944. doi:10.1126/science.aaw1944

18. Uneputty A, Dávila-Lezama A, Garibo D, et al. Strategies Applied to Modify Structured and Smooth Surfaces: A Step Closer to Reduce Bacterial Adhesion and Biofilm Formation. *Coll and Int Sci Comm*. 2022;46:100560. doi:https://doi.org/10.1016/j.colcom.2021.100560

19. Teixeira-Santos R, Gomes LC, Mergulhão FJM. Recent Advances in Antimicrobial Surfaces for Urinary Catheters. *Curr Opin Biomed Eng*. 2022;22:100394. doi:https://doi.org/10.1016/j.cobme.2022.100394

20. Ong KS, Mawang CI, Daniel-Jambun D, Lim YY, Lee SM. Current Anti-Biofilm Strategies and Potential of Antioxidants in Biofilm Control. *Expert Rev Anti Infect Ther*. 2018;16(11):855-864. doi:10.1080/14787210.2018.1535898

21. Imani SM, Ladouceur L, Marshall T, Maclachlan R, Soleymani L, Didar TF. Antimicrobial Nanomaterials and Coatings: Current Mechanisms and Future Perspectives to Control the Spread of Viruses Including SARS-CoV-2. *ACS Nano*. 2020;14(10):12341-12369. doi:10.1021/acsnano.0c05937

22. Kearney L, Francis E, Clover A. New Technologies in Global Burn Care - a Review of Recent Advances. *Int J Burns Trauma*. 2018;8:77-87.

23. Brouillard C, Bursztejn AC, Latarche C, et al. Silver Absorption and Toxicity Evaluation of Silver Wound Dressings in 40 Patients with Chronic Eounds. *JEADV*. 2018;32(12):2295-2299. doi:https://doi.org/10.1111/jdv.15055

24. Panáček A, Kvítek L, Smékalová M, et al. Bacterial Resistance to Silver Nanoparticles and How to Overcome It. *Nat Nanotechnol*. 2018;13(1):65-71. doi:10.1038/s41565-017-0013-y

25. Siddique MH, Aslam B, Imran M, et al. Effect of Silver Nanoparticles on Biofilm Formation and EPS Production of Multidrug-Resistant Klebsiella pneumoniae. *Biomed Res Int*. 2020;2020. doi:10.1155/2020/6398165

26. Gifre-Renom L, Ugarte Berzal E, Martens E, et al. Recombinant Protein-Based Nanoparticles: Elucidating Their Inflammatory Effects In Vivo and Their Potential as a New Therapeutic Format. *Pharmaceutics*. 2020;12:450. doi:10.3390/pharmaceutics12050450

27. Roca R, Lisowski L, Aris A, Garcia-Fruitos E. The Future of Recombinant Host Defense Peptides. *Microb Cell Fact*. 2022;21. doi:10.1186/s12934-022-01991-2

28. Méndez-Samperio P. Peptidomimetics as a New Generation of Antimicrobial Agents: Current Progress. *Infect Drug Resist*. 2014;7:229-237. https://api.semanticscholar.org/CorpusID:3288783

29. Wilson SS, Wiens ME, Smith JG. Antiviral Mechanisms of Human Defensins. *J Mol Biol*. 2013;425(24):4965-4980. doi:https://doi.org/10.1016/j.jmb.2013.09.038

30. Peschel A, Sahl H. Peschel, A. & Sahl, H.G. The co-evolution of host cationic antimicrobial peptides and microbial resistance. Nat. Rev. Microbiol. 4, 529-536. *Nat Rev Microbiol*. 2006;4:529-536. doi:10.1038/nrmicro1441

31. Ehlers MM, Strasheim W, Lowe M, Ueckermann V, Kock MM. Molecular Epidemiology of Staphylococcus epidermidis Implicated in Catheter-Related Bloodstream Infections at an Academic Hospital in Pretoria, South Africa. *Front Microbiol*. 2018;9. doi:10.3389/fmicb.2018.00417

32. López-Cano A, Ferrer-Miralles N, Sánchez J, et al. A Novel Generation of Tailored Antimicrobial Drugs Based on Recombinant Multidomain Proteins. *Pharmaceutics*. 2023;15(4). doi:10.3390/pharmaceutics15041068

33. Roca-Pinilla R, López-Cano A, Saubi C, Garcia-Fruitós E, Arís A. A new generation of recombinant polypeptides combines multiple protein domains for effective antimicrobial activity. *Microb Cell Fact*. 2020;19(1):122. doi:10.1186/s12934-020-01380-7

34. Schellekens Y, Van Trimpont B, Goelen PJ, et al. Tin-free Catalysts for the Production of Aliphatic Thermoplastic Polyurethanes. *Green Chem*. 2014;16(9):4401-4407. doi:10.1039/C4GC00873A

35. Chen Q, Zhang Z, Qi Y. Effect of Bismuth Neodecanoate Content on Properties of Silicone Tie-Coatings. *Int J of Adhes Adhes*. 2024;128:103532. doi:https://doi.org/10.1016/j.ijadhadh.2023.103532

36. Coenye T, Prijck K, Wever B, Nelis HJ. Use of the Modified Robbins Device to Study the In Vitro Biofilm Removal Efficacy of NitrAdine, a Novel Disinfecting Formula for the Mantainance of Oral Medical Devices. *J Appl Microbiol*. 2008;105:733-740. doi:10.1111/j.1365-2672.2008.03784.x

Manuscript #1

Title: Stable Surface Coating of Thermoplastic Polyurethane Catheters with Tailored Recombinant Multidomain Protein -Towards In Vivo Infection Prevention

Authors: Xavier Rodríguez Rodríguez, Adrià López-Cano, Karla Mayolo-Deloisa, Inmaculada Gómez-Sánchez, Paula Bierge, Oscar Q Pich, Nora Ventosa, Cristina García-de-la-Maria, José M. Miró, Oriol Gasch, Jaume Veciana, Judith Guasch, Elena Garcia-Fruitós, Anna Arís, Imma Ratera and the FUNCATH investigators

Publication: *In preparation*

Stable Surface Coating of Thermoplastic Polyurethane Catheters with Tailored Recombinant Multidomain Protein -Towards *In Vivo* Infection Prevention

Xavier Rodríguez Rodríguez,[1,2] Adrià López-Cano,[3] Karla Mayolo-Deloisa,[1,4] Inmaculada Gómez-Sánchez,[5,6] Paula Bierge,[5,6] Oscar Q Pich,[5,6] Nora Ventosa,[1,2] Cristina García-de-la-Maria,[6] José M. Miró,[6,7] Oriol Gasch,[8] Jaume Veciana,[1,2] Judith Guasch,[1,2,9], Elena Garcia-Fruitós,[3] Anna Arís,[3] Imma Ratera[1,2] and the FUNCATH investigators[10]

[1] Institute of Materials Science of Barcelona (ICMAB-CSIC), Campus UAB, Bellaterra, 08193, Spain.

[2] Networking Research Center on Bioengineering, Biomaterials and Nanomedicine (CIBER-BBN), Campus UAB, Bellaterra, 08193, Spain.

[3] IRTA, Torre Marimon, Ctra C-59, Km 12,1, 08140 Caldes de Montbui, Barcelona, Spain.

[4] Tecnologico de Monterrey, Institute for Obesity Research, School of Engineering and Sciences, Av. Eugenio Garza Sada 2001, 64849 Monterrey, Nuevo León, México.

[5] Laboratori de Recerca en Microbiologia i Malalties Infeccioses, Hospital Universitari Parc Taulí, Institut d'Investigació i Innovació Parc Taulí (I3PT-CERCA), Universitat Autònoma de Barcelona, 08208, Sabadell, Spain.

[6] Infectious Diseases Service. Hospital Clinic-FCRB-IDIBAPS. Universitat de Barcelona, Barcelona, Spain.

[7] Infectious Diseases Biomedical Research Networking Center (CIBERINFEC), Instituto de Salud Carlos III, Madrid, Spain.

[8] Servei de Malalties Infeccioses, Hospital Universitari Parc Taulí, Institut d'Investigació i Innovació Parc Taulí (I3PT-CERCA), Universitat Autònoma de Barcelona, 08208, Sabadell (Spain).

[9] Dynamic Biomimetics for Cancer Immunotherapy, Max Planck Partner Group, ICMAB-CSIC, Campus UAB, Bellaterra, 08193, Spain.

[10] FUNCATH Investigators are indicated in the Appendix.

ABSTRACT: Managing the formation of bacterial biofilms on thermoplastic polyurethane (TPU) bloodstream (central venous) catheters is a critical focus to prevent associated infections that occurs both internally and externally. Our aim was to develop a catheter coating ready for *in vivo* central venous application. For this we proposed to i) find an alternative to the commonly reported UV activation of the TPU that do not allow the activation of the inner side of the catheter, and use a strategy that allow the modification of the inner and outer surface of the TPU catheter; ii) confer to the surfaces broad spectrum antibiofilm properties, iii) create stable surfaces with enduring antibiofilm properties even after sterilization, allowing long shelf life, iv) biocompatibility and, iv) ability of withstanding the pressure of a flow simulating the bloodstream around it. Thus, in this investigation we explored the potential to chemically modify the inner and outer surface of the TPU catheter firstly, activating TPU with hexamethylene diisocyanate (HDI) using a biocompatible catalyst, and secondly, facilitating an interfacial reaction with polyethylene glycol (PEG) derivatives. Then, we have anchored an antimicrobial recombinant multidomain protein (ARMP) which combines different Host Defense Peptides (HDPs) in a single polypeptide, through a straightforward bioclickable reaction between the PEG-maleimide terminated self-assembled monolayers (SAMs) on the TPU and the cysteine (-thiol) terminated ARMP.

The functionalized catheters were characterized by FTR-IR and XPS and its biocompatibility was analysed using Peripheral Blood Mononuclear Cells (PBMCs) and a propidium iodide (PI) cell viability test. The antibiofilm activity of functionalized polyurethane surfaces was evaluated against methicillin-resistant *Staphylococcus epidermidis* (MRSE). Furthermore, stability of the recombinant multidomain protein with antimicrobial activity was assessed under conditions that mimic the flow and pressure encountered by real catheters using an *in vitro* dynamic model.

In summary, recently reported ARMP were effectively attached to the outer and also to the inner surface of TPU catheters, exhibiting a reduction of MRSE biofilm formation, which is one of the most predominant bacteria related with nosocomial infections in intravascular catheters. Moreover, the functionalized catheters not only proved antibiofilm activity but also cytocompatibility with human blood cells and high stability after pressure flow and also after storage during 3 months at 37ºC which is an advantage considering its real medical *in vivo* application.

1. Introduction

Medical Devices (MDs) have played a transformative role in revolutionizing healthcare, contributing to improved diagnostics, treatments, and patient outcomes. Presently, there is a pressing demand for antimicrobial and antibiofilm surfaces to combat bacterial colonization on MDs and enhance patient care standards. This global concern stems from the escalating use of medical devices over the years, leading to a rise in healthcare-associated infections (HAIs).[1] HAIs are directly linked to increased morbidity, mortality, and substantial clinical expenses.[2,3] Among them, bloodstream catheter infections, primarily caused by biofilm formation, are particularly prevalent, accounting for 43.4% of cases.[4] Biofilm, a complex bacterial structure encased in a self-produced extracellular polymeric substance, shields pathogens from mechanical stress and immune responses, rendering them more resilient to antibiotics compared to their planktonic state.[5,6] Thermoplastic Polyurethane (TPU) have gained significant attention in medical stent and catheter production due to their moldability, cost-effectiveness, biocompatibility, robust mechanical properties, surface characteristics and chemical inertness. However, once implanted in the human body, indwelling TPU catheters provide a conducive environment for bacterial adhesion and colonization on its inside and outside surface, if no antibiotics are used. Hence, there is an urgent imperative to prevent biofilm formation on TPU surfaces to mitigate subsequent infections because when biofilms are formed not only provide a conducive environment for bacterial growth but also make it challenging for antibiotics and the immune system to eliminate the infection. Biofilm formation is considered the underlying reason responsible for the lack of success of antimicrobial agents. Moreover, the growing emergence of antibiotic-resistant microorganisms due to the consumption of antibiotics (67% by 2030) makes the treatment of infections really a challenge to overcome.[7]

To prevent catheter-related infections, some coatings have been developed to reduce bacterial adhesion by altering the physicochemical properties of the substrate.[8] Other strategies have been reported, including antimicrobial surface coating via simple adsorption, facilitated by weak interactions, which is the easiest and most common method, enabling rapid release of active compounds and also covalent coating using UV activation of the chemical inert outer surface of the TPU catheters. However, the formation of bacterial biofilms on TPU bloodstream (central venous) catheters is critical

and it occurs both internally and externally. For more enduring functionality, that can support the flow of the stream, covalent bonding through surface functionalization offers greater stability but due to its chemically inert properties, only few antimicrobial agents have been covalently bonded to TPU surfaces.[9,10]

Silver-based products belong to the most used local treatments for active coatings to prevent catheter-related infections,[11] but it is hampered by costs, environmental concerns, and safety considerations.[12,13] Moreover, its use is limited due to its toxicity and silver-resistant bacteria, able to avoid silver ions by ion-pumps and biofilms formation have been repeatedly observed.[14,15] Therefore, considering the global health threat of antibiotic resistant microorganisms, there is an urgent need to develop new cost-efficient antimicrobial coatings for catheters with a superior biocompatibility and improved antimicrobial activity.

Among new antimicrobial molecules, we have reported the use of antimicrobial peptides (AMPs) synthesized by the innate immunity known as Host Defense Peptides (HDPs), which arises as an interesting alternative.[16,17] These peptides are cationic amphiphilic peptides able to kill bacteria through the disruption of their basic cell wall structures.[18] They present broad-spectrum microbicide activity against Gram-negative and Gram-positive bacteria, including those resistant to antibiotics.[19] Importantly, the development of bacterial resistance against HDPs is expected to be rare, because they act rapidly against integral components of the bacterial structure.[20]

Recently, we have developed a new generation of tailored antimicrobials, using a rational design of antimicrobial recombinant multidomain proteins (ARMP) based on the combination of different HDPs in a single polypeptide which have proven to be broad-spectrum antimicrobials.[21] Therefore, these peptides could be useful to fight infections such as the ones related to *Staphylococcus epidermidis*, which is one of the most prevalent pathogens implicated in catheter related infections.[22] Additionally, surface biofunctionalization strategies developed recently[23–28] have been employed to covalently attach these innovative recombinant AMPs onto gold model surfaces, resulting in highly effective antibiofilm surfaces.[29] But, up to now there are no reports on immobilizing ARMPs based on HDP on catheter surfaces to inhibit biofilm formation.

As mentioned, TPU is one of the polymers mostly used for MDs, especially catheters. It is very convenient for its mechanical and inert properties but on the other side, its inert surface is very challenging to be modified in a robust and stable manner. Recently, we have reported a protocol of surface activation and covalent coating of TPU discs and

catheters with polyethylene glycol (PEG) based SAMs of HDPs through a click reaction, with good antibiofilm properties against different Gram-negative and Gram-positive bacteria strains. The conjugation of AMPs with PEG based molecular materials that exclude the bacterial adhesion is found to present good synergy and excellent antibiofilm properties being an interesting and promising alternative to fight against HAIs.

But up to now, there are no reports about the inhibition of biofilm formation on the inner and outer surface of TPU catheters using broad spectrum ARMPs based on HDPs as alternative to silver or antibiotics.

Here, as alternative to silver and antibiotics we have developed a strategy to chemically modify the inner and outer surface of TPU to obtain medical grade TPU catheters that are biocompatible, present high stability with time and under a bloodstream flow and prevent infection, using ARMPs with a bioclickable strategy and a novel biocompatible catalyst. Specifically, we have activated and coated catheters with a mixture of pegylated SAMs and ARMPs. A cytocompatibility test was done using human blood cells and a stability study was assessed *in vitro* using a Modified Robbins Device (MRD). Specifically, it was measured the antibiofilm activity of the ARMP functionalized surfaces against methicillin-resistant *S. epidermidis* (MRSE) after incubation in the MRD. This bioreactor represents an *in-vitro* dynamic model that mimics the flow pressure of serum found *in-vivo* in real catheters, showing to be very promising considering the medical application of our antimicrobial strategy.

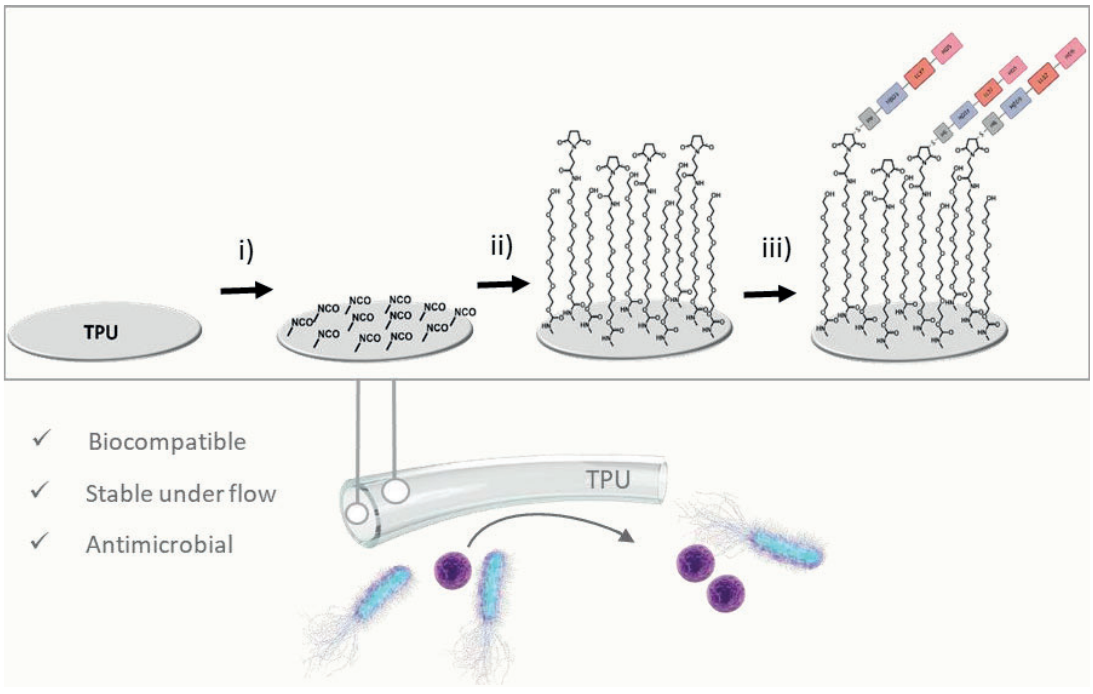


Figure 1. Scheme of the ARMP functionalization of the catheters via 3 steps reaction: i) activation of the TPU surface with hexamethylene diisocyanate (HDI); ii) grafting of different PEG molecules onto the TPU surface and iii) click reaction with the ARMP through a Michael addition reaction.

2. Materials and Methods

2.1. Materials

The dibutyltin dilaurate 95% (DD), bismuth neodecanoate, hexamethylene diisocyanate 98% (HDI), poly(ethylene) glycol 4000 (PEG4K) and poly(ethylene) glycol maleimide (Mal-PEG5K-OH) were purchased from Merk. Thermoplastic Polyurethane (TPU) beads were ordered from Lubrizol (Tecothane 2085A-B20 and Tecothane 1085A). Toluene was ordered from Chem-Lab. Medical grate catheters of 1.05 mm and 2 mm inner and outer diameter were acquired from Raumedic (Helmbrechts, Germany) and made from the same TPU (Tecothane 1085A) used previously for the discs.

2.2. Antimicrobial recombinant multidomain protein (ARMP) production

The ARMP D5L37βD3, which was previously designed,[21] was used. For that, *Escherichia coli* BL21 (DE3) carrying pET22b-D5L37βD3 plasmid was used for recombinant protein production. Cultures were grown in 2 L shake flasks at 37ºC and 250 rpm with 500 mL LB broth with ampicillin at 100 μg/mL. An overnight (O/N) culture was used as inoculum in fresh LB medium, starting at OD600= 0.05. Recombinant protein expression was induced by 1 mM IPTG when cultures reached an OD600 = 0.4–0.6. After 3 h of production, the whole culture was harvested (6,000 *x g*, 15 min, 4ºC). Pellets from 500 mL were resuspended in 30 mL of binding buffer (500 mM NaCl, 20 mM Tris, 20 mM imidazole) with EDTA-free protease inhibitor (Roche). Bacteria were sonicated (4 cycles, 5 min (0.5 s on, 0.5 s off) at 10% amplitude (Branson SFX550 Sonifier) and centrifugated (15,000 *x g*, 45 min, 4ºC), collecting the supernatant. Supernatant was filtered using a pore diameter of 0.2 μm and purified by Immobilized Metal Affinity Chromatography (IMAC) in an ÄKTA Start (GE Healthcare) using 1 mL HiTrap chelating HP columns (GE Healthcare), following established protocols.[30]

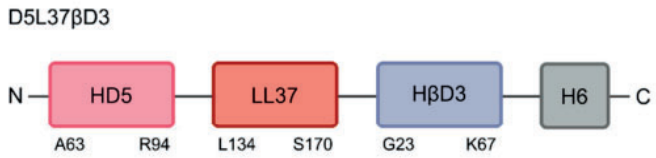


Figure 2. Schematic representation of D5L37βD3 which combines human alfa defensin 5 (HD5), cathelicidin LL37 and human beta defensin 3 (HβD3) in a single polypeptide. The construct also has an H6-tag at C-terminal for protein purification purposes.

2.3. Functionalization of the inner and outside surface of TPU catheters with pegylated mixed SAMs and maleimide termination

The surface modification of the medical grade TPU catheters was done in a two-step's procedure. Both steps were carried out under argon atmosphere, using dried toluene as solvent (and swelling agent) and bismuth neodecanoate as biocompatible catalyst. In the first step, the 5 cm of TPU catheters were functionalized with HDI. TPU catheters were immersed into 40 mL of toluene solution containing 5% (v/v) HDI and 0.25% (v/v) bismuth neodecanoate for 1h at 70 °C. Then, the catheters were washed with dried toluene for 30 min. In the second step, PEG4K and Mal-PEG5K-OH was grafted as a mixed self-assembly monolayer (SAM) onto the TPU surface by letting the hydroxyl groups reacts with the isocyanate ends groups of HDI. To do it, TPU catheters were immersed in a 10% (w/v) of PEG4K solution (or a mixed solution of 40% Mal-PEG5K-OH and PEG4K) in dried toluene inside a cylinder of Teflon with 4 mm diameter and 55 mm length and left to react overnight at 45°C. After that, the samples were washed to remove all the unreacted monomer with toluene, isopropyl alcohol and MilliQ water for 15 min each. The TPU catheters were finally dried in a vacuum oven at 45°C overnight. (see Figure 1)

2.4. Antimicrobial recombinant multidomain proteins (ARMP) anchoring on the prefunctionalized TPU medical grade catheters

ARMP were anchored via a bioclick reaction between the thiol of the cysteine group of the protein and the maleimide termination of the mixed SAM of the prefunctionalized catheters (see 4.3). Thus, catheters functionalized with a mixed SAM of PEG4K and Mal-PEG5K-OH, were immersed in 500 µL of a 10 µM ARMP solution inside a x mL cylindrical homemade Teflon reservoir (xx mm diameter, x mm length) for 1 h at room temperature. With this procedure it was obtained successfully the desired mixed ARMP-PEG SAMs (Figure 1).

2.5. Sterilization method

It has been used the same sterilization process use in the hospital for *in vivo* application which is based on incubation at 55ºC for 1 h at a relative humidity between 40 and 80% in an ethylene oxide sterilizer. After this time, there is an aeration process of 12 h to desorb the ethylene oxide before the manipulation of the sterile catheter.

2. 6. Characterization techniques

Attenuated total reflectance Fourier transform infrared (ATR-FTIR) spectroscopy were obtained in a Spectrophotometer Jasco 4700, using an Attenuated Total Reflectance accessory. Resolution was 2 and the number of scans 32.

XPS measurements were performed at room temperature with a SPECS PHOIBOS 150 hemispherical analyzer (SPECS GmbH, Berlin, Germany)) in a base pressure of $5x10^{-10}$ mbar using monochromatic Al K alpha radiation (1486.74 eV) as excitation source operated at 300W. The energy resolution as measured by the FWHM of the Ag 3d5/2 peak for a sputtered silver foil was 0.62 eV. Charge neutralization was done through a flood gun. AFM characterization was performed using a Keysight 5100 AFM in tapping mode with an AppNano FORT tip in ambient conditions.

2.7. Biocompatibility study

PBMC purification

PBMCs were isolated from buffy coats obtained from adult donors provided by "Banc de Sang i Teixits" (Barcelona, Spain) after the approval of the research project by the "Ethics Committee on Animal and Human Experimentation" of the Autonomous University of Barcelona (Nr. CEEAH 4951). To summarize, PBMCs were separated by density gradient centrifugation from the peripheral blood using Ficoll-Plus-Paque (#70-1440-02; GE Healthcare, Chicago, IL, USA) or Lymphoprep (#07811; Stemcell Technologies, Vancouver, British Columbia, Canada). The interphase layer was collected and incubated with Red Blood Cell Lysis Buffer (#00-4333-57; eBioscience, San Diego, CA, USA) to eliminate remaining red blood cells and washed twice with phosphate-buffered saline (PBS). Isolated PBMCs were counted and directly used or frozen down in heat-inactivated fetal bovine serum (FBS; #10270106, Gibco, Billings, MT, USA) supplemented with 10% dimethyl sulfoxide (#D2650; Merck, Rahway, NJ, USA).

Cell viability test

To measure the cell viability, a propidium iodide (PI) viability test was used. Cath-TPU, Cath-TPU-PEG and Cath-TPU-PEG-ARMP were incubated with 10^5 PBMCs for 5 days. As positive control, PBMCs were incubated in appropriate medium also for 5 days. Then they were stained with 0.5 µL of propidium iodide (1 mg/ml, Sigma-Aldrich) during 5 min at room temperature before the flow cytometry measurements were carried out by a CytoFLEX LX U3-V5-B3-Y5-R3-I0 Flow Cytometer which has 5 active lasers (355 nm, 405 nm, 488 nm, 561 nm, 638 nm) and 19 channels for fluorescence detection. The complete system is supplied with computer workstation, Lenovo ThinkCentre M720, Intel® Core™ i5-8500T @ 2.10GHz, with CytExpert Acquisition software, sheath and waste containers with harness.

2.8. *In vitro* static antibiofilm assay

To evaluate the performance of the TPU, TPU linked with PEG, and TPU with PEG-MAL and anchored ARMP, the selected bacteria (methicillin-resistant *Staphylococcus epidermidis* (MRSE)), were initially grown O/N in Brain heart infusion (BHI) medium in the presence of 0.5% glucose to promote biofilm formation. For this purpose, catheters were placed in a 50 mL Falcon tubes filled with MRSE bacterial culture and incubated O/N at 37°C with an oscillatory motion to facilitate biofilm formation on the catheter.

The following day, the culture medium in the Falcon tubes was removed by aspiration, and the catheters were washed with Ringer's solution to remove non-attached bacteria. The catheters were then placed in 15 mL of Ringer's solution and sonicated for 1 min at 45 kHz, followed by 1 min of cooling, and another 1-min sonication to effectively detach the biofilm. The tubes were then centrifuged for 10 min at 3,000 x *g* to pellet the biomass, and the supernatant was discarded.

The biomass was fixed by adding methanol for 15 min, after which the methanol was removed, and the tubes dried for 10 min at 37°C. The dried biofilm was stained with 0.1% crystal violet (CV) for 20 min. After staining, the CV was removed, and the stained biofilm was washed twice to remove excess CV. Finally, the CV was recovered for quantification by adding 100 µL of 70% ethanol and measuring the absorbance at OD600 using a spectrophotometer.

2.9. *In vitro* dynamic antibiofilm assay

To simulate the blood flow through a catheter as it would occur in a human body, an experiment was conducted using a Modified Robbins Device bioreactor (Tyler Research, Edmonton, Canada) designed to mimic the flow over circular TPU discs exposed to the lumen of the tube.

Circular sections, with or without adhered ARMP, were subjected to a flow (1ml/min) of 1% Muller-Hinton broth medium at 37ºC for 24h to study the stability of the coating determining whether the ARMP binding to the catheter remained stable over time.

After the flow exposure, the TPU discs were processed and stained according to the methodology described in Section 2.8, with the only variation being the use of a 48-well plate for bacterial growth. The subsequent processing, once the biofilm was formed on the TPU discs, followed the same procedure as previously described.

3. Results and discussion

3.1. Functionalization and characterization of the inner and outside surface of TPU catheters with ARMP

The previously reported activity of the ARMP D5L37βD3 against MRSE in planktonic growth, but also when forming biofilms,[21] led us to analyze the potential of this surface-anchored protein.

First, to move towards the use of functionalized catheters for *in vivo* experiments, we studied the biocompatibility of the used chemical strategy (see SI) using TPU discs functionalized with the PEG SAM using two different catalysts (see SI). To perform the cell viability tests, it was used human PBMCs since for the final application, intravascular catheters, will be in contact with blood. A dead/alive test was done with propidium iodide. As shown in Figure S2, the functionalized TPU-PEG substrate using dibutyltin dilaurate as a catalyst presents high toxicity which has already been reported for Tin catalysts and would not allow to use this strategy for in-vivo evaluation.[31] To increase the biocompatibility of the developed strategy, the catalyst used for the first activation step has been changed to a greener one called bismuth bismuyth neodecanoate (Figure S1) which has recently gained significant attention as a potential alternative to toxic catalysts.[32] As it is observed in Figure S2, the toxicity of the PEG-TPU discs has been lowered using the novel catalyst.

Once optimized the biocompatibility of the strategy used, the new multidomain protein, D5L37βD3, was anchored to the medical grade TPU catheters following the three-steps procedure. In the first step, the catheters were functionalized with HDI using the biocompatible catalyst, bismuyth neodecanoate. In the second step, PEG4K for the control SAMs (TPU-PEG) and 60% of PEG4k and 40% of Mal-PEG5K-OH, for the mixed SAMs (TPU-PEG-Mal), were grafted onto the TPU surface to obtain the functionalized TPU. The length of the maleimide tail was longer than the PEG one to increase the availability of the reactive unit towards the click reaction with the protein. Specifically, TPU catheters were immersed in the different PEG solutions in dried toluene and left to react O/N at 45°C letting the hydroxyl groups reacts with the isocyanate ends groups of the activated TPU surface. In the last step, the ARMP, D5L37βD3, was anchored to the prefunctionalized TPU surface via a click Diels-Alder reaction between the thiol of the terminal cysteine (C) group of the protein (Figure 2) and the maleimide terminated group of the mixed SAM (Figure 1).

The functionalized the TPU catheters were characterized using ATR-FTIR technique. In the TPU material, two distinct peaks corresponding to stretching vibrations can be seen at 3,500 and 3,000 cm^{-1} for NH and 1,800 and 1640 cm^{-1} for C=O, respectively. According to the spectra in Figure 2, a band at 2250 cm^{-1} may be seen in the X trace but not on the unmodified TPU. This outcome shows that the isocyanate molecules were successful in functionalizing the TPU. This peak definitely disappeared in the second step of the reaction, showing that the functionalization was successful once the isocyanate groups interacted with the PEG molecules. As expected, PEG modification results in new peaks in the spectra (Figure 2). In particular, we observe peaks at 842 cm^{-1} and 957 cm^{-1}, which are attributable to the bending vibrations of CH_2CH_2O and C-O-C, respectively, and at 1,343 cm^{-1} and 1,466 cm^{-1}, which are associated with the bending vibrations of CH_2 and CH_3. Thus, by comparing the functionalized discs (TPU-PEG) with the functionalized catheters (Cath-TPU-PEG), it can be confirmed the correct functionalization of the catheters both inside and outside. Based on the existence of the characteristic peaks the ATR-FTIR study shows that the modification of TPU surfaces of the catheters were effective both inside and outside (Figure 3).

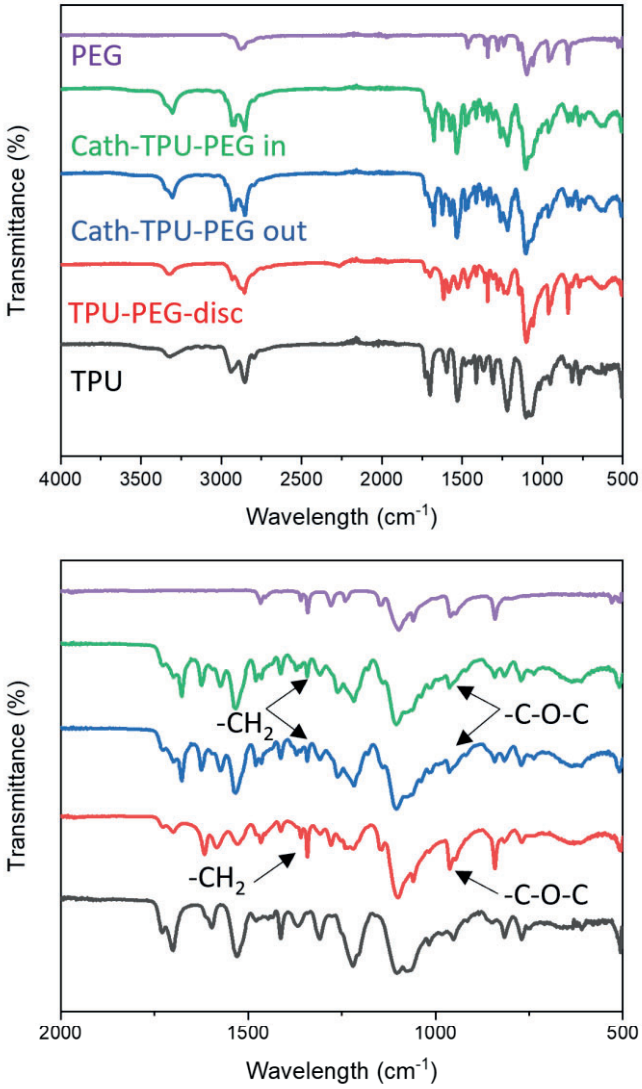


Figure 3. FTIR spectra were: (black) unmodified thermoplastic polyurethane (TPU) catheter, (red) functionalization of the TPU disc with a PEG4K self-assembled monolayer (SAM), (blue) functionalization of the outside of the TPU catheter with PEG SAM (TPU-PEG-Catheter-Out), (green) functionalization of the inside of the TPU catheter with a PEG4K SAM (violet) PEG4K.

3.2 PBMCs biocompatibility study

The biocompatibility study of the Cath-TPU-PEG-ARMP catheters obtained using the biocompatible catalyst, was demonstrated performing a cell viability tests with PBMCs and a dead/alive test with PI (Figure 4). Both the unmodified and PEG functionalized catheters with the Bi catalyst, do not present toxicity to PBMCs. Moreover, although

slightly more cytotoxic than untreated catheters, catheters impregnated with the protein are also suitable for use *in vitro* and *in vivo* tests.

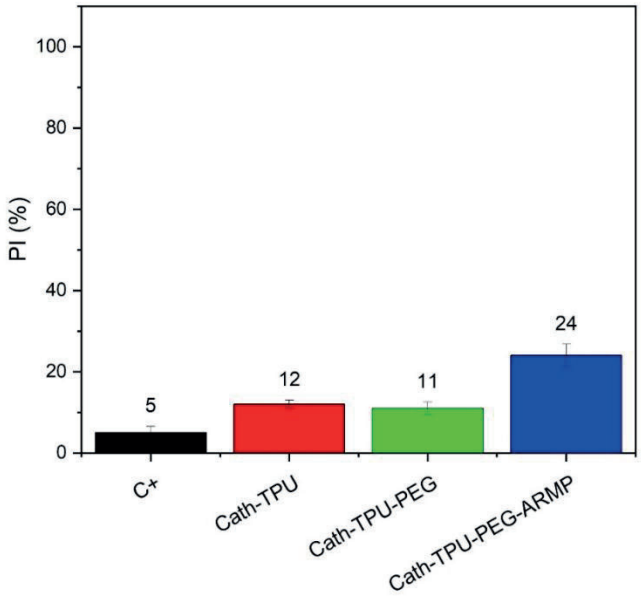


Figure 4. Propidium iodide viability test of peripheral blood mononuclear cells (PBMCs) (black), PBMCs with unmodified medical grade TPU catheter (red), PBMCs with PEG functionalized TPU catheter (Cath-TPU-PEG) (green), PBMCs with protein anchored to TPU catheter (Cath-TPU-PEG-ARMP) (blue).

3.3 *In vitro* biofilm assay: static and dynamic models

To evaluate the ability of the functionalized catheter to avoid the formation of biofilms, two types of *in vitro* studies were performed; the static and dynamic, which was performed using a Modified Robbins Device (MRD). This model will be used to mimic and study the influence of the fluid flow that the catheter will sense in the *in vivo* study.

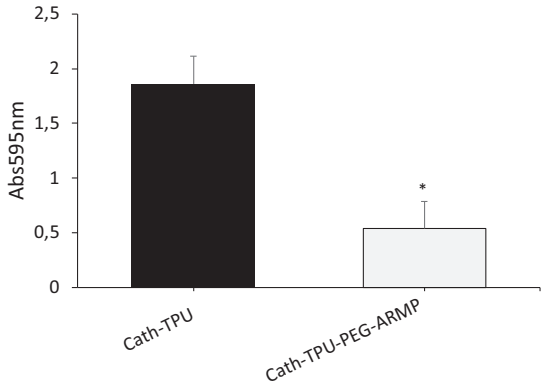
3.3.1. *In vitro* static antibiofilm assay and stability study

Inhibition of the biofilm formation was studied using catheters functionalized with PEG and with mixed SAMs of the ARMP D5L37βD3 (Cath-TPU-PEG-ARMP). To evaluate the effect of the sterilization process needed for the *in vivo* experiment on the performance of the catheters, the assay was done before and after the sterilization process with ethylene oxide, which is used in the hospitals.

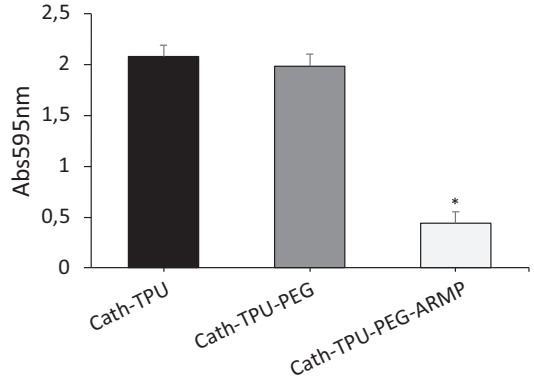
The bacterial strain chosen for this study is the MRSE, which is one of the most predominant bacteria related with HAIs related to intravascular catheters. Moreover, it is well characterized, and it has been shown to build mature and reproducible biofilms. Biofilms were grown in Brain Heart Infusion (BHI) broth medium with glucose and the suspension was incubated with the catheters (5 cm length) at 37 °C overnight with a gentle rotation. During this time, a biofilm formed in the lumen and on the outside of the catheters, which was quantified by the CV assay (Figure 5). CV is a cationic dye that binds to bacteria and to the extracellular polymeric substances forming the biofilm.

The decrease of absorbance shown in Figure 5A proved that there was a good inhibition of the biofilm formation by the Cath-TPU-PEG-ARMP when compared with catheters without ARMP (Cath-TPU). This confirms that the activity of the novel multidomain protein D5L37βD3, anchored on the catheter, impairs the biofilm formation. Moreover, in Figure 5B, it is observed that, after the sterilization process by ethylene oxide there still inhibition of the biofilm formation, confirming that the sterilization process is not affecting protein antibiofilm activity. Stability tests were also carried out 3 months after sterilization the catheters stored at 37 °C and as it is observed in Figure 5C there was no loss of antibiofilm activity after this period. This result is remarkable because simulates the physiological temperature and the time that the catheter can be implanted without losing its antimicrobial activity. Additionally, it shows that it will allow reasonable shelf storage time of the manufactured catheters.

A



B



C

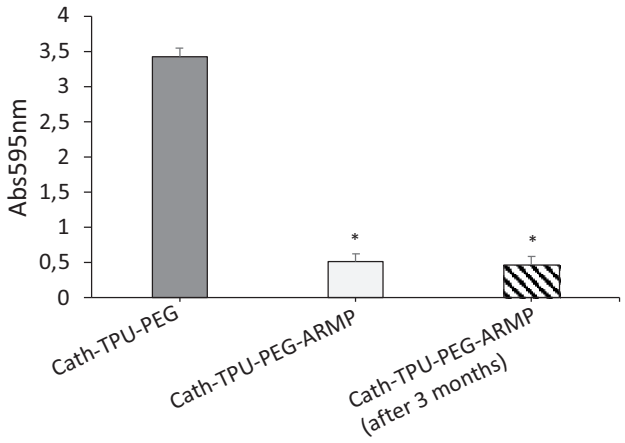


Figure 5. Determination of the inhibition of MRSE biofilm formation by (A) Cath-TPU and Cath-TPU-PEG-ARMP (P=0.0202); (B) Cath-TPU, Cath-TPU-PEG and Cath-TPU-PEG-ARMP after the sterilization process by ethylene oxide ($p<0.0001$); and (C) Cath-TPU-PEG, Cath-TPU-PEG-ARMP Cath-TPU-PEG-ARMP after 3 months at 37 °C once sterilized by ethylene oxide ($p<0.0001$).

3.3.2 *In vitro* dynamic antibiofilm assay

To better mimic a vascular catheter, an *in vitro* dynamic model of bacterial biofilm formation was done using a MRD (Figure S3). Using this model, we assessed the activity of the D5L37βD3 coating on the catheter after exposure to a circulating flow (1ml/min) of 1% Muller-Hinton broth medium at 37ºC for 24h. To perform the experiment, we used different discs of TPU (coated and non-coated), which were fixed on the bioreactor.

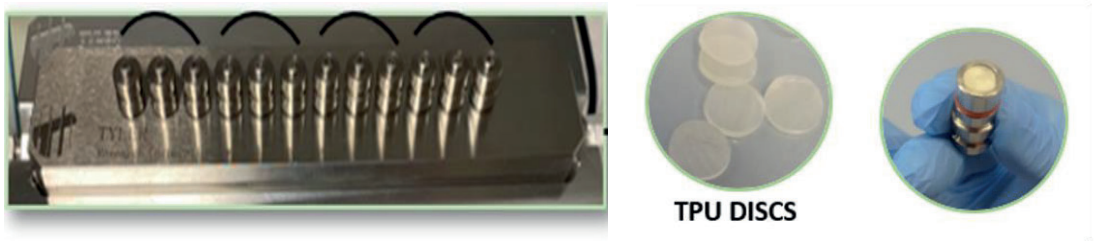


Figure 6. Bioreactor used for the in vitro dynamic model. Left) Inner part of the bioreactor showing the 12 positions where the 12 TPU discs with different coatings are attached and the inlet and outlet of the circulating flow; Right) TPU discs used for the functionalization simulating the surface of the catheter and a coupon with the disc sticked on it.

After optimizing the *in vitro* dynamic model, several experiments were conducted under various conditions to evaluate the stability of the functionalized discs in the dynamic model.

To check if there is detachment of the D5L37βD3 protein due to the mechanical strength of the flow we characterized the discs chemically and biologically by XPS and a biofilm static assay, respectively. The XPS analysis of the nitrogen (N2p) atoms shows the same intensity of the peaks before and after the *in vitro* dynamic experiment confirming the presence of the protein on the surface of the discs (Figure 7).

To determine if the antimicrobial surface is still active after the flow, an *in vitro* static biofilm assay was performed. As shown in Table 1, there are two orders of magnitude of difference between the bacteria grown on the TPU-PEG-ARMP and the two controls (TPU and TPU-PEG), which is a clear indication that the protein is still active even after the *in vitro* dynamic experiment with a flow of 1 mL/min. This result demonstrates the robustness of the protein anchoring strategy and the protein antibiofilm activity.

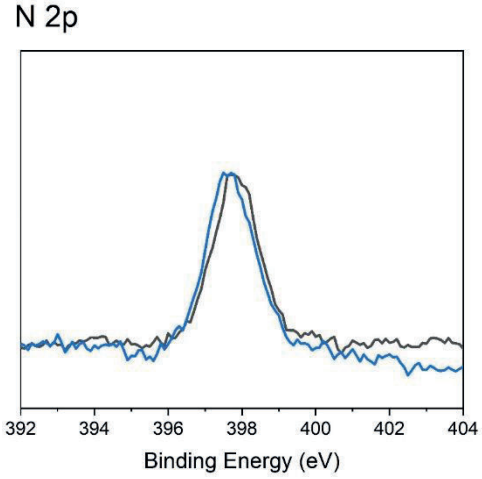


Figure 7. XPS spectra of N2p for TPU-PEG-ARMP (black) and TPU-PEG-ARMP after the *in vitro* dynamic experiment (blue).

TPU	TPU-PEG	TPU-PEG-ARMP
$3.47x10^5 \pm 1.33x10^4$ CFU/mL	$6.33x10^6 \pm 3.25x10^5$ CFU/mL	$5.01x10^4 \pm 3.25x10^4$ CFU/mL

Table 1. *In vitro* biofilm assay against MRSE of the discs of TPU, TPU-PEG and TPU-PEG-ARMP after the *in vitro* dynamic experiment.

TPU	TPU-PEG	TPU-PEG-ARMP
$3,5x10^5$ CFU/mL	$6,3x10^6$CFU/mL	$5,0x10^4$ CFU/mL

Table 1. *In vitro* biofilm assay against MRSE of the discs of TPU, TPU-PEG and TPU-PEG-ARMP after the *in vitro* dynamic experiment.

4. Conclusions

In this study, a functional coating for thermoplastic polyurethane (TPU) catheters suitable for *in-vivo* application in central veins has been successfully developed. This strategy permits the modification of both the inner and outer surfaces of the TPU catheter. The modified surfaces demonstrated broad-spectrum antibiofilm properties and durable stability even after sterilization and storing at 37ºC during 3 months, allowing for a long shelf life.

To achieve these objectives, TPU was activated with hexamethylene diisocyanate (HDI) using a biocompatible catalyst and facilitating an interfacial reaction with polyethylene glycol (PEG) derivatives. Subsequently, an antimicrobial recombinant multidomain protein (ARMP), which combines different Host Defense Peptides (HDPs) in a single polypeptide, was anchored through a straightforward bioclickable reaction between the PEG-maleimide terminated self-assembled monolayers (SAMs) on the TPU and the cysteine (-thiol) terminated ARMP.

The functionalized catheters were characterized by FTR-IR and XPS, and their biocompatibility was analyzed using Peripheral Blood Mononuclear Cells (PBMCs) and a propidium iodide (PI) cell viability test. The antibiofilm activity of the functionalized polyurethane surfaces was evaluated against MRSE. Furthermore, the stability of the recombinant protein with antimicrobial activity was assessed under conditions that mimic the flow and pressure encountered by real catheters using an *in-vitro* dynamic model.

It has been demonstrated that the recently reported ARMPs effectively attach to both the outer and inner surfaces of TPU catheters, exhibits a reduction in MRSE biofilm formation, one of the most predominant bacteria associated with nosocomial infections, in intravascular catheters. Moreover, the functionalized catheters not only showed antibiofilm activity but also cytocompatibility with human blood cells and high stability after pressure flow and storage for 3 months at 37ºC, which is an advantage considering their real medical *in-vivo* application.

In conclusion, it has been developed a novel and stable catheter, inner and outer, coating strategy alternative to silver and antibiotics to be used for prevention of infection using ARMPs using and a clickable strategy. These results do create a pathway of research to assess these and other peptides anchoring to MD surfaces, such as pacemakers, orthopaedic prosthesis, etc. as an interesting and promising alternative to fight against nosocomial infections.

5. Acknowledgements

Financial support by the MICIU of Spain (projects PID2019-105622RBI00, PID2020-115296RA-I00, PID2022-137332OB-I00, CEX2019-000917-S, CEX2023- 001263-S), CSIC (project 2023AEP092), the Marató de TV3 foundation (project number 201812-30-31-32-33 and 202326-30-31-32-33) and the Generalitat de Catalunya (project SGR Cat 2021-00438 and 2021-01552). The authors are also grateful for the financial support received from Instituto de Salud Carlos III through and the Networking Research Center on Bioengineering, Biomaterials, and Nanomedicine (CIBER-BBN). J.G. is grateful to the Max Planck Institute for Medical Research (Heidelberg, Germany) for their collaboration through the Max Planck Partner Group "Dynamic Biomimetics for Cancer Immunotherapy". ICMAB-CSIC acknowledges support from the Severo Ochoa Programme for Centres of Excellence in R&D (FUNFUTURE, CEX2019-000917-S). JMM received a personal 80:20 research grant from the Institut d'Investigacions Biomèdiques August Pi i Sunyer (IDIBAPS), Barcelona, Spain, during 2017–24. This work has been developed inside the Materials Science PhD program of Universitat Autonoma de Barcelona. XRR was supported by a grant PTA2021-020955-I funded by MCIN/AEI/10.13039/501100011033 and the FSE. This project has received funding from the European Union's Horizon 2020 research and innovation program under the Marie Skłodowska-Curie grant agreement No. 801342 (Tecniospring INDUSTRY) and the Government of Catalonia's Agency for Business Competitiveness (ACCIOÅL; TECSPR19-1-0065). AL-C received a pre-doctoral fellowship from Generalitat de Catalunya (FI-AGAUR) and PB was supported by a PFIS predoctoral fellowship (FI20/00009) from the Instituto de Salud Carlos III. The authors are indebted to CERCA Programme (Generalitat de Catalunya) and the European Social Fund for supporting our research. The authors also acknowledge the ICTS NANBIOSIS for the support of the Biomaterial Processing and Nanostructuring Unit (U6) at ICMAB-CSIC

(https://www.nanbiosis.es/portfolio/u6- biomaterialprocessing-and-nanostructuring-unit/).

Conflicts of Interest: J.M.M. has received consulting honoraria and/or research grants from Angelini, Contrafect, Cubist, Genentech, Gilead Sciences, Jansen, Lysovant, Medtronic, MSD, Novartis, Pfizer and ViiV Healthcare, outside the submitted work.

FUNCATH investigators: Hospital Clinic-IDIBAPS, University of Barcelona, Barcelona, Spain: J.M.M., C.G.-d.-l.-M., Maria A. Cañas-Pacheco, Javier Garcia-Gonzalez, Marta Hernández-Meneses, Guillermo Cuervo and Asunción Moreno. Institute of Materials Science of Barcelona (ICMAB-CSIC): I.R., J.G., J.V and X.R.R. Hospital Universitari Parc Taulí: Oriol Gasch, O.Q.P. and P.B. IRTA: A.L.C., E.G.-F. and A.A.

6. Bibliography

1. Zhu Z, Wang Z, Li S, Yuan X. Antimicrobial strategies for urinary catheters. *J Biomed Mater Res A*. 2019;107(2):445-467. doi:https://doi.org/10.1002/jbm.a.36561
2. Faustino CMC, Lemos SMC, Monge N, Ribeiro IAC. A scope at antifouling strategies to prevent catheter-associated infections. *Adv Colloid Interface Sci*. 2020;284:102230. doi:https://doi.org/10.1016/j.cis.2020.102230
3. Zhang S, Vaida J, Parenti J, Lindsey BA, Xing M, Li B. Programmed Multidrug Delivery Based on Bio-Inspired Capsule-Integrated Nanocoatings for Infected Bone Defect Treatment. *ACS Appl Mater Interfaces*. 2021;13(10):12454-12462. doi:10.1021/acsami.0c20332
4. Ricardo SIC, Anjos IIL, Monge N, Faustino CMC, Ribeiro IAC. A Glance at Antimicrobial Strategies to Prevent Catheter-Associated Medical Infections. *ACS Infect Dis*. 2020;6(12):3109-3130. doi:10.1021/acsinfecdis.0c00526

5. Shen Y, Li P, Chen X, et al. Activity of Sodium Lauryl Sulfate, Rhamnolipids, and N-Acetylcysteine Against Biofilms of Five Common Pathogens. *Microbial Drug Resistance*. 2019;26(3):290-299. doi:10.1089/mdr.2018.0385

6. Valentin JDP, Qin XH, Fessele C, et al. Substrate viscosity plays an important role in bacterial adhesion under fluid flow. *J Colloid Interface Sci*. 2019;552:247-257. doi:https://doi.org/10.1016/j.jcis.2019.05.043

7. Van Boeckel TP, Pires J, Silvester R, et al. Global Trends in Antimicrobial Resistance in Animals in Low- and Middle-Income Countries. *Sci*. 2019;365(6459):eaaw1944. doi:10.1126/science.aaw1944

8. Uneputty A, Dávila-Lezama A, Garibo D, et al. Strategies applied to modify structured and smooth surfaces: A step closer to reduce bacterial adhesion and biofilm formation. *Colloids and Interface Science Communications*. 2022;46:100560. doi:10.1016/j.colcom.2021.100560

9. Qi F, Qian Y, Shao N, et al. Practical Preparation of Infection-Resistant Biomedical Surfaces from Antimicrobial β-Peptide Polymers. *ACS Appl Mater Interfaces*. 2019;11(21):18907-18913. doi:10.1021/acsami.9b02915

10. Lu Z, Wu Y, Cong Z, et al. Effective and biocompatible antibacterial surfaces via facile synthesis and surface modification of peptide polymers. *Bioact Mater*. 2021;6(12):4531-4541. doi:https://doi.org/10.1016/j.bioactmat.2021.05.008

11. Imani SM, Ladouceur L, Marshall T, Maclachlan R, Soleymani L, Didar TF. Antimicrobial Nanomaterials and Coatings: Current Mechanisms and Future Perspectives to Control the Spread of Viruses Including SARS-CoV-2. *ACS Nano*. 2020;14(10):12341-12369. doi:10.1021/acsnano.0c05937

12. Kearney L, Francis E, Clover A. New technologies in global burn care - a review of recent advances. *Int J Burns Trauma*. 2018;8:77-87.

13. Brouillard C, Bursztejn AC, Latarche C, et al. Silver Absorption and Toxicity Evaluation of Silver Wound Dressings in 40 Patients with Chronic Eounds. *JEADV*. 2018;32(12):2295-2299. doi:https://doi.org/10.1111/jdv.15055

14. Panáček A, Kvítek L, Smékalová M, et al. Bacterial Resistance to Silver Nanoparticles and How to Overcome It. *Nat Nanotechnol*. 2018;13(1):65-71. doi:10.1038/s41565-017-0013-y

15. Siddique MH, Aslam B, Imran M, et al. Effect of Silver Nanoparticles on Biofilm Formation and EPS Production of Multidrug-Resistant Klebsiella pneumoniae. *Biomed Res Int*. 2020;2020. doi:10.1155/2020/6398165

16. Gifre-Renom L, Ugarte Berzal E, Martens E, et al. Recombinant Protein-Based Nanoparticles: Elucidating Their Inflammatory Effects In Vivo and Their Potential as a New Therapeutic Format. *Pharmaceutics*. 2020;12:450. doi:10.3390/pharmaceutics12050450

17. Roca R, Lisowski L, Aris A, Garcia-Fruitos E. The Future of Recombinant Host Defense Peptides. *Microb Cell Fact*. 2022;21. doi:10.1186/s12934-022-01991-2

18. Méndez-Samperio P. Peptidomimetics as a New Generation of Antimicrobial Agents: Current Progress. *Infect Drug Resist*. 2014;7:229-237. https://api.semanticscholar.org/CorpusID:3288783

19. Wilson SS, Wiens ME, Smith JG. Antiviral Mechanisms of Human Defensins. *J Mol Biol*. 2013;425(24):4965-4980. doi:https://doi.org/10.1016/j.jmb.2013.09.038

20. Peschel A, Sahl H. Peschel, A. & Sahl, H.G. The co-evolution of host cationic antimicrobial peptides and microbial resistance. Nat. Rev. Microbiol. 4, 529-536. *Nat Rev Microbiol*. 2006;4:529-536. doi:10.1038/nrmicro1441

21. López-Cano A, Ferrer-Miralles N, Sánchez J, et al. A Novel Generation of Tailored Antimicrobial Drugs Based on Recombinant Multidomain Proteins. *Pharmaceutics*. 2023;15(4). doi:10.3390/pharmaceutics15041068

22. Ehlers MM, Strasheim W, Lowe M, Ueckermann V, Kock MM. Molecular Epidemiology of Staphylococcus epidermidis Implicated in Catheter-Related Bloodstream Infections at an Academic Hospital in Pretoria, South Africa. *Front Microbiol*. 2018;9. doi:10.3389/fmicb.2018.00417

23. Tatkiewicz WI, Seras-Franzoso J, García-Fruitós E, et al. Two-Dimensional Microscale Engineering of Protein-Based Nanoparticles for Cell Guidance. *ACS Nano*. 2013;7(6):4774-4784. doi:10.1021/nn400907f

24. Tatkiewicz WI, Seras-Franzoso J, Garcia-Fruitós E, et al. Surface-Bound Gradient Deposition of Protein Nanoparticles for Cell Motility Studies. *ACS Appl Mater Interfaces*. 2018;10(30):25779-25786. doi:10.1021/acsami.8b06821

25. Tatkiewicz WI, Seras-Franzoso J, García-Fruitós E, et al. High-Throughput Cell Motility Studies on Surface-Bound Protein Nanoparticles with Diverse Structural and Compositional Characteristics. *ACS Biomater Sci Eng*. 2019;5(10):5470-5480. doi:10.1021/acsbiomaterials.9b01085

26. Coronel Meneses D, Sánchez-Trasviña C, Ratera I, Mayolo-Deloisa K. Strategies for surface coatings of implantable cardiac medical devices. *Front Bioeng Biotechnol*. 2023;11:1-26. doi:10.3389/fbioe.2023.1173260

27. Díez-Gil C, Martínez R, Ratera I, Tárraga A, Molina P, Veciana J. Nanocomposite membranes as highly selective and sensitive mercury(ii) detectors. *J Mater Chem*. 2008;18(17):1997-2002. doi:10.1039/B800708J

28. Martínez-Miguel M, Kyvik AR, M. Ernst L, et al. Stable anchoring of bacteria-based protein nanoparticles for surface enhanced cell guidance. *J Mater Chem B*. 2020;8(23):5080-5088. doi:10.1039/D0TB00702A

29. Kyvik AR, Roca-Pinilla R, Mayolo-Deloisa K, et al. Antibiofilm surfaces based on the immobilization of a novel recombinant antimicrobial multidomain protein using self-assembled monolayers. *Mater Adv*. 2023;4(10):2354-2364. doi:10.1039/D2MA00978A

30. López-Cano A, Martínez-Miguel M, Guasch J, Ratera I, Arís A, Garcia-Fruitós E. Exploring the impact of the recombinant Escherichia coli strain on defensins antimicrobial activity: BL21 versus Origami strain. *Microb Cell Fact*. 2022;21(1):77. doi:10.1186/s12934-022-01803-7

31. Schellekens Y, Van Trimpont B, Goelen PJ, et al. Tin-free Catalysts for the Production of Aliphatic Thermoplastic Polyurethanes. *Green Chem*. 2014;16(9):4401-4407. doi:10.1039/C4GC00873A

32. Chen Q, Zhang Z, Qi Y. Effect of Bismuth Neodecanoate Content on Properties of Silicone Tie-Coatings. *Int J of Adhes Adhes*. 2024;128:103532. doi:https://doi.org/10.1016/j.ijadhadh.2023.103532

Supplementary Information

Stable Surface Coating of Thermoplastic Polyurethane Catheters with Tailored Recombinant Multidomain Protein - Towards In Vivo Infection Prevention

Xavier Rodríguez Rodríguez,[1,2] Adrià López-Cano,[3] Karla Mayolo-Deloisa,[1,4] Oscar Q Pich,[5,6] Paula Bierge,[5,6] Nora Ventosa,[1,2] Cristina García-de-la-Maria,[6] José M. Miró,[6,7] Oriol Gasch,[8] Jaume Veciana,[1,2] Judith Guasch,[1,2,9] Elena Garcia-Fruitós,[3] Anna Arís,[3] Imma Ratera[1,2] and the FUNCATH investigators[10]

[1] Institute of Materials Science of Barcelona (ICMAB-CSIC), Campus UAB, Bellaterra, 08193, Spain.

[2] Networking Research Center on Bioengineering, Biomaterials and Nanomedicine (CIBER-BBN), Campus UAB, Bellaterra, 08193, Spain.

[3] IRTA, Torre Marimon, Ctra C-59, Km 12,1, 08140 Caldes de Montbui, Barcelona, Spain

[4] Tecnologico de Monterrey, Institute for Obesity Research, School of Engineering and Sciences, Av. Eugenio Garza Sada 2001, 64849 Monterrey, Nuevo León, México.

[5] Laboratori de Recerca en Microbiologia i Malalties Infeccioses, Hospital Universitari Parc Taulí, Institut d'Investigació i Innovació Parc Taulí (I3PT-CERCA), Universitat Autònoma de Barcelona, 08208, Sabadell, Spain.

[6] Infectious Diseases Service. Hospital Clinic-FCRB-IDIBAPS. Universitat de Barcelona, Barcelona, Spain.

[7] Infectious Diseases Biomedical Research Networking Center (CIBERINFEC), Instituto de Salud Carlos III, Madrid, Spain.

[8] Servei de Malalties Infeccioses, Hospital Universitari Parc Taulí, Institut d'Investigació i Innovació Parc Taulí (I3PT-CERCA), Universitat Autònoma de Barcelona, 08208, Sabadell (Spain)

[9] Dynamic Biomimetics for Cancer Immunotherapy, Max Planck Partner Group, ICMAB-CSIC, Campus UAB, Bellaterra, 08193, Spain.

[10] FUNCATH Investigators are indicated in the Appendix.

1. TPU discs fabrication

The TPU discs fabrication was based in an extrusion process of TPU beads. These beads were melted to form a TPU bar of 7.8 mm diameter and then they were cut in 1 mm thickness pieces. From them, discs of 7,5 mm of diameter were cut with a punch.

2. Functionalization of the TPU discs with the PEG SAMs using two different catalysts

The TPU discs were sonicated with isopropyl alcohol for 15 min. Then, the TPU surfaces were dried under a gentle N_2 flow. After, the modification of the surface of the TPU was done in a three-steps procedure. All steps were carried out under argon atmosphere, using dried toluene as solvent and dibutyltin dilaurate 95% or the more biocompatible bismuth neodecanoate, as the catalyst (Figure S1). In the first step, the surface of the TPU discs were activated with HDI. Specifically, TPU samples were immersed into 5 mL of toluene containing 5% (v/v) HDI and 0.25% (v/v) dibutyltin dilaurate 95% for 1h at 70°C. Then, the TPU sample was washed with dried toluene for 30 min. In the second step, PEG4K were grafted onto the TPU surface by letting the hydroxyl groups react with the isocyanate end groups of the activated surface to obtain a TPU-PEG homogeneous SAM. Specifically, the TPU surfaces were immersed in a 10% (w/v) of PEG4K solution in dried toluene and left to react overnight at 45°C. After that, the samples were washed in order to remove all the unreacted monomer with toluene, isopropyl alcohol and MilliQ water for 15 min each. The TPU disc were finally dried in a vacuum oven at 45°C overnight.

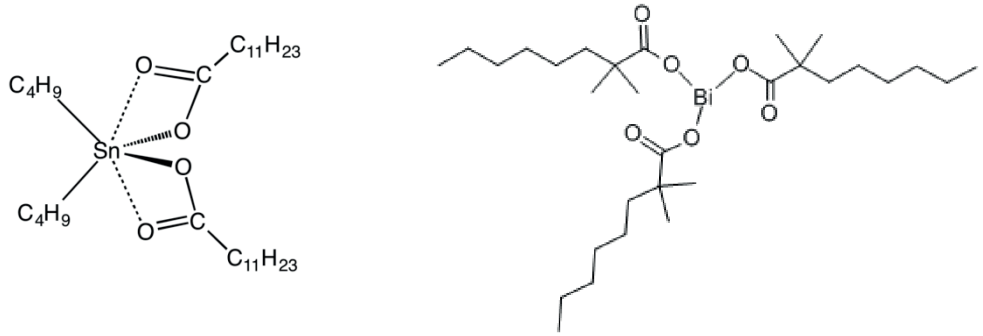


Figure S1. Left) Dibutyltin dilaurate 95% and Right) the more biocompatible bismuth neodecanoate

3. Study of the biocompatibility of the catalysts

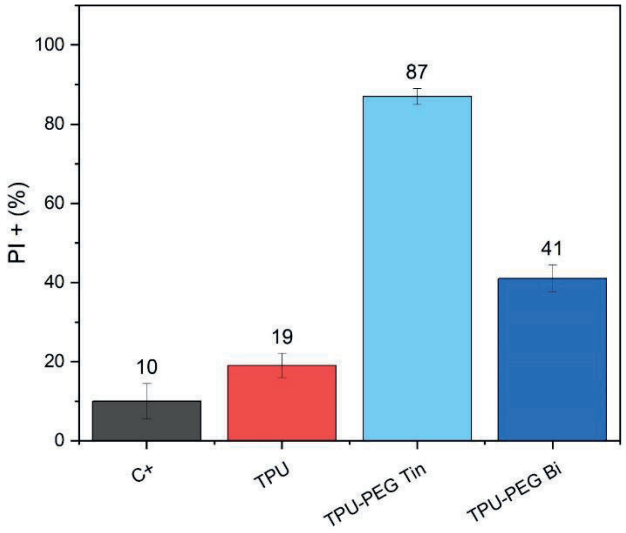


Figure S2. Viability test of PBMCs using propidium iodide: in solution (black), on an unmodified TPU disc (red), on a TPU-PEG disc using the dibutyltin dilaurate catalyst (light blue), and on a TPU-PEG disc using bismuth neodecanoate catalyst (dark blue).

4. *In vitro* dynamic antibiofilm assay

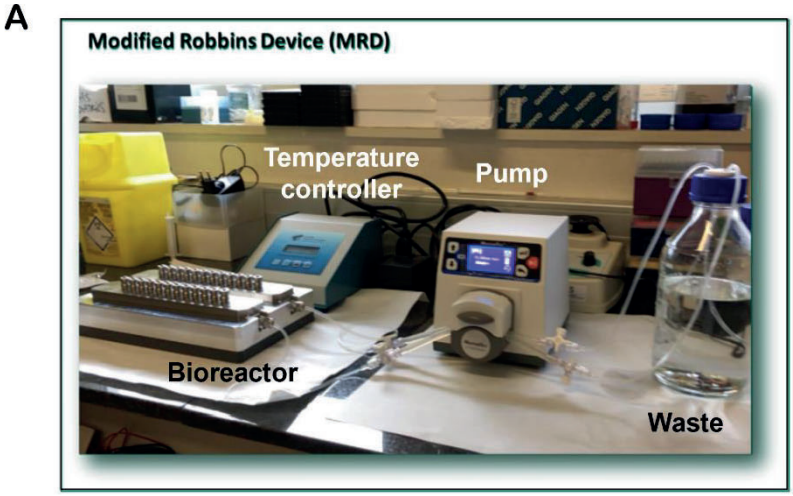


Figure S3. Picture of the different parts of the bioreactor used for the in vitro dynamic model (bioreactor, temperature controller, pump and waste).

Chapter 5

A ratiometric nanothermometer based on radical excimer-based organic nanoparticles for *in vivo* sensing

5.1. Introduction

Temperature is a physical parameter vital for all biological process. Biological entities, such as cells and tissues, are a good example of a heat-generating object that operates within narrow limits of a few degrees.[1] However, it is still not completely understood today how cells sense and respond to temperature at molecular and organelle levels.[2] So, monitoring temperature in these systems is a vital yet challenging task.

Nanothermometry aims to extract information of the local temperature of a given system with sub-micrometric spatial resolution.[3] Such knowledge is required for the complete understanding of micrometric and nanostructured systems whose dynamics and performance are strongly determined by temperature. Recently, the thermal sensing of cells has been a topic of interest in biology, for example in diagnosis or hyperthermia treatments.[1,4–6]

In vivo sensors must be independent of environmental conditions, such as pH, viscosity, ionic strength together with no cytotoxicity.[7] Several systems have been explored as nanothermometers like organic dyes,[8,9] quantum dots,[10] Ln^{3+} doped systems,[11–13] inorganic-organic or polymer systems.[14–17] These luminous detectors utilize the fluorophore emission's thermal dependency to measure temperature but still have some concerns regarding cytotoxicity or stability in biological conditions.

Recently, researchers have suggested the use of organic nanoparticles (ONPs) comprising radical species to achieve nanoscale resolution in the fluorescence imaging of biological entitites *in vitro*.[18,19] Most notably, their luminescent properties enable contactless systems. Fluorescent ONPs have various applications, including drug delivery, bio-imaging, optoelectronics, and sensing (Figure 5.1).

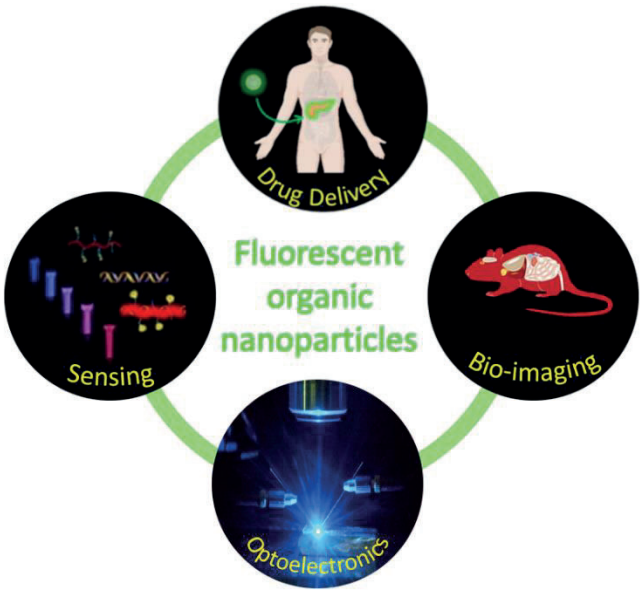


Figure 5.1. Fluorescent organic nanoparticles applications in different fields. Adapted from reference 16.

In order to be used as luminescent nanothermometers, fluorescent organic probes need to be sub-micrometer size with a narrow particle distribution showing monodispersity, present a high fluorescent quantum yield, be bio- and water compatible, have an environment-independent optical behavior, a large stokes-shift and a ratiometric output with a dual emission sensing system. Several cited ratiometric approaches primarily consist of a combination of minimum a pair of fluorescent components with differeing emission energies within a single particle.[20,21]

Organic molecules with free radicals containing one or more unbonded electrons, making them intriguing building blocks. In particular, triphenylmethyl radicals are metal-free open-shell organic molecules that exhibit strong persistence and stability.[22,23] There are different derivatives according to the atoms employed to create the halogenated precursor or the radical, such as tris(2,4,6-tribromophenyl) methyl, tris(2,4,6-trichlorophenyl) methyl (TTM), and perchlorotriphenylmethyl radicals.[24]

Electroactive species, such as trityl radicals, can be reduced to a carbanion or oxidized to a carbonium ion, also known as a carbocation, as opposed to the non-electroactive hydrogenated precursor αH.[25] Additionally, because of their electrical open-shell nature—that is, the unpaired electron in their singly-occupied molecular orbital—they are also paramagnetic. Furthermore, because of the unpaired electron in the ground level of their electrical structure, they have unique optical capabilities (absorption and fluorescence). Finally, the phenyl groups turn and the particle take on a propeller-like structure due to the trityl radicals showing chirality. Depending on the left- or right-handed torsion, the molecules can be split into their positive or negative enantiomers, respectively.

Recently, our group has reported the dual emission of the tris(2,4,6-trichlorophenyl)methyl radical (TTM), present as monomer and excimer, inside organic nanoparticles (TTMd-ONPs) made with the optically neutral tris(2,4,6-trichlorophenyl)methane (TTM-αH), which acts as a matrix (Figure 5.2).[19]

An excimer is a complex formed between two fluorophore molecules of the same type, one in the excited state and the other in the ground state.[26] The monomer emission is almost unaltered varying temperature, which is used as an internal reference, while the excimer emission's intensity decreases upon increasing the temperature due to excimer thermal dissociation. Excimer-based fluorescent probes present some advantages: there is a red-shifted of the excimer emission from the monomer band, so it has a larger Stokes-shift that reduces complexity and maximizes efficiency in both thermal sensing and nanosensor preparation because both emissions originate from the same species. Moreover, only one wavelength is needed for the excitation of both emitting varieties and no correction for the different bleaching degrees is required.

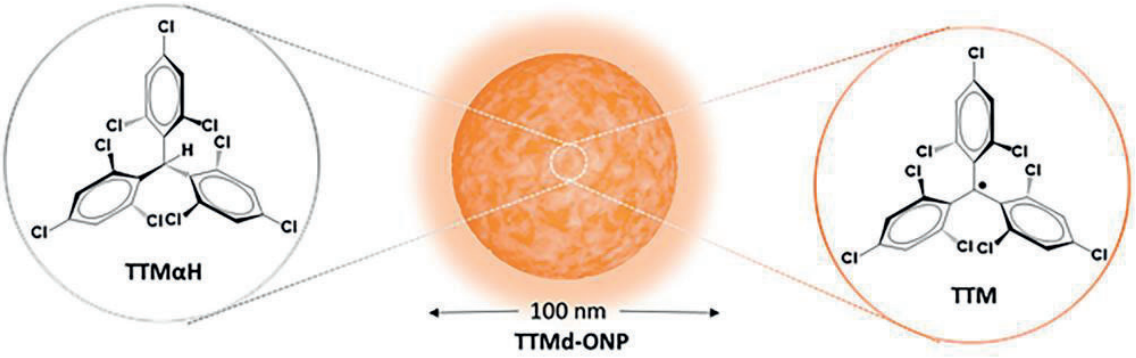


Figure 5.2. TTM-αH (matrix) and TTM radical (optically active) molecules, which compose TTMd-ONPs.

5.2. Objectives

The objectives of this chapter are based on the research that I have performed in relation to the development of a ratiometric nanothermometer based on radical excimer-based ONPs, and are the following:

1) Morphological and physicochemical characterization of TTMd-ONPs by dynamic light scattering (DLS) and transmission electron microcopy (TEM).
2) Spectroscopic characterization of TTMd-ONPs by ultraviolet-visible spectroscopy (UV-Vis) and spectroluminescence: dependence with temperature.
3) Study the biocompatibility of the TTMd-ONPs with a viability assay.
4) Local sensing of temperature at the nanoscale performing an *in-vitro* assay.

The results obtained in this chapter are part of the publication #3: Ratiometric Nanothermometer Based on a Radical Excimer for In Vivo Sensing. *Small* 2023, 19, 2207806. https://doi.org/10.1002/smll.202207806

5.3. ONPs preparation and characterization

The particles were prepared using the re-precipitation method, a easy and rapid technique for creating particles in suspension. Initially, the not hydrophilic compounds (TTM-αH and TTM radical) are dissolved in an organic solvent, tetrahydrofuran (THF), which is miscible with water. This solution is then injected into water under vigorous stirring. The mixing of the hydrophobic and hydrophilic phases leads to ONPs formation. Finally, the organic solvent is removed through dialysis, especially if biological assays are the final goal (Figure 5.3). Different percentages of the free-electron TTM molecule can be introduced in relation to TTM-αH, expressed as molar %. Previous work has optimized the percentage of radical doping, identifying 20% as an effective ratio for investigating the excimer thermal dissociation of TTMd-ONPs.[19]

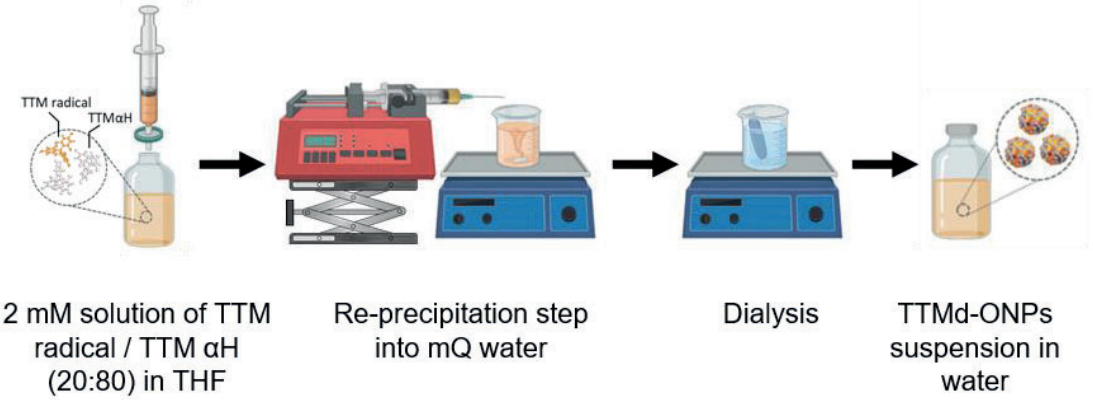


Figure 5.3. Schematic illustration of the re-precipitation method for preparing ONPs in water. Created with BioRender.com. Adapted from reference 16.

The ONPs were characterized before and after dialysis using several techniques. First, it was obtained the absorbance spectra of the dissolution (Figure 5.4A, blue line). To correct the background light scattering caused by the particles (100-200 nm particles scatter light at low wavelengths), a pure dispersion of TTM-αH ONPs was used. As expected, the emission spectrum displayed a red-shifted excimeric band with a large Stokes shift (Figure 5.4A, red line). To confirm that the radical's magnetic properties remained active in the ONPs, we use electron paramagnetic resonance (EPR) to characterize it (Figure 5.4B). Additionally, dynamic light scattering (DLS) revealed a hydrodynamic diameter of 100-150 nm (Figure 5.4C) with a polydispersity index of 0.03, indicating a highly monodisperse distribution. Negative Z-potentials close to -45 mV were measured, confirming the stability of the ONPs in water. Finally, TEM was used to verify the size

and spherical shape of the ONPs (Figure 5.4D).

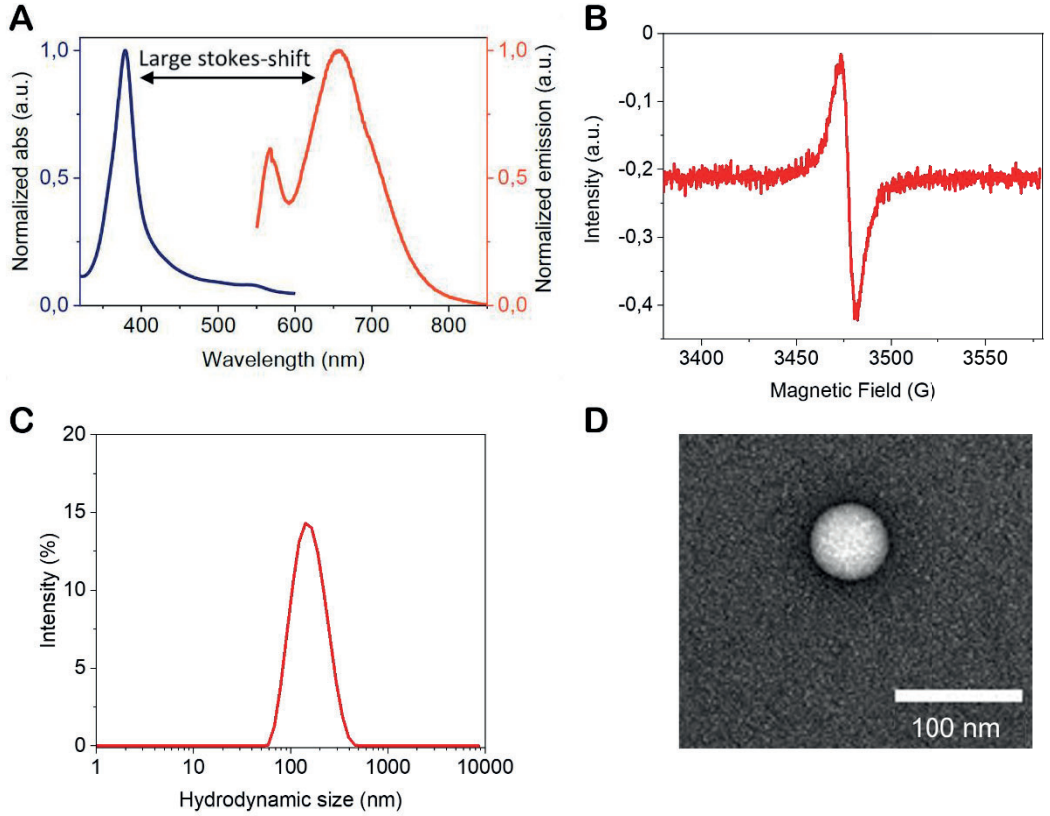


Figure 5.4. Aqueous suspension (+ 5% v/v THF) of 20% TTMd-ONPs. a) Normalized absorbance and emission spectra, exhibiting large Stokes-shift distance, b) EPR signal and c) DLS size distribution at RT, and d) TEM image of a single TTMd-ONP.

5.4. Temperature dependence of excimer emission: reversibility study and sensitivity

The fluorescence emission of the water suspensions of TTMd-ONPs was measured before dialysis. As previously reported,[19] the emission displays two bands when the percentage of radical doping exceeds 6.5%. The monomer band, at a shorter wavelength (572 nm), and the broader excimer emission band in the near-infrared region (665 nm) (Figure 5.5A). Temperature affects the dissociation of the excimers. Therefore, the fluorescence emission of the suspensions was recorded over a temperature range of 5 to 55 °C (278 to 328 K). The 665 nm excimer emission band is significantly quenched when the degrees increase, whereas the 572 nm monomer emission band is only slightly altered by the temperature change (Figure 5.5B). Interestingly, the equilibrium of the fluorescence intensity of excimers (I_E) and monomers (I_M), which is dependent on the temperature, can be seen for aqueous solutions of TTMd-ONPs with the corresponding isostilbic point (594 nm). To further confirm the system's reversibility, two temperature sequences from 5 to 55 °C were conducted (Figure 5.5C). Additionally, other ONPs with different percentages of radical doping (15%, 25% w/w TTM) were prepared, showing similar results to those with 20% doping, to optimize the ratiometric sensitivity of the ONPs (see SI of publication #2).

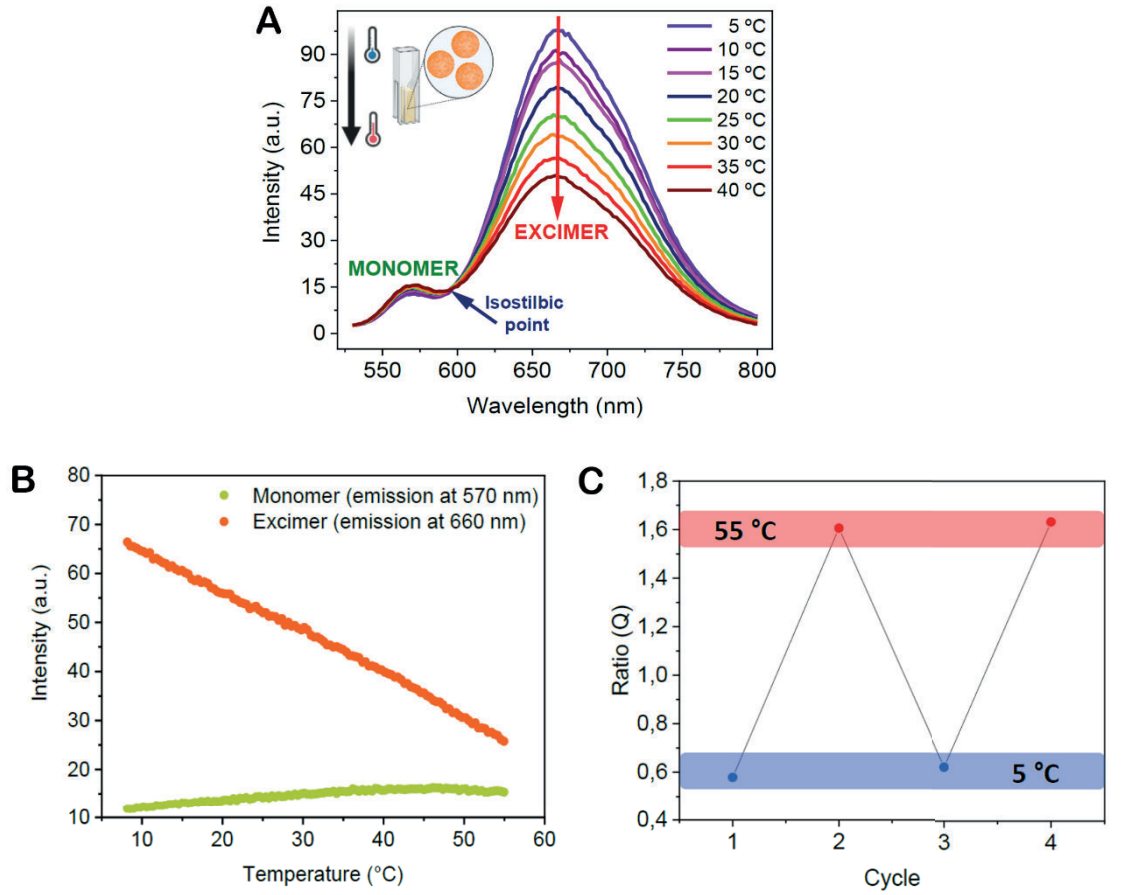


Figure 5.5. a) Spectra of fluorescence emission between 278 and 313 K, b) Maximun emission intensities of monomer (green) and excimer (orange) at different temperatures, c) IM/IE ratios of the 20 % TTMd-ONPs suspension (before dialysis) under temperature cycles of 5 °C and 55 °C.

All the measurements let us to determine the temperature sensitivity (S), using the following relation:

$$S = \frac{\partial Q(T)/\partial T}{Q} \times 100\% \ , \ [\% \cdot K^{-1}] \qquad \textbf{Equation 5.1}$$

where $Q(T)$ is the ratiometric output of the detector, defined as the ratio of the fluorescent intensities, I_M/I_E. Here, I_M represents the intensity at the peak of the monomer, and I_E represents the intensity at the peak of the excimer. Another useful parameter for comparing efficiency is the system's temperature resolution (ΔT), which is the lowest degree change that produces a noticeable variation in fluorescence. The next formula determined it:

$$\Delta T = \frac{\delta Q}{S_a} \ , \ [\text{degree}] \qquad \textbf{Equation 5.2}$$

Where δQ is the uncertainty of the measured change of luminescence, which means the standard deviation, and S_a is the absolute sensitivity. The better sensitivity was obtained by the TTMd-ONPs with 20 % of TTM, in particular, a maximum of sensitivity S_{max} = 3.6 %K^{-1} at T_{max} = 30 °C, with an average sensitivity, between 32 and 42 °C, of 3.4 %K^{-1} which

is one of the greatest values reported for nanothermometers based on small fluorescent metal-free organic molecules,[27] and a temperature resolution of $\Delta T_{min} = 0.3$ °C (obtained with equation 5.2).

Since the ultimate goal is to use the TTMd-ONPs as no contact nanothermometers for biosensing, the organic solvent used in its preparation (THF) was removed by dialysis. Removing the THF slightly reduces the system's sensitivity. ONPs dispersed in pure MilliQ water exhibited a maximum sensitivity (Smax) of 2.82% K^{-1} at a temperature (Tmax) of 37 °C and an average sensitivity of 2.78% K^{-1} in the 32-42 °C range. This change in sensitivity is likely due to the removal of the solvent that may have remained inside the ONPs after its preparation. Despite this, the sensitivity remains higher than 2% K^{-1}, which is very favorable, considering that the quality threshold for useful nanothermometers in biosensing is set at 0.5% K^{-1}. The dialysis had minimal impact on the colloidal properties. Post-dialysis, the ONPs maintained a uniform monomodal size distribution, featuring a Z-potential of -42 mV, a medium diameter of 106 ± 21 nm, and a spherical shape.

5.5. Cell viability test

Due to the highly sensitivity to temperature changes obtained with the TTMd-ONPs, we were interested to study the capability of NPs to detect nanoscale local temperature changes for *in vivo* biological applications. Before, a viability assay was performed to evaluate the cytotoxicity of the ONPs. We analysed the metabolic activity of COS-7 cells, which are a kidney fibroblast-like cell line, with an MTT assay. Utilizing a high-water content while treating cells (50% vol. water in media) reduced the viability of the cell culture to 70%, probably due to osmotic pressure in the cells. Based on the MTT analysis presented in figure 5.6, the viability of the cells was not affected by concentrations below 35 nM (25% water-media).

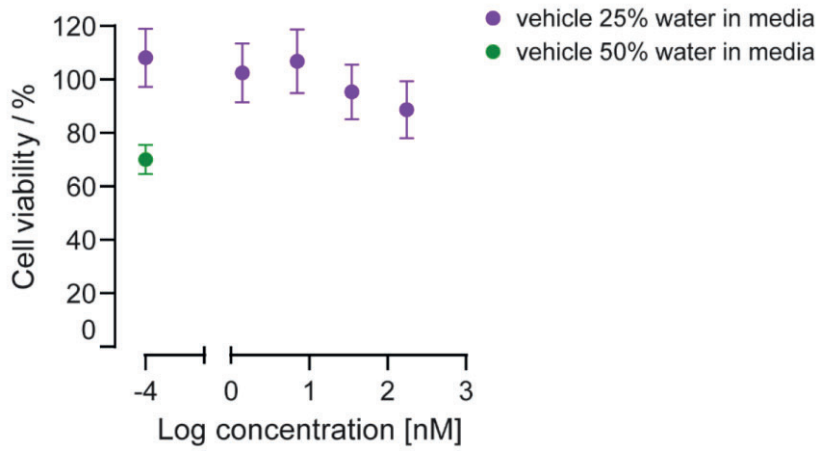


Figure 5.6. MTT assay of COS-7 cells at several concentrations of TTMd-ONPs. Absorbance was taken at 570 nm after 48 hours. The condition with 50% water-medium is represented in green, while the results with a 25% water proportion are shown in purple.

5.6. Local sensing of temperature

In order to advance toward the nanothermometer's application, and after confirming that TTMd-ONPs are not toxic, we investigated whether isolated ONPs could sense local temperature at the nanoscale. In collaboration with Prof. P. Gorostiza's group at IBEC in Spain, we developed a fluidic system to test this capability in cells. We deposited on top of a poly-L-lysinie glass a solution containing 20% TTMd-ONPs. This coverslip was then integrated into a custom-made fluidic system designed to be cooled and warmed with a 20 degrees range (Figure 5.7).

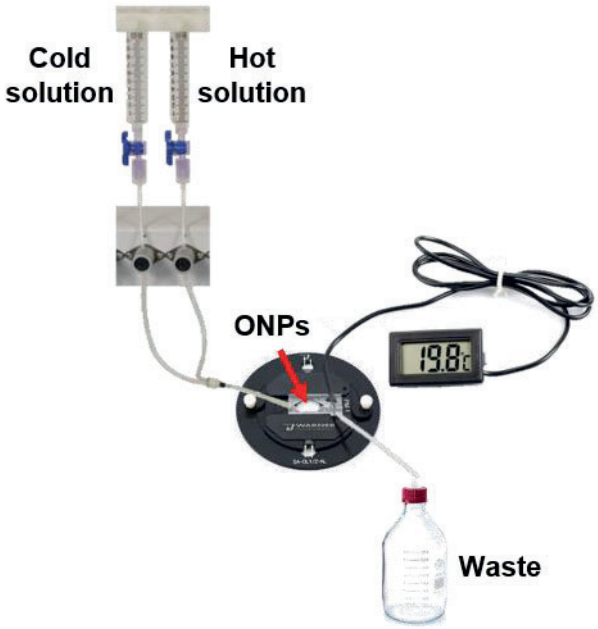


Figure 5.7. Scheme of the fluidic system built in collaboration with the P. Gorostiza's group (IBEC, Spain).

Using this setup, an optical microscope was used for examining the ONPs, and two separate filters were used to track variations in their fluorescence signal. One filter, set at 510-560 nm (Figure 5.8A), recorded the emission of monomers, while the other, set at 595-670 nm (Figure 5.8B), captured the emission from excimers, with excitation at λ_{exc} = 377 nm. For every measurement, two cold/hot cycles were conducted, selecting various regions of interest (ROIs), each of whose fluorescence signals was examined independently (Figure 5.8A and B) (see SI of publication #3 for additional ROIs). As expected, the monomer fluorescence intensities of the ONPs stayed mostly unchanged with a 20-degree temperature change (Figure 5.8C and E), whereas the excimer signals varied inversely with temperature changes (Figure 5.8D and F). This result illustrates the ability of TTMd-ONPs to detect temperature alterations at the sub-micron level, serving as ratiometric temperature sensing nanoprobes.

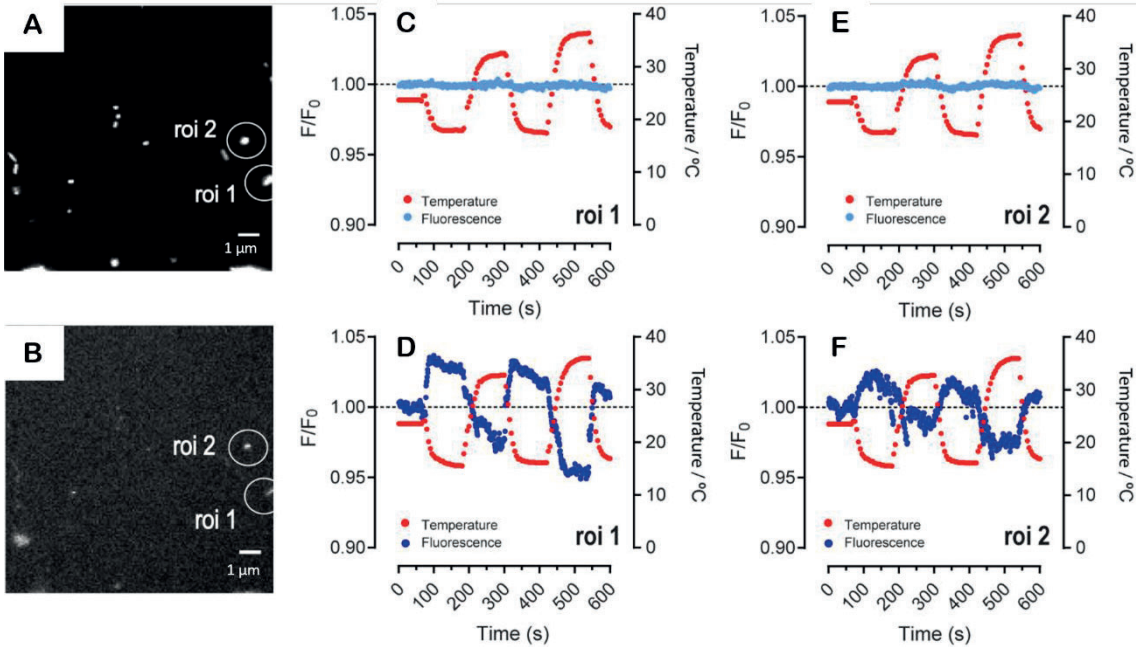


Figure 5.8. Representative fluorescence images of a) monomers and b) excimers (scale bar 1 µm). Fluctuations of the relative fluorescence intensity signals over time as a result of temperature variations for the monomer (c and e) and excimer (d and f).

5.7. Summary and future perspectives

To summarize, in the framework of this thesis, stable TTMd-ONPs were successfully prepared in water suspensions and their effectiveness as ratiometric fluorescent nanothermometers was proved. Remarkable temperature sensitivity (3.3 $\%K^{-1}$ at RT) and resolution were obtained. The unusual optical characteristics, due to the open-shell nature of the radical, result in ratiometric fluorescence emission, with a temperature-dependent excimer band (5 °C to 55 °C range, 298 K to 328 K) and a relatively stable monomer band. Additionally, we demonstrated that the ONPs suspension exhibits reversible behavior with temperature changes.

Importantly, this thesis proved that TTMd-ONPs are non-cytotoxic and emit in the deep red/NIR region, which is a transparency window for biological tissues, thus enabling deep-tissue penetration for in vivo applications.

In collaboration with Dr. Nerea González, another PhD candidate in our group, we investigated the stability of the ONPs in various environments with different pH levels. We also conducted *in vivo* thermometry assays with Caenorhabditis elegans worms. These experiments showed that TTMd-ONPs are able to locally observe temperature changes within the worms from 5 to 40 °C, highlighting their potential for biological thermometry.

For future steps, it would be interesting to use the developed nanothermometers to monitor intracellular temperature. Additionally, increasing the excitation wavelength

from the UV-Vis range to the safer infrared regions for biological and biomedical applications would be beneficial. Furthermore, the magnetic properties of TTMd-ONPs make them promising for dual-mode bioimaging applications, offering both magnetic contrast for MRI and luminescence simultaneously, which is a growing area of interest.

5.8. References

1. Zhou H, Sharma M, Berezin O, Zuckerman D, Berezin MY. Nanothermometry: From Microscopy to Thermal Treatments. *Chem Phys Chem*. 2016;17(1):27-36. doi:https://doi.org/10.1002/cphc.201500753

2. Wang C, Ling L, Yao Y, Song Q. One-step synthesis of fluorescent smart thermo-responsive copper clusters: A potential nanothermometer in living cells. *Nano Res*. 2015;8(6):1975-1986. doi:10.1007/s12274-015-0707-0

3. Quintanilla M, Henriksen-Lacey M, Renero-Lecuna C, Liz-Marzán LM. Challenges for optical nanothermometry in biological environments. *Chem Soc Rev*. 2022;51(11):4223-4242. doi:10.1039/D2CS00069E

4. Kucsko G, Maurer PC, Yao NY, et al. Nanometre-scale thermometry in a living cell. *Nature*. 2013;500(7460):54-58. doi:10.1038/nature12373

5. Okabe K, Sakaguchi R, Shi B, Kiyonaka S. Intracellular thermometry with fluorescent sensors for thermal biology. *Pflugers Arch*. 2018;470(5):717-731. doi:10.1007/s00424-018-2113-4

6. Zhou J, del Rosal B, Jaque D, Uchiyama S, Jin D. Advances and challenges for fluorescence nanothermometry. *Nat Methods*. 2020;17(10):967-980. doi:10.1038/s41592-020-0957-y

7. Rong G, Corrie SR, Clark HA. In Vivo Biosensing: Progress and Perspectives. *ACS Sens*. 2017;2(3):327-338. doi:10.1021/acssensors.6b00834

8. Lupton JM. A molecular thermometer based on long-lived emission from platinum octaethyl porphyrin. *Appl Phys Lett*. 2002;81(13):2478-2480. doi:10.1063/1.1509115

9. Chandrasekharan N, Kelly LA. A Dual Fluorescence Temperature Sensor Based on Perylene/Exciplex Interconversion. *J Am Chem Soc*. 2001;123(40):9898-9899. doi:10.1021/ja016153j

10. Vlaskin VA, Janssen N, van Rijssel J, Beaulac R, Gamelin DR. Tunable Dual Emission in Doped Semiconductor Nanocrystals. *Nano Lett*. 2010;10(9):3670-3674. doi:10.1021/nl102135k

11. Cerón EN, Ortgies DH, Del Rosal B, et al. Hybrid nanostructures for high-sensitivity luminescence nanothermometry in the second biological window. *Adv Mater*. 2015;27(32):4781-4787. doi:10.1002/adma.201501014

12. Rohani S, Quintanilla M, Tuccio S, et al. Enhanced Luminescence, Collective Heating, and Nanothermometry in an Ensemble System Composed of Lanthanide-Doped Upconverting Nanoparticles and Gold Nanorods. *Adv Opt Mater*. 2015;3(11):1606-1613. doi:https://doi.org/10.1002/adom.201500380

13. Wang X, Liu Q, Bu Y, Liu CS, Liu T, Yan X. Optical temperature sensing of rare-earth ion doped phosphors. *RSC Adv*. 2015;5(105):86219-86236. doi:10.1039/C5RA16986K

14. Li J, Sun CL, Shen R, et al. An Electrochemically Switched Smart Surface for Peptide Immobilization and Conformation Control. *J Am Chem Soc*. 2014;136(31):11050-11056. doi:10.1021/ja5048285

15. Tseng AA, Chen K, Chen CD, Ma KJ. Electron beam lithography in nanoscale fabrication: recent development. *IEEE Trans Electron Packag Manuf*. 2003;26(2):141-149. doi:10.1109/TEPM.2003.817714

16. Tseng CW, Huang DC, Tao YT. Electric Bistability Induced by Incorporating Self-Assembled Monolayers/aggregated Clusters of Azobenzene Derivatives in Pentacene-Based Thin-Film Transistors. *ACS Appl Mater Interfaces*. 2012;4(10):5483-5491. doi:10.1021/am3013906

17. Zhang H, Jiang J, Gao P, et al. Dual-Emissive Phosphorescent Polymer Probe for Accurate Temperature Sensing in Living Cells and Zebrafish Using Ratiometric and Phosphorescence Lifetime Imaging Microscopy. *ACS Appl Mater Interfaces*. 2018;10(21):17542-17550. doi:10.1021/acsami.8b01565

18. Li X, Tan W, Bai X, Li F. Stable Near-infrared-emitting Radical Nanoparticles for Fluorescence Imaging. *Chemical Research in Chinese Universities*. 2023;39(2):192-196. doi:10.1007/s40242-023-2365-1

19. Blasi D, Nikolaidou DM, Terenziani F, Ratera I, Veciana J. Excimers from stable and persistent supramolecular radical-pairs in red/NIR-emitting organic nanoparticles and polymeric films. *Phys Chem Chem Phys*. 2017;19(13):9313-9319. doi:10.1039/C7CP00623C

20. Zhang H, Jiang J, Gao P, et al. Dual-Emissive Phosphorescent Polymer Probe for Accurate Temperature Sensing in Living Cells and Zebrafish Using Ratiometric and Phosphorescence Lifetime Imaging Microscopy. *ACS Applied Materials & Interfaces*. 2018;10(21):17542-17550. doi:10.1021/acsami.8b01565

21. Fu J, Zhou L, Chen Y, et al. Dual-mode optical thermometry and multicolor anti-counterfeiting based on Bi3+/Er3+ co-activated BaGd2O4 phosphor. *Journal of the American Ceramic Society*. 2023;106(2):1333-1343. doi:https://doi.org/10.1111/jace.18836

22. Ratera I, Veciana J. Playing with organic radicals as building blocks for functional molecular materials. *Chem Soc Rev*. 2012;41(1):303-349. doi:10.1039/C1CS15165G

23. Artizzu F, Atzori M. *Functional Molecular Materials: An Introductory Textbook*.; 2018. doi:10.1201/9781351233668

24. Ratera I, Vidal-Gancedo J, Maspoch D, Bromley ST, Crivillers N, Mas-Torrent M. Perspectives for polychlorinated trityl radicals. *J Mater Chem C Mater*. 2021;9(33):10610-10623. doi:10.1039/D1TC02196F

25. Steeger M, Griesbeck S, Schmiedel A, et al. On the relation of energy and electron transfer in multidimensional chromophores based on polychlorinated triphenylmethyl radicals and triarylamines. *Phys Chem Chem Phy*. 2015;17(17):11848-11867. doi:10.1039/C4CP05929H

26. Kaur A, Lim Z, Yang K, New EJ. 8.14 - Fluorescent Sensors for Biological Metal Ions. In: Atwood JL, ed. *Compr Supramol Chem II*. Elsevier; 2017:295-317. doi:https://doi.org/10.1016/B978-0-12-409547-2.12612-5

27. Bradac C, Lim SF, Chang HC, Aharonovich I. Optical Nanoscale Thermometry: From Fundamental Mechanisms to Emerging Practical Applications. *Advanced Optical Materials*. 2020;8(15):2000183. doi:https://doi.org/10.1002/adom.202000183

28. Brites CDS, Lima PP, Silva NJO, et al. Thermometry at the nanoscale. *Nanoscale*. 2012;4(16):4799-4829. doi:10.1039/C2NR30663H

Publication #3

Title: Ratiometric Nanothermometer Based on a Radical Excimer for In Vivo Sensing

Authors: Davide Blasi, Nerea Gonzalez-Pato, Xavier Rodriguez Rodriguez, Iñigo Diez-Zabala, Sumithra Yasaswini Srinivasan, Núria Camarero, Oriol Esquivias, Mònica Roldán, Judith Guasch, Anna Laromaine, Pau Gorostiza, Jaume Veciana, and Imma Ratera

Publication: *Small* 2023, 19, 2207806.

NANO · MICRO small
www.small-journal.com

Ratiometric Nanothermometer Based on a Radical Excimer for In Vivo Sensing

Davide Blasi, Nerea Gonzalez-Pato, Xavier Rodriguez Rodriguez, Iñigo Diez-Zabala, Sumithra Yasaswini Srinivasan, Núria Camarero, Oriol Esquivias, Mònica Roldán, Judith Guasch, Anna Laromaine, Pau Gorostiza, Jaume Veciana, and Imma Ratera**

Ratiometric fluorescent nanothermometers with near-infrared emission play an important role in in vivo sensing since they can be used as intracellular thermal sensing probes with high spatial resolution and high sensitivity, to investigate cellular functions of interest in diagnosis and therapy, where current approaches are not effective. Herein, the temperature-dependent fluorescence of organic nanoparticles is designed, synthesized, and studied based on the dual emission, generated by monomer and excimer species, of the tris(2,4,6-trichlorophenyl) methyl radical (TTM) doping organic nanoparticles (TTMd-ONPs), made of optically neutral tris(2,4,6-trichlorophenyl)methane (TTM-αH), acting as a matrix. The excimer emission intensity of TTMd-ONPs decreases with increasing temperatures whereas the monomer emission is almost independent and can be used as an internal reference. TTMd-ONPs show a great temperature sensitivity (3.4% K^{-1} at 328 K) and a wide temperature response at ambient conditions with excellent reversibility and high colloidal stability. In addition, TTMd-ONPs are not cytotoxic and their ratiometric outputs are unaffected by changes in the environment. Individual TTMd-ONPs are able to sense temperature changes at the nano-micro-scale. In vivo thermometry experiments in *Caenorhabditis elegans* (*C. elegans*) worms show that TTMd-ONPs can locally monitor internal body temperature changes with spatio-temporal resolution and high sensitivity, offering multiple applications in the biological nanothermometry field.

1. Introduction

Nanothermometry is becoming a fundamental topic in several technological and scientific fields like electronics and biology.[1–6] Indeed, the miniaturization and the increment in power density in micro and optoelectronic devices require accurate temperature determination with high spatial resolution of the thermal effects (self-heating, heat dissipation, etc.) to optimize device performance.[1–4] In biology, during the last years a rising interest in intracellular thermal sensing has appeared,[5–7] for instance in diagnosis (sensing the heat production in cancer and inflammatory processes)[8,9] and in hyperthermia therapy, where monitoring the temperature during the treatment is fundamental to avoid an over-generation of heat that can burn the surrounding tumor's tissue.[10–12] Nanothermometry for biology is still challenging since bio-sensors should exhibit high sensitivity, accuracy, and spatial resolution, together with

D. Blasi, N. Gonzalez-Pato, X. Rodriguez Rodriguez, I. Diez-Zabala, S. Y. Srinivasan, O. Esquivias, J. Guasch, A. Laromaine, J. Veciana, I. Ratera
Institut de Ciència de Materials de Barcelona (ICMAB-CSIC)
Bellaterra 08193, Spain
E-mail: vecianaj@icmab.es; iratera@icmab.es

D. Blasi
Dipartimento di Chimica
Università degli Studi di Bari "Aldo Moro"
Bari 70125, Italy

N. Gonzalez-Pato, X. Rodriguez Rodriguez, J. Guasch, P. Gorostiza, J. Veciana, I. Ratera
Networking Research Center on Bioengineering
Biomaterials and Nanomedicine (CIBER-BBN)
Campus UAB
Bellaterra 08193, Spain

The ORCID identification number(s) for the author(s) of this article can be found under https://doi.org/10.1002/smll.202207806.

© 2023 The Authors. Small published by Wiley-VCH GmbH. This is an open access article under the terms of the Creative Commons Attribution License, which permits use, distribution and reproduction in any medium, provided the original work is properly cited.

DOI: 10.1002/smll.202207806

N. Camarero, P. Gorostiza
Institute for Bioengineering of Catalonia (IBEC)
The Barcelona Institute of Science and Technology
Clúster, Baldiri Reixac 10-12, Barcelona 08028, Spain

M. Roldán
Unitat de Microscòpia Confocal i Imatge Cellular
Servei de Medicina Genètica i Molecular
Institut Pediàtric de Malaties Rares (IPER)
Hospital Sant Joan de Déu
Esplugues de Llobregat 08950, Spain

J. Guasch
Dynamic Biomimetics for Cancer Immunotherapy
Max Planck Partner Group
ICMAB-CSIC
Campus UAB
Bellaterra 08193, Spain

P. Gorostiza
Catalan Institution for Research and Advanced Studies (ICREA)
Barcelona 08010, Spain

no cytotoxicity and optical and colloidal stabilities being such properties unaffected by changes in pH, concentration, ionic strength, and viscosity typical affecting biological media.[13] Several systems have been explored as nanothermometers meeting all these requirements, such as organic molecular dyes,[14,15] quantum dots (QDs),[16] Ln^{3+} doped systems,[10,17,18] polymers, and hybrid organic-inorganic systems.[19–22] All these luminescent sensors exploit the thermal dependence of a fluorophore emission for determining the temperature. These changes can be observed as variations in luminescence intensity, emission band shape, polarization, lifetime, or broadening of the emission bandwidth.[23]

Intensity-based sensors offer the possibility to work with a simple set-up,[24] reducing costs and time for data analysis.[25] Despite its simplicity, an absolute emission intensity measurement can lead to errors due to fluctuations in the active fluorophore concentration inside the cell or tissue due to aggregation or photodegradation. To overcome these problems, a ratiometric output with a dual emission sensing system is needed, also called luminescent intensity ratio (LIR). The simplest strategy, in order to have a dual emission, is to bind together two different emitting species with different thermal quenching of the emission, or exploit different states of aggregation of the same fluorophore, like in the case of excimers.[12,15,24,26,27]

Recently, organic nanoparticles (ONPs)[28] and radical-based ONPs have been proposed as fluorescence probes for in vitro bioimaging.[29] Indeed, polyhalogenated trityl radicals can achieve long-wavelength emission without the need of an extended conjugated system.[30,31] In addition, it is possible to further red-shift radical emission into the biological transparency window (650 – 950 nm) through the formation of excimers. These excimers, obtained by dispersing radical species in rigid hosts (generally the closed-shell radical precursor) have been studied during the last years due to the possibility to modulate their association/dissociation via the application of an external magnetic field at liquid helium temperature.[32,33] However, tuning the radical excimer association/dissociation by varying the external temperature has never been reported.

In this work, we propose a highly sensitive full-organic contactless nanothermometer based on organic radical nanoparticles (TTMd-ONPs) consisting of the optically neutral tris(2,4,6-trichlorophenyl)methane (TTM-αH) as a matrix and the tris(2,4,6-trichlorophenyl)methyl radical (TTM) as dopant (**Figure 1**). These nanoparticles exhibit a dual emission due to the presence of radical monomers and excimers inside the particle. Increasing temperatures cause a decrease in the excimer emission intensity without a significant alteration of the monomer emission, which allows to use it as an internal reference. This system offers a simple and reproducible nanoscopic sensor, entirely based on two small metal-free molecules, the open-shell TTM radical and its close-shell precursor, the TTM-αH, which are processed as TTMd-ONPs in a single-step self-assembly process, using the re-precipitation method. Achieving a ratiometric output using excimers instead of two different emitting species simplifies and optimizes the preparation of the nano-sensor as well as the thermal sensing, since both emissions come from the same compound and thus, a single wavelength can excite both emitting species. Thus, no correction for different bleaching rates is needed as in the case of hybrid systems. Moreover, excimers of the TTMd-ONPs emit in the region of deep-red/near infrared (NIR) (the first transparency windows of biological tissues), offering the opportunity to penetrate in the deep-tissue for in vivo applications.[34] In addition, TTMd-ONPs, owing to their metal-free formulation, are non-cytotoxic and their ratiometric outputs are unaffected by changes in pH and ionic strength that may occur under physiological conditions. Moreover, thanks to the magnetic properties of the TTMd-ONPs, could also be used as dual-mode bioimaging, coupling luminescence, and magnetic resonance.[35]

2. Results and Discussion

In previous works, we reported, for the first time, that TTM radical was able to form excimers when dispersed in rigid matrices (polymers or ONPs), like in TTMd-ONPs.[36,37] Radical excimers in ONPs are extremely promising since they are efficient emitters in the NIR, constituting an attractive system for optoelectronics.[32,33] These TTMd-ONPs were characterized by an average size distribution of ≈100 nm, spherical shape, and high colloidal stability in water. In addition, these radical doped systems can also play a relevant role in bio-imaging and bio-sensing since they are water dispersible and present unique optical properties. Indeed, they show a huge Stock's shift and an efficient emission in the first biological transparency window (650 – 950 nm), which minimizes self-absorption effects and shows better tissue penetration compared to UV-visible wavelengths,[38] together with microsecond lifetimes that allow filtering self-fluorescence signals simply applying a delay between excitation and detection. Therefore, the optical

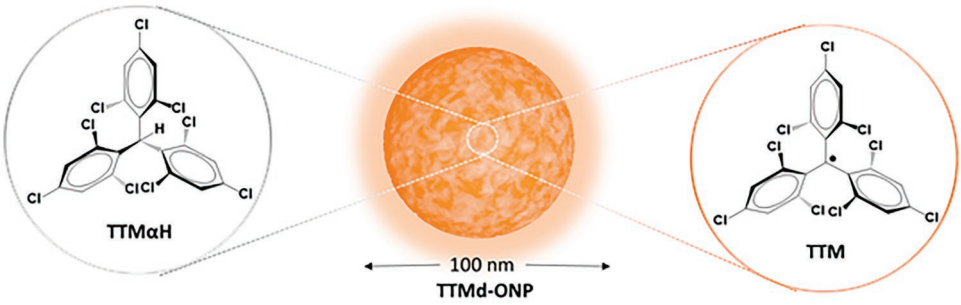


Figure 1. Molecular structures of TTM-αH and the TTM radical molecules and idealized representation of TTMd-ONPs made of a blend of TTM-αH, acting as a matrix and the optically active TTM radical.

© 2023 The Authors. Small published by Wiley-VCH GmbH

16136829, 2023, 32, Downloaded from https://onlinelibrary.wiley.com/doi/10.1002/smll.202207806 by Csic Organización Central Om (Oficialia Mayor) (Urici), Wiley Online Library on [30/05/2024]. See the Terms and Conditions (https://onlinelibrary.wiley.com/terms-and-conditions) on Wiley Online Library for rules of use; OA articles are governed by the applicable Creative Commons License

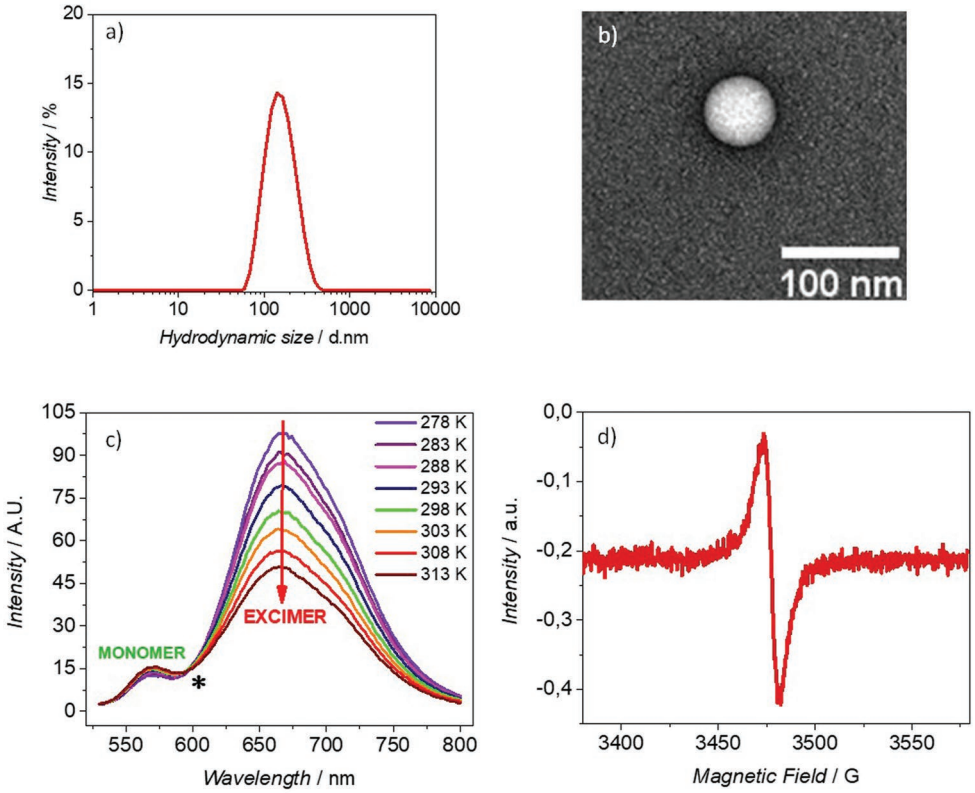


Figure 2. TTMd-ONPs 20% water suspension (with 5% in vol of THF); a) dynamic light scattering (DLS) size distribution at RT and b) representative TEM image of one TTMd-ONP; c) fluorescence emission spectra changing the temperature in the range 278 – 313 K (step 5 K). The isostilbic point is marked with an asterisk. d) EPR signal at RT.

properties of TTM radical doped ONPs offer outstanding opportunities as contactless nanothermometer. To accomplish such objective, we started investigating the TTMd-ONPs composed of 20% w/w of TTM radical dispersed in the TTM-αH matrix. These ONPs were prepared by slow dropping of a THF solution of the two mixed molecules into MilliQ water as reported.[36,37] The resulting water suspension of ONPs (with 5% in vol of THF), showed an average hydrodynamic diameter of 100 nm with negative Z-potentials close to –45 mV (**Figure 2**a). Figure 2 shows the emission spectra of these particles as a function of temperature in the 278 –313 K range. The excimer emission at 665 nm is strongly quenched upon increasing the temperature, while the monomer emission at 572 nm is weakly affected by the thermal variation. The system exhibits an isostilbic point at 594 nm clearly indicating a temperature-controlled equilibrium between monomers and excimers (Figure S1a, Supporting Information). Moreover, electron paramagnetic resonance (EPR) measurements of TTMd-ONPs (Figure 2d) demonstrate that the radical magnetic properties are preserved inside the nanoparticles.

Figure 3a,b shows the absorption spectra of water suspension of TTMd-ONPs and the temperature-dependence of the excimer (orange) and monomer (blue) maximum emission intensities. Interestingly, as it can be seen following the temperature-dependence of the luminescent intensity ratio, LIR = I_M/I_E, the process is completely reversible (Figure 3c; Figure S1b, Supporting Information), so collections of TTMd-ONPs can be used to monitor real-time temperature variations of their suspensions. We already observed in our previous work that changing the TTM doping concentration in ONPs, allows tuning both the monomer/excimer fluorescence intensity ratio and the maximum wavelength of the excimer emission band, which is red-shifted upon increasing the radical concentration.[25,36,37] For this reason, ONPs with different % of doping were prepared (15, 20, 25% w/w of TTM) and the resulting suspensions of ONPs in water with a 5% of THF showed average sizes and Z-potentials values of 100 nm, with narrow size distribution, and –45 mV, respectively.

The thermometric parameter I_M/I_E at different temperatures were fitted with the empirical Equation (1).[25,39,40]

$$\mathrm{LIR} = \frac{I_M}{I_E} = a + b\exp(cT) \quad (1)$$

where I_M and I_E correspond to the maximum intensity of fluorescence emission of the monomer and excimer respectively, and a, b, and c are constants.

To determine the performance of the nanothermometric system we evaluated the luminescent intensity ratio (LIR) and compare the results with other reported sensors determining the absolute sensitivity (S_a), using Equation S1 (Supporting Information).

However, to compare LIR of systems, that are different in nature, it is preferable to use the relative sensitivity (S_r)

© 2023 The Authors. Small published by Wiley-VCH GmbH

16136829, 2023, 32, Downloaded from https://onlinelibrary.wiley.com/doi/10.1002/smll.202207806 by Csic Organización Central Om (Oficialia Mayor) (Urici), Wiley Online Library on [30/05/2024]. See the Terms and Conditions (https://onlinelibrary.wiley.com/terms-and-conditions) on Wiley Online Library for rules of use; OA articles are governed by the applicable Creative Commons License

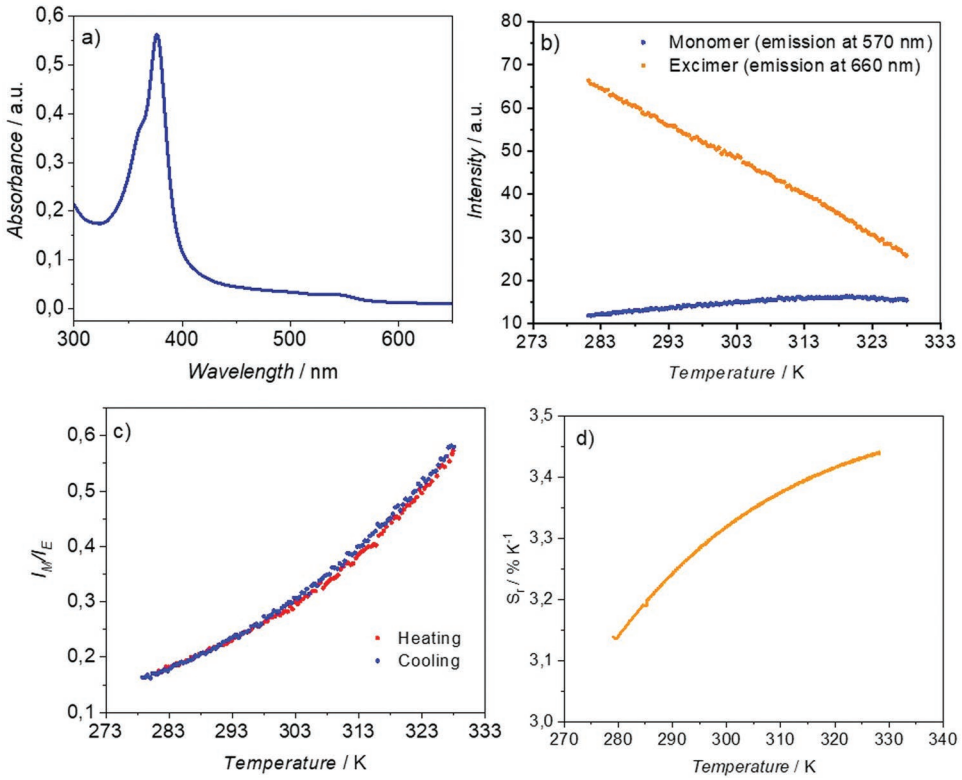


Figure 3. TTMd-ONPs 20% water suspension (with a 5% of THF); a) absorption spectrum, b) temperature-dependent excimer (orange) and monomer (blue) maximum emission intensities, c) luminescent intensity ratio of monomer over excimer in one cycle heating/cooling showing the high reversibility of temperature sensing of the ONPs and d) relative sensitivity of the particles with increasing temperature.

parameter and not the absolute sensitivity (S_a) value, given by Equation (2).[25,39,40]

$$S_r = \left|\frac{\partial Q / \partial T}{Q}\right| \times 100\%, \ [\%\cdot K^{-1}] \quad (2)$$

Temperature dependence of ratiometric output $Q(T)$ was obtained by fitting the experimental I_M/I_E ratio with the empirical Equation (1), for the three TTMd-ONPs samples (Figure S2, Supporting Information). Afterwards, to evaluate the performance of every sample as nanothermometer, it was calculated the values of the absolute and relative sensitivity, using Equations S1 (Supporting Information) and 2, respectively (Figure S2, Supporting Information). TTMd-ONPs with 20% of TTM exhibited the best relative sensitivity all along the investigated temperature range, showing a thermal relative sensitivity at RT of S_r = 3.3%K^{-1} (T = 298 K); one of the highest values reported for nanothermometers based on small fluorescent metal-free organic molecules using an intensity-based method for the thermal detection.[41] The smallest detectable temperature change or minimum temperature resolution was estimated, using Equation S2 (Supporting Information), as ΔT_{min} = 0.3 degree, which is very good compared with other reported systems.[8,42] Hence, 20% TTMd-ONPs suspension was chosen as the optimal suspension for further studies (Figure 3).

To use the TTMd-ONPs as contactless nanothermometers for bio-sensing, the suspension was dialyzed to remove the remaining organic solvent (THF), present due to particle preparation. Dialysis caused a small reduction of the relative sensitivity since ONPs dispersed in pure MilliQ water showed a S_r = 2.3% K^{-1} (T = 298 K) (Figure S3, Supporting Information). This sensitivity change is attributed to the elimination of THF traces that may be trapped into the ONPs during the self-assembly process. It is remarkable, that above 283 K the sensitivity remains above 2% K^{-1}, which is a very promising result considering the generally accepted value of 0.5% K^{-1} quality threshold for useful biosensing nanothermometers,[25] which is exceed by our ONPs in the whole temperature range. The effect of the dialysis did not affect the ONPs morphology, size, or size distribution. Thus, ONPs presented a uniform monomodal size distribution, with an average diameter of 106 ± 21 nm (Figure S4, Supporting Information), a Z-potential of –42 mV and a spherical shape, exactly as observed for samples after preparation.[37]

To move on toward biological applications of 20% TTMd-ONPs as nanothermometers, their spectroscopic and colloidal properties were tested in conditions more similar to those of intracellular and biological environments. First, we verified that the ratiometric output or LIR thermometric parameter of TTMd-ONPs suspensions is independent of concentration fluctuations because this issue is fundamental in bio-imaging since ONPs could accumulate differently in specific areas of the analyzed cells or tissues. With this aim, the thermometric parameter of 20% TTMd-ONPs in pure MilliQ water was compared with the 1:3 dilution (20% TTMd-ONPs dil). Results in Figure S5 (Supporting Information) demonstrate that both

© 2023 The Authors. Small published by Wiley-VCH GmbH

16136829, 2023, 32, Downloaded from https://onlinelibrary.wiley.com/doi/10.1002/smll.202207806 by Csic Organización Central Om (Oficialia Mayor) (Urici), Wiley Online Library on [30/05/2024]. See the Terms and Conditions (https://onlinelibrary.wiley.com/terms-and-conditions) on Wiley Online Library for rules of use; OA articles are governed by the applicable Creative Commons License

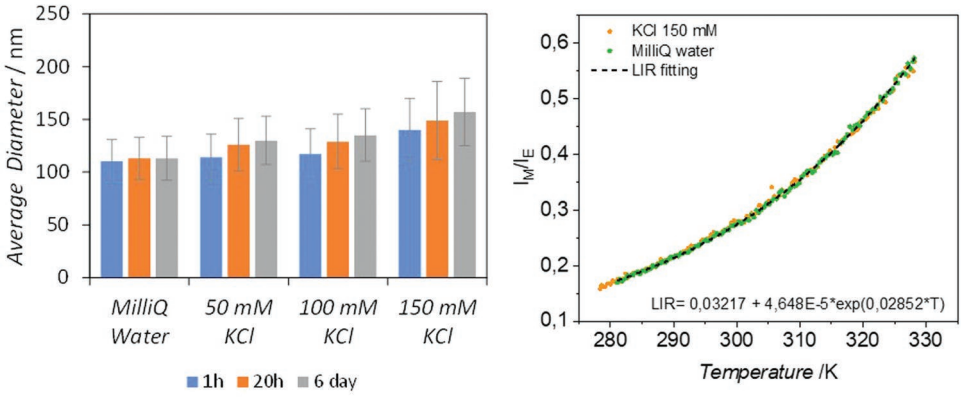


Figure 4. Effect of the ionic strength on the optical and colloidal properties of 20% TTMd-ONPs water suspensions. KCl was added in three concentrations: 50, 100, and 150 mM. Left) Size stability by DLS; right) stability of fluorescence intensity ratios as a function of temperature.

suspensions exhibit the same ratiometric output and sensitivity. The effect of the ionic strength on the optical and colloidal properties was also analyzed because it is well known that the presence of salts can affect the colloidal stability of the suspensions enhancing aggregation of ONPs with concomitant optical changes. The most abundant ion in the cytoplasm is potassium, with a concentration of ≈139 mM.[27] Thus, in order to evaluate the effect of the K^+ ion on the optical properties and the colloidal stability of 20% TTMd-ONPs suspensions, KCl was added in a fresh-dialyzed sample in three different concentrations: 50, 100, and 150 mM. The three resulting suspensions and the suspension in pure MilliQ water were analyzed by dynamic light scattering (DLS) technique at 1 h, 20 h, and 6 days after the addition of the potassium salt, and the results are reported in **Figure 4**. In pure water, the system is extremely stable and no appreciable changes occur during six days; a result that can be ascribed to the highly negative values of the Z-potential of ONPs preventing their aggregation. Adding higher amounts of KCl salt slightly destabilizes the suspensions, but small signals of aggregation can be observed only after six days with the largest salt concentration of 150 mM assayed. Nevertheless, no changes in the optical response of the ONPs were associated with this aggregation since the fluorescence intensity rations of the sample in MilliQ water and the one with KCl at 150 mM, after six days are not significantly different (Figure 4). This result shows that suspensions of a collection of isolated ONPs and those with some degree of aggregation exhibit the same emissive properties.

Another key parameter to consider for biosensing applications of ONPs is the pH. The regulation of the pH is a fundamental process for cell's correct growth and function. Indeed, cellular metabolic activities, with CO_2 and lactic acid production, can modify the intracellular pH-inducing complex H_3O^+ transporting processes.[43–45] Consequently, the optical properties and colloidal stability of 20% TTMd-ONPs suspensions were tested in the range of pH 5–8 using phosphate-buffered saline (PBS) solutions (Table S1, Supporting Information). Analyzing the DLS data of suspensions at three different pH values during 4 days (Figure S6, Supporting Information), shows that the most acidic media (pH 5) promotes a small aggregation of the particles after 4 days, while the suspension at pH 8 does not show any signal of aggregation. This result is consistent with the fact that ONPs present a negative value of Z-potential. Also, in this case, the I_M/I_E luminescent intensity ratios of the three suspensions are not significantly different.

As the last physicochemical characterization, we checked the colloidal and emission stability of the 20% TTMd-ONPs suspensions after prolonged thermal stress in order to evaluate the possibility to use such nanoparticles also as nanothermometers in hyperthermia therapy. PBS was added to a fresh dialyzed sample to buffer the pH at 5.0, 6.5, and 8.0, with an ionic strength of 150 mM (Table S2, Supporting Information). The resulting suspensions together with the nanoparticles in MilliQ water were heated for 2 h at 323 K and DLS analysis was performed before heating, and after 1 h and 2 h of heating (Figure S7, Supporting Information). In MilliQ water the heating process does not induce any growth of particles while in the presence of PBS there is a slight tendency to increase particle size which is almost independent of the pH. Prolonged heating at 323 K did not induce any precipitation or drastic aggregation; thus, the 20% TTMd-ONPs is a robust system to be considered as a fluorescent nanothermometer suitable also for sensing in different environmental conditions relevant for in vivo applications, i.e., hyperthermia therapy.

To use TTMd-ONPs as nanothermometers for cellular biosensing we performed a viability assay[46] evaluating the metabolic activity of cells in the presence of 20% TTMd-ONPs suspensions using the 3-(4,-5-dimethylthiazo-l-2yl-)2,-5diphenyltrtrazolium bromide (MTT) colorimetric assay. The obtained cell viability results with COS-7 cells, a kidney fibroblast-like cell line (Figure S8, Supporting Information), indicate that such cells are viable in all tested concentrations of ONPs. Additionally, tsa201 embryonic adherent cells, a transformed human kidney cell line, were incubated with the ONPs suspension. Fluorescence microscopy images showed healthy cell morphologies which support the good biocompatibility of the ONPs (Figure S9, Supporting Information).

Once we have demonstrated that suspensions of TTMd-ONPs are not cytotoxic and permit us to sense the temperature of their aqueous surrounding media with high sensitivity, we addressed if isolated nanoparticles might sense the local temperature at the nanoscale. We incubated 20% TTMd-ONPs suspensions at a given concentration on top of a small glass coverslip treated with poly-L-Lys for ONP attachment, which

© 2023 The Authors. Small published by Wiley-VCH GmbH

16136829, 2023, 32, Downloaded from https://onlinelibrary.wiley.com/doi/10.1002/smll.202207806 by Csic Organización Central Om (Oficialia Mayor) (Urici), Wiley Online Library on [30/05/2024]. See the Terms and Conditions (https://onlinelibrary.wiley.com/terms-and-conditions) on Wiley Online Library for rules of use; OA articles are governed by the applicable Creative Commons License

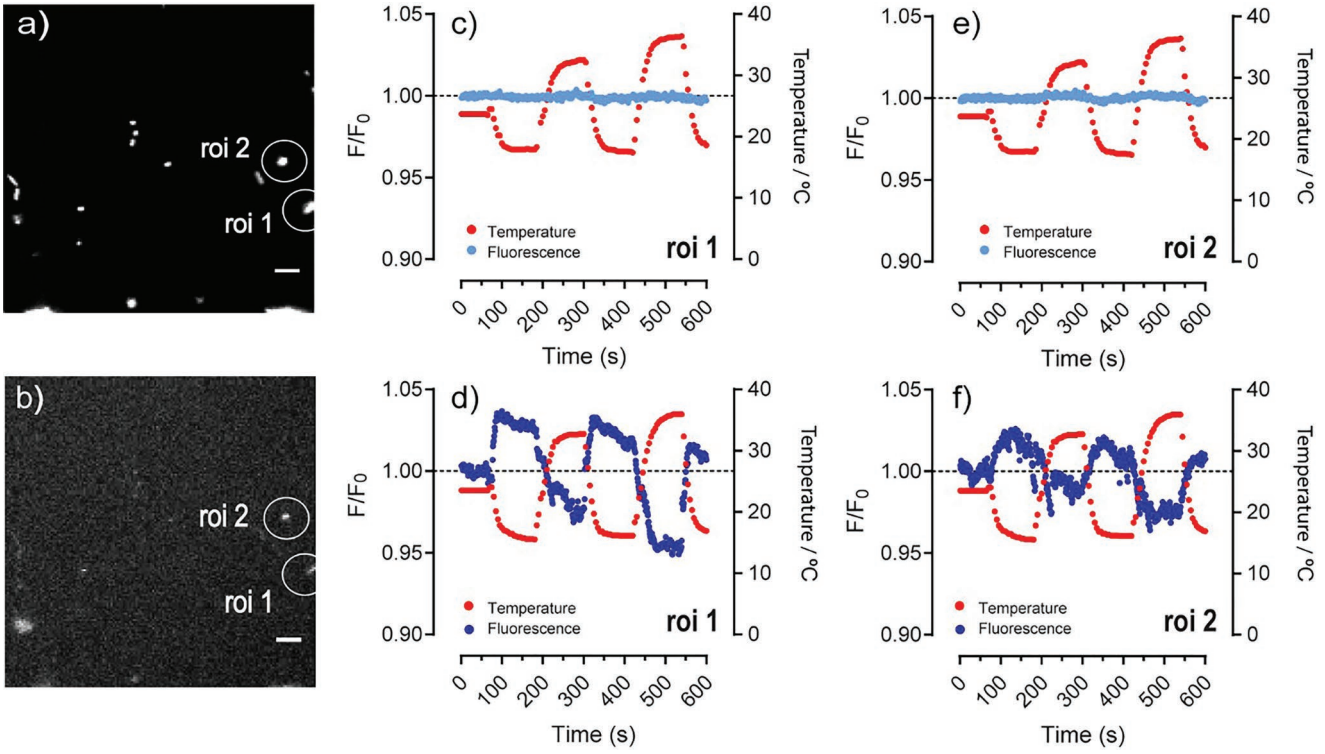


Figure 5. Representative images and fluorescence intensity versus time traces of 20% TTMd-ONPs in response to sequential temperature gradients. Images and emissive signals for ROIs #1 and # 2 were recorded with a fluorescence inverted microscope exciting at λ_{exc} = 377 nm and detecting the emission with a 510–560 nm filter for the monomers (a) and with a 595–670 nm filter for the excimers (b). Scale bar 1 μM. Variation of the fluorescence intensity ratio (F/F_0) emitted by the monomers (c,e) and by the excimers (d,f) in a temperature interval of ≈20 degrees.

was connected to a fluidic system. We placed under the coverslip a system to cool down and warm up the sample with a temperature amplitude of +/−20 degrees. To test for reversibility and homogeneity, we performed two cold-hot cycles in each measurement, choosing different regions of interest (ROIs) whose fluorescence signals were analyzed separately (**Figure 5**). To record the TTMd-ONPs fluorescence signals, we employed an inverted fluorescence microscope exciting at λ_{exc} = 377 nm (using a monochromatic light source based on a xenon lamp) and reading the emissions with two different dichroic filters: the first one at 510–560 nm recording the emission of monomers and the second one at 595–670 nm for the excimer's emission (Figure 5a,b). Interestingly, the monomer fluorescence intensities of nanoparticles in two ROIs remained almost constant in a temperature interval of ≈20 degrees (Figure 5c,e), while the excimer signals were inversely proportional to it (Figure 5d,f). This result demonstrates that TTMd-ONPs can sense temperature changes locally at the nanoscale, and behave as ratiometric temperature nanoprobes. For statistical analysis of fluorescence emission signals, see Figure S10 (Supporting Information).

After demonstrating the temperature sensing capability of 20% TTMd-ONPs at the submicron scale, we measured the temperature in living *Caenorhabditis elegans (C. elegans)* worms as an in vivo model system. *C. elegans* is a 1 mm long nematodes, with a short life cycle, rapid reproduction, optical transparency, and physiological similarity with humans.[47] Therefore, *C. elegans* offer experimental simplicity and valuable information as an animal model to test bioimaging probes,[42,48] for nanothermometry experiments using nanoparticles.[42,49,50]

Before using our ONPs in *C. elegans*, we carried out several control experiments of the ONPs´ behavior in the environment of *C. elegans*. First, we checked if the M9 buffer, the saline medium commonly used to maintain and expose ONPs to *C. elegans*, affected the hydrodynamic sizes and size distributions of the 20% TTMd-ONPs over time. During the first 24 h (time of ONPs exposure to *C. elegans*) no significant changes in the average hydrodynamic size and size distributions of ONPs occurred (Figure S11, Supporting Information). So, the nanoparticles preserve their original average diameter of ≈100 nm, which is an appropriate size to be ingested by the worms. The L4 larval stage worms were treated with 55 μg mL^{-1} suspension of 20% TTMd-ONPs in liquid M9 buffer for 24 h (**Figure 6**; Figure S12, Supporting Information). After 24 h of exposure 97% of worms were alive with no significant difference from the control group, which demonstrates that ONPs are not lethal for the worms. Similarly, we also measured body length after exposure to examine the growth and development of *C. elegans* from the L4 to the egg-bearing adult stage during the 24 h, and found that the ONPs did not affect the rate of development significantly. The survival and development assays confirm that the TTMd-ONPs do not show any biological toxicity in *C. elegans*. A third control experiment was employed to determine the survival rate of *C. elegans* at different temperatures. This test helped to identify at which temperature the worms died to determine the temperature range to use the worms as

© 2023 The Authors. Small published by Wiley-VCH GmbH

16136829, 2023, 32, Downloaded from https://onlinelibrary.wiley.com/doi/10.1002/smll.202207806 by Csic Organización Central Om (Oficialia Mayor) (Urici), Wiley Online Library on [30/05/2024]. See the Terms and Conditions (https://onlinelibrary.wiley.com/terms-and-conditions) on Wiley Online Library for rules of use; OA articles are governed by the applicable Creative Commons License

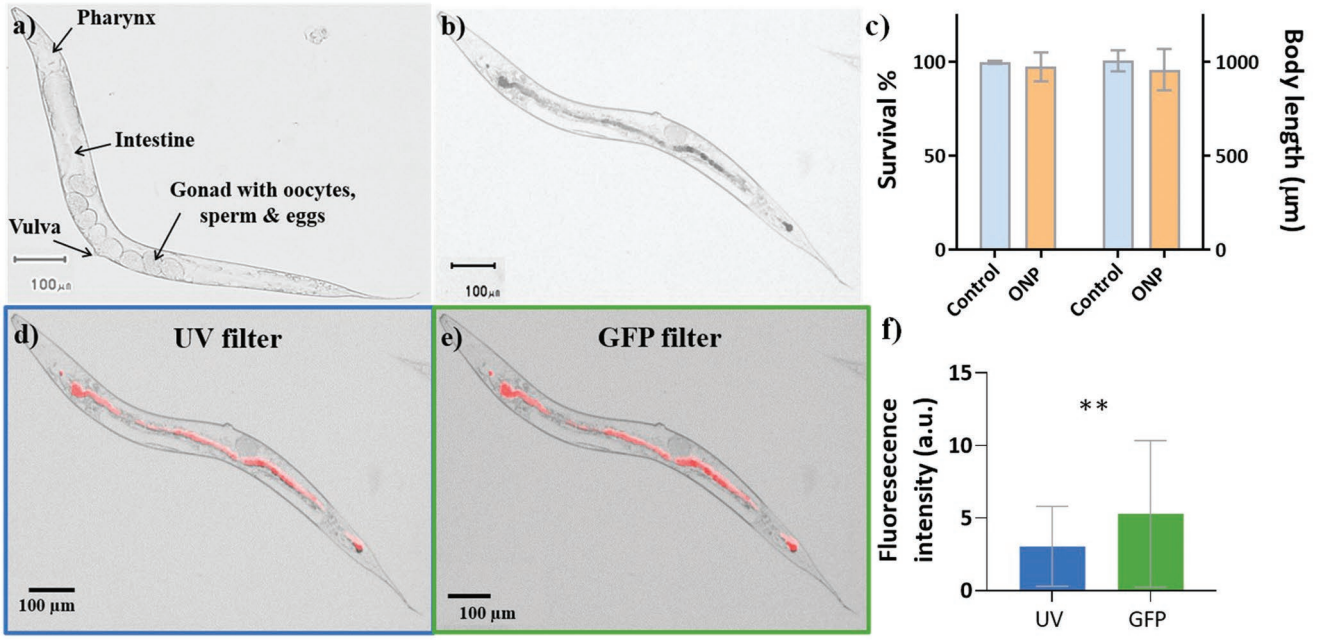


Figure 6. a) Untreated control *C. elegans* where some anatomical parts of the worm are described; b) *C. elegans* treated with ONPs. c) Survival rate and body length of *C. elegans* with and without ONPs. Treated worms under d) UV filter (>510 nm), e) GFP filter (>590 nm), where the TTM-ONPs are visualized in the intestine; f) comparative fluorescence intensity of ONPs under the two filters.

a model system to test the TTMd-ONPs as nanothermometers. *C. elegans* were heated up with steps of 5 K starting from 293 until 328 K. For each temperature, after two minutes of stabilization, a few drops of the worms' suspension were observed under the microscope to count the dead and alive worms. The survival rate at 293 K was considered as the positive control since some worms could have died for other reasons. Table S3 (Supporting Information) shows survival rates obtained in the studied temperature range, showing that, at 308 K, 72% of worms were still alive which declined drastically at temperatures higher than 313 K (Figure S13, Supporting Information). This result indicates that *C. elegans* can be used as an in vivo model system for validating ONPs as nanothermometers but only at temperatures below 313 K.

Then, we proceeded to observe the *C. elegans* exposed to 55 µg mL^{-1} of the 20% TTMd-ONPs with a fluorescence microscope using UV (> 510 nm) and Green (> 590 nm) long pass filters at RT to visualize ingested ONPs (Figure 6). The ONPs were ingested orally and passed through the pharynx to the intestines. Higher accumulation of ONPs can be observed near the pharynx since it acts as a filter-grinder and ONPs might concentrate there.[51]

After visualizing the nanoparticles within the worms, the output emission intensity of the ONPs was measured to check the validity of the luminescent ONPs as an in vivo nanothermometer. Taking advantage of the transparency of the worms, we proceeded in the same way as with the 20% TTMd-ONPs aqueous suspensions, measuring the emission of a suspension of *C. elegans* exposed to ONPs and control *C. elegans* in a cuvette. We compared the emission spectra of a suspension of *C. elegans* with a suspension of *C. elegans* exposed to ONPs at 278 and 298 K (Figure S14, Supporting Information). Interestingly, in the untreated *C. elegans* suspension, an emission band at 523 nm appears when the worms are alive which is attributed to their tissue autofluorescence, that overlaps with the monomer band of the ONPs.[52] The intensity of this band increases significantly when the sample is heated at 328 K and remains intense when the suspension was cooled down to 278 K. Indeed, the increase of this band has been attributed to the death of the worms with the temperature and the denaturation of proteins.[53] In the literature, a model predicts that 1% of the *C. elegans* proteome should be denatured at 320 K and 50% of their proteome is denatured at 326 K.[54] These results indicate that *C. elegans* cannot be used as model systems for evaluating in vivo the performances of ONPs as nanothermometers at temperatures higher than 313 K.

Finally, to determine the sensitivity of 20% TTMd-ONPs inside the worms as nanothermometers and to compare it with the free nanoparticles, further emission spectra were performed. For both suspensions, an emission scan was performed at 278 K with an excitation wavelength of 377 nm to obtain the maxima of the monomer and excimer emission bands of the TTMd-ONPs in the two samples. Then, a thermal scan was performed, recording only the maximum intensity for the excimer and monomer bands, every 0.5 K, from 278 K until 313 K with a heating rate of 0.8 K min^{-1}. Finally, to check the reversibility of the system the inverse thermal scan was carried out, from 313 to 278 K. The luminescence intensity ratio (Q) between the maximum of the monomer, corrected by subtracting the emission of the worms due to its autofluorescence at 523 nm, and the maximum of excimer was plotted and fitted using the LIR empirical Equation (1) through data points at different temperatures. Then, deriving the LIR function of Q with respect to temperature, the thermal absolute sensitivity

© 2023 The Authors. Small published by Wiley-VCH GmbH

16136829, 2023, 32, Downloaded from https://onlinelibrary.wiley.com/doi/10.1002/smll.202207806 by Csic Organización Central Om (Oficialia Mayor) (Urici), Wiley Online Library on [30/05/2024]. See the Terms and Conditions (https://onlinelibrary.wiley.com/terms-and-conditions) on Wiley Online Library for rules of use; OA articles are governed by the applicable Creative Commons License

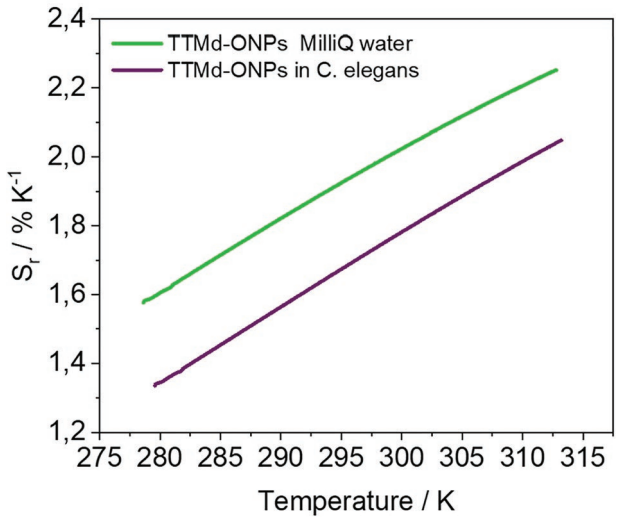


Figure 7. Relative sensitivity of TTMd-ONP as nanothermometer at different temperatures in water suspension (green) and inside *C. elegans* (violet).

values for both samples were obtained using Equation S1, and the relative sensitivity was determined using Equation (2). As observed in **Figure 7**, the sensitivity of the ONPs ingested in *C. elegans* (TTMd-ONP *C. elegans*) was successfully measured and found to be very significant, $S_r = 1.7\%\ K^{-1}$ ($T = 298$ K). The relative temperature sensitivity is always higher than 1% K^{-1} in the whole evaluated temperature range, which is twice the threshold quality value of 0.5% K^{-1} set in the literature for nanothermometry applications.[25] In addition we also estimated a minimum temperature resolution of $\Delta T_{min} = 0.6$ degrees, using Equation S2 (Supporting Information), which is also a very promising result for future applications of TTMd-ONPs as in vivo fluorescent nanothermometers.

The possibility to measure changes of temperature dependent fluorescence emission, of organic nanoparticles in a live organism is very promising, but to use them in practical applications, it is necessary to show the performance of this nanothermometer locally at the submicron scale. Hence, we have measured temperature changes inside individual *C. elegans* in a localized area of their intestine, using a confocal microscope. For confocal measurements, *C. elegans* were immobilized using NemaGel, and changes in temperature were recorded by tracking the fluorescence emission intensity at two wavelength ranges, 420–570 and 620–720 nm to record the emission associated with the monomer and the excimer, respectively. A 3D representation of the *C. elegans* intestine with the ingested TTMd-ONPs is represented in Figure S15 (Supporting Information) with also a zoom of a small area showing emission of monomer (green) and excimer (red) of a single TTMd-ONPs particle/aggregate.

Three different temperature ranges were studied starting from 290–293 K by cooling the microscope cage with dry ice, then increasing it to 297–300 K and finally to 307–308 K, by using a heater coupled to the confocal. For each temperature at least 6 measurements were recorded to have statistical data. In **Figure 8**a is represented the ratio between monomer and excimer emission in the bottom region of the intestine of the *C. elegans*, the data for the top region is represented in Figure S16 (Supporting Information).

As demonstrated above, with increasing temperature, the ratio between the monomer and excimer emissions bands (Q) increases and the same behavior is shown locally inside an individual *C. elegans*. These results demonstrate that these ONPs can be used to measure the temperature in a small localized area of a single animal.

Even though the deviation for each temperature range is broad because every *C. elegans* is different and can metabolize the TTMd-ONPs in different ways, similar ratiometric behavior to that obtained in vitro is observed. When increasing the temperature, the fluorescence emission intensity decreases for the red frame (420–570 nm) and keeps constant for the green one (620–720 nm). For a better understanding of the data, Figure 8b shows the same *C. elegans* animal at two different temperatures. At higher temperature a decrease of fluorescence intensity of the nanoparticles at higher wavelengths is observed, supporting the reported data.

3. Conclusion

We have developed organic radical TTMd-ONPs, as ratiometric nanothermometers based on a radical excimer for in vivo sensing with excellent temperature sensitivity 3.4% K^{-1} (at 328 K), reversibility and high colloidal stability. One of the advantages of the described system is its simplicity since both the host and guest molecules forming the nanoparticles are small metal-free organic molecules which allow higher control on the molecular structure, higher reproducibility of the synthesis, and easier purification than polymers. Moreover, both the host and the guest molecules, the TTM-αH and TTM radical, respectively, are processed as nanoparticles by the self-assembly of the two molecules in a simple single-step process using the re-precipitation method. Thanks to the simplicity of the synthesis of the two molecules and their self-assembly properties, TTMd-ONPs constitute an example of a cost-effective thermal sensor. In pure water the suspension of TTMd-ONPs is colloidally stable offering the possibility to be stored for a long time without aggregation or radical-leaking phenomena. The colloidal properties are preserved even increasing the ionic strength and varying the pH in the range of 5 – 8. Furthermore, TTMd-ONPs show two emission bands with a ratiometric output or LIR thermometric parameter, that is independent of dilution, particle aggregation, ionic strength, and pH, while was strongly affected by changes in temperature, showing a completely reversible behavior without any hysteresis. The second strength of TTMd-ONPs is provided by the open-shell electronic configuration of the TTM radical emitter molecule, present as a monomer or as an excimer, which ensures better optical performances than close-shell fluorophores. Indeed, sensors based on organic closed-shell fluorophores show low values of Stokes shift and short lifetimes (≈ ns), which make these systems subjected to use inner-filter effects and showing scattering problems. Thanks to the large Stokes shift and their large emission lifetime (for both the monomer and the excimer emission) TTMd-ONPs can avoid problems related to the autofluorescence of the biological tissue or the scattering of the

© 2023 The Authors. Small published by Wiley-VCH GmbH

16136829, 2023, 32, Downloaded from https://onlinelibrary.wiley.com/doi/10.1002/smll.202207806 by Csic Organización Central Om (Oficialia Mayor) (Urici), Wiley Online Library on [30/05/2024]. See the Terms and Conditions (https://onlinelibrary.wiley.com/terms-and-conditions) on Wiley Online Library for rules of use; OA articles are governed by the applicable Creative Commons License

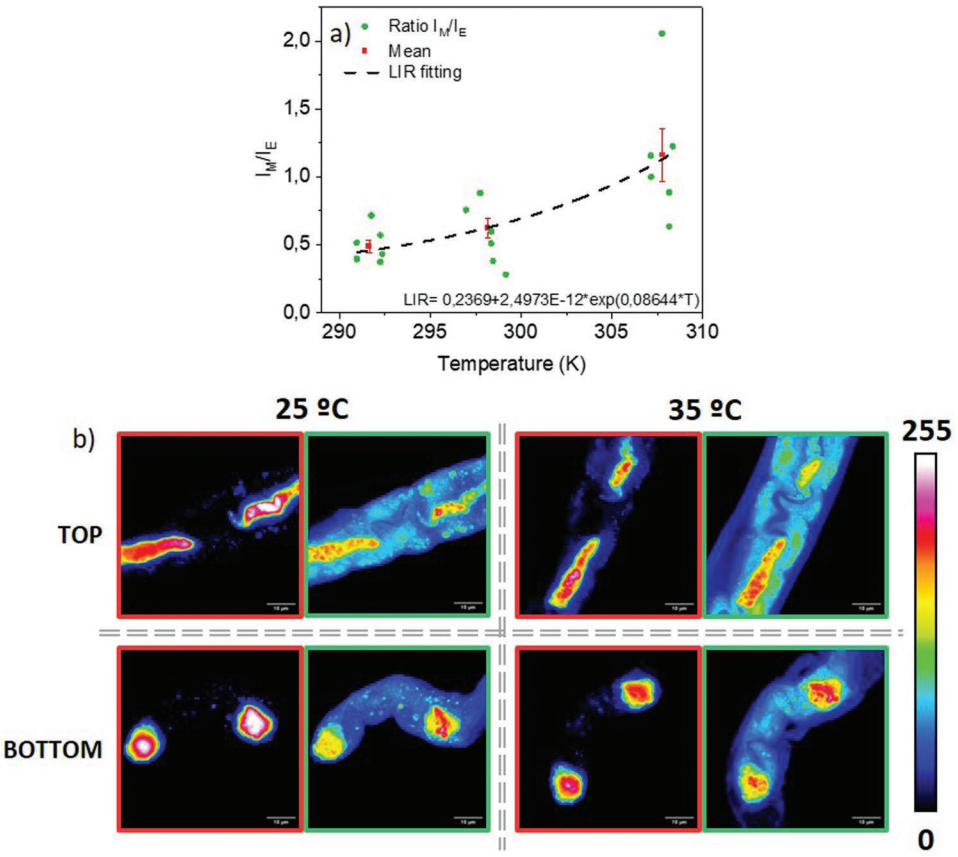


Figure 8. a) Local measurement of the ratio (Q) I_M/I_E between monomer and excimer maxima fluorescence emission at increasing temperature of the TTMd-ONPs inside *C. elegans*, from a region of the bottom of the body. Red points represent the average of the ratios and the error bars are the standard errors caused by different worms for the same temperature range, for $n = 6$ and $p = 0.9917$, 0.9994, and 0.9959, respectively; b) representative confocal images of the top and bottom parts from the same *C. elegans* with TTMd-ONPs inside the intestine at two different temperatures, 298 K (left) and 308 K (right). The green frame represents the 420–570 nm detection wavelength and the red frame the 620–720 nm wavelength. Scale bar 10 µM. The color scale shows pixels with the lowest intensity (0) to the highest intensity (4095).

excitation light. Since simply applying a delay between the excitation and the detection it is possible to considerably increase the signal to noise ratio. Therefore, TTMd-ONPs constitute a small-molecule-based luminescence ratiometric sensor able to join the strengths of both organic and inorganic sensors but being all-organic. TTMd-ONPs emit in the region of deep-red/NIR (i.e., the first transparency windows of biological tissues), offering the opportunity to obtain a deep-tissue penetration for in vivo applications. In addition, TTMd-ONPs are not cytotoxic and their ratiometric outputs are unaffected by changes of small aggregations, pH or ionic strength that may occur under physiological conditions. Finally, in vivo thermometry experiments made with *Caenorhabditis elegans* worms indicated that TTMd-ONPs could monitor locally in vivo the temperature changes at the sub-micron scale from 278 to 313 K, with a high sensitivity indicating the considerable potential applications of TTMd-ONPs in the biological thermometry field. In addition, thanks to the chiroptical and magnetic properties of polyhalogenated trityl radicals,[55,56] new nanothermometers are being designed, enhancing the optical outputs and versatility of these systems for biological and clinical research.[57] Moreover, to use these systems in a biological environment, both, the excitation and the emission wavelength are required to be in the biological window. In a work in progress we are studying the use of TTMd-ONPs as two-photon microscopy probe to increase the excitation wavelength in order to have both the excitation and the emission wavelengths in the biological window increasing its penetration capacity into tissues and cells without damage.

Supporting Information

Supporting Information is available from the Wiley Online Library or from the author.

Acknowledgements

D.B. and N.G.-P. contributed equally to this work. The authors are grateful for the financial support received from the Spanish Government (PID2020-115296RA-I00, PID2019-105622RB-I00, PDI2021-122645OB-I00, RTI2018-096273-B-I00 and PID2019-111493RB-I00) funded by MICIN and the "Ramón y Cajal" program (RYC-2017-22614), the Generalitat de Catalunya (SGR-918, 2017SGR765, SGR Cat 2021-00438, 2017-SGR-1442, and 2021-SGR-1410, 2021-SGR-00446), and the Networking Research Center on Bioengineering, Biomaterials, and Nanomedicine (CIBER-BBN). DB gratefully acknoledges the REFIN (Return for Future

© 2023 The Authors. Small published by Wiley-VCH GmbH

16136829, 2023, 32, Downloaded from https://onlinelibrary.wiley.com/doi/10.1002/smll.202207806 by Csic Organización Central Om (Oficialia Mayor) (Urici), Wiley Online Library on [30/05/2024]. See the Terms and Conditions (https://onlinelibrary.wiley.com/terms-and-conditions) on Wiley Online Library for rules of use; OA articles are governed by the applicable Creative Commons License

Innovation) action for funding, an ininitiative co - funded by European Union through the POR Puglia 2014 - 2020 (ID grant: 2455F798). This research was also supported by the European Union's Horizon 2020 research and innovation program H2020-MSCA-COFUND-2016 (DOC-FAM, grant agreement Nr. 754397), Human Brain Project WaveScaES (SGA2-785907 and SGA3-945539), DEEPER (ICT36-2020-101016787), and the Marie Skłodowka-Curie grant agreement Nr. 101007804 (Micro4Nano). Support from Fundaluce and CaixaHealth (ID 100010434) are also acknowledged. The work was supported as well by the Max Planck Society through the Max Planck Partner Group "Dynamic Biomimetics for Cancer Immunotherapy" in collaboration with the Max Planck for Medical Research (Heidelberg, Germany). ICMAB-CSIC acknowledges support from the Severo Ochoa Programme for Centres of Excellence in R&D (FUNFUTURE, CEX2019-000917-S). IBEC acknowledges support from the CERCA programme of AGAUR/ Generalitat de Catalunya and the Severo Ochoa Programme. This work had been developed inside the "Biochemistry, Molecular Biology and Biomedicine" and "Materials Science" Ph.D. programs of UAB. Nerea Gonzalez-Pato acknowledges the financial support from the FPU fellowship (FPU17/02551) from the Spanish Ministry.

Conflict of Interest

The authors declare no conflict of interest.

Data Availability Statement

The data that support the findings of this study are available from the corresponding author upon reasonable request.

Keywords

Caenorhabditis elegans, excimer emission, in vivo sensing, luminescence, organic radical nanoparticles, ratiometric nanothermometers, trityl radicals

Received: December 13, 2022
Revised: March 24, 2023
Published online: April 14, 2023

[1] A. Majumdar, *Annu. Rev. Mater. Sci.* **1999**, *29*, 505.
[2] D. Halbertal, J. Cuppens, M. B. Shalom, L. Embon, N. Shadmi, Y. Anahory, H. R. Naren, J. Sarkar, A. Uri, Y. Ronen, Y. Myasoedov, L. S. Levitov, E. Joselevich, A. K. Geim, E. Zeldov, *Nature* **2016**, *539*, 407.
[3] M. Tzur, B. Desiatov, I. Goykhman, M. Grajower, U. Levy, *Opt. Express* **2013**, *21*, 29195.
[4] O. Yarimaga, S. Lee, D. Y. Ham, J. M. Choi, S. G. Kwon, M. Im, S. Kim, J. M. Kim, Y. K. Choi, *Macromol. Chem. Phys.* **2011**, *212*, 1211.
[5] K. Okabe, N. Inada, C. Gota, Y. Harada, T. Funatsu, S. Uchiyama, *Nat. Commun.* **2012**, *3*, 705.
[6] G. Kucsko, P. C. Maurer, N. Y. Yao, M. Kubo, H. J. Noh, P. K. Lo, H. Park, M. D. Lukin, *Nature* **2013**, *500*, 54.
[7] K. Okabe, R. Sakaguchi, B. Shi, S. Kiyonaka, *Pflugers Arch. Eur. J. Physiol.* **2018**, *470*, 717.
[8] J. Zhou, B. del Rosal, D. Jaque, S. Uchiyama, D. Jin, *Nat. Methods* **2020**, *17*, 967.
[9] M. Monti, L. Brandt, J. Ikomi-Kumm, H. Olsson, *Scand. J. Haematol.* **1986**, *36*, 353.
[10] E. N. Cerõn, D. H. Ortgies, B. Del Rosal, F. Ren, A. Benayas, F. Vetrone, D. Ma, F. Sanz-Rodríguez, J. G. Solé, D. Jaque, E. M. Rodríguez, *Adv. Mater.* **2015**, *27*, 4781.
[11] L. Meng, S. Jiang, M. Song, F. Yan, W. Zhang, B. Xu, W. Tian, *ACS Appl. Mater. Interfaces* **2020**, *12*, 26842.
[12] H. Zhou, M. Sharma, O. Berezin, D. Zuckerman, M. Y. Berezin, *ChemPhysChem* **2016**, *17*, 27.
[13] M. Quintanilla, M. Henriksen-Lacey, C. Renero-Lecuna, L. M. Liz-Marzán, *Chem. Soc. Rev.* **2022**, *51*, 4223.
[14] J. M. Lupton, *Appl. Phys. Lett.* **2002**, *81*, 2478.
[15] N. Chandrasekharan, L. A. Kelly, *J. Am. Chem. Soc.* **2001**, *123*, 9898.
[16] V. A. Vlaskin, N. Janssen, J. Van Rijssel, R. Beaulac, D. R. Gamelin, *Nano Lett.* **2010**, *10*, 3670.
[17] S. Rohani, M. Quintanilla, S. Tuccio, F. De Angelis, E. Cantelar, A. O. Govorov, L. Razzari, F. Vetrone, *Adv. Opt. Mater.* **2015**, *3*, 1606.
[18] X. Wang, Q. Liu, Y. Bu, C. S. Liu, T. Liu, X. Yan, *RSC Adv.* **2015**, *5*, 86219.
[19] J. Li, C. Sun, R. Shen, X. Cao, B. Zhou, D. Bai, H. Zhang, *J. Am. Chem. Soc.* **2014**, *136*, 11050.
[20] A. A. Tseng, K. Chen, C. D. Chen, K. J. Ma, *IEEE Trans. Electron. Packag. Manuf.* **2003**, *26*, 141.
[21] C.-W. Tseng, D.-C. Huang, Y.-T. Tao, *ACS Appl. Mater. Interfaces* **2012**, *4*, 5483.
[22] H. Zhang, J. Jiang, P. Gao, T. Yang, K. Y. Zhang, Z. Chen, S. Liu, W. Huang, Q. Zhao, *ACS Appl. Mater. Interfaces* **2018**, *10*, 17542.
[23] J. Daniel, F. Vetrone, *Nanoscale* **2012**, *4*, 4301.
[24] T. Barilero, T. L. Saux, C. Gosse, L. Jullien, *Anal. Chem.* **2009**, *81*, 7988.
[25] C. D. S. Brites, P. P. Lima, N. J. O. Silva, A. Millán, V. S. Amaral, F. Palacio, L. D. Carlos, *Nanoscale* **2012**, *4*, 4799.
[26] L. Jethi, M. M. Krause, P. Kambhampati, *J. Phys. Chem. Lett.* **2015**, *6*, 718.
[27] C. Gota, K. Okabe, T. Funatsu, Y. Harada, S. Uchiyama, *J. Am. Chem. Soc.* **2009**, *131*, 2766.
[28] S. Sinha, Z. Kelemen, E. Hümpfner, I. Ratera, J. P. Malval, J. P. Jurado, C. Viñas, F. Teixidor, R. Núñez, *Chem. Commun.* **2022**, *58*, 4016.
[29] X. Bai, W. Tan, A. Abdurahman, X. Li, F. Li, *Dyes Pigm.* **2022**, *202*, 110260.
[30] D. Mesto, Y. Dai, C. N. Dibenedetto, A. Punzi, J. Krajčovič, M. Striccoli, F. Negri, D. Blasi, *Euro. J. Org. Chem.* **2023**, *26*, 202201030.
[31] I. Ratera, J. Vidal-Gancedo, D. Maspoch, S. T. Bromley, N. Crivillers, M. Mas-Torrent, *J. Mater. Chem. C* **2021**, *9*, 10610.
[32] K. Kato, S. Kimura, T. Kusamoto, H. Nishihara, Y. Teki, *Angew. Chem., Int. Ed.* **2019**, *58*, 2606.
[33] S. Kimura, T. Kusamoto, S. Kimura, K. Kato, Y. Teki, H. Nishihara, *Angew. Chem., Int. Ed.* **2018**, *57*, 12711.
[34] A. Jana, L. Bai, X. Li, H. Ågren, Y. Zhao, *ACS Appl. Mater. Interfaces* **2016**, *8*, 2336.
[35] X. He, X. Shen, D. Li, Y. Liu, K. Jia, X. Liu, *ACS Appl. Bio Mater.* **2018**, *1*, 520.
[36] D. Blasi, *Molecular and Supramolecular Strategies for Highly Luminescent Trityl Radicals and Their Sensing Applications*, **2017**.
[37] D. Blasi, D. M. Nikolaidou, F. Terenziani, I. Ratera, J. Veciana, *Phys. Chem. Chem. Phys.* **2017**, *19*, 9313.
[38] J. Mérian, J. Gravier, F. Navarro, I. Texier, *Molecules* **2012**, *17*, 5564.
[39] M. Jia, Z. Sun, M. Zhang, H. Xu, Z. Fu, *Nanoscale* **2020**, *12*, 20776.
[40] H. Xu, M. Jia, Z. Wang, Y. Wei, Z. Fu, *ACS Appl. Mater. Interfaces* **2021**, *13*, 61506.
[41] Y. Sun, M. Fu, M. Bian, Q. Zhu, *Biotechnol. Bioeng.* **2023**, *120*, 7.
[42] M. Fujiwara, S. Sun, A. Dohms, Y. Nishimura, K. Suto, Y. Takezawa, K. Oshimi, L. Zhao, N. Sadzak, Y. Umehara, Y. Teki, N. Komatsu, O. Benson, Y. Shikano, E. Kage-Nakadai, *Sci. Adv.* **2020**, *6*, eaba9636.
[43] J. Kurkdjian, A. Guern, *Annu. Rev. Plant Physiol. Plant Mol. Biol.* **1989**, *40*, 271.

© 2023 The Authors. Small published by Wiley-VCH GmbH

16136829, 2023, 32, Downloaded from https://onlinelibrary.wiley.com/doi/10.1002/smll.202207806 by Csic Organización Central Om (Oficialia Mayor) (Urici), Wiley Online Library on [30/05/2024]. See the Terms and Conditions (https://onlinelibrary.wiley.com/terms-and-conditions) on Wiley Online Library for rules of use; OA articles are governed by the applicable Creative Commons License

[44] A. Hulikova, A. L. Harris, R. D. Vaughan-Jones, P. Swietach, *J. Cell. Physiol.* **2013**, *228*, 743.
[45] T. Bagar, K. Altenbach, N. D. Read, M. Benčina, *Eukaryotic Cell* **2009**, *8*, 703.
[46] Ö. S. Aslantürk, in *Genotoxicity – A Predictable Risk to Our Actual World*, (Eds: M. L. Larramendy, S. Soloneski) IntechOpen, London **2018**, https://doi.org/10.5772/interopen.69556.
[47] L. Gonzalez-Moragas, A. Roig, A. Laromaine, *Adv. Colloid Interface Sci.* **2015**, *219*, 10.
[48] J. Chen, C. Guo, M. Wang, L. Huang, L. Wang, C. Mi, J. Li, X. Fang, C. Mao, S. Xu, *J. Mater. Chem.* **2011**, *21*, 2632.
[49] T. Kimata, H. Sasakura, N. Ohnishi, N. Nishio, I. Mori, *Worm* **2012**, *1*, 31.
[50] J. S. Donner, S. A. Thompson, C. Alonso-Ortega, J. Morales, L. G. Rico, S. I. C. O. Santos, R. Quidant, *ACS Nano* **2013**, *7*, 8666.
[51] Z. F. Altun, D. Hall, *Alimentary System, Pharynx, in Worm Atlas* **2009**, http://dx.doi.org/doi:10.3908/wormatlas.1.3.
[52] Z. Pincus, T. C. Mazer, F. J. Slack, *Aging* **2016**, *8*, 889.
[53] D. Jones, E. P. M. Candido, *J. Exp. Zool.* **1999**, *284*, 147.
[54] K. Ghosh, K. Dill, *Biophys. J.* **2010**, *99*, 3996.
[55] P. Mayorga-Burrezo, V. G. Jiménez, D. Blasi, T. Parella, I. Ratera, A. G. Campaña, J. Veciana, *Chem. – Eur. J.* **2020**, *26*, 3776.
[56] P. Mayorga Burrezo, V. G. Jiménez, D. Blasi, I. Ratera, A. G. Campaña, J. Veciana, *Angew. Chem., Int. Ed.* **2019**, *58*, 16282.
[57] C. He, H. He, J. Chang, B. Chen, H. Ma, M. J. Booth, *Light: Sci. Appl.* **2021**, *10*, 194.

© 2023 The Authors. Small published by Wiley-VCH GmbH

16136829, 2023, 32, Downloaded from https://onlinelibrary.wiley.com/doi/10.1002/smll.202207806 by Csic Organización Central Om (Oficialia Mayor) (Urici), Wiley Online Library on [30/05/2024]. See the Terms and Conditions (https://onlinelibrary.wiley.com/terms-and-conditions) on Wiley Online Library for rules of use; OA articles are governed by the applicable Creative Commons License

NANO MICRO small

Supporting Information

for *Small,* DOI: 10.1002/smll.202207806

Ratiometric Nanothermometer Based on a Radical Excimer for In Vivo Sensing

Davide Blasi, Nerea Gonzalez-Pato, Xavier Rodriguez Rodriguez, Iñigo Diez-Zabala, Sumithra Yasaswini Srinivasan, Núria Camarero, Oriol Esquivias, Mònica Roldán, Judith Guasch, Anna Laromaine, Pau Gorostiza, Jaume Veciana, and Imma Ratera**

Supporting Information

Ratiometric nanothermometer based on a radical excimer for *in vivo* sensing

Davide Blasi,[⊥] Nerea Gonzalez-Pato,[⊥] Xavier Rodriguez-Rodriguez, Iñigo Diez-Zabala, Sumithra Yasaswini Srinivasan, Núria Camarero, Oriol Esquivias, Mònica Roldán, Judith Guasch, Anna Laromaine, Pau Gorostiza, Jaume Veciana, Imma Ratera**

D. Blasi, N. Gonzalez-Pato, X. Rodriguez-Rodriguez, I. Diez-Zabala, S. Y. Srinivasan, O. Esquivias, J. Guasch, A. Laromaine, J. Veciana, I. Ratera

Institut de Ciència de Materials de Barcelona (ICMAB-CSIC), 08193 Bellaterra, Spain.

E-mail: iratera@icmab.es, jveciana@icamb.es

D. Blasi,
Dipartimento di Chimica, Università degli Studi di Bari "Aldo Moro", 70125 – Bari, Italy
N. Gonzalez-Pato, X. Rodriguez-Rodriguez, J. Guasch, P. Gorostiza, J. Veciana, I. Ratera
Networking Research Center on Bioengineering, Biomaterials and Nanomedicine (CIBER-BBN), Campus UAB, Bellaterra, 08193, Spain.
N. Camarero, P. Gorostiza
Institute for Bioengineering of Catalonia (IBEC), The Barcelona Institute of Science and Technology, Ed. Hèlix | Baldiri Reixac 15-2, 08028-Barcelona Spain
M. Roldán
Unitat de Microscòpia Confocal i Imatge Cellular, Servei de Medicina Genètica i Molecular, Institut Pediàtric de Malaties Rares (IPER), Hospital Sant Joan de Déu, 08950 Esplugues de Llobregat, Spain
J. Guasch
Dynamic Biomimetics for Cancer Immunotherapy, Max Planck Partner Group, ICMAB-CSIC, Campus UAB, Bellaterra, 08193, Spain.
P. Gorostiza
Catalan Institution for Research and Advanced Studies (ICREA)

[⊥] Davide Blasi, Nerea Gonzalez-Pato contributed equally to this work

Keywords**:** ratiometric nanothermometer, luminescence, organic radical nanoparticles, excimer emission, in-vivo sensing, *Caenorhabditis elegans*

The data that support the findings of this study are available from the corresponding author upon reasonable request.

1. Materials, reagents, and solvents

Tris(2,4,6-trichlorophenyl) methyl radical (TTM) and tris(2,4,6-trichlorophenyl) methane (TTM-αH) were synthesized as previously reported.[1,2] Tetrahydrofuran (THF, HPLC grade from Chem-Lab.) and ultrapure MilliQ water were used for the preparation of ONPs using the re-precipitation method.[3]

2. Equipment and measurements

Absorbance measurements were performed using a V-780 UV-Visible/NIR Spectrophotometer from JASCO. We used quartz glass cuvettes with path lengths of 1 cm, as they are transparent in the UV-visible-NIR range. The range of wavelengths recorded was from 250 nm to 850 nm. First, a cuvette with the solvent (blank) was placed inside the spectrophotometer to obtain its absorption spectra, which will be later subtracted from the absorbance values obtained from the sample, to obtain the real absorbance values of the ONPs.

A Cary Eclipse Fluorescence Spectrophotometer coupled with a temperature controller was used to measure the fluorescent emission intensity of prepared suspensions. The fluorimeter had a multi-holder with four cavities for measuring quartz glass cuvettes. One cuvette of 1 cm path length was filled with water, containing the temperature probe to have a precise value of the temperature inside the cuvettes. For the ONPs suspensions, 1 cm path length cuvettes were also used while stirring with a magnetic stir bar, whereas for the *C. elegans* a 1 cm path length sub-micro cuvette was used because the worms precipitated at the bottom at higher volumes; so low volumes were preferable to concentrate all the worms in a small volume. An excitation wavelength of 377 nm was used for all measurements. First, an emission scan from 400 nm to 850 nm at 298 K and 278 K was recorded to obtain the maximum fluorescence intensities wavelengths of the monomer and excimer bands. Then, the samples were heated from 278 K to 328 K with a heat ramp of 0.8 K min^{-1} and then cooled down from 328 K to 278 K. Fluorescence intensity at the maximum of the monomer and excimer bands was recorded every 0.5 K. Between both temperature ramps, another complete scan was performed at 328 K. The ratio between the maximum emission of the monomer band and that of the excimer band Q (T), was fitted with an empirical equation (LIR, Equation 1). This fitting was

numerically derived with respect to temperature, dQ(T)/dT, to estimate the absolute sensitivity (S_a) values for each temperature using Equation S1, and from these values it is possible to calculate the relative sensitivity (S_r).

Dynamic Light Dynamic Light Scattering (DLS) measurements were performed with a Zetasizer Nano ZS from Malvern Instruments at RT, for colloidal characterizations and to study their stability at different temperatures. This equipment allows to measure the hydrodynamic size and the Z-potential of the ONPs. In each measurement, the equipment performs 3 replicates.

3. Statistical Analysis

For the calculation of sensitivity, it was used an empirical Equation 1, and its derivative Equation S1 and 2. Sample size for dialysis measurements is n=3 and for confocal fluorescence intensity in C. elegans n=6 and p was calculated using the normal distribution function and cumulative normal distribution table. The software used for analysis and graphical representation was OriginPro. Confocal image quantification was performed using ImageJ/Fiji software, and 3D representation images were deconvoluted using the software Huygens Professional Software v17.10.0p8 (Scientific Volume Imaging B.V., Leiden, The Netherlands) and Imaris x64 v7.2.1 software (Bitplane, Zurich Switzerland) with Surpass Mode.

4. Preparation of TTM radical doped ONPs suspensions

A 2 mM solution of molecular components containing 20 % w/w of TTM radical and 80 % w/w of TTM-αH was prepared in THF (2 mL). The resulting red solution was filtered through a PTFE filter of 220 nm and a diameter of 1.3 cm to remove possible impurities. Then, to prepare the ONP suspension, 0.5 mL of the latter solution (unless elsewhere indicated) was slowly dropped at a speed of 1 mL h^{-1} with a 1 mL Hamilton syringe (Ref: CAL81330), and a syringe pump (KDS 100 Legacy Single Syringe Infusion Pump - 220 VAC) into MilliQ water (9.5 mL, unless elsewhere indicated) at RT, under vigorous stirring (1000 rpm) and the resulting 20 % TTMd-ONP suspension was stored at 277 K in the dark. For the preparation of ONP suspensions with 15 % and 25 % w/w of TTM radical, the same protocol was used. In all cases, the resulting TTMd-ONPs suspensions have 5 % v/v of THF in water (unless elsewhere indicated). For some experiments the remaining TTF solvent was removed by dialysis, as follows: 10 mL of ONPs suspension were dialyzed in 2 L of MilliQ water. Water was changed approximately every 8 hours during 48 hours (three times per day). After dialyzing the ONPs suspensions, different amounts of KCl salt were added to yield aqueous ONPs suspensions with different ionic strengths corresponding to 50, 100, and 150 mM

KCl concentrations. PBS solutions at different *pH* were also prepared adding to the dialyzed ONPs suspensions KCl to achieve a concentration of 100 mM and Na_2HPO_4 and NaH_2PO_4, as reported in **Table S1**. Finally, the *pH* was adjusted by adding 2 N HCl or NaOH aqueous solution until the desired *pH* value was obtained. The *pH* values were measured with a *pH* meter HI 5521 (Hanna Instruments).

Table S1. Amounts of mono- and bi-basic sodium phosphate salts used for the preparation of PBS solutions at different *pH*. KCl in a concentration of 100 mM was added to suspensions to increase the ionic strength to a value of ~150 mM.

pH	Na_2HPO_4 (mM)	NaH_2PO_4 (mM)
5	0.11	8.22
6.5	2.512	6.29
8	7.76	0.57

ONPs suspensions for the thermal stress study were prepared without the addition of KCl, but adding Na_2HPO_4 and NaH_2PO_4, as reported in Table S2, to understand the role played by the different ions on the colloidal stability. Finally, the *pH* was adjusted by adding 2 N HCl or NaOH aqueous solutions until the desired *pH* value was obtained.

Table S2. Amounts of mono- and bi-basic sodium phosphate salts used for the preparation of 25 mM solution (ionic strength corresponding to 150 mM KCl), used for the thermal stress analysis.

pH	Na_2HPO_4 (mM)	NaH_2PO_4 (mM)
5	0.33	24.67
6.5	7.535	17.465
8	23.29	1.71

5. Effect of temperature changes on ONPs emissions

The luminescence intensity of ONPs suspensions was recorded with a Cary Eclipse Fluorescence Spectrophotometer coupled with a temperature controller. The multi-holder of the fluorimeter has four holders for cuvettes. Two cuvettes were filled with water, used as a reference, and the other two with the ONP suspensions. We introduced a thermo-couple in the cuvettes in order to effectively measure the temperature and inside all of them (references and sample) were stirred by a

little magnetic stirrer achieving a uniform temperature control. The emission spectra of ONPs suspensions were tested in the range of temperature 278 – 328 K with a temperature ramp of 1 K min^{-1}. The analyzed samples were excited with a wavelength of 377 nm (at the absorption maximum of ONPs) and it was recorded the intensity at the maximum of monomer (I_M) and excimer (I_E) bands each 0.5 K. In all measurements it was not recorded the entire emission spectrum was not recorded to avoid possible photobleaching effects.

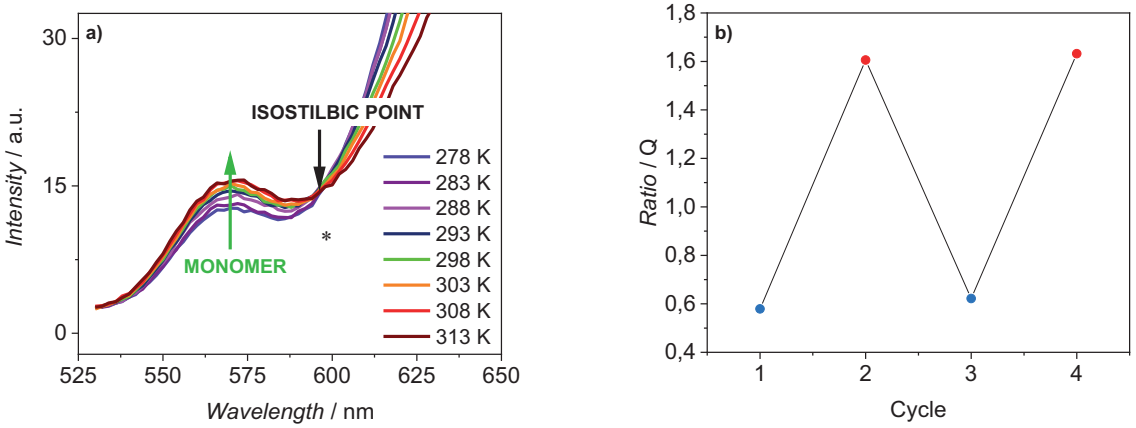


Figure S1. a) Zoom of the temperature effect on the monomer emission showing the isostilbic point; b) Reversibility of the fluorescence emission in water, where Q is the ratiometric output of the sensor, given by the fluorescent intensity ratio, I_M/I_E, where I_M is the intensity at the maximum of the monomer band, and I_E is the intensity at the maximum of the excimer one.

6. Optimization of the ratiometric sensitivity and accuracy of ONPs with different radical doping levels

Temperature dependence of fluorescent intensity ratios, I_M/I_E, of ONPs suspensions were fitted with the empirical equation LIR=a+b·exp(c·T), using Origin 2015® software, and the resulting functions were derived with respect to the temperature ($\partial Q(T)/\partial T$) and the corresponding sensitivity values, S (given in % K^{-1}), were estimated following the Equation S1 for the absolute sensitivity and Equation 2, for the relative sensitivity.

$$S_a = \left|\frac{\partial Q}{\partial T}\right| \times 100\% \ , \ [\% \cdot K^{-1}] \qquad \text{(S1)}$$

where $Q(T)$ is the ratiometric output or LIR of the sensor, given by the fluorescence intensity ratio, I_M/I_E, where I_M is the intensity at the maximum of the monomer band, and I_E is the intensity at the excimer maximum (**Figure S2d**).

The temperature dependence of suspensions of TTMd-ONPs with different TTM radical doping of 15, 20, and 25 % are given in Figure S2a-c and the resulting sensitivities, absolute and relative, in the temperature range of 278-328 K in Figure S2d and e, respectively.

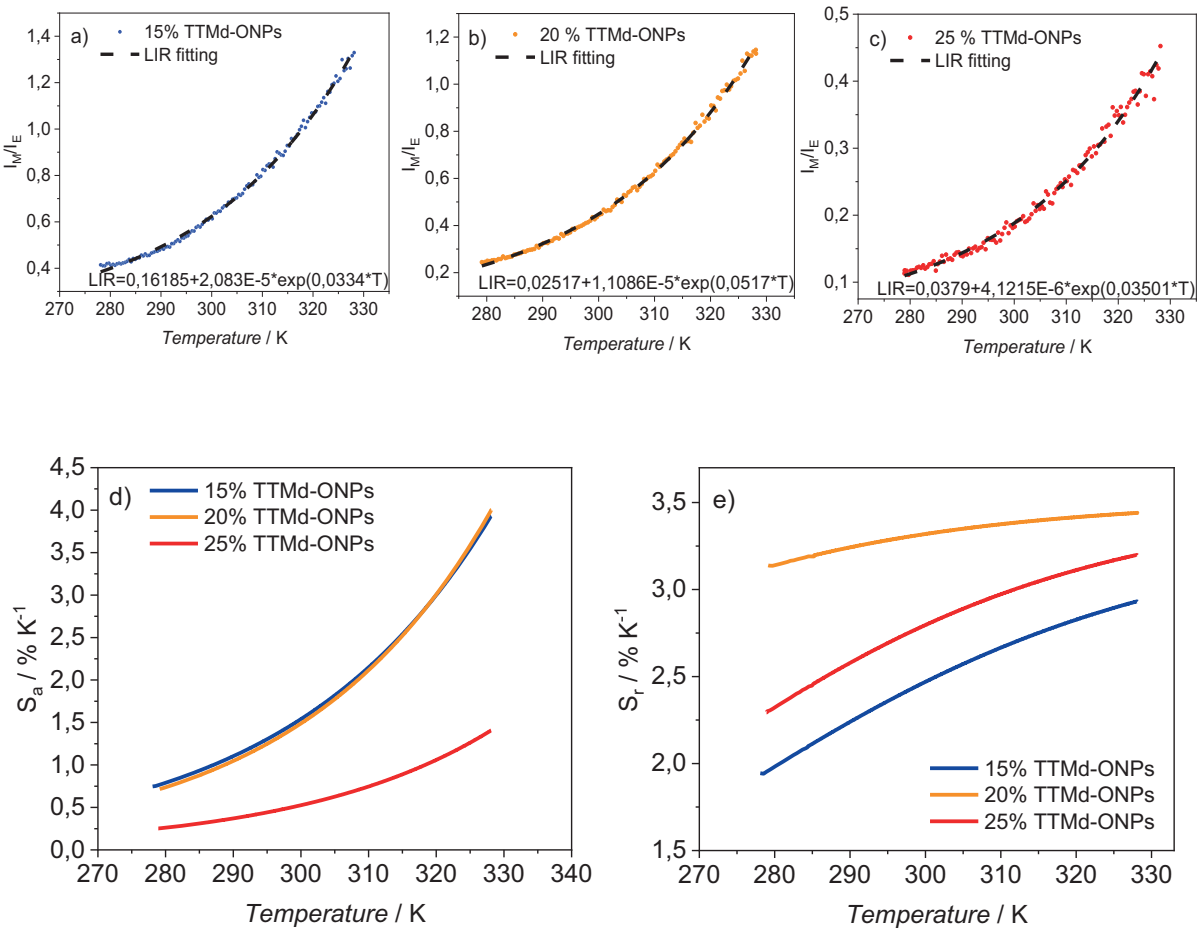


Figure S2. Temperature-dependent ratiometric outputs of TTMd-ONPs suspensions with radical doping of a) 15 %, b) 20 % and c) 25 %. d) Absolute and e) relative sensitivities of the 15, 20, and 25 % TTMd-ONPs suspensions.

The smallest detectable temperature changes, or minimum temperature resolution, ΔT_{min}, is another crucial parameter to characterize the accuracy of a nanothermometer. This parameter can be estimated by the following expression, [4]

$$\Delta T_{min} = \frac{\sigma Q}{S_a} \quad \text{(S2)}$$

where σQ is the uncertainty of the measured ratio (I_M/I_E), which apparently is similar at all the studied temperature range, and S_a is the absolute sensitivity.

7. Effect on the ratiometric sensitivity of dialyzed ONPs suspensions

Finally, as obtained, the aqueous suspension of 20 % TTMd-ONPs was dialyzed in order to remove all content of the organic THF solvent used for their preparation by the re-precipitation method. After the dialysis, the maxima fluorescence intensity ratio, I_M/I_E, was recorded and the sensitivity for the dialyzed suspension was calculated as before. In Figure S3 the temperature dependence of I_M/I_E and the variation of the sensitivities of a 20 % TTMd-ONPs suspension before and after the dialysis are compared with the variation of the sensitivities of a 20 % TTMd-ONPs suspension before and after the dialysis is compared.

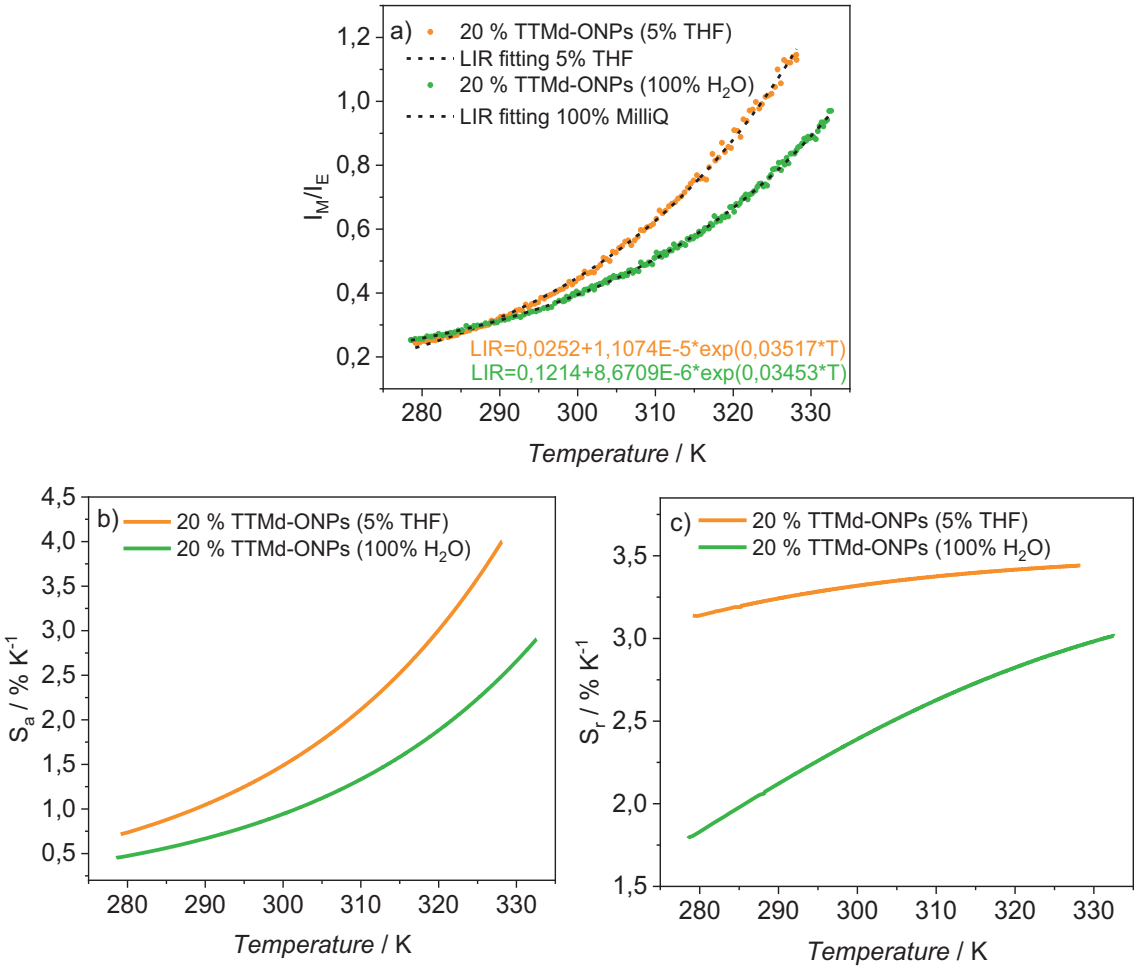


Figure S3. a) Temperature-dependent ratiometric output of 20 % TTMd-ONPs suspension before and after the dialysis. b) Absolute and c) relative temperature sensitivities of 20 % TTMd-ONPs suspensions before and after the dialysis.

8. Characterization of colloidal properties of TTMd-ONPs

Sizes of 20 % TTMd-ONPs were determined by Dynamic Light Scattering (DLS) which was performed with a Malvern Nano ZS using a laser at 633 nm at RT. Each measure consisted of 13

scans and the reported values are given as the averaged value of three measures of 100-150 nm with a low polydispersity index > 0.2, expressed in nm, implying a high monodispersity (Figure S4 right). Due to the high ionic strength of suspensions containing KCl and buffer salts, it was not possible to estimate their Z-potentials. 20 % TTMd-ONPs were also characterized using transmission electron microscopy (TEM) with the aid of negative staining. For that, one drop of the suspension was applied to glow-discharged carbon-coated copper grids (SPI) for 3 min. Subsequently, one drop of 2 % uranyl acetate was placed on the grid for 1-2 min before being drained off. The grid was then placed in a transmission electron microscope (Jeol JEM 1400) operating at an accelerating voltage of 120 kV. Images were acquired using an Orius SC200 (Gatan) showing that ONPs have a spherical morphology (Figure S4 left).[2]

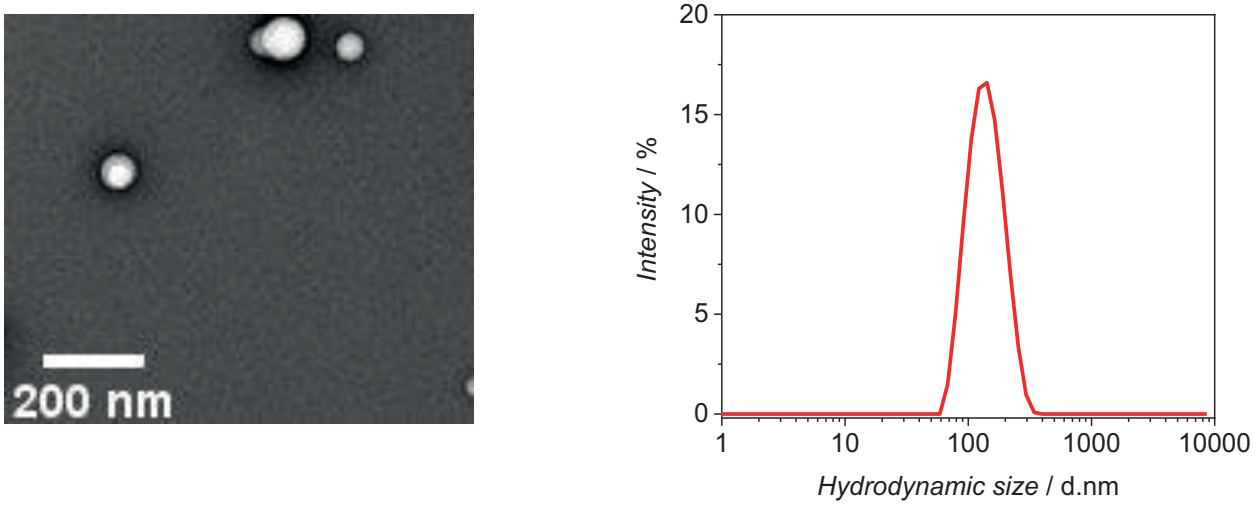


Figure S4. Left) TEM images of 20 % TTMd-ONPs after the dialysis. The size and the morphology of the ONPs are unaffected by the dialysis process showing a spherical morphology. Right) Size distribution of 20 % TTMd-ONPs after the dialysis obtained by DLS.

9. Effect of concentration changes on ratiometric sensitivity of ONPs suspensions

To use the ONPs as ratiometric nanothermometer, it is important to verify that the thermometric parameter (I_M/I_E) is independent of possible concentration fluctuations of ONPs since they may accumulate differently in specific areas of the analyzed cells or tissues. The thermometric parameter of 20 % TTMd-ONPs in pure MilliQ water was compared with the one derived by a 1 to 3 volumetric dilution of the original suspension (20 % TTMd-ONPs dil). Results are presented in Figure S5 where it is shown that the outputs of the two suspensions are not exactly the same. In particular, the signal of the diluted sample seems to be slightly shifted compared to the concentrated one. This difference is ascribed to the different scattering in the two suspensions. In order to verify

this assumption, the two signals were normalized with respect to the maximum and the resulting normalized graphs were identical, demonstrating that both suspensions exhibit the same ratiometric outputs as well as the same sensitivities.

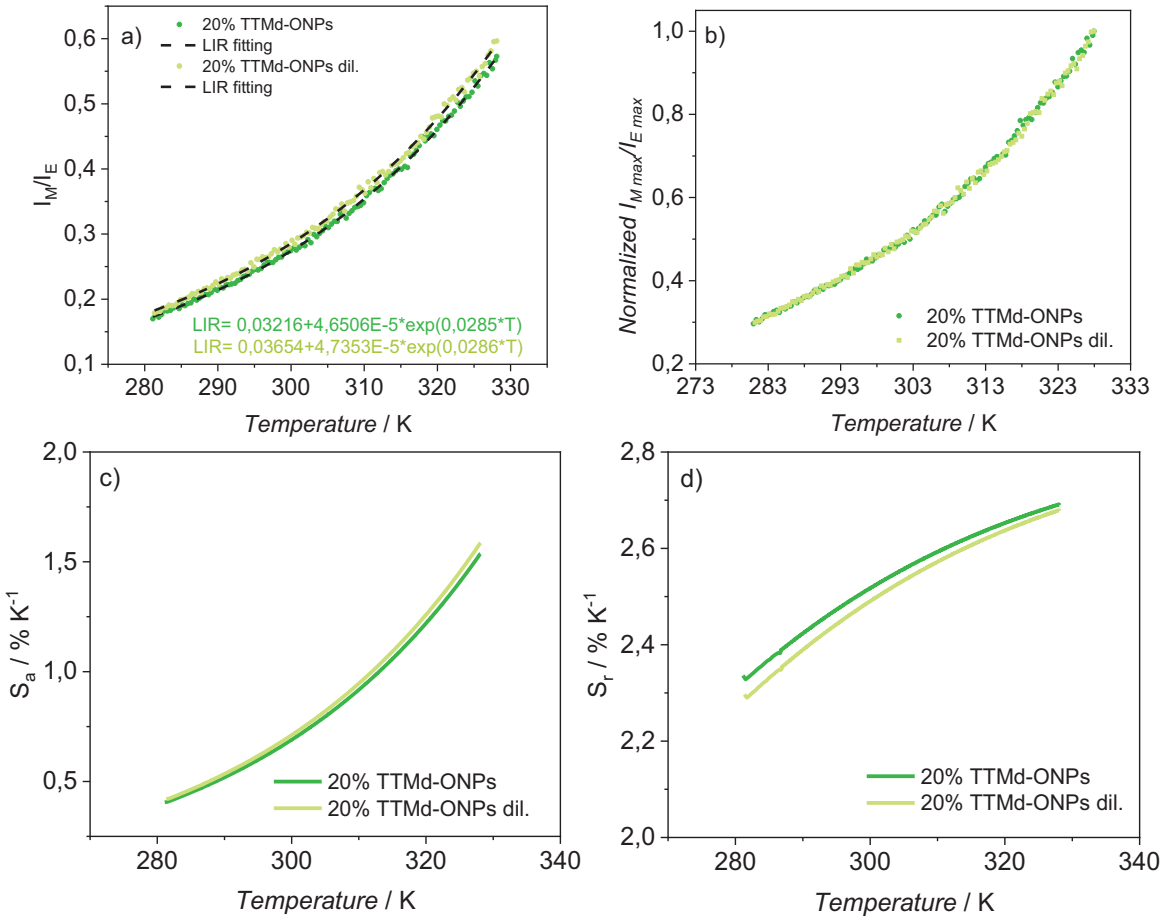


Figure S5. a) Temperature-dependent ratiometric outputs of 20 % TTMd-ONPs suspension in pure MilliQ water and after its 1 to 3 volumetric dilution. b) Normalized temperature-dependent ratiometric output of 20 % TTMd-ONPs suspensions in pure MilliQ water and after its 1 to 3 volumetric dilution 1 to 3. c) Absolute and d) relative temperature-dependent sensitivities of 20 % TTMd-ONPs suspensions in pure MilliQ water and after its 1 to 3 dilution.

10. Effect of *pH* changes over time and temperature of ONPs suspension

To evaluate the stability of the ONPs at different *pH* the size of the ONPs was followed by DLS with time and the fluorescence emission at increasing temperature, and both result in stable nanoparticles at a different *pH*.

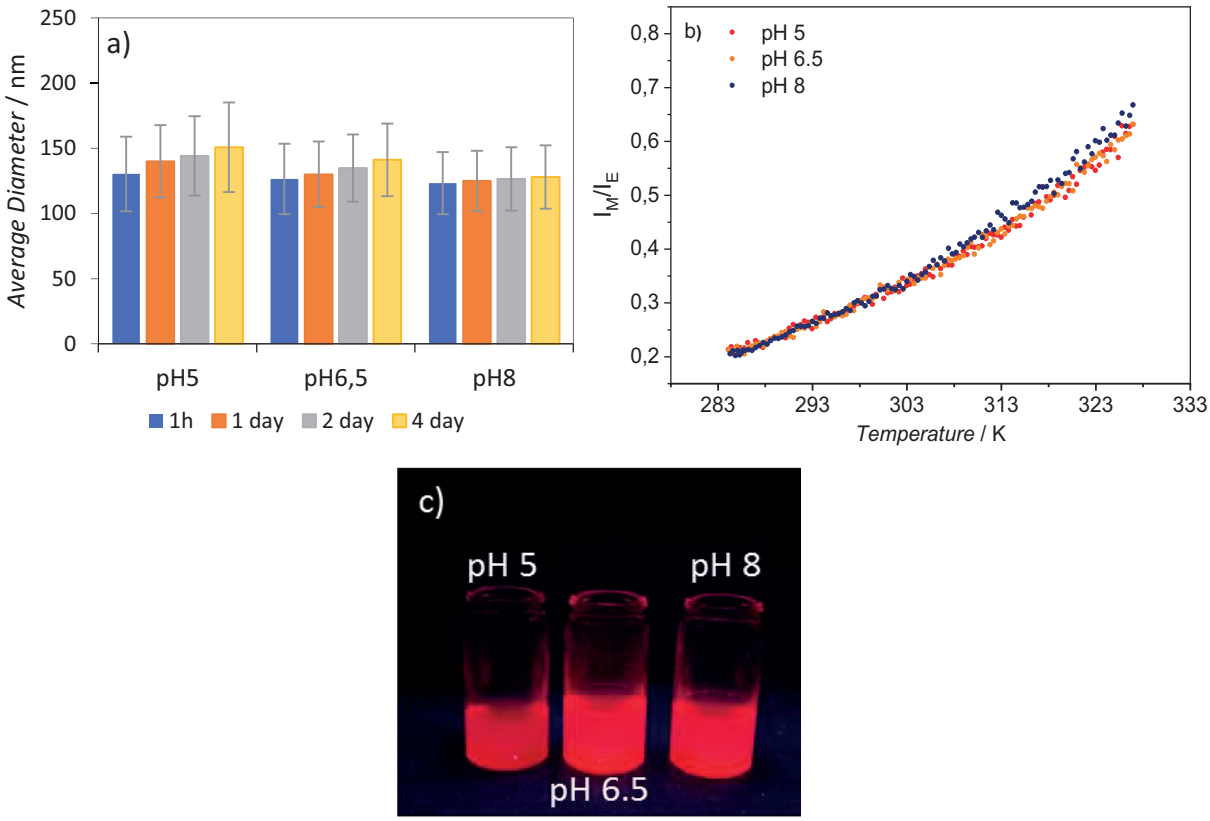


Figure S6. Effect of *pH* on the optical properties and colloidal stability of 20 % TTMd-ONPs suspensions at three different *pH* in the range 5-8 using PBS as buffer media. a) DLS measurement showing a slight increase of ONPs particle size in acidic *pH* during 4-day storing for n=3. b) Evolution of the I_M/I_E fluorescence intensity ratios with temperature changes in the range of 283-328 K. c) Appearance of 20 % TTMd-ONPs suspensions in PBS solution at *pH* of 5, 6.5, and 8 with an λ_{exc} of 365 nm at 298 K.

11. Effect of thermal stress of the colloidal properties of ONPs suspensions at different conditions

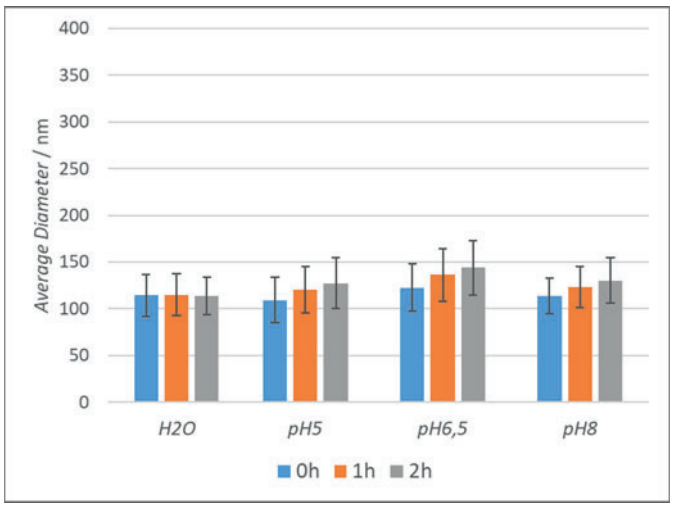


Figure S7. Effect of prolonged thermal stress for two hours at 50 °C on the colloidal stability of 20 % TTMd-ONPs in different conditions, as observed by DLS: pure MilliQ water (H_2O) and PBS solutions with an ionic strength of 150 mM at different *pH* (*pH* 5, *pH* 6.5 and *pH* 8) for n=3.

12. Cell viability, biocompatibility, and fluorescence imaging of ONPs

A (3-[4,5-dimethylthiazol-2-yl]-2,5 diphenyl tetrazolium bromide) (MTT) colorimetric assay was used to evaluate the metabolic activity of cells in the presence of TTMd-ONPs suspensions. For such assay, 5000 COS-7 cells (Monkey African green kidney, SV40 transformed fibroblast-like cells, ATCC) were seeded in a 96-well plate. Different concentrations of ONPs were added, ranging from a 0.7 μM of TTMd-ONPs to 1.4 nM. As the ONPs are conserved in water, the maximum concentration that could be tested in the MTT assay was 175 nM (vehicle 25% water in media). As it is shown in Figure S8, treating cells with a higher proportion of water (vehicle 50% water in media) decreased the viability of the cell culture to 70 %. According to the MTT data shown in Figure S8, concentrations below 35 nM (25% water-media) do not compromise the viability of the treated cells.

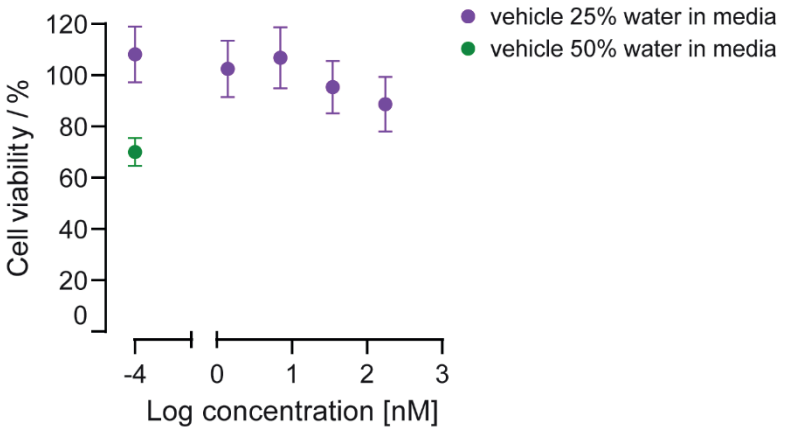


Figure S8. Cell viability assay with COS-7 cells at different ONPs concentrations. The absorbance measurements were performed at 570 nm after 48 h. It can be seen that the 50-50 % water-medium condition induces a negative effect on the culture viability. On the other hand, the concentrations that contain a 25 % proportion of water show no negative impact on the culture.

To further check the biocompatibility of TTMd-ONPs, an in vitro assay on tsa201 cells, a transformed human kidney (293; Sigma Nr. 85120602) cell line stable expressing an SV40 temperature-sensitive T antigen, was also performed using a fluorescence optical microscope. Tsa201 cells were grown on glass supports treated with poly-lysine one day before the measurements. Cells were incubated with a 1:10 dilution of 20 % TTMd-ONPS in MilliQ water suspension for 4 h at 37 °C. Before being analyzed, samples were washed with a buffer solution at room temperature (140 mM NaCl, 5.4 mM KCl, 1 mM MgCl2, 10 mM Hepes, 10 mM Glucose, and 2 mM $CaCl_2$, *pH* 7.4) to remove the excess of ONPs. Acquisition of the images was done with an inverted fully-motorized digital microscope (iMIC 2000, Till Photonics) using an exposure time of 200 ms. ONPs were excited at 380 nm with a polychrome V light source (Till Photonics) using a 505 nm dichroic beam splitter (Chroma Technology). Emission from the excimer was filtered by an ET630/75 nm emission filter (Chroma Technology) and finally collected by a cooled CCD camera (Interline Transfer IMAGO QE, Till Photonics). In Figure S9 are reported the bright field, the fluorescence images, and the merged images of tsa201 cells irradiated at 380 nm after the incubation (4 hours at 37 °C) with 20 % TTMd-ONPs. In such images the luminescence of the ONPs is observed, which confirms their stability in the cell environment, as well as the cells, with ONPs on their cellular membrane, present a healthy aspect (no apoptotic cell morphology) supporting a good biocompatibility of the ONPs.

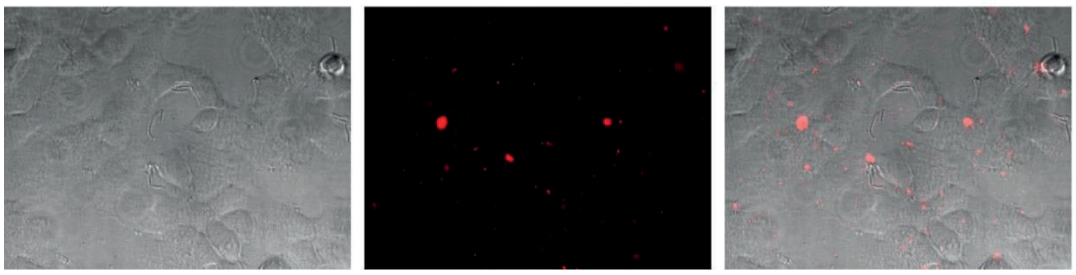


Figure S9. From left to right: bright field image, fluorescence image and merged image of Tsa 201 cells incubated 4 hours at 37 °C with 20 % TTMd-ONPs. Red spots represent the fluorescence of the TTMd-ONPs.

13. Effect of the temperature in the emission of a collection of 20 % TTMd-ONPs deposited on a treated glass surface.

TTMd-ONPs (20 % in MilliQ water (H2O) were incubated on poly-L-Lys (Sigma-Aldrich) pre-treated glass coverslips (16-mm diameter, Fisher Scientific) mounted on a recording chamber (Open Diamond Bath Imaging Chamber for Round Coverslips from Warner Instruments) for 1 hour. After that, the coverslips were washed with an imaging buffer solution at room temperature (140 mM NaCl, 5.4 mM KCl, 1 mM MgCl2, 10 mM Hepes, 10 mM Glucose, and 2 mM CaCl2, *pH* 7.4) to remove nanoparticles that remained in suspension. Imaging was performed on an IX71 inverted microscope (Olympus) with a UApo/340, 40x/1.35 oil immersion objective (Olympus). Nanoparticles were excited during 25 ms every 1 s at 377 nm using a Polychrome V monochromic light source (Till Photonics) equipped with a Xenon Short Arc lamp (Ushio) and a 505 nm dichroic beam splitter (Chroma Technology) and a 585 nm dichroic beam splitter (Chroma Technology). Emission from the monomer was filtered by a D535/40 nm emission filter (Chroma Technology) and for the excimer by an ET630/75 nm emission filter (Chroma Technology) and finally collected by a C9100-13 EM-CCD camera (Hamamatsu).

Temperature variation in the recording chamber was carried out by perfusing the imaging buffer solution that was previously heated or kept cold. Fast switching of both solutions was done with a VC-6 six-channel valve controller (Warner Instruments Corp.). The temperature in the recording chamber was monitored using a K-type digital thermometer (Kosmon) at the accessory pool of the recording chamber.

Imaging analysis was done with FIJI software (ImageJ) and analysis of the obtained data was done with Excel and Prism Graphpad software.

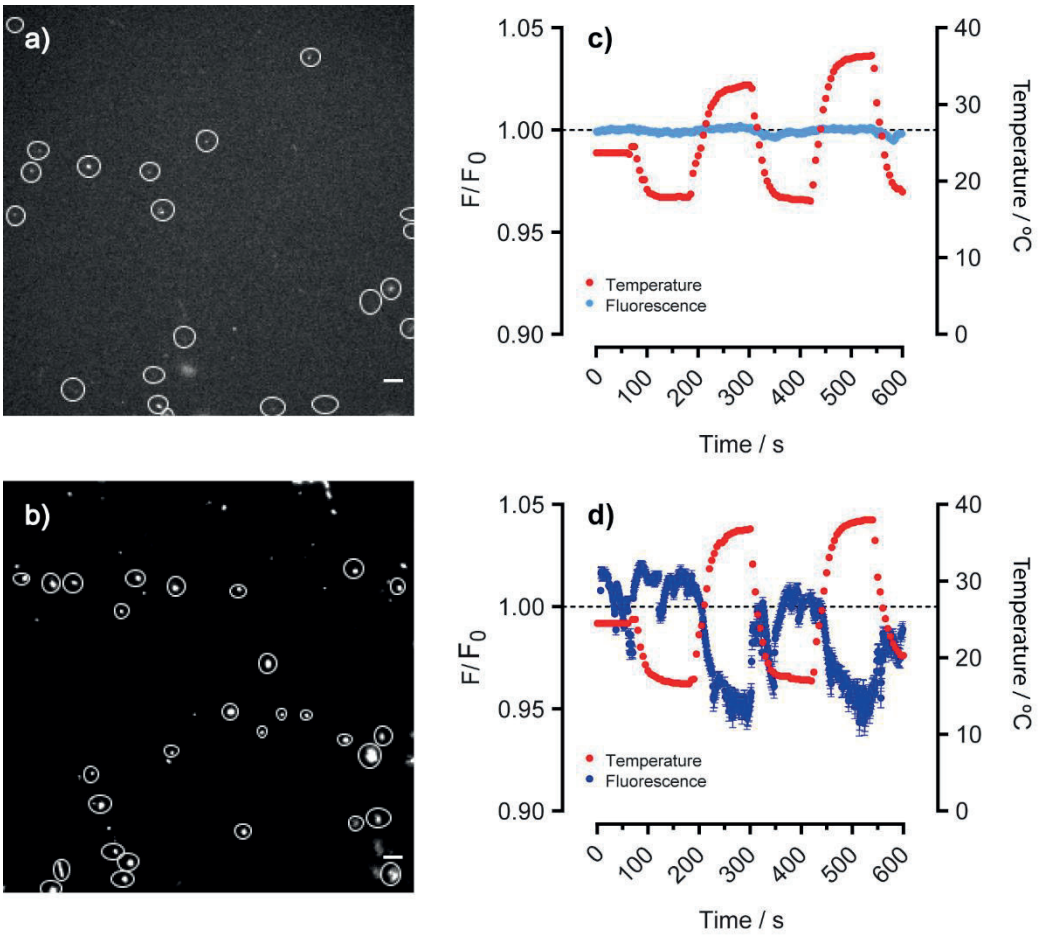


Figure S10. Fluorescence microscopy images corresponding to TTMd-ONPs with different aggregation levels excited at λ_{exc}= 377 nm and detected with a 510-560 nm filter, corresponding to the emission of monomers (a), and with a 595-670 nm filter for the excimers (b). Real-time variation of relative fluorescence intensity signals (F/F_0) with temperature changes up to 20 degrees emitted by the monomers (c) and by the excimers (d), in all nanoparticles inside ROIs shown in a) and b) respectively (N=21 for the monomer and N=29 for the excimer). ROIs shown in b) and plotted in d) correspond to 29 of the 35 total selected ROIs, that displayed temperature-dependent changes in relative fluorescence intensity (83 % of the selected ROIs). Scale bar, 10 µm.

14. Stability of ONPs in M9 buffer

15. M9 buffer (3 g of KH_2PO_4, 6 g of Na_2HPO_4, 1 mL of 1 M of $MgSO_4$ and 5 g of NaCl per liter of miliQ H_2O)

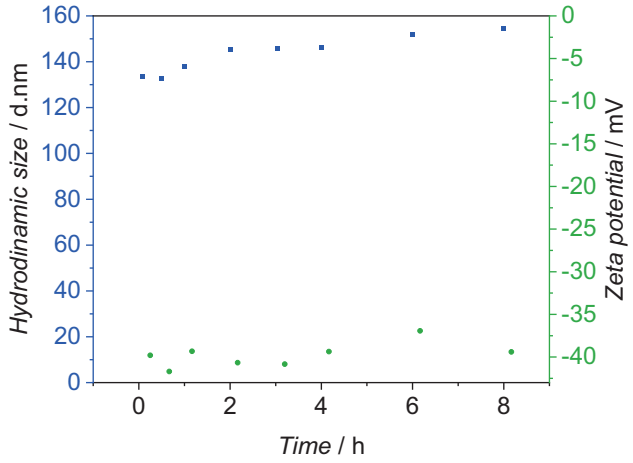


Figure S11. Effect of M9 buffer on the colloidal stability of 20 % TTMd-ONPs during 8 hours.

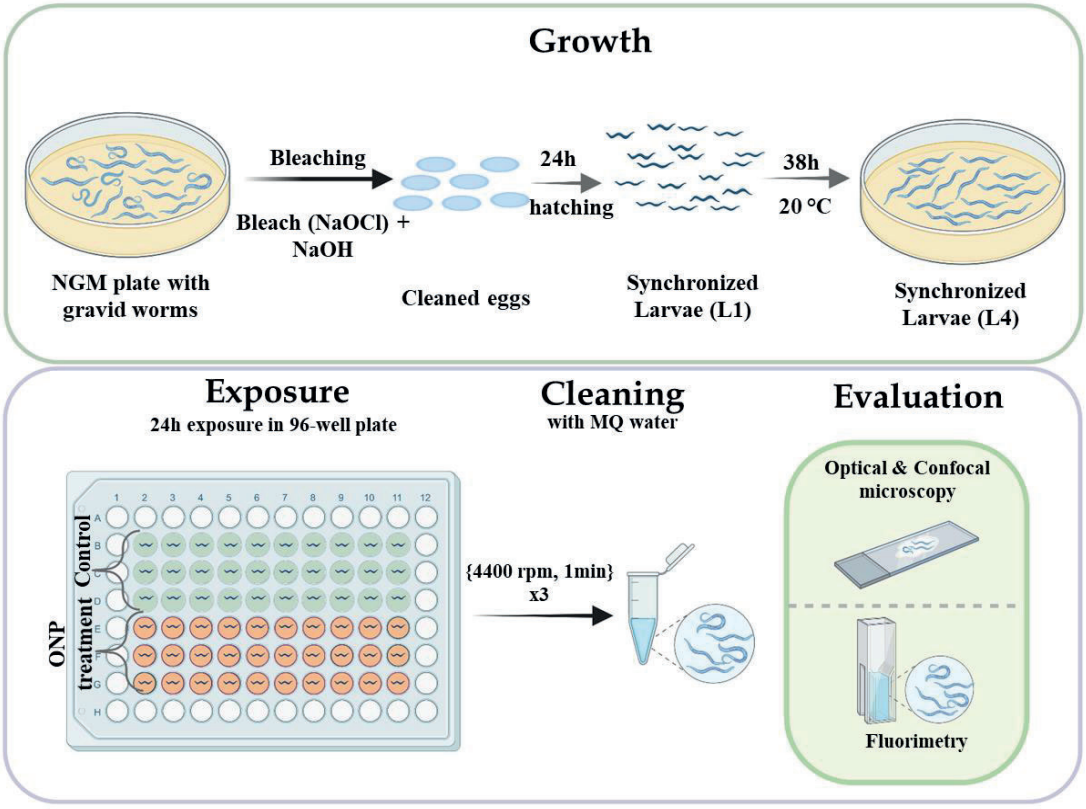
16. Growth, treatment of *C. elegans* with ONPs and imaging.

The *C. elegans* used in this work are wild-type strain (N2), purchased from Caenorhabditis Genetics Center, Minnesota (USA). Nematode growth media plates (NGM) containing agar, peptone and NaCl were used for maintaining the worms at 293 K in the laboratory. M9 buffer (3 g of KH_2PO_4, 6 g of Na_2HPO_4, 1 mL of 1 M of $MgSO_4$ and 5 g of NaCl per liter of miliQ H_2O), is used to maintain the worms alive and healthy in liquid environment such as during hatching from eggs to larva and during exposure of the worms to the nanoparticles. The *Escherichia coli* strain OP50 is used as a bacterial food source in the laboratory for *C. elegans*. Usually, 550 µL of OP50 is spread on top of the solidified NGM plates and incubated at 303 K overnight prior to further use for *C. elegans* cultivation.

For liquid exposure of ONPs to *C. elegans*, heat-killed OP50 is used. The liquid culture with alive OP50 is heat-killed at 353 K for 30 min and washed to remove debris and toxins from heat treatment. The warms are re-suspended in equal volume of M9 buffer. It is important to use heat-killed OP50 so that they do not interfere with the ingestion of ONPs during co-administration to *C. elegans*.

C. elegans are exposed to the nanoparticles when all of them have attained a synchronized L4 larval stage. First, eggs from gravid worms are collected through a process called bleaching (Figure S12).

When the NGM plates reach confluency with mostly gravid worms, the worms are treated with household bleach (sodium hypochlorite) and sodium hydroxide under vortex or vigorous shaking. This process dissolves the mother worms and releases the eggs into the solution, which is washed several times with M9 buffer by centrifugation to clean the excess bleach mixture and debris. The eggs were placed in M9 solution and kept for 24 hours to hatch and become Larvae (L1). Bleaching and collecting eggs is crucial for experiments where age synchronized population is needed, such as in the case of studying the effect of treatment of any substance. The synchronized L1 population is then transferred to NGM plates containing OP50 and the worms are grown at 293 K for ≈38 hours, or until the population is at a synchronized L4 larval stage. L4 worms were collected from NGM plates in M9 buffer and exposed to ONPs in a 96-well plate. The experiment consists of two treatment groups, untreated (control) and ONP-treated *C. elegans.* The exposure in liquid system is carried out for 24 hours so that at the end of exposure during imaging and analysis, we have a population of a single generation of fully-grown adult worms with eggs inside. Each well consists of ≈20-25 worms (in 3 µL M9), 5 µL of OP50, 42 µL of M9, and lastly, 50 µL of TTM ONPs aqueous suspension (110 µg mL^{-1}) for ONP treated group or 50 µL MilliQ water for the control



group. In total, we will have 50 µL of M9 buffer and 50 µL MilliQ water per well to provide an optimal system for both ONPs dispersion as well as *C. elegans* growth condition.

Figure S12. Growth of synchronized population of *C. elegans,* exposure to ONPs & evaluation of ONP inside the worms.

After 24 hours, the worms were washed several times with MilliQ water by centrifugation remove all debris and excess non-ingested nanoparticles in order to obtain clean control and treated worms. For microscopic imaging, *C. elegans* were fixed using 8 % PFA in equal volume to the worms' suspension. When the worms are fixed, and no swimming movement is observed (~2 min), the slide is sealed using a cover glass and nail polish. The imaging was carried out with a fluorescence microscopy Olympus BX51 microscope with digital camera Olympus DP20 y reflected fluorescence system Olympus U-RFL-T at magnifications 5X and 20X, with UV and GFP filters. The intensity of fluorescence under both the filters war quantified using ImageJ and statistical analysis was performed using Mann Whitney test.

17. Survival rates of *C elegans* to ingested ONPs and temperature changes

After 24 hours of exposure, both the untreated control and the ONP treated worms are counted by observing directly under the microscope. Worms are considered dead if they are not moving even after a gentle push with a filament. The survival rate is calculated as,

$$\{Number\ of\ alive\ worms \div total\ number\ of\ worms\} \times 100$$

Body length of the worms in the control and treated group was measured from the microscopic images using ImageJ. In the second control experiment, the survival rate of *C. elegans* at different temperatures was investigated. A healthy synchronized adult population of *C. elegans* was collected in an Eppendorf tube in M9 buffer. Then, the Eppendorf tube was placed in a thermo-shaker (BioSan TS-100), equipped with a plate (BioSan SC-24 block) for Eppendorf tubes. The sensitivity of worms to different temperatures was calculated, in the temperature range from 293-328 K with steps of 5 K. Worms were incubated at each temperature was 2 min to disperse the heating and stabilize the solution to the temperature. A known volume of the suspension was added to the glass slide to count number of dead and alive worms at each temperature. Sometimes, under extreme conditions, the *C. elegans* enter a stage called Dauer state (dormant state), which is adopted to protect themselves from stressful conditions. In this stage, the worms remain motionless, so they can be confused with dead ones. Therefore, after heating up to 328 K, worms were placed on a plate with food until the next day, to check if they can recover into their normal life cycle. However, none of the worms recovered after heating to 328 K and were declared as dead. Table S3 shows the observed survival rates at the assayed temperatures showing that *C. elegans* can be used as an in

vivo model system for validating ONPs as nanothermometers only at temperatures between 293 and 308 K.

Table S3. Survival rates of *C. elegans* at different temperatures

Temperature (K)	Total worms	Dead worms	Survival rate (%)
293	124	3	98
298	70	10	86
303	55	14	75
308	65	18	72
313	62	51	17
318	60	60	0
323	56	56	0
328	51	51	0

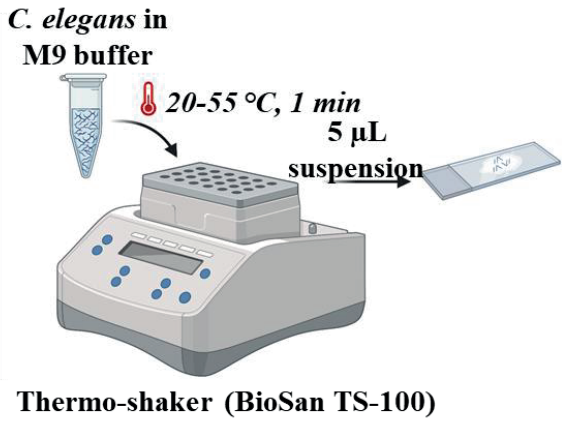


Figure S13. Experimental setup for measuring temperature sensitivity of *C. elegans*

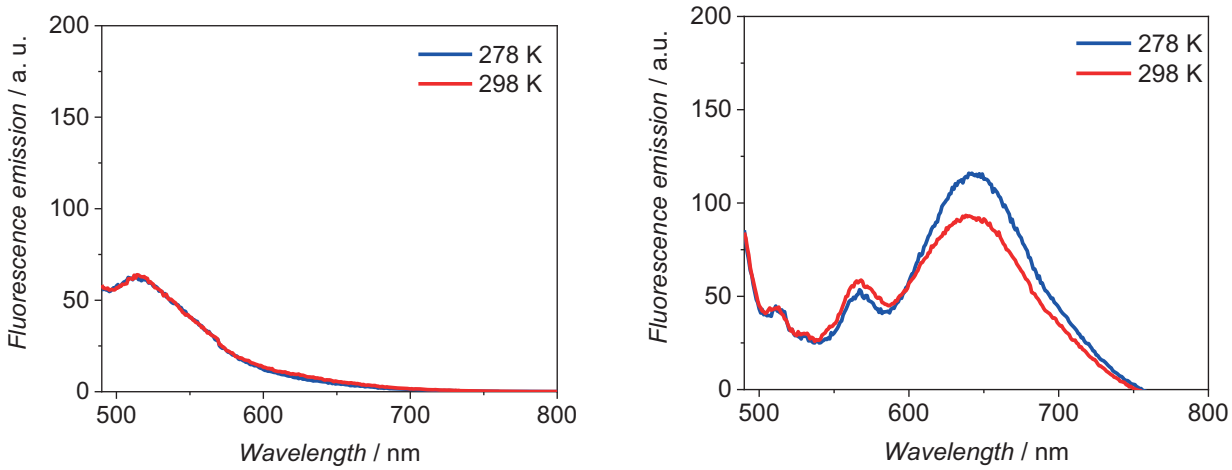


Figure S14. Left) Emission spectra of *C. elegans* control group without TTMd-ONPs. Right) Emission spectra at two different temperatures *C. elegans* exposed to 20 % TTMd-ONPs. Spectra recorded at two different temperatures with an excitation wavelength λ_{exc} =337 nm.

18. Preparation of samples for confocal microscopy

To record a local temperature, change confocal images were taken at different temperatures, focusing on a single *C. elegans*. To ensure a good acquisition of the images and avoid movement of live *C. elegans*, NemaGel (InVivo Biosystems) was used to immobilize them. Briefly, a drop of the sample (*C. elegans* suspension in M9) was placed in the middle of a 35 mm diameter plate (ibiTreat; Ibidi GmbH, Germany) and a drop of NemaGel was placed on the cover glass. The cover glass was then inverted and gently placed over the liquid drop of worms so that NemaGel is able to trap and immobilize the worms. After 2 mins, the worms are immobilized and visualized under the microscope.

19. Confocal Microscopy and Image Processing

Confocal microscopy analysis was performed on a Leica TCS SP8 microscope equipped with a white light laser and Hybrid spectral detectors (Leica Microsystems GmbH, Mannheim, Germany). The confocal images were acquired using an HC PL APO 63×/1.4 oil immersion objective with a 1 AU pinhole. Both types of nanoparticles were excited with a blue diode laser (405 nm) and detected in the 420–570 nm and the 620–720 nm range, respectively. Fluorescence and transmitted light imaging were combined to study the nanoparticles' distribution inside *C. elegans*. An image acquisition sequence xyz for both channels was used to acquire the 3D stacks. The image format chosen was 12-bit and 1024 × 1024 pixels resolution. Ten sections (step size= 1.5 μm) were acquired to get an image volume stack along the organism thickness. Appropriate negative controls were used to adjust confocal settings and avoid non-specific fluorescence artifacts. Image quantification of the integrated density (sum of the intensity of all the pixels in the area delimited by the mask) was performed using ImageJ/Fiji software (NIH, Bethesda, MD, USA). The ratio of red versus green fluorescence was calculated within a representative region of each image. Finally, 3D representation images were deconvoluted using the software Huygens Professional Software v17.10.0p8 (Scientific Volume Imaging B.V., Leiden, The Netherlands) in order to improve image quality and resolution. 3D models were generated with Imaris x64 v7.2.1 software (Bitplane, Zurich Switzerland) with Surpass Mode.

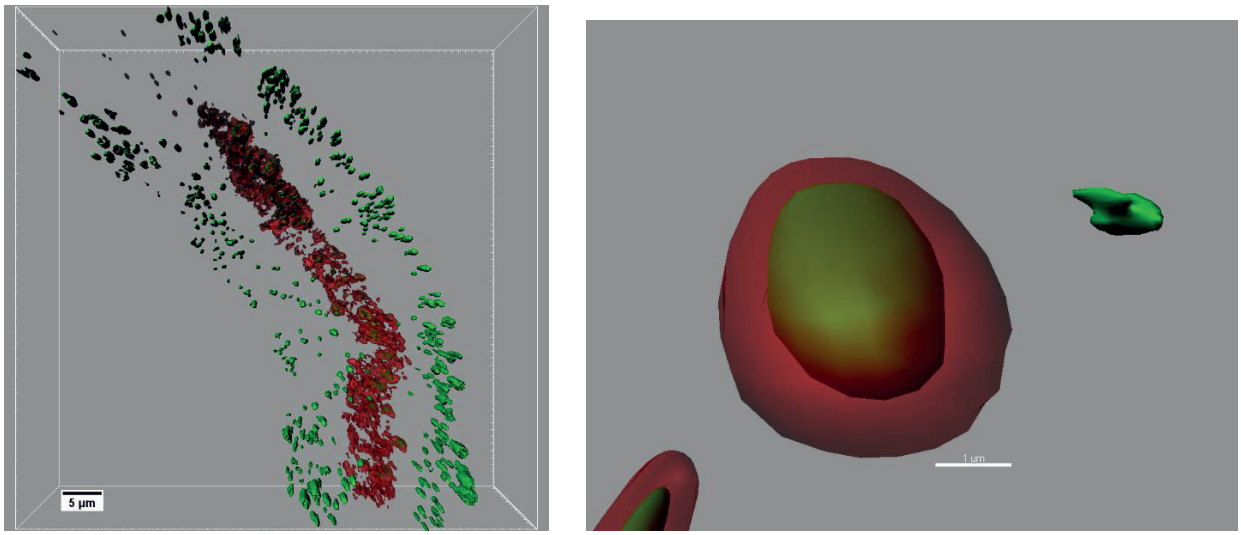


Figure S15. Representative 3D model reconstruction from the confocal stack images of a *C. elegans.* Left) Part of the body, showing the TTMd-ONPs (red) inside the intestine and the lipids (green); Right) Zoom of a small area showing emission of monomer (green) and excimer (red) of a single TTMd-ONPs particle/aggregate. The shell structure of the two different emissions is due to the treatment of the images with two emission channels for which the most intense luminescence stays always outside.

20. Ratiometic output (Q) from confocal analysis of the top part of *C. elegans*

Confocal images were analyzed to see if the ratio (Q) with temperature was following the same trend as the suspension of the ONPs. Figure S16 represents the data of the top part of the *C. elegans* body. Around the pharynx of *C. elegans* a higher amount of lipids is concentrated, which are autofluorescence and influence the overall fluorescence emission.

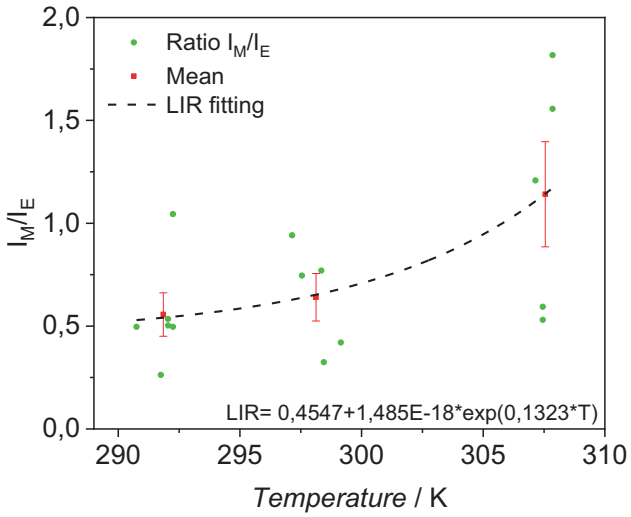


Figure S16. Ratio (Q) between monomer and excimer maxima fluorescence emission at an increasing temperature of the TTMd-ONPs inside *C elegans*, from a region of the top of the body. Red points represent the average of the ratios and the error bars are the deviation caused by different worms for the same temperature range, for n= 6 and p= 0.8419, 0.7675 and 0.7390, respectively.

References

[1] M. Ballester, J. Riera, J. Castañer, C. Rovira, O. Armet, *Synthesis (Stuttg).* **1986**, 64.

[2] O. Armet, J. Veciana, C. Rovira, J. Riera, J. Castaner, E. Molins, J. Rius, C. Mirvitlles Torras, S. Olivella, J. Brichfeus, *J. Phys. Chem.* **2013**, *91*, 5608.

[3] H. Kasai, H. S. Nalwa, H. Oikawa, S. Okada, H. Matsuda, N. Minami, A. Kakuta, K. Ono, A. Mukoh, H. Nakanishi, *Jpn. J. Appl. Phys.* **1992**, *31*, L1132.

[4] J. Zhou, B. del Rosal, D. Jaque, S. Uchiyama, D. Jin, *Nat. Methods* **2020**, *17*, 967.

Chapter 6
General conclusions and future perspectives

The convergence of nanotechnology and molecular design has propelled the development of functional nanostructured molecular materials, unlocking unprecedented potential for their utilization in diverse biological applications. This doctoral dissertation has focused on the preparation and characterization of biologically applicable functional nanostructured molecular materials in an effort to address current biological challenges.

Several conclusions have been reached from the research performed:

- In response to the demand for new antimicrobial agents to fight the current antibiotic crisis, a novel biofunctionalized surface with antibacterial properties has been designed, synthetized, and thoroughly characterized. The strategy is based on the successful immobilization of novel antimicrobial proteins on gold using SAMs. A biofilm assay confirmed the bactericidal effect of the functionalized surface. Other potential uses for this promising platform include coating surfaces of relevant medical devices (like catheters) or for food packaging materials.

- After using a gold model surface, a new methodology to functionalize medical grade TPU surfaces, in a disc shape, has been successfully developed using a three-step procedure. After a key activation step, TPU discs were functionalized with mixed SAMs of PEG derivatives and the antimicrobial proteins were anchored to them in order to confer bactericidal properties to the TPU surface. The strategy was confirmed through a multi-technique characterization approach which include XPS, CA, FTIR-ATR, SEM and AFM. Additionally, the biofilm assay verified that immobilizing the antimicrobial protein prevents three important hospital-associated bacterial strains from forming biofilms. This strategy opens up new perspectives for the use of controlled covalent anchoring of bioactive molecules on TPU for different biomedical applications such as coating the surfaces of medical devices like catheters to avoid nosocomial infections.

- The developed strategy has been adapted for the functionalization of the inner and outer surface of real TPU catheters. The strategy has been optimized to become biocompatible to human cells and highly stable in static (after sterilization and 3 months stored at 37°C) and dynamic conditions, mimicking

the real *in vivo* flow with an MRD. Following these insights, *in vivo* experiments in a rabbit model were carried out. However, the coating of the catheters developed could not inhibit biofilm formation *in-vivo*. In this configuration, the established functionalization may be primarily used to prevent infections, rather than treating them once arisen. In the future, the coating will be improved to enhance the accessibility of the active proteins to the biofilm-forming bacteria.

- Finally, it has been used another strategy using nanotechnology and molecular design to develop functional nanostructured molecular materials based on ONPs for biomedical applications. For instance, the trichlorotriphenylmethyl (TTM) radical has been used to synthesize fluorescent ONPs with high sensitivity and stability in various conditions. The ONPs exhibit fluorescence at two different emission wavelengths, one linked to excimer species and the other to monomers. The excimer band, which is in the attractive "first biological window", is studied at different temperatures and shows extremely sensitive ratiometric nanothermometer behavior. Finally, it was shown that these ONPs were not cytotoxic, enabling the use of the ratiometric nanothermometer in an *in vivo* experiment with Caenorhabditis elegans (C. elegans).

Based on these conclusions, this PhD provides insights into different strategies based on nanostructured functional molecular materials to modify surfaces using SAMs and also ONPs for different biomedical applications. Specifically, the use of SAMs to coat the TPU catheters can be transferred to other surfaces like TPU bandages to avoid wound infection or titanium to avoid infections of implants or cardiac medical devices, which is future work in the group. Regarding the application of the radical based ONPs, opens up the possibility to measure internal cell temperature which is a very interesting strategy to obtain more sensitive and selective diagnosis tools.

Annex I: Scientific contributions

Publications that conform this thesis:

Kyvik, A. R.; Roca-Pinilla, R.; Mayolo-Deloisa, K.; Rodriguez Rodriguez, X.; Martinez-Miguel, M.; Martos, M.; Köber, M.; Ventosa, N.; Veciana, J.; Guasch, J.; García-Fruitós, E.; Arís, A.; Ratera, I. Antibiofilm Surfaces Based on the Immobilization of a Novel Recombinant Antimicrobial Multidomain Protein Using Self-Assembled Monolayers. *Mater. Adv.* **2023**, 4 (10), 2354– 2364, DOI: 10.1039/D2MA00978A

Blasi, D.; Gonzalez-Pato, N.; Rodriguez Rodriguez, X.; Diez-Zabala, I.; Srinivasan, S. Y.; Camarero, N.; Esquivias, O.; Roldán, M.; Guasch, J.; Laromaine, A.; Gorostiza, P.; Veciana, J.; Ratera, I. Ratiometric Nanothermometer Based on a Radical Excimer for In Vivo Sensing. *Small* **2023**, 19, 2207806. DOI: 10.1002/smll.202207806

Rodriguez Rodriguez, X.; Lopez-Cano, A.; Mayolo-Deloisa, K.; Pich, O.; Bierge, P.; Ventosa, N.; García-de-la-Maria, C.; Miró, J.; Gasch, O.; Veciana, J.; Guasch, J.; Arís, A.; Garcia Fruitos, E.; Ratera, I. Activating Thermoplastic Polyurethane Surfaces with Polyethylene Glycol-Based Recombinant Human α-Defensin 5 Self-Assembled Monolayers for Infection Prevention. Submitted. **2024**

Rodriguez Rodriguez, X.; Lopez-Cano, A.; Mayolo-Deloisa, K.; Gómez-Sánchez, I.; Bierge, P.; Pich, Oscar; Ventosa, N.; García-de-la-Maria, C.; Miró, J.; Gasch, O.; Veciana, J.; Guasch, J.; Garcia Fruitos, E.; Arís, A.; Ratera, I. Stable Surface Coating of Thermoplastic Polyurethane Catheters with Tailored Recombinant Multidomain Protein -Towards In-Vivo Infection Prevention. Manuscript to be submitted.

Publications within the scope of this thesis

López-Cano, A.; Ferrer-Miralles, N.; Sánchez, J.; Carratalá, J.V.; Rodriguez, X.R.; Ratera, I.; Guasch, J.; Pich, O.Q.; Bierge, P.; Garcia-de-la-Maria, C.; et al. A Novel Generation of Tailored Antimicrobial Drugs Based on Recombinant Multidomain Proteins. *Pharmaceutics* **2023**, 15, 1068, DOI: 10.3390/pharmaceutics15041068

Publications outside the scope of this thesis

Pérez del Río, E., Santos, F., Rodriguez Rodriguez, X., Martínez-Miguel, M., Roca-Pinilla, R., Arís, A., Garcia-Fruitós, E., Veciana, J., Spatz, J. P., Ratera, I., Guasch, J. CCL21-loaded 3D hydrogels for T cell expansion and differentiation. *Biomaterials,* **2020**, 259, 120313. DOI: 10.1016/j.biomaterials.2020.120313

Santos, F.; Valderas-Gutiérrez, J.; Pérez Del Río, E.; Castellote-Borrell, M.; Rodriguez, X.R.; Veciana, J.; Ratera, I.; Guasch, J. Enhanced human T cell expansion with inverse opal hydrogels. *Biomater. Sci*. **2022**, 10, 3730–3738. DOI: 10.1039/D2BM00486K

González-Pato, N., Rodriguez, X. R., Pellizzi, N., Fasolato, C., Guasch, J., Postorino, P., Veciana, J., Goñi, A. R., & Ratera, I. Electroactive substrates for surface-enhanced Raman spectroscopy based on overgrown gold-nanoparticle arrays by electrodeposition on indium tin oxide. *Materials Advances*, **2023**, 4(5), 1378–1388. DOI: 10.1039/D2MA00914E

European Patents

Guasch, Judit; Ratera, Imma; Veciana, Jaume; Pérez, Eduardo; Martínez, Marc; Rodríguez, Xavier; Santos, Roberto Fabião; Mateos, Miguel Ángel; Engel, Elisabeth. A SYNTHETIC HYDROGEL AND ITS USE FOR IMMUNOTHERAPY AND 3DPRINTING. EP3913048, 2021 (in national phases in Europe and USA).

Contributions at scientific conferences

- **Poster**

Rodriguez Rodriguez, X., Kyvik, A., Roca-Pinilla, R., Martinez-Miguel, M, Martos, M., Veciana, J., Guasch, J., Garcia-Fruitós, E., Arís, A., Ratera, I. Anti-biofilm surfaces based on the immobilization of a novel recombinant antimicrobial protein using SAMs. NanoBioMed (NBM2020) Flash oral presentation. Online Conference 2020.

Rodriguez Rodriguez, X., Lopez-Cano, A., Roca-Pinilla, R., Kyvik, A., Veciana, J., Guasch, J., Arís, A., Garcia-Fruitós, E., Ratera, I. Thermoplastic polyurethane modified with a self-assembly monolayer to immobilize antimicrobial proteins as anti-biofilm coating. E-MRS 2021 Fall Meeting. Flash oral presentation. Online conference 2021.

- **Oral presentations**

Rodriguez Rodriguez, X., Kyvik, A., Roca-Pinilla, R., Martinez-Miguel, M, Martos, M., Veciana, J., Guasch, J., Garcia-Fruitós, E., Arís, A., Ratera, I. Anti-biofilm surfaces based on the immobilization of a novel recombinant antimicrobial protein using SAMs. The 5th Scientific Meeting of PhD students at UAB campus (JPhD2020) Online conference 2020.

Contributions in scientific projects

Research activities presented in this manuscript have been conducted in the framework of different research projects and networks:

FUNCATH. Prevention of vascular catheter-related infections by the FUNctionalization of CATHeters with antimicrobial agents of broad spectrum. La Fundació de TV3 Ref.: 75/C/2018. Nr. 201812; 06/2020 to 05/2023; Coord.: Dr. Oriol Gasch; PI: I. Ratera.

MOL4BIO. Processing molecules to create hybrid materials hierarchically structured for biomedical applications; MICIIN PID2019-105622RB-I00; 06/2020 to 12/2023; PI: N. Ventosa and I. Ratera

NANORESIST. Engineering Novel Nanodelivery Systems against Antimicrobioal Resistance; EU-MSCA; ACCIO TECNIO Spring Industry TECSPR19-1-0065; 05/2021 to 04/23; PI: K. Mayolo; Scientific supervisor: I. Ratera

CIBER-BBN. Networking Research Center on Bioengineering, Biomaterials and Nanomedicine. PI: N. Ventosa